CONTRIBUTION TO THE DEVELOPMENT OF IMPLICIT LARGE EDDY SIMULATIONS METHODS FOR COMPRESSIBLE TURBULENT FLOWS

A THESIS SUBMITTED TO
THE GRADUATE SCHOOL OF NATURAL AND APPLIED SCIENCES
OF
MIDDLE EAST TECHNICAL UNIVERSITY

BY

MEHMET KARACA

IN PARTIAL FULFILLMENT OF THE REQUIREMENTS
FOR
THE DEGREE OF DOCTOR OF PHILOSOPHY
IN
AEROSPACE ENGINEERING

DECEMBER 2011

Approval of the thesis:

CONTRIBUTION TO THE DEVELOPMENT OF IMPLICIT LARGE EDDY SIMULATIONS METHODS FOR COMPRESSIBLE TURBULENT FLOWS

submitted by **MEHMET KARACA** in partial fulfillment of the requirements for the degree of **Doctor of Philosophy in Aerospace Engineering Department, Middle East Technical University** by,

Prof. Dr. Canan Özgen
Dean, Graduate School of **Natural and Applied Sciences** _____

Prof. Dr. Ozan Tekinalp
Head of Department, **Aerospace Engineering** _____

Prof. Dr. I. Sinan Akmandor
Supervisor, **Aerospace Eng. Dep., METU** _____

Asst. Prof. Dr. Ivan Fedioun
Supervisor, **Mechanical and Energy Eng. Dep., Orléans Univ.** _____

Examining Committee Members:

Research Dir. Iskender Gökalp
ICARE, CNRS _____

Prof. Dr. I. Sinan Akmandor
Aerospace Eng. Dep., METU _____

Assist. Prof. Dr. Ivan Fedioun
Mechanical and Energy Eng. Dep., Orléans Uni. _____

Prof. Dr. Luc Vervisch
Mechanical Eng. Dep., INSA-Rouen _____

Prof. Dr. Metin Muradoglu
Mechanical Eng. Dep., Koc Univ. _____

Prof. Dr. Unver Kaynak
Mechanical Eng. Dep., TOBB ETU Univ. _____

Assist. Prof. Dr. Oguz Uzol
Aerospace Eng. Dep., METU _____

Date: _____

I hereby declare that all information in this document has been obtained and presented in accordance with academic rules and ethical conduct. I also declare that, as required by these rules and conduct, I have fully cited and referenced all material and results that are not original to this work.

Name, Last Name: MEHMET KARACA

Signature :

ABSTRACT

CONTRIBUTION TO THE DEVELOPMENT OF IMPLICIT LARGE EDDY SIMULATIONS METHODS FOR COMPRESSIBLE TURBULENT FLOWS

Karaca, Mehmet

Ph.D., Department of Aerospace Engineering

Supervisor : Prof. Dr. I. Sinan Akmandor

Supervisor : Asst. Prof. Dr. Ivan Fedioun

December 2011, 157 pages

This work is intended to compare Large Eddy Simulation and Implicit Large Eddy Simulation (LES and ILES) for a turbulent, non-reacting or reacting high speed H2 jet in co-flowing air, typical of scramjet engines. Numerical simulations are performed at resolutions ranging from 32×32×128 to 256×256×1024, using a 5th order WENO scheme. Physical LES are carried out with the Smagorinsky and the Selective Structure Function models associated to molecular diffusion. Implicit LES are performed with and without molecular diffusion, by solving either the Navier-Stokes or the Euler equations. In the nonreacting case, the Smagorinsky model is too dissipative. The Selective Structure Function leads to better results, but does not show any superiority compared to ILES, whatever the grid resolution. In the reacting case, a molecular viscous cut-off in the simulation is mandatory to set a physical width for the reaction zone in the ILES approach, hence to achieve grid-convergence. It is also found that ILES/LES are less sensitive to the inlet conditions than the RANS approach. The first chapter is an introduction to the context of this study. In the second chapter, the governing equations for multispecies reacting flows are presented, with emphasis on the thermodynamic and transport models. In the third chapter, physical LES equations and explicit sub-grid modeling strategies

are detailed. Some properties of the numerical scheme are also investigated. In chapter four, the numerical scheme and some aspects of the solver are explained. Finally, non-reacting and reacting numerical experiments are presented and the results are discussed.

Keywords: turbulent, combustion, LES, implicit, compressible

ÖZ

SIKIŞTIRILABİLİR VE TEPKİMELİ TÜRBÜLANSLI AKIMLAR İÇİN ZIMNI BÜYÜK GİRDAP BENZETİMİ YÖNTEMLERI GELİŞ TİRİLMESINE KATKI

Karaca, Mehmet
Doktora, Havacılık ve Uzay Mühendisli Bölümü
Tez Yöneticisi : Prof. Dr. I. Sinan Akmandor
Ortak Tez Yöneticisi : Yrd. Doç. Dr. Ivan Fedioun

Aralık 2011, 157 sayfa

Bu çalışmada scramjet motorlarına özgü yüksek hızda, türbülanslı, tepkimesiz veya tepkimeli, eş-hava akışında H2 jeti için uygulanan Büyük Girdap Benzetimi ve Zımni Büyük Girdap Benzetimi (BGB ve ZBGB) metodlarının karşılaştırılması amaçlanmaktadır. Sayısal sımülasyonlar, 5. seviye WENO şemasını kullanarak, $32 \times 32 \times 128$, $256 \times 256 \times 1024$ arasında degişen çözünürlüklerde yapılmıştır. Fiziksel BGB, Smagorinsky ve Seçici Yapısal Fonksiyonu modelleriyle bilikte moleküler difüzyon uygulanılarak yansıtılmaktadır. Örtülü BGB, moleküler difüzyon eklenip çıkarılarak elde edilen Navier-Stokes veya Euler denklemleri çözülerek yapılmıştır. Tepkimesiz durumda, Smagorinsky modeli çok tüketimlidir. Seçici Yapısal Fonksiyonu daha iyi sonuçlar vermektadir, ancak ZBGB ile karşılaştırıldıgında, ag çözünür- lügü ne olursa olsun herhangi bir üstünlük göstermez. Tepkimeli durumda, ZBGB yaklaşımı için reaksiyon bölgesinde fiziksel bir et kalınlıgı ve ag yakınsaması saglayan moleküler viskozite zorunludur. Ayrıca, BGB ve ZBGB metodlarının giriş şartlarına RANS yaklaşımına görece daha az duyarlı oldugu görülmüştür. İlk bölümde, bu çalısma baglaminda bir giriş yapılmaktadır. İkinci bölümde, çok türlü tepkimeli akışları temsil eden denklemler, termodinamik ve taşıma modelleri üzerinde durularak sunulmustur. Üçüncü bölümde, fizik-

sel BGB denklemler ve ag-altı modelleme stratejileri ayrıntılı olarak verilmektedir, sayısal şemanın bazı özellikleri de incelenmistir. Dördüncü bölümde, sayısal şema ve çözücünün bazı yönleri açıklanmıştır. Son olarak, tepkimesiz ve tepkimeli sayısal deneylerin sonuçları tartışılmaktadır.

Anahtar Kelimeler: türbülanslı, yanma, ZBGB, Zımni, sıkıştırılabilir

dedicated to my family.

ACKNOWLEDGMENTS

I would like to express my sincerest thanks to all those who gave me the possibility to complete this work at ICARE of CNRS, as a joint PhD between the Middle East Technical University and the Orléans University.

I would like start with my two supervisors Dr. Sinan Akmandor and Dr. Ivan Fedioun. I would like to express my sincerest thanks to Dr. Sinan Akmandor for his infinite support, consistent inspiration and for helping me get through this long journey, as a member of my family. I would like to thank Dr. Ivan Fedioun for his great efforts for transmitting me his immense knowledge on the numerical simulation of fluid flows, for his desire to achieve better and lots of good ideas

I am deeply indebted to Dr. Iskender Gökalp for offering me the opportunity to do my PhD work at ICARE of CNRS and supporting me in every sense, during my stay in France.

I would like to thank the French Embassy in Turkey for providing the funds for my stay in France and TUBITAK for the support during my stay in Turkey.

I also express my sincere thanks to all the ICARE colleagues for their support, encouragement and camaraderie.

TABLE OF CONTENTS

ABSTRACT iv

ÖZ vi

ACKNOWLEDGMENTS ix

TABLE OF CONTENTS x

LIST OF TABLES xv

LIST OF FIGURES xvii

CHAPTERS

1 INTRODUCTION 1

2 CONSERVATION LAWS FOR COMPRESSIBLE MULTICOMPONENT REACTING FLOWS 7

2.1 CONSERVATION OF MASS AND CHEMICAL SPECIES 7

2.1.1 STATIC VARIABLES FOR A MIXTURE 7

2.1.2 CONSERVATION OF SPECIES AND MASS 8

2.1.3 MOLECULAR DIFFUSION OF SPECIES 9

2.1.4 CHEMICAL KINETICS 12

2.2 EQUATION OF MOTION 13

2.2.1 THE EQUATION OF STATE 13

2.2.2 MOLECULAR DIFFUSION OF MOMENTUM 13

2.3 ENERGY EQUATION 14

2.3.1 INTERNAL ENERGY, ENTHALPY AND SPECIFIC HEATS 14

2.3.2 MOLECULAR DIFFUSION OF HEAT AND ENTHALPY 15

2.3.3 TEMPERATURE EVALUATION 16

2.4 SUMMARY OF SYSTEM OF EQUATIONS 16

3 LARGE EDDY SIMULATION 18
3.1 FILTERING THE NAVIER-STOKES EQUATIONS 20
3.1.1 CONSERVATION OF MASS 22
3.1.2 CONSERVATION OF CHEMICAL SPECIES 23
3.1.3 EQUATION OF MOTION 23
3.1.4 ENERGY EQUATION 25
3.1.5 SPECIAL ATTENTION FOR W_5 AND IDEAL GAS EQUATION 25
3.2 EXPLICIT SUB-GRID MODELING 27
3.2.1 CLOSING THE FILTERED EQUATION OF MOTION . 27
3.2.1.1 THE SMAGORINSKY MODEL 27
3.2.1.2 THE YOSHIZAWA MODEL 28
3.2.1.3 THE SELECTIVE STRUCTURE FUNCTION MODEL 29
3.2.2 CLOSING THE FILTERED ENERGY EQUATION . . . 30
3.2.3 CLOSING THE FILTERED SPECIES EQUATION 30
3.3 Implicit LES 30
3.3.1 MWN ANALYSIS 31
3.3.2 THE INTERACTION BETWEEN NUMERICAL ERRORS AND EXPLICIT SUB-GRID MODELING 34
4 THE WENO SOLVER 36
4.1 TRANSFORMATION BETWEEN CONSERVATIVE, PRIMITIVE AND CHARACTERISTIC FORMS 37
4.2 CONSERVATIVE FORM FOR DIFFERENTIAL OPERATOR . . . 38
4.3 WENO SCHEME 39
4.3.1 ENO APPROXIMATION 40
4.3.2 1D WENO RECONSTRUCTION PROCEDURE 41
4.3.3 FLUX SPLITTING 42
4.3.4 SOLUTION FOR SYSTEM OF EQUATIONS 43
4.4 TIME DISCRETIZATION 44
4.4.1 RK_P TVD TIME STEPPING 44
4.4.2 CALCULATING THE TIME STEP 45

4.5 BOUNDARY CONDITIONS 46
4.5.1 LODI SYSTEM 46
4.5.2 FREE NON-REFLECTING BCS 48
4.5.3 PHYSICAL NON-REFLECTING INLET BOUNDARY CONDITIONS 48
4.5.3.1 SUBSONIC FORCED NON-REFLECTING INLET 48
4.5.3.2 SUPERSONIC FORCED NON-REFLECTING INLET 49
4.6 SOME SPECIFICITIES 49
4.6.1 THE LARROUTUROU METHOD 49
4.6.1.1 IDEA OF LARROUTUROU 49
4.6.1.2 APPLICATION TO WENO SOLVER 50
4.6.2 STRUCTURE OF THE CODE 50
4.6.3 THE QUESTION OF D_{H0} 50
4.6.4 THE METRICS 52
4.6.5 PARALLEL IMPLEMENTATION 53
4.6.6 LES STRATEGIES 54
5 NUMERICAL EXPERIMENTS 55
5.1 NON-REACTING CASE 56
5.1.1 TEST CASE DESCRIPTION 56
5.1.2 PHYSICAL AND NUMERICAL PARAMETERS 58
5.1.3 FLOW STRUCTURE 63
5.1.4 STATISTICAL RESULTS 70
5.1.5 VARIATION OF VELOCITY, SPECIES MASS FRACTION AND PRESSURE 76
5.1.6 IS THE DNS LEVEL REACHED ? 86
5.1.7 CONCLUSIONS 87
5.2 REACTING CASE 88
5.2.1 TEST CASE DESCRIPTION 88
5.2.2 INLET FIELD 90
5.2.2.1 SIMPLE PROFILE 91

5.2.2.2 IMPROVED PROFILE 92
5.2.3 NUMERICAL PARAMETERS 94
5.2.3.1 FLOW PARAMETERS 94
5.2.3.2 SPATIAL PARAMETERS 94
5.2.3.3 TIME PARAMETERS 95
5.2.4 RESULTS 97
5.2.4.1 RESULTS FOR SIMPLE INLET PROFILE . 97
5.2.4.1.1 FLAME STRUCTURE 97
5.2.4.1.2 STATISTICAL RESULTS 103
5.2.4.2 RESULTS FOR IMPROVED INLET PROFILE 110
5.2.4.2.1 FLAME STRUCTURE 111
5.2.4.2.2 STATISTICAL RESULTS 114
5.2.5 CONCLUSIONS 115
6 CONCLUSIONS 118
BIBLIOGRAPHY 120
REFERENCES 120
APPENDICES
A TRANSPORT COEFFICIENTS 128
B THERMODYNAMIC DATA 130
C CHEMICAL KINETICS 132
D TRANSFORMATION MATRICES FOR SYSTEM OF N_{SP}+5 EQUATIONS 134
E TRANSFORMATION MATRICES FOR SYSTEM OF N_{SP}+4 EQUATIONS 137
E.1 TRANSFORMATION MATRICES BETWEEN THE PRIMITIVE VARIABLES AND THE CONSERVATIVE VARIABLES 137
E.2 TRANSFORMATION MATRICES BETWEEN THE PRIMITIVE VARIABLES AND THE CHARACTERISTIC VARIABLES 139
E.3 TRANSFORMATION MATRICES BETWEEN THE CONSERVATIVE VARIABLES AND THE CHARACTERISTIC VARIABLES . 141
F WAVE AMPLITUDES AND LODI SYSTEM IN TERMS OF PRIMITIVE VARIABLES 145
G WENO COEFFICIENTS 148

H COMPRESSIBLE TEMPORAL MIXING LAYER *A PRIORI* TESTS 153
I COMPUTATIONAL HOURS 157

LIST OF TABLES

TABLES

Table 5.1 Physical parameters for the non-reacting air/H_2 jet. In bold, data from Eggers [32], other values are computed. 58

Table 5.2 Ratios of approximate Kolmogorov scale and Taylor microscale to the minimum grid spacing. 61

Table 5.3 Coefficients which are used for the inlet velocity profile. 61

Table 5.4 The slope and fictitious center of inverse normalized time averaged velocity. 76

Table 5.5 The slope and fictitious center of inverse normalized time averaged hydrogen mass fraction. 76

Table 5.6 LAERTE inlet hyperbolic tangent profile coefficients for equation 5.6. . . . 92

Table 5.7 LAERTE experimental conditions. 94

Table 5.8 Ratios of approximate Taylor micro-scale and Kolmogorov scale to the minimum grid spacing. 95

Table A.1 Thermal conductivity coefficients for second order polynomial fit (i.e. equation 2.50). 128

Table A.2 Coefficients of viscosity for second order polynomial fit (i.e. equation 2.37). 128

Table A.3 Power law fitted diffusion coefficients for P_0(=1bar), T (i.e. equation 2.21). 129

Table B.1 Thermodynamic property data format. 130

Table B.2 Thermodynamic properties. (Burcat [14]). 131

Table C.1 Efficiency of the species for the ONERA scheme. 132

Table C.2 H_2/air Chemical reaction mechanism by ONERA. 133

Table G.1 Coefficients c_{rj} for k=1 to 6. 148

Table G.2 Coefficients d_r for k=1 to 6. 149

Table H.1 D.N.S. physical and numerical parameters for the O_2/N_2 pair. 154

Table H.2 D.N.S physical and numerical parameters for the O_2/H_2 pair. 155

Table I.1 Relative cost of LES and MILES, non-reacting and reacting. 157

LIST OF FIGURES

FIGURES

Figure 1.1 Leduc 010, 1949, 680 km/h. 2

Figure 1.2 The rocket-powered X-15 (M=6.7 in 1967). 2

Figure 1.3 Schematic of a scramjet [3]. 2

Figure 1.4 Specific impulse vs. flight conditions for various engine concepts. Red : H_2, Blue : Kerosene 3

Figure 1.5 Flight envelop of different engine concepts. 3

Figure 1.6 The X43 in the NASA LaRC M=10 wind tunnel. 4

Figure 1.7 The Boeing X51-A. 4

Figure 1.8 The CAD view of the LEA vehicle. 4

Figure 1.9 The LEA flight test mission. 4

Figure 3.1 Linear Modified Wave Number without (top) and with (bottom) non-linear WENO weight. Left : real part, right : imaginary part. (a) 3^{rd} order WENO, (b) 5^{th} order WENO, (c) 7^{th} order WENO, (d) 9^{th} order WENO, (e) 11^{th} order WENO, (f) 1^{st} order upwind FD, (g) 2^{nd} order upwind FD 33

Figure 3.2 Interaction indicator eq. (3.89) for C = 0, 0.1, 1 and 10. Left: real part, right: imaginary part. 35

Figure 4.1 Transformations between different forms for the Euler system of equations. 38

Figure 4.2 5^{th} order WENO stencil demonstration. 40

Figure 4.3 ECBC subsonic flux directions 47

Figure 4.4 ECBC supersonic flux directions 47

Figure 4.5 Direction of the waves for subsonic and supersonic conditions for both $u > 0$ (black arrows) and $u < 0$ (red arrows) cases. 47

Figure 4.6 Schematic diagram of structure of the code. 51

Figure 4.7 Coordinate transformation for clustering the grid 52

Figure 4.8 A. Speedup curves for WENO code on clusters VARGAS and Phoebus, B. 2D MPI cartesian topology. 53

Figure 5.1 Schematic diagram of Eggers jet. 57

Figure 5.2 Shear layer convective velocity and Mach numbers[8]. 59

Figure 5.3 Inlet velocity profile for the non-reacting air/H_2 Eggers jet. 59

Figure 5.4 Grid for the Eggers jet of resolution 32×32×128 60

Figure 5.5 Inlet velocity profile for the non-reacting air/H_2 Eggers jet. 61

Figure 5.6 Radial distribution of confinement function, samples of generated 'random' field and the noise applied on transverse velocity components. 62

Figure 5.7 Eggers jet results on 32×32×128 grid. Instantaneous structure of the flow visualized using iso-Q. Pressure and Hydrogen mass fraction in the symmetry planes for different approaches. 65

Figure 5.8 Eggers jet results on 64×64×256 grid. Instantaneous structure of the flow visualized using iso-Q. Pressure and Hydrogen mass fraction in the symmetry planes for different approaches. 66

Figure 5.9 Eggers jet result on 128×128×512 grid with reduced Smagorinsky constant. Instantaneous structure of the flow visualized using iso-Q. Pressure and Hydrogen mass fraction in the symmetry planes for different approaches. 67

Figure 5.10 Eggers jet results on 128×128×512 grid. Instantaneous structure of the flow visualized using iso-Q. Pressure and Hydrogen mass fraction in the symmetry planes for different approaches. 68

Figure 5.11 Eggers jet results on 256×256×512 grid. Instantaneous structure of the flow visualized using iso-Q. Pressure and Hydrogen mass fraction in the symmetry planes for different approaches. 69

Figure 5.12 Eggers jet : axial velocity decay. Clockwise from top-left : LES_SM, LES_SSF, MILES_NS and MILES_EULER 70

Figure 5.13 Eggers jet : transverse velocity profiles at x =0.06, 0.11, 0.18 and 0.29 m from the exit. Resolution 128×128×512 71

Figure 5.14 Eggers jet : transverse velocity profiles at x =0.06, 0.11, 0.18 and 0.29 m from the exit. Resolution 256×256×512 72

Figure 5.15 Eggers jet : H_2 mass fraction axial decay. Clockwise from top-left : LES_SM, LES_SSF, MILES_NS and MILES_EULER 73

Figure 5.16 Definitions for inverse normalized time averaged quantity. 73

Figure 5.17 Variables for inverse normalized average quantity. 74

Figure 5.18 Variation of the inverse normalized quantities Q^* on the axis of turbulent jet. 74

Figure 5.19 The inverse normalized velocity $Q_{*\,U}$(left) and the inverse normalized H_2 mass fraction $Q_{*Y_{H_2}}$(right) for 64×64×256, 128×128×512 and 256×256×512 resolutions (from upper to lower). 75

Figure 5.20 Instantaneous axial velocity component on the jet axis at 256×256×512. . 77

Figure 5.21 Eggers jet: Resolved turbulent kinetic energy, resolution 128×128×512. . . 79

Figure 5.22 Eggers jet: Nitrogen mass fraction variance, resolution 128×128×512. . . 79

Figure 5.23 Eggers jet: Resolved turbulent kinetic energy, resolution 256×256×512. . . 79

Figure 5.24 Eggers jet: Nitrogen mass fraction variance, resolution 256×256×512. . . 79

Figure 5.25 Sub-figures demonstrating from top : instantaneous velocity over symmetry axis, sampled time variation and spectra of sampled data of 128×128×512 grid solutions (velocity in m/s and frequency in kHz). 80

Figure 5.26 Sub-figures demonstrating from top : instantaneous velocity over symmetry axis, sampled time variation and spectra of sampled data of 256×256×512 grid solutions (velocity in m/s and frequency in kHz). 81

Figure 5.27 Sub-figures demonstrating from top : instantaneous hydrogen mass fraction over symmetry axis, sampled time variation and spectra of sampled data of 128×128×512 grid solutions (frequency in kHz). 82

Figure 5.28 Sub-figures demonstrating from top : instantaneous hydrogen mass fraction over symmetry axis, sampled time variation and spectra of sampled data of 256×256×512 grid solutions (frequency in kHz). 83

Figure 5.29 Sub-figures demonstrating from top : instantaneous pressure over symmetry axis, sampled time variation and spectra of sampled data of 128×128×512 grid solutions (pressure in Pa and frequency in kHz). 84

Figure 5.30 Sub-figures demonstrating from top : instantaneous pressure over symmetry axis, sampled time variation and spectra of sampled data of 256×256×512 grid solutions (pressure in Pa and frequency in kHz). 85

Figure 5.31 Eddy-viscosity ratio, LES_SM. 86

Figure 5.32 Eddy-viscosity ratio, LES_SSF. 87

Figure 5.33 Schema of the LAERTE experiment. 88

Figure 5.34 Experimental data available. From left to right: temperature, velocity and OH molar concentration. 89

Figure 5.35 Initial field data taken from RANS solutions Davidenko [22]; from left to right radial profiles for temperature, velocity and species concentrations. 90

Figure 5.36 Simplified initial field data deduced from RANS solutions by Davidenko [22]; from left to right radial profiles for temperature, velocity and species concentrations. 91

Figure 5.37 Inlet velocity profile for the reacting air/H_2 LAERTE jet. 92

Figure 5.38 Initial field data deduced from Davidenko RANS solutions [22] including shock patterns at inlet; from left to right radial profiles for temperature, velocity and species concentrations 93

Figure 5.39 0D constant pressure tests for stoichiometric H_2/air (left) and stoichiometric vitiated H_2/air (right) mixtures. The dashed lines refer to the stable solutions and the solid lines to the unstable ones. 95

Figure 5.40 0D constant volume tests for stoichiometric H_2/air (left) and stoichiometric vitiated H_2/air (right) mixtures. The dashed lines refer to the stable solutions and the solid lines to the unstable one. 96

Figure 5.41 Fuel/oxidizer mixture fraction distribution. 98

Figure 5.42 Instantaneous iso-surfaces of the stoichiometric mixture fraction, temperature contours and water mass fraction contours on the symmetry planes for 64×64×256 grid. From top to bottom : LES_SSF, MILES_NS, MILES_EULER. 100

Figure 5.43 Instantaneous iso-surfaces of the stoichiometric mixture fraction, temperature contours and water mass fraction contours in the symmetry planes for 128×128×512 grid. From top to bottom : LES_SSF, MILES_NS, MILES_EULER. 101

Figure 5.44 Instantaneous iso-surfaces of the stoichiometric mixture fraction, temperature contours and water mass fraction contours in the symmetry planes for 256×256×1024 grid. From top to bottom : LES_SSF, MILES_NS, MILES_EULER. 102

Figure 5.45 Instantaneous axial velocity component on the jet axis and in the main shear region. MILES_NS, 256×256×1024. 103

Figure 5.46 Scatter plots of temperature. Top to bottom : LES_SSF, MILES_NS, MILES_EULER. Left to right : 64×64×256, 128×128×512, 256×256×1024. 105

Figure 5.47 Scatter plots of O_2 mass fraction. Top to bottom : LES_SSF, MILES_NS, MILES_EULER. Left to right : 64×64×256, 128×128×512, 256×256×1024. . . . 106

Figure 5.48 Average profiles of velocity, H_2 mass fraction and temperature at the center line of the jet and maximum temperature at the transverse sections along x axis. Left to right : 64×64×256, 128×128×512, 256×256×1024. 107

Figure 5.49 Tranverse profiles of axial velocity (left) and temperature (right) at x = 210 mm. Top to bottom : 64×64×256, 128×128×512, 256×256×1024. 109

Figure 5.50 Eddy-viscosity, LES_SSF 110

Figure 5.51 Flame structure of LAERTE chamber with precise initial field, including strong shock patterns. 112

Figure 5.52 Pressure contours on the symmetry axis, of LAERTE chamber with precise initial field. 113

Figure 5.53 Wall pressure axial distribution numerical results and experimental data. . 114

Figure 5.54 Maximum temperature distribution along the jet axis computed over normal planes. 114

Figure 5.55 Transverse OH concentration profiles at x=0.21 m along the axis. 115

Figure 5.56 Experimental transverse profiles of axial velocity (left) and temperature (right) at x=10 mm, x=72 mm, x=210 mm and x=288 mm. 116

Figure H.1 Computational box for the temporal direct numerical simulation 153

Figure H.2 Subrid terms (H.1). Relative magnitude: O_2/N_2 156

Figure H.3 same as Figure H.2: O_2/H_2 156

Figure H.4 Subrid terms (H.3). Relative magnitude: O_2/N_2 156

Figure H.5 same as Figure H.4: O_2/H_2 156

Figure H.6 Subrid terms (H.4). Relative magnitude: O_2/N_2 156
Figure H.7 same as Figure H.6: O_2/H_2 156

CHAPTER 1

INTRODUCTION

The mankind's desire to fly higher, faster and farther sustained the development of propulsion systems since the first powered flight of Wright brothers in 1903. In the early years of aviation, René Lorin patented an air-breathing device which compresses the incoming air by its inlet (diffuser) and expands it by its exhaust (nozzle) without any moving parts. This engine was the first ramjet concept. At that time, this concept would not be realized since a ramjet can not produce thrust at zero speed. Similar independent concepts were developed in different countries.

This initial interest in ramjets seemed to be reduced in favor of the sustained development of gas turbine engine, the concept of which was first patented in 1791, by John Barber (UK patent no. 1833). Sir Frank Whittle (England) ran the W2/700 engine, and in 1936 Von Ohain (Germany) ran his engine with H_2. During the second world war (WWII), German flew the first operational ramjet, ground launched V-1 Bomb Flyer which was launched by a solid propellant booster. The first ramjet powered aircraft Leduc 0.10 (Figure 1.1) which was carried aloft by a mother airplane was launched in 1947, in France. Later, after WWII, operational ground launched ramjets were developed as missiles like Talos in US and VEGA in France.

Access to space gave a big impetus for hypersonic flight. The first hypersonic manned rocket powered aircraft called X-15 (Figure 1.2) was built in 60's by North American Society on behalf of NASA. The X-15 was flying at $\approx$15 km and reached Mach 6.7 in 1967. This airplane was used to collect experimental data at hypersonic flight regimes at high altitude and to make component tests. The engines driving high-speed flight vehicles had limitations imposed by propulsion: air-breathing engines (turbojet, ramjet) do not reach hypersonic speeds and rocket

Figure 1.1: Leduc 010, 1949, 680 km/h.

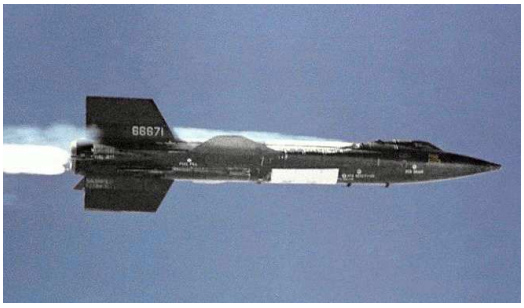

Figure 1.2: The rocket-powered X-15 (M=6.7 in 1967).

engines have the disadvantage of requiring the carriage of oxidant. The scramjet (supersonic combustion ramjet) development which has begun in 1955s permitted to remove these drawbacks. In a ramjet, the flow is subsonic since there is a throat on the flow path. Multi-shocks at the inlet cause high amount of losses at flow velocities higher than Mach 6 (Figure 1.3). On the contrary, in a scramjet, the flow remains supersonic throughout the combustion process, resulting in more efficient operation at hypersonic speeds of the airplane. Figure 1.4 shows

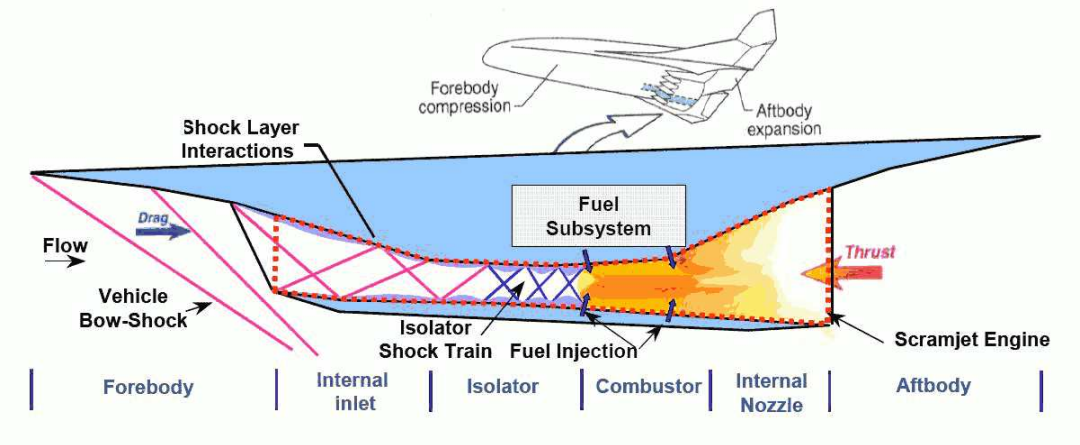

Figure 1.3: Schematic of a scramjet [3].

the specific impulse vs operating condition of various engine concepts. Rocket engines specific impulse values are about 400 s which is less compared to scramjet. Figure 1.5 shows the altitude limitation vs Mach number and the so-called flight corridor of scramjets. As seen in the Figure, the optimal altitude for scramjet flight at Mach=6 is around 25 km. United States having the hypersonic test capability of X-15, started the NASA hypersonic research engine HRE (hypersonic research engine) program in 1964, and France launched ESOPE (Etude de

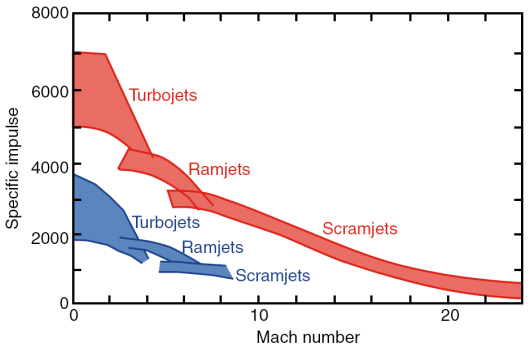

Figure 1.4: Specific impulse vs. flight conditions for various engine concepts. Red : H_2, Blue : Kerosene

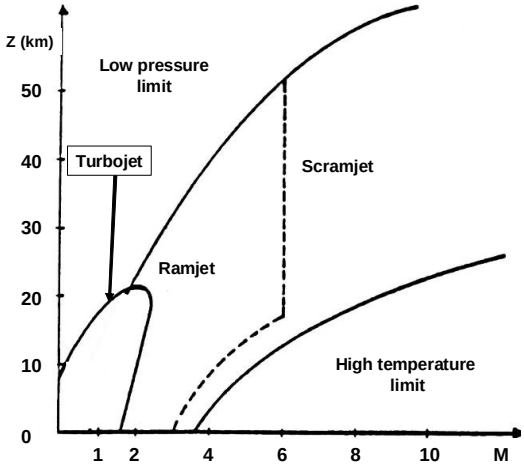

Figure 1.5: Flight envelop of different engine concepts.

Statoréacteur comme Organe de Propulseur Evolué) program in 1966. However, these attempts terminated due to limited technology and interest focused on integrated rocket ramjet (IRR) technology.

In the mid 1980's, the NASP (National AeroSpace Plane) program was initiated with the goal of flying a reusable launch vehicle, the X-30, powered by a single stage combined cycle engine to Mach 25. Also, at the same time, the PREPHA (Programme de REcherche en Propulsion Hypersonique Avancée) program was launched in France. Considering the state of technology, the goals of these projects were aggressive; eventually these projects were abandoned leaving extensive experience and significant contributions behind. Research in Europe continued with the JAPHAR project (Joint Airbreathing Propulsion for Hypersonic Application Research) co-directed by ONERA (France) and DLR (Germany). These studies have been conducted from 1997 to 2002 as the preliminary study of a dual-mode ramjet hypersonic vehicle.

At the same time, the Hyper-X program launched in the United States aimed to fly a small scale scramjet powered demonstrator at Mach 10. This target was reached in November 2004 by the X-43A (Figure 1.6). Later, the X-51 Waverider program was initiated to demonstrate sustained flight of 300 s with a scramjet powered aircraft. The X-51 was planned to accelerate from Mach 4.7 to beyond Mach 6. The first powered flight test was conducted on 26 May 2010 over 200 s at Mach 5 (Figure 1.7). In Europe, after JAPHAR, the PROMETHEE program and

Figure 1.6: The X43 in the NASA LaRC M=10 wind tunnel.

Figure 1.7: The Boeing X51-A.

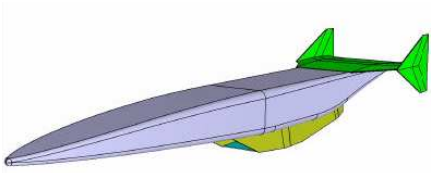

Figure 1.8: The CAD view of the LEA vehicle.

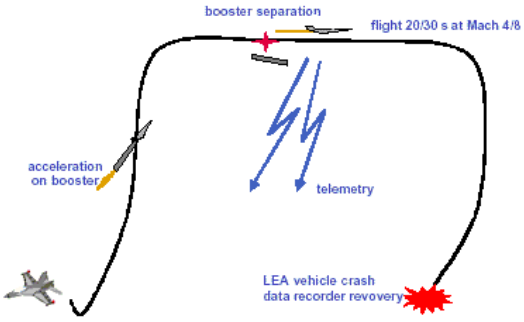

Figure 1.9: The LEA flight test mission.

now LEA (Figure 1.8) program is aimed to develop and launch an experimental hypersonic test vehicle by ONERA-MBDA. The first flight planned to be at 20-30 km altitude from Mach 4 to beyond Mach 8. This experimental vehicle is planned to be delivered to proper altitude and accelerated to the required Mach number by Russian Tu-22 aircraft and Volna launcher (Figure 1.9).

In the present review, some of the hypersonic flight projects were listed. More thorough information about history may be found in references [22, 38, 37, 99, 77, 45, 124].

In a scramjet, the main design considerations are:

- The forebody and the intake act as a diffuser capturing and compressing air with the highest possible efficiency. They contribute to the moment and drag of the vehicle. The flow includes leading bow shock and isentropic or oblique turning shock waves. The transition on the forebody is highly important due to high heating involved.
- The pressure is increased in the isolator which acts as a component of the diffuser.

Oblique shocks penetrating into the combustion chamber are formed in the isolator.

- In the combustion chamber, the fuel is delivered into the flow, mixes and burns in the available chamber length. The (turbulent) mixing and chemical reactions in the supersonic flow conditions have to be complete within less than one millisecond.

- Finally, expansion occurs in the exhaust nozzle and aftbody. The design of the expansion system contributes to the propulsive efficiency and the moments on the vehicle.

The context of this work is the numerical simulation of turbulent mixing and reacting flow in scramjet combustion chamber. Shock waves are inherently present in the flow and require the use of dissipative numerical schemes for stable simulations, whatever the approach retained to model turbulence. Until quite recently, Reynolds averaged calculations (RANS) have been the standard approach to the problem (e.g. [74]). However, turbulence models extended to highly compressible flows and large heat release must be finely tuned, with some uncertainty when extrapolated to different configurations [23, 22]. Direct Numerical Simulation (DNS) of such complex flows is not feasible and may probably never be. LES is a more attractive technique [50] now at hand thanks to the increase in computing power. The purpose of the present thesis is the comparison of the Large Eddy Simulations (LES) and Monotone Integrated Large Eddy Simulation (MILES) numerical approaches in the context of high speed jets. In the former the contribution of the sub-grid motions are modeled based on flow physics and in MILES *algorithms designed to satisfy the physical requirements of positivity and causality, in effect have a matching sub-grid model built in* [11].

At ICARE the studies related to this topic were initiated by the thesis of Lardjane [80] in which 1D and 2D analysis of numerical methods for turbulent mixing in high density ratio binary systems have been conducted. Later, in the thesis by Gougeon [59], 2D numerical simulations are developed for compressible reacting flows. In the present study, the 2D simulations are extended to full 3D. Closure models for the filtered set of equations are applied for LES and different LES strategies are compared.

The thesis is organized as follows. Chapter 2 presents the governing equations for multicomponent compressible reacting flows, with emphasis on the thermodynamic and transport models. In chapter 3, physical LES equations are detailed; the explicit SGS modeling strategies are explained and dissipation and dispersion characteristics of different numerical approaches

are discussed. In the same chapter, a simple 1D linear analysis of the interaction between the WENO scheme and SGS model is also proposed. Chapter 4 is devoted to numerics. The details of the numerical scheme and some aspects of the solver are explained in this chapter. In chapter 5, both the non-reacting (section 5.1) and reacting (section 5.2) test cases and the results are presented. Finally, conclusions of this study are given in chapter 6.

CHAPTER 2

CONSERVATION LAWS FOR COMPRESSIBLE MULTICOMPONENT REACTING FLOWS

In this study, high speed non-reacting and reacting flows are simulated. The cases are high Reynolds number flows near atmospheric conditions, hence the Knudsen number is small and the continuum assumption holds. The system is assumed to be in local thermodynamic equilibrium, having a single temperature. The Navier-Stokes equations for three-dimensional multi-species flows are considered as the governing equations. Perfect gas equation of state is applied for the relation between pressure, temperature and density.

The description of coupled, time dependent, partial differential equations governing the convective flow, diffusion of species and source terms for chemical reactions is presented in this chapter. This set of equations is well known and can be found in many popular textbooks [78, 98, 104, 125, 128]. The purpose of this chapter is to state precisely the notations and definitions used in this study and to establish references for the following chapters.

2.1 CONSERVATION OF MASS AND CHEMICAL SPECIES

2.1.1 STATIC VARIABLES FOR A MIXTURE

Let consider an homogeneous mixture of N_{sp} species $\alpha = 1, ..., N_{sp}$. The density of the mixture may be computed as the sum of partial densities ρ_α

$$\rho(p, T, Y_\alpha) = \sum_{\alpha=1}^{N_{sp}} \rho_\alpha(p, T) \tag{2.1}$$

Species mass fractions Y_α are

$$Y_\alpha = \frac{\rho_\alpha}{\rho} \quad ; \quad \sum_{\alpha=1}^{N_{sp}} Y_\alpha = 1 \tag{2.2}$$

Species can also be characterized with their molar concentrations and mole fractions. Molar concentration of species α in the mixture is expressed in the following way

$$C_\alpha = \frac{\rho_\alpha}{M_\alpha} = \frac{\rho Y_\alpha}{M_\alpha} \tag{2.3}$$

M_α is the molar mass of the species α. The overall molar concentration of the mixture is

$$C = \sum_{\alpha=1}^{N_{sp}} C_\alpha \tag{2.4}$$

Mole fractions can be directly computed from molar concentrations as

$$X_\alpha = \frac{C_\alpha}{C} \quad ; \quad \sum_{\alpha=1}^{N_{sp}} X_\alpha = 1 \tag{2.5}$$

A simple relation between mass fractions, mole fractions and molar mass is

$$X_\alpha M_\alpha = Y_\alpha M \tag{2.6}$$

Average molar mass of the mixture may be computed using both variables X_α and Y_α as

$$M = \frac{\rho}{C} = \sum_{\alpha=1}^{N_{sp}} X_\alpha M_\alpha = \left(\sum_{\alpha=1}^{N_{sp}} \frac{Y_\alpha}{M_\alpha} \right)^{-1} \tag{2.7}$$

2.1.2 CONSERVATION OF SPECIES AND MASS

In an infinitesimal control volume, the change of species mass fractions, for chemically reacting flows, is due to convection, diffusion of species and source terms of reactions.

$$\frac{\partial \rho Y_\alpha}{\partial t} + \frac{\partial [\rho Y_\alpha (u_j + V_{\alpha j})]}{\partial x_j} = \dot{\omega}_\alpha \tag{2.8}$$

In this relation u_j is the convective velocity, $V_{\alpha j}$ is the diffusion velocity of species α in direction x_j and $\dot{\omega}_\alpha$ is the source term for species α. The diffusion velocity in equation (2.8) may be used to express the species mass flux

$$J_{\alpha j} = \rho Y_\alpha V_{\alpha j} \tag{2.9}$$

The species conservation equation (2.8) turns out to be

$$\frac{\partial \rho Y_\alpha}{\partial t} + \frac{\partial \rho u_j Y_\alpha}{\partial x_j} = -\frac{\partial J_{\alpha j}}{\partial x_j} + \dot{\omega}_\alpha \tag{2.10}$$

Both the sum of the source terms $\dot{\omega}_\alpha$ and species mass flux $J_{\alpha j}$ must be zero to satisfy conservation of mass.

$$\sum_{\alpha=1}^{N_{sp}} \dot{\omega}_\alpha = 0 \quad ; \quad \sum_{\alpha=1}^{N_{sp}} Y_\alpha V_{\alpha j} = 0 \tag{2.11}$$

The sum of species equations gives conservation of mass. The change of mass in the control volume is due to convection

$$\frac{\partial \rho}{\partial t} + \frac{\partial \rho u_j}{\partial x_j} = 0 \tag{2.12}$$

2.1.3 MOLECULAR DIFFUSION OF SPECIES

The species diffusion velocity $V_{\alpha j}$ in equation (2.8) can be expressed according to kinetic theory of gases [16, 36, 44, 66].

$$V_{\alpha j} = -\sum_{\beta=1}^{N_{sp}} \left(D_\alpha^T \frac{\partial \ln T}{\partial x_j} + D_{\alpha\beta} d_{\beta j} \right) \tag{2.13}$$

The first term on the r.h.s. is the thermal diffusion also known as the Soret effect [95]. In reacting flows, since temperature gradients take large values, Soret effect may be significant. However, in this study, it is neglected for simplicity.

In the second term on the r.h.s., $d_{\alpha j}$ is the diffusion driving force of species α in direction x_j. This term can be derived by elementary analysis [104, 128].

$$d_{\alpha j} = \frac{\partial X_\alpha}{\partial x_j} + (X_\alpha - Y_\alpha) \frac{\partial \ln p}{\partial x_j} + \frac{\rho}{p} \sum_{\beta=1}^{N_{sp}} Y_\beta Y_\alpha (b_{\beta j} - b_{\alpha j}) \tag{2.14}$$

$D_{\alpha\beta}$ is the coefficient for the inter-diffusion of species α and β in the presence of any number of other species. The diffusion coefficients take the name “binary diffusion coefficients” with notation $\mathcal{D}_{\alpha\beta}$, when there exists two species only. $\mathcal{D}_{\alpha\beta}$ can be computed algebraically [16, 66]. In equation (2.13) the diffusion velocities are explicit. However, the multicomponent diffusion coefficients $D_{\alpha\beta}$ are not (as $N_{sp} > 2$) . They can be approximated in terms of Sonine polynomial expansion as a function of the primitive variables and binary diffusion coefficients. A system of equations for the coefficients needs to be solved [36]. This procedure is explained in detail by Dixon-Lewis [27] and Coffee & Heimerl [18]. This task is computationally expensive.

An alternative method can be derived using the dual formulation of equation (2.13), neglecting

the Soret effect.

$$d_{\alpha j} = -\sum_{\beta=1}^{N_{sp}} \Delta_{\alpha\beta} V_{\alpha j} \tag{2.15}$$

The dual multicomponent diffusion coefficients $\Delta_{\alpha\beta}$ are not known but can be approximated using the first term of a Sonine polynomial expansion. The Stefan-Maxwell diffusion equations are then obtained [55, 95].

$$d_{\alpha j} = \sum_{\beta=1_{\alpha\neq\beta}}^{N_{sp}} \frac{X_\alpha X_\beta}{\mathcal{D}_{\alpha\beta}} V_{\beta j} - \left(\sum_{\beta=1_{\alpha\neq\beta}}^{N_{sp}} \frac{X_\alpha X_\beta}{\mathcal{D}_{\alpha\beta}} \right) V_{\alpha j} \tag{2.16}$$

$\mathcal{D}_{\alpha\beta}$ denotes the usual binary diffusion coefficient for two component mixing. The difficulty of computing diffusion coefficients, $D_{\alpha\beta}$ (for $N_{sp} > 2$) is avoided in this formulation. Even so, solving this system of equations is still computationally expensive [54].

In this work, Fick's law is applied for computing diffusion velocities. Fick's law provides close approximations at low computational cost when compared to the two methods that are explained above [25, 35, 65]. The diffusion coefficient $D_{\alpha m}$ is assumed to be the proportionality factor between the diffusion velocity of each species and the gradient of species mole fraction in the diffusion direction.

$$V_{\alpha j} = -\frac{D_{\alpha m}}{X_\alpha} X_{\alpha,j} \tag{2.17}$$

This formulation can be obtained from the Stefan-Maxwell equation (2.16) assuming the body force per unit mass $b_{\alpha j}$ to be equal for each species and the barotropic (pressure gradient driven) diffusion is negligible [128].

The multicomponent diffusion coefficient of each species in the mixture is computed applying the simple approximation suggested by Hirschfelder-Curtiss [1, 66].

$$D_{\alpha m} = \frac{1 - Y_\alpha}{\sum_{\beta=1_{\alpha\neq\beta}} X_\beta / \mathcal{D}_{\alpha\beta}} \tag{2.18}$$

This approximation is obtained as follows :

- Relation between $D_{\alpha\beta}$ and $\mathcal{D}_{\alpha\beta}$ is obtained using the following algebraic relation with the physical constraints $\sum_\beta Y_\beta D_{\beta\alpha} = 0$ for $\alpha = 1, .., N_{sp}$ to solve the Stefan-Maxwell system.

  $$\Delta D = I - \frac{Y \otimes U}{< U, Y >} \tag{2.19}$$

  where $U = {}^T\{1, 1, 1, .., 1\}$. Both Δ and D are assumed to be symmetric and positive definite on $U^\perp$ and $Y^\perp$ respectively.

Here, the dual diffusion coefficients are approximated as the first term of the Sonine series expansion

$$\Delta_{\alpha\beta} = \frac{X_\alpha X_\beta}{\mathcal{D}_{\alpha\beta}} \tag{2.20}$$

- Later, this relation is substituted in equation (2.13) assuming pressure is constant, body force per unit mass for each species are equal and thermal diffusion is negligible.
- The approximation (2.18) is obtained substituting $D_{\alpha\beta}$ into Fick's Law (2.17).

The binary ($\mathcal{D}_{\alpha\beta} = \mathcal{D}_{\beta\alpha}$) diffusion coefficients for species α and β are defined in terms of temperature and pressure. The values are computed applying power law interpolation over the CHEMKIN model [73].

$$\mathcal{D}_{\alpha\beta} = \frac{1}{P} a_{\alpha\beta 0} T^{b_{\alpha\beta}} \quad (\mathrm{m}^2/\mathrm{s}) \tag{2.21}$$

The coefficients $a_{\alpha\beta 0}$ and $b_{\alpha\beta}$ for the variation of $\mathcal{D}_{\alpha\beta}$ with temperature at atmospheric pressure are tabulated in appendix A. The subscript $_0$ stands for atmospheric conditions.

The species mole fractions are considered as independent variables since the diffusion velocities are approximated using Fick's law (2.17). However, this method causes violation of global mass conservation [54, 97]. The sum of species equations by definition must necessarily result in conservation of mass, in conservative formulation. This condition is not satisfied for Fick's assumption, unless all diffusion coefficients are equal.

One approach for this problem is discarding one of the species equations from the system. The mass fraction of this final species is calculated fulfilling the sum of the species mass fractions to unity. Also, there are many reasons for the existence of inaccuracies in the solution of Navier-Stokes equations. This last species is chosen to be a diluent in order to absorb the inconsistencies. It is chosen as N_2 in the present work since it is an inert species. However, in case of diffusion flames all the species are deficient either in the fuel or oxidizer side. Since the mass fractions of each species are critical at shear layer, this method will result in loss of accuracy. Another approach for preventing the violation of conservation of mass is introducing an artificial correction velocity for all species, which forces the sum of diffusion fluxes to be zero.

$$V_j^c = -\sum_{\beta=1}^{N_{sp}} Y_\beta V_{\beta j} \tag{2.22}$$

The correction velocity is related to the molecular diffusion. It is more convenient to write it on the right hand side of equation (2.10). The corrected mass flux is written as

$$J_{\alpha j}^c = \rho Y_\alpha \left(V_{\alpha j} + V_j^c \right) \tag{2.23}$$

So, the final form of the species conservation equation is

$$\frac{\partial \rho Y_\alpha}{\partial t} + \frac{\partial \left(\rho Y_\alpha u_j\right)}{\partial x_j} = -J^c_{\alpha j,j} + \dot{\omega}_\alpha \tag{2.24}$$

2.1.4 CHEMICAL KINETICS

The source term in (2.24) is calculated assuming finite rate chemistry, using Arrhenius laws for the reaction rates. The system of N_{reac} reversible chemical reactions occurring in the flow may be symbolized as follows

$$\sum_{\alpha=1}^{N_{sp}} \nu'_{\alpha j} A_\alpha \rightleftarrows \sum_{\alpha=1}^{N_{sp}} \nu''_{\alpha j} A_\alpha \qquad j = 1, ..., N_{reac} \tag{2.25}$$

where A_α is the chemical symbol of species α, and ν' and ν'' are the stoichiometric coefficients of reactants and products. The chemical scheme gives for each reversible reaction j, the forward K_{fj} and backward K_{bj} reaction rates, as the coefficients (A, b, E_{act}) of the Arrhenius law

$$K = AT^b \exp\left(-\frac{E_{act}}{\mathcal{R}T}\right) \tag{2.26}$$

These coefficients are related by the equilibrium constant K_{ej} of the reaction

$$K_{ej} = \frac{K_{fj}}{K_{bj}} = \left(\frac{P_{atm}}{\mathcal{R}T}\right)^{\sum_{\alpha=1}^{Nsp} \nu''_{\alpha j} - \nu'_{\alpha j}} \exp\left(\frac{\Delta S^0_j}{\mathcal{R}} - \frac{\Delta H^0_j}{\mathcal{R}T}\right) \tag{2.27}$$

In (2.26) E_{act} is the activation energy of the reaction, and $\mathcal{R} = 8314.51$ (J/K.kmol) is the universal gas constant. The production rate of species α due to the N_{reac} reversible reactions is computed with the following relation.

$$\dot{\omega}_\alpha = M_\alpha \sum_{j=1}^{N_{reac}} \left(\nu''_{\alpha j} - \nu'_{\alpha j}\right) \left[K_{fj} \prod_{\beta=1}^{N_{sp}} \left(\frac{\rho Y_\beta}{M_\beta}\right)^{\nu'_{\alpha j}} - K_{bj} \prod_{\beta=1}^{N_{sp}} \left(\frac{\rho Y_\beta}{M_\beta}\right)^{\nu''_{\alpha j}} \right] \tag{2.28}$$

Detailed chemistry has a valuable effect on flow simulation. However, each additional species increases the number of equations and the amount of data to handle. The reaction of H_2/air mixtures which may be considered to be well known [65] was studied in this work. The 7 species, 14 reactions mechanism of ONERA, which was tested by Davidenko [22], is used for the calculations. The mechanism with coefficients for equation (2.26) is tabulated in appendix B.

2.2 EQUATION OF MOTION

The momentum equation, which is the same for reacting and non-reacting cases, represents the dynamics of the flow, in the Navier-Stokes system

$$\frac{\partial \rho u_i}{\partial t} + \frac{\partial \left(\rho u_i u_j + p\delta_{ij}\right)}{\partial x_j} = \rho f_i + \frac{\partial \tau_{ij}}{\partial x_j} \tag{2.29}$$

Body forces f_i are neglected in this work. Pressure p is calculated applying Dalton's law

$$p = \sum_{\alpha=1}^{N_{sp}} p_\alpha \tag{2.30}$$

2.2.1 THE EQUATION OF STATE

Each species satisfies the equation of state for ideal gases

$$p_\alpha = \rho_\alpha \frac{\mathcal{R}}{M_\alpha} T = \rho_\alpha r_\alpha T \tag{2.31}$$

$r_\alpha = \mathcal{R}/M_\alpha$ (J.kg^{-1}.K^{-1}) is the gas constant of species α. The mixture constant and its equation of state are derived using equations (2.7), (2.30) and (2.31).

$$r = \mathcal{R} \sum_{\alpha=1}^{N_{sp}} \frac{Y_\alpha}{M_\alpha} \quad ; \quad p = \rho \mathcal{R} T \sum_{\alpha=1}^{N_{sp}} \frac{Y_\alpha}{M_\alpha} = \rho r T \tag{2.32}$$

2.2.2 MOLECULAR DIFFUSION OF MOMENTUM

The stress tensor of fluid flow σ_{ij}, in terms of the inviscid (p:pressure) and the viscous (τ_{ij}) contributions, is

$$\sigma_{ij} = -p\delta_{ij} + \tau_{ij} \tag{2.33}$$

The viscous stress for a Newtonian fluid (the stress is linearly proportional to the strain rate) is assumed to be symmetric and may be written as

$$\tau_{ij} = \lambda \delta_{ij} u_{k,k} + 2\mu S^*_{ij} \quad ; \quad S^*_{ij} = \frac{1}{2}\left(\frac{\partial u_i}{\partial x_j} + \frac{\partial u_j}{\partial x_i}\right) \tag{2.34}$$

Stokes assumption which states that pressure forms the trace and viscous part forms the deviatoric part of the stress tensor ($\tau_{ii} = 0$) is applied, resulting in $\lambda = -2/3\mu$

$$\tau_{ij} = \mu S_{ij} = \mu\left(u_{i,j} + u_{j,i} - \frac{2}{3} u_{k,k}\delta_{ij}\right) \tag{2.35}$$

S^*_{ij} is one half of the rate of strain tensor S_{ij}, for an incompressible flow. The viscosity μ of the mixture is computed as a function of mole fractions and partial viscosities applying Wilke's empirical formula [127]

$$\mu = \sum_{\alpha=1}^{N_{sp}} \frac{X_\alpha \mu_\alpha}{\sum_{\beta=1}^{N_{sp}} X_\beta \phi_{\alpha\beta}} \quad ; \quad \phi_{\alpha\beta} = \frac{\left(1 + \sqrt{\frac{\mu_\alpha}{\mu_\beta}} \left(\frac{M_\beta}{M_\alpha}\right)^{1/4}\right)^2}{\sqrt{8\left(1 + \frac{M_\alpha}{M_\beta}\right)}} \tag{2.36}$$

Molecular viscosity μ_α of species α are computed using second order polynomials depending on temperature which were generated over the CHEMKIN model

$$\mu_\alpha = \mu_{\alpha 0} + \mu_{\alpha 1} T + \mu_{\alpha 2} T^2 \quad \text{(kg/m.s)} \tag{2.37}$$

The coefficients $\mu_{\alpha 0}$, $\mu_{\alpha 1}$ and $\mu_{\alpha 2}$ for each species α are tabulated in appendix A.

2.3 ENERGY EQUATION

The energy equation may be written in terms of total energy, internal energy, enthalpy or temperature. Total energy is chosen as the variable of the energy equation since this is the only variable to write the energy equation in conservation form. In total energy, the potential part is neglected

$$e_t = e + \frac{1}{2} u_i u_i = h - \frac{p}{\rho} + k \tag{2.38}$$

Here, e is the internal energy, h is the enthalpy and k is the kinetic energy of the mixture per unit mass. The total energy equation for an infinitesimal control volume, neglecting the work done by body forces and assuming there is no heat source term (i.e. electric spark, magnetic energy ...) is as follows

$$\frac{\partial \rho e_t}{\partial t} + \frac{\partial \left[u_j (\rho e_t + p)\right]}{\partial x_j} = -\frac{\partial q_j}{\partial x_j} + \frac{\partial \tau_{ij} u_i}{\partial x_j} \tag{2.39}$$

2.3.1 INTERNAL ENERGY, ENTHALPY AND SPECIFIC HEATS

Internal energy per unit mass e_α, enthalpy per unit mass $h_\alpha = e_\alpha + p_\alpha/\rho_\alpha$, and the specific heats Cp_α and Cv_α of species α depend on temperature only, according to the perfect gas assumption

$$de_\alpha = Cv_\alpha(T)dT \tag{2.40}$$

$$dh_\alpha = Cp_\alpha(T)dT \tag{2.41}$$

The enthalpy of species α is obtained by integration of equation (2.41) from a reference temperature T_0. This represents the summation of the sensible enthalpy $h_{s\alpha}$ and of the enthalpy of formation $\Delta h^0_{f,\alpha}$ where superscript ^{0} represents reference conditions

$$\begin{aligned} h_\alpha(T) &= h_{s\alpha}(T) + \Delta h^0_{f,\alpha} \\ &= \int_{T_0}^{T} Cp_\alpha(\theta)d\theta + \Delta h^0_{f,\alpha} \end{aligned} \tag{2.42}$$

The specific heats of species satisfy Mayer relation

$$r_\alpha = Cp_\alpha(T) - Cv_\alpha(T) \tag{2.43}$$

and the ratio of specific heats depends on temperature

$$\gamma_\alpha(T) = \frac{Cp_\alpha(T)}{Cv_\alpha(T)} \tag{2.44}$$

Specific heats of the mixture are approximated with mass weighted formulas

$$Cp\,(Y_\alpha, T) = \sum_{\alpha=1}^{N_{sp}} Cp_\alpha(T)Y_\alpha \qquad ; \qquad Cv\,(Y_\alpha, T) = \sum_{\alpha=1}^{N_{sp}} Cv_\alpha(T)Y_\alpha \tag{2.45}$$

Specific heats Cp_α are tabulated as fourth order polynomials (CHEMKIN format tables), for two different temperature ranges of ($T_{\min}$-1000) and (1000-$T_{\max}$). The data for specific heats at constant pressure Cp_α (J/kg.K) and enthalpy of formation $\Delta h^0_{f,\alpha}$ taken from Burcat polynomial database [14], are presented in Appendix B.2. The speed of sound in the mixture is

$$c^2 = \gamma r T = \gamma \frac{p}{\rho} \tag{2.46}$$

The internal energy and enthalpy of the mixture are computed by mass weighted averaging

$$e = \sum_{\alpha=1}^{N_{sp}} e_\alpha Y_\alpha \quad ; \quad h = \sum_{\alpha=1}^{N_{sp}} h_\alpha Y_\alpha \tag{2.47}$$

The final form of the total energy in equation (2.39) is

$$e_t = \sum_{\alpha=1}^{N_{sp}} \left(\Delta h^0_{f\alpha} + \int_{T_0}^{T} Cp_\alpha(\theta)d\theta \right) Y_\alpha - rT + \frac{1}{2}u_i u_i \tag{2.48}$$

2.3.2 MOLECULAR DIFFUSION OF HEAT AND ENTHALPY

Kinetic theory suggests the heat flux expression $\dot{q}_j$, in direction x_j as

$$\dot{q}_j = \sum_{\alpha=1}^{N_{sp}} h_\alpha J^c_{\alpha j} - \lambda T_{,j} - p \sum_{\alpha=1}^{N_{sp}} D^T_\alpha d_{\alpha j} \tag{2.49}$$

where $d_{\alpha j}$ is the diffusion driving force of specie α given in equation (2.14). The terms of equation (2.49), from left to right, are :

- Partial enthalpy flux of specie α.
- Heat transfer by conduction computed by Fourier law. λ is the coefficient of thermal conductivity. It is approximated like μ in equation (2.36). Also, the coefficient of partial conductivity λ_α of species α is computed over CHEMKIN model as

$$\lambda_\alpha = \lambda_{\alpha 0} + \lambda_{\alpha 1} T + \lambda_{\alpha 2} T^2 \quad \text{(W/m.K)} \tag{2.50}$$

  The constants $\lambda_{\alpha 0}$, $\lambda_{\alpha 1}$ and $\lambda_{\alpha 2}$ are tabulated in appendix A.
- The third term, which is assumed to be negligible compared to conductive heat flux, refers to the heat transfer that is induced by concentration gradients (Dufour effect) [36].

2.3.3 TEMPERATURE EVALUATION

Since the species enthalpy h_α in total energy depends on temperature non-linearly, analytical derivation is not possible. Temperature field may be computed from the total energy e_t, iteratively. Newton-Raphson iteration is applied for temperature calculations [59, 80].

$$f(T) = e_t - \left(\sum_{\alpha=1}^{Nsp} h_\alpha Y_\alpha - rT + \frac{1}{2} u_i u_i \right) \tag{2.51}$$

Given a value for e_t, temperature is iterated for convergence of $f(T)$ to zero

$$T^{it+1} = T^{it} - \frac{f(T^{it})}{f'(T^{it})} \tag{2.52}$$

where *it* is the iteration step. The temperature iteration is initialized with the value from the previous step.

2.4 SUMMARY OF SYSTEM OF EQUATIONS

In summary, the system equations which serves as the basis for the simulations presented in this work is

$$\frac{\partial \vec{U}}{\partial t} + \frac{\partial \vec{F}}{\partial x} + \frac{\partial \vec{G}}{\partial y} + \frac{\partial \vec{H}}{\partial z} = \vec{V} + \vec{S} \tag{2.53}$$

The vector of dependent variables $\vec{U}$, the convective flux vectors $\vec{F}$, $\vec{G}$, $\vec{H}$, the vector of viscous stress $\vec{V}$ and the vector of source terms $\vec{S}$ are given as follows

$$\vec{U} = \begin{bmatrix} \rho \\ \rho u \\ \rho v \\ \rho w \\ \rho e_t \\ \rho Y_1 \\ \vdots \\ \rho Y_{N_{sp}-1} \end{bmatrix} \quad \vec{F} = \begin{bmatrix} \rho u \\ \rho u^2 + p \\ \rho uv \\ \rho uw \\ (\rho e_t + p)u \\ \rho u Y_1 \\ \vdots \\ \rho u Y_{N_{sp}-1} \end{bmatrix} \quad \vec{G} = \begin{bmatrix} \rho v \\ \rho vu \\ \rho v^2 + p \\ \rho vw \\ (\rho e_t + p)v \\ \rho v Y_1 \\ \vdots \\ \rho v Y_{N_{sp}-1} \end{bmatrix} \quad \vec{H} = \begin{bmatrix} \rho w \\ \rho wu \\ \rho wv \\ \rho w^2 + p \\ (\rho e_t + p)w \\ \rho w Y_1 \\ \vdots \\ \rho w Y_{N_{sp}-1} \end{bmatrix}$$

$$\vec{V} = \begin{bmatrix} 0 \\ \tau_{xx,x} + \tau_{xy,y} + \tau_{xz,z} \\ \tau_{yx,x} + \tau_{yy,y} + \tau_{yz,z} \\ \tau_{zx,x} + \tau_{zy,y} + \tau_{zz,z} \\ \left\{ \begin{array}{c} -q_{x,x} + (u\tau_{xx})_{,x} + \left(v\tau_{yx}\right)_{,x} + (w\tau_{zx})_{,x} \\ -q_{y,y} + \left(u\tau_{xy}\right)_{,y} + \left(v\tau_{yy}\right)_{,y} + \left(w\tau_{zy}\right)_{,y} \\ -q_{z,z} + (u\tau_{xz})_{,z} + \left(v\tau_{yz}\right)_{,z} + (w\tau_{zz})_{,z} \end{array} \right\} \\ -J^c_{1x,x} - J^c_{1y,y} - J^c_{1z,z} \\ \vdots \\ -J^c_{(N_{sp}-1)x,x} - J^c_{(N_{sp}-1)y,y} - J^c_{(N_{sp}-1)z,z} \end{bmatrix} \quad ; \quad \vec{S} = \begin{bmatrix} 0 \\ 0 \\ 0 \\ 0 \\ 0 \\ \dot{\omega}_\alpha \\ \vdots \\ \dot{\omega}_{N_{sp}-1} \end{bmatrix} \tag{2.54}$$

CHAPTER 3

LARGE EDDY SIMULATION

Turbulent flow problems in the context of this thesis are at high Reynolds numbers and the range of flow scales is fairly wide. Resolution of all scales in realistic or industrial configurations is impossible and it seems to remain so in near future despite the drastic improvement in computational capabilities. Large Eddy Simulation (LES) is suitable and affordable for the simulation of the problems concerned.

Before putting forward the arguments that support the idea of LES one may ask the question: what is being resolved during LES calculations? As Pope [107] does, a clear distinction between real and resolved flow fields have to be carried out. When a field of any turbulent flow variable $U(x,y,z,t)$ is considered, the resolved field of this variable $W(x,y,z,t)$ is the numerical solution of the set of filtered Navier-Stokes equations over a grid. In the context of LES, W is intended to be statistically related to the filtered field $\bar{U}$ which is obtained by applying a low pass filter of characteristic width Δ to U. As the filter width is reduced down to the smallest scales (Kolmogorov microscale η), the statistics of the solution obtained by applying an accurate numerical method and proper boundary conditions converge to a condition where all energy containing contribution may be represented by W. This is the DNS level which is obtained when the oscillations with smaller wavelengths than the grid cut-off have no energy. The statistics at DNS level match those of $\bar{U}$. The resolved variables for LES are commonly considered as "filtered" forms of the solution at the DNS level, in *a priori* tests. This filter is not precisely defined for numerical schemes having dissipation property, linked to the resolving efficiency. In appropriate LES the statistics achieve an intermediate asymptote as Δ is in the inertial sub-range.

After four decades of intensive developments [87, 109, 110, 115] and from a theoretical point of view, LES is now a well-established technique for incompressible flows,. Intricate interac-

tions between numeric and sub-grid modeling are well understood in academic configurations [43, 52, 76]. Multilevel/multiresolution approaches like Detached-Eddy Simulations (DES) have been developed (see [111] for review), allowing robust and efficient simulations for industrial configurations. Nevertheless, certain aspects of LES such as those in complex physics -shocked flows, multi-component, multiphase, reacting flows, or in complex geometries, remain unclear despite some outstanding achievements [9, 13]. Following S.B. Pope [107], one should first make the distinction between pure physical LES and pure numerical LES.

In the former, filtered equations are solved for the large scales of motion, and the effect of the unresolved turbulent scales, or sub-grid scales (SGS) on the resolved ones is taken into account via a physically sound explicit sub-grid model. Higher-order non-dissipative numerics are needed to avoid interactions between numerical errors and sub-grid modeling. Solving the filtered Navier-Stokes equations in Fourier space with spectral methods is ideal for academic flows. In this case, the low-pass filter is a sharp Fourier cutoff, and spectral sub-grid eddy viscosity closures can be derived from analytical theories [17, 96]. This ideal situation is forcefully limited to homogeneous turbulence in cubic computational domains. High accuracy can also be achieved in physical space on more general configurations (though still very simple) with higher-order centered compact finite difference schemes [83] that include Structure Function models, either standard [96], selective [21] or filtered [30]. Nevertheless, none of these methods can handle sharp gradients or shocked flows without any numerical filtering or artificial viscosity, which already raises the question of competition between numerics and models. If multi-species, reacting variable density flows are considered, the situation is more complicated.

In pure numerical LES, shock-capturing methods are used to solve the Navier-Stokes or Euler equations without any explicit filtering. There is no explicit sub-grid model: small scale fluctuations are damped by the numerical diffusion. This approach which is denoted -highly controversial in the combustion community- is called implicit LES (ILES), or Monotone Integrated LES (MILES) [60, 91]. High-resolution methods are required to avoid a significant impact of the numerics on the turbulent flow statistics. An evaluation of the effects of numerical diffusion on the DNS and LES of compressible turbulence (non-reacting) has been done by E. Garnier [46, 47] for mainly academic demonstrational flows. Several shock-capturing schemes were tested, and the 5^{th} order WENO scheme [69, 88, 112] was found to perform well. This approach has been widely used since. A recent successful MILES has been re-

ported for the simulation of multicomponent Richtmyer-Meshkov turbulent mixing carried out with the Euler equations [119], surprisingly, there are very few attempts to apply this technique to reacting flows [15, 117].

Intermediate between pure physical and pure numerical LES are all other situations, where both explicit sub-grid modeling and robust dissipative schemes are used –although this was not recommended by E. Garnier [47]. Many, if not all, LES of practical (or industrial) interest are carried out that way on irregular or even unstructured grids, with old RANS solvers upgraded for SGS modeling. Hybrid methods have also been developed (e.g. [31, 56]), where the flow solver switches from a second or a fourth-order central scheme away from discontinuities to a shock-capturing scheme, depending on an empirically designed stiffness sensor. Whatever the method, in most of practical physical LES, some SGS terms are systematically neglected, or crudely modeled. As such, irregular grids induce a second-order commutation error [53], and the physically sound part of the SGS model that mimics the small-scale mixing and scalar dissipation rate interacts with the numerical diffusion: both (grid and SGS model) smooth out the flow field. In summary, firstly, filtered conservative variables are introduced which are so-called resolved variables. Then, the set of governing equations satisfied by filtered variables are presented. Finally, two different physical LES modeling strategies are explained, and the dissipation and dispersion characteristics of different schemes for numerical LES are discussed.

3.1 FILTERING THE NAVIER-STOKES EQUATIONS

A filter operation makes the distinction between the large scales $\overline{f}$ and the small scales f' of a continuous function f, i.e. $f = \overline{f} + f'$. It is considered that the projection of function f on a coarse grid acts as an implicit filtering operation, due to the Nyquist cut-off wavelength.

The filtered part for a homogeneous filter may be standardly defined as

$$\overline{f}(x) = \int_{\Omega} G_{\Delta}(x - \xi)\, f(\xi)\, d\xi \tag{3.1}$$

where x and ξ are coordinates in the domain Ω and Δ is the "filter width" associated with the filter kernel G_{Δ} which necessarily satisfies

$$\int_{\Omega} G_{\Delta}(\xi)\, d\xi = 1 \tag{3.2}$$

Filtering and derivative commute if the filter is homogeneous [53, 122].

The multicomponent compressible LES equations are similar to the mono-species form given by C.G. Speziale and co-workers [34, 116], but thermodynamics is different. As in the mono-species case, filtered multicomponent equations can be cast in different ways, leading to different SGS modeling strategies ([84, 122, 123] and Garnier et al.[48] for a review). The derivations done in several ways are presented in the literature with more or less details [56, 104, 121]. The way to display LES mathematically is to define the resolved variables (computable quantities) then state the governing equations with separate resolved and SGS terms. This separation enables introduction of models for SGS terms. Primary computable quantities are the resolved field variables $\overrightarrow{W}$ advanced in time.

$$\overrightarrow{W} = {}^{T}\{W_1, W_2, \ldots, W_{5+N_{sp}}\} \tag{3.3}$$

In the compressible formulation, if a Reynolds-like decomposition is introduced, filtering the continuity equation (2.12) will lead to an uncomputable variable $\overline{\rho u_i}$.

$$\begin{aligned} u_i = \overline{u_i} + u_i' \;;\; \rho = \overline{\rho} + \rho' \quad \Rightarrow \quad \overline{\rho u_i} &= \overline{\rho}\,\overline{u_i} + (\overline{\overline{\rho}\,\overline{u_i}} - \overline{\rho}\,\overline{u_i}) \quad \rightarrow \quad \text{Leonard term} \\ &+ (\overline{\overline{\rho}\, u_i' + \rho'\,\overline{u_i'}}) \quad \rightarrow \quad \text{cross term} \\ &+ \overline{\rho' u_i'} \quad \rightarrow \quad \text{Reynolds term} \end{aligned} \tag{3.4}$$

The Reynolds term in RANS formulation and all three extra terms in LES formulation are non-zero so that $\overline{\rho u_i} \neq \overline{\rho}\,\overline{u_i}$. Favre introduced the concept of mass weighted filtering for compressible RANS equations [39, 40].

$$u_i = \tilde{u}_i + u_i'' \qquad \tilde{u}_i = \frac{\overline{\rho u_i}}{\overline{\rho}} \tag{3.5}$$

Favre variables are only mathematical definitions which eliminate some of the SGS terms in the LES equations. Despite the loss of physics, Favre variables introduce mathematical simplicity. Theoretically, the set of NS equations (2.53) are filtered and Favre variables are introduced in these equations. The variables obtained solving the filtered set of equations also

include numerical errors.

$$\vec{W} = \begin{bmatrix} \overline{\rho} \\ \overline{\rho u} \\ \overline{\rho v} \\ \overline{\rho w} \\ \overline{\rho e_t} \\ \overline{\rho Y_1} \\ \vdots \\ \overline{\rho Y_{N_{sp}-1}} \end{bmatrix} = \begin{bmatrix} \overline{\rho} \\ \overline{\rho}\widetilde{u} \\ \overline{\rho}\widetilde{v} \\ \overline{\rho}\widetilde{w} \\ \overline{\rho}\widetilde{e_t} \\ \overline{\rho}\widetilde{Y_1} \\ \vdots \\ \widetilde{\overline{\rho} Y_{N_{sp}-1}} \end{bmatrix}$$

Given the $W_j^{'s}$ one can obtain directly the Favre-filtered values $\widetilde{u_i}$, $\widetilde{e_t}$ and $\widetilde{Y_\alpha}$ which are secondary computable quantities. However, temperature and pressure fields are also needed during the simulation. Temperature may be deduced from W_5 and pressure through ideal gas equation of state. Particular attention will be given on this term at the end of this section.
Filtered equations with Favre variables are presented hereafter. The filtered quantities $\overline{\phi}$ or $\widetilde{\phi}$ are split into the sum of a part $\hat{\phi}$ computable out of primary or secondary quantities plus an uncomputable part $\check{\phi}$ (SGS).

$$\overline{\phi} = \hat{\phi} + \check{\phi} \tag{3.6}$$

3.1.1 CONSERVATION OF MASS

Consider the continuity equation (2.12) in conservative form, filtered with a linear filter which may commute with derivatives

$$\frac{\partial \overline{\rho}}{\partial t} + \left(\overline{\rho u_j}\right)_{,j} = 0 \tag{3.7}$$

The convective term ($\overline{\rho u_i}$) is uncomputable so Favre variable is introduced for a straightforward filtered equation (3.7)

$$\frac{\partial W_1}{\partial t} + \left(\overline{\rho}\widetilde{u}_j\right)_{,j} = 0 \tag{3.8}$$

Since Favre filtering does not commute with derivatives, Favre variables are introduced after commuting the “bar-filter” with partial differential operator.

3.1.2 CONSERVATION OF CHEMICAL SPECIES

The species conservation equation (2.24) after filtering operation is

$$\frac{\partial \overline{\rho Y_\alpha}}{\partial t} + \left(\overline{\rho u_j Y_\alpha}\right)_{,j} = -\overline{J^c_{\alpha j,j}} + \overline{\dot{\omega}_\alpha} \tag{3.9}$$

Introducing Favre variables into (3.9) yields

$$\frac{\partial W_{5+\alpha}}{\partial t} + \left(\overline{\rho}\widetilde{u_j}\widetilde{Y_\alpha}\right)_{,j} = -\overline{J^c_{\alpha j,j}} + \overline{\dot{\omega}_\alpha} - \left[\overline{\rho}\left(\widetilde{u_j Y_\alpha} - \widetilde{u_j}\widetilde{Y_\alpha}\right)\right]_{,j} \tag{3.10}$$

The filtered corrected species mass flux term can be split into computable and uncomputable components, as explained in relation (3.6)

$$\overline{J^c_{\alpha j}} \;=\; \hat{J}^c_{\alpha j} + \check{J}^c_{\alpha j} \tag{3.11}$$

The resolved corrected mass flux $\hat{J}^c_{\alpha j}$ of species α in the direction x_j is computed from equations (2.17)- (2.23) using resolved variables.

$$\hat{J}^c_{\alpha j} \;=\; \overline{\rho}\left(\widetilde{D_{\alpha m}}\widetilde{X_{\alpha,j}}\frac{M_\alpha}{\widetilde{M}} + \widetilde{V^c_j}\widetilde{Y_\alpha}\right) \tag{3.12}$$

$$\check{J}^c_{\alpha j} \;=\; \overline{\rho\left(D_{\alpha m}X_{\alpha,j}\frac{M_\alpha}{M} + V^c_j Y_\alpha\right)} - \overline{\rho}\left(\widetilde{D_{\alpha m}}\widetilde{X_\alpha}, j\frac{M_\alpha}{\widetilde{M}} + \widetilde{V^c_j}\widetilde{Y_\alpha}\right) \tag{3.13}$$

So the filtered species conservation equation reads

$$\frac{\partial W_{5+\alpha}}{\partial t} + \left(\overline{\rho}\widetilde{u_j}\widetilde{Y_\alpha}\right)_{,j} = -\hat{J}^c_{\alpha j,j} + \hat{\omega}_\alpha + \left(C_{1\alpha j} + C_{2\alpha j}\right)_{,j} + C_{3\alpha} \tag{3.14}$$

where

$$C_{1\alpha j} \;=\; -\overline{\rho}\left(\widetilde{u_j Y_\alpha} - \widetilde{u_j}\widetilde{Y_\alpha}\right) \tag{3.15}$$

$$C_{2\alpha j} \;=\; -\check{J}^c_{\alpha j} \tag{3.16}$$

$$C_{3\alpha} \;=\; \check{\omega}_\alpha \tag{3.17}$$

In *a priori* LES tests presented in appendix H it has been shown that the $C_{2\alpha j}$ term is generally negligible. On the other hand, the $C_{3\alpha}$ term is the cornerstone of reacting LES [42, 80, 81].

3.1.3 EQUATION OF MOTION

Filtering equation of motion (2.29) and commuting the filter with partial derivative gives

$$\frac{\partial \overline{\rho u_i}}{\partial t} + \left(\overline{\rho u_i u_j}\right)_{,j} = -\overline{p}_{,j} + \overline{\tau_{ij}}_{,j} \tag{3.18}$$

Filtered viscous stress and pressure need special attention.

In the viscous stress , viscosity is not constant

$$\mu = \mu(Y_\alpha, T) \tag{3.19}$$

As a result, the filtered viscous stress is uncomputable and may be split into uncomputable and computable parts

$$\overline{\tau}_{ij} = \hat{\tau}_{ij} + \check{\tau}_{ij} \tag{3.20}$$

$$\hat{\tau}_{ij} = \widetilde{\mu}\widetilde{S_{ij}} \quad ; \quad \tilde{\mu} = \mu(\tilde{Y}_\alpha, \hat{T}) \tag{3.21}$$

$$\check{\tau}_{ij} = \overline{\mu S_{ij}} - \widetilde{\mu}\widetilde{S_{ij}} \tag{3.22}$$

where $\hat{T}$ is the computable temperature (will be explained in detail in the section for W_5) and the filtered strain tensor for compressible flow is

$$\widetilde{S_{ij}} = \widetilde{u}_{i,j} + \widetilde{u}_{j,i} - \frac{2}{3}\widetilde{u}_{k,k}\delta_{ij} \tag{3.23}$$

Since the pressure is calculated using the temperature via the equation of state, it has an uncomputable part like the temperature. Specific to multicomponent flows, the uncomputable filtered pressure reads

$$\overline{p} = \hat{p} + \check{p} \tag{3.24}$$

$$\hat{p} = \overline{\rho}\widetilde{r}\hat{T} = \overline{\rho}\left(\mathcal{R}\sum_{\alpha=1}^{N_{sp}}\frac{1}{W_\alpha}\widetilde{Y_\alpha}\right)\hat{T} \tag{3.25}$$

$$\check{p} = \overline{\rho}\left(\widetilde{rT} - \widetilde{r}\hat{T}\right) \tag{3.26}$$

Considering (3.20) and (3.24), the Favre variable introduced equation of motion yields

$$\frac{\partial W_{1+i}}{\partial t} + \left(\overline{\rho}\widetilde{u_i}\widetilde{u_j} + \hat{p}\delta_{ij}\right)_{,j} = \hat{\tau}_{ij,j} + \left(A_{1ij} + A_{2ij} + A_3\delta_{ij}\right)_{,j} \tag{3.27}$$

$$A_{1ij} = -\overline{\rho}\left(\widetilde{u_i u_j} - \widetilde{u_i}\widetilde{u_j}\right) \tag{3.28}$$

$$A_{2ij} = \check{\tau}_{ij} \tag{3.29}$$

$$A_3 = -\check{p} \tag{3.30}$$

The A_{1ij} term is the most important one and is common to mono-species compressible LES equations. It reduces to Germano's central moments [51] in the incompressible limit. The A_{2ij} term appears because the filtered viscous stress is uncomputable as explained and neglected in most compressible LES [122, 123]. It was shown in *a priori* tests presented in appendix H that the $A_{3,i}$ term may overcome $A_{1ij,j}$ in some cases. This is never considered in any multicomponent, non-reacting or reacting LES.

3.1.4 ENERGY EQUATION

Filtering and commuting the filter with derivative for the energy equation (2.39) gives

$$\frac{\partial \overline{\rho e_t}}{\partial t} + \overline{(\rho u_j e_t)}_{,j} + \overline{(p u_j)}_{,j} = -\overline{q_j}_{,j} + \overline{(\tau_{ij} u_i)}_{,j} \tag{3.31}$$

Then, introducing Favre variables in the filtered total energy equation (3.31) yields

$$\frac{\partial W_5}{\partial t} + \left[(\overline{\rho}\widetilde{e_t} + \hat{p})\,\widetilde{u_j}\right]_{,j} = \left(\widetilde{u_i}\hat{\tau}_{ij}\right)_{,j} - \hat{q}_{j,j} + \left(B_{1j} + B_{2j} + B_{3j} + B_{4j}\right)_{,j} \tag{3.32}$$

$$B_{1j} = -\overline{\rho}\left(\widetilde{e_t u_j} - \widetilde{e_t}\widetilde{u_j}\right) \tag{3.33}$$

$$B_{2j} = -\left(\overline{p u_j} - \hat{p}\widetilde{u_j}\right) \tag{3.34}$$

$$B_{3j} = \overline{u_i \tau_{ij}} - \widetilde{u_i}\hat{\tau}_{ij} \tag{3.35}$$

$$B_{4j} = -\breve{q}_j \tag{3.36}$$

Equation (3.32) and term B_{4j} involve respectively the resolved and SGS parts of the uncomputable filtered heat flux. As explained in section 2.3.3, temperature can not be deduced directly but it is computed out of e_t

$$\overline{q}_j = \hat{q}_j + \breve{q}_j \tag{3.37}$$

$$\hat{q}_j = -\widetilde{\lambda}\hat{T}_{,j} + \sum_\alpha \hat{h}_\alpha \hat{J}^c_{\alpha j} \tag{3.38}$$

$$\breve{q}_j = -\left(\overline{\lambda T}_{,j} - \widetilde{\lambda}\hat{T}_{,j}\right) + \sum_\alpha \left(\overline{h_\alpha J^c_{\alpha j}} - \hat{h}_\alpha \hat{J}^c_{\alpha j}\right) \tag{3.39}$$

In (3.38), $\widetilde{\lambda}$ is uncomputable and is obtained the same way as (3.19).

3.1.5 SPECIAL ATTENTION FOR W_5 AND IDEAL GAS EQUATION

The total energy is used for construction of the conservative variable in the energy equation. Temperature and pressure are computed from this term. Hence the W_5 term deserves particular attention.

$$\begin{aligned} \overline{\rho e_t} &= \overline{\rho(e + \frac{1}{2}u_i u_i)} \\ &= \overline{\rho}\widetilde{h} - \overline{p} + \overline{\rho}\widetilde{k} \end{aligned} \tag{3.40}$$

The filtered pressure, the Favre-filtered static enthalpy and the Favre-filtered kinetic energy per unit mass are uncomputable.

$$\overline{\rho e_t} = \overline{\rho}\widetilde{e_t} = \overline{\rho}\hat{e}_t + \overline{\rho}\check{e}_t \tag{3.41}$$

$$\overline{\rho}\hat{e}_t = \overline{\rho}\hat{h} - \hat{p} + \overline{\rho}\hat{k} \tag{3.42}$$

$$\overline{\rho}\check{e}_t = \overline{\rho}\check{h} - \check{p} + \overline{\rho}\check{k} \tag{3.43}$$

The split uncomputable pressure is given in equation (3.24). The Favre-filtered static enthalpy is written as

$$\widetilde{h} = \hat{h} + \check{h} \tag{3.44}$$

$$\hat{h} = \sum_{\alpha} \hat{h}_\alpha \widetilde{Y}_\alpha \tag{3.45}$$

$$\check{h} = \sum_{\alpha} \left(\widetilde{h_\alpha Y_\alpha} - \hat{h}_\alpha \widetilde{Y}_\alpha \right) \tag{3.46}$$

where

$$\hat{h}_\alpha = \Delta h^0_\alpha + \int_{T_0}^{\hat{T}} C_{p\alpha}(\theta) d\theta \tag{3.47}$$

The Favre-filtered kinetic energy is :

$$\widetilde{k} = \hat{k} + \check{k} \tag{3.48}$$

$$\hat{k} = \frac{1}{2}\widetilde{u_i}\widetilde{u_i} \tag{3.49}$$

$$\check{k} = \frac{1}{2}\left(\widetilde{u_i u_i} - \widetilde{u_i}\widetilde{u_i}\right) \equiv k_{sgs} \tag{3.50}$$

In equation (3.25), and at the upper integration limit in (3.47), the resolved temperature $\hat{T}$ has been used instead of the Favre-filtered temperature $\widetilde{T}$. Given numbers for the $W_j^{'s}$, $\widetilde{T}$ could theoretically be obtained by finding iteratively (e.g. via a Newton-Raphson procedure) the value which produces a posteriori the proper W_5 value from equation (3.40). In practice, since (3.43) is seldom (if ever) explicitly modeled in multicomponent LES, only the analytic expression of the computable part $\overline{\rho}\hat{e}_t$, equation (3.42), is used to find the resolved temperature $\hat{T}$ such that

$$W_5 = \overline{\rho}\left[\sum_{\alpha}\left(\Delta h^0_\alpha + \int_{T_0}^{\hat{T}} C_{p\alpha}(\theta) d\theta\right)\widetilde{Y}_\alpha - \widetilde{r}\hat{T} + \frac{1}{2}\widetilde{u_i}\widetilde{u_i}\right] \tag{3.51}$$

So, unless the uncomputable total energy per unit volume $\overline{\rho}\check{e}_t$ is properly modeled, the Favre-filtered temperature is uncomputable.

3.2 EXPLICIT SUB-GRID MODELING

In the present study, as in most physical compressible/multicomponent LES, the SGS terms which do not emanate from convective parts of hyperbolic governing equations $\left[A_{2ij},\ A_3,\ B_{3j},\ B_{4j}\ \text{and}\ C_{2\alpha j}\right]$ will not be explicitly modeled. One can consider that they are simply neglected, or put together with the dominant dynamic terms A_{1ij}, B_{1j} and $C_{1\alpha j}$. For the main A_{1ij} sub-grid term in equation (3.27), a classical sub-grid eddy-viscosity assumption is made for the deviatoric part of the SGS tensor

$$A_{1ij}^{D} = A_{1ij} - \frac{1}{3}A_{1kk}\delta_{ij} = \mu_{sgs}^{t}\widetilde{S_{ij}} \tag{3.52}$$

so that

$$\overline{\rho}\left(\widetilde{u_i u_j} - \widetilde{u_i}\widetilde{u_j}\right) - \frac{2}{3}\overline{\rho}k_{sgs}\delta_{ij} = -\mu_{sgs}^{t}\widetilde{S_{ij}} \tag{3.53}$$

Two SGS models are implemented : the Smagorinsky (SM) model [115] extended to compressible flows, and the Selective Structure Function (SSF) model [21, 96].

3.2.1 CLOSING THE FILTERED EQUATION OF MOTION

3.2.1.1 THE SMAGORINSKY MODEL

The first known application of the idea of physical LES is by Joseph Smagorinsky [115]. The turbulent viscosity μ_{sgs}^{t} is dimensionally equal to $\bar{\rho}ul$. The velocity may be approximated by assuming the energy dissipation is equal to the energy transfered to small scales, with no backscattering.

$$\epsilon \approx \rho\frac{u^3}{l} \approx \rho\frac{u^3}{\Delta} \tag{3.54}$$

In this relation, the characteristic length is taken as the filter width Δ

$$\mu_{sgs}^{t} = \bar{\rho}\left(\frac{\Delta\epsilon}{\rho}\right)^{1/3}\Delta \tag{3.55}$$

The main assumption for the model states that production $\mathcal{P}_{k_{sgs}}$ is equal to dissipation for the sub-grid kinetic energy

$$\mathcal{P}_{k_{sgs}} = A_{1ij}^{D}\widetilde{u_i}_{,j} = \mu_{sgs}^{t}\widetilde{S_{ij}}\widetilde{u_i}_{,j} \tag{3.56}$$

When one substitute the production into equation (3.55) for dissipation, the turbulent viscosity reads

$$\mu_{sgs}^{t} = \bar{\rho}^{2/3}\left(\mu_{sgs}^{t}\widetilde{S_{ij}}\widetilde{u_i}_{,j}\right)^{1/3}\Delta^{4/3} \tag{3.57}$$

The usual form of the compressible SM model is [34, 49]

$$\mu_{sgs}^{t} = \overline{\rho}(C_S\Delta)^2|\widetilde{S^*}| \tag{3.58}$$

$$|\widetilde{S^*}| = \left(2\widetilde{S_{ij}^*}\widetilde{S_{ij}^*}\right)^{1/2} \tag{3.59}$$

It is common to apply the equation (3.59) for construction of SM model which is only valid for incompressible case. However, considering the sub-grid scale production term $A_{1ij}^{D}\widetilde{u}_{i,j}$ [56], the traceless closure (3.53) leads rather to

$$|\widetilde{S^*}| = \left(\widetilde{S_{ij}}\widetilde{S_{ij}^*}\right)^{1/2} \tag{3.60}$$

This is the expression implemented in the present study. In the SM model, the filter width, or turbulence resolution length scale Δ, is multiplied by the model constant. The product $C_S\Delta$ can be written as $\lambda\Delta c$ where $\Delta c = (\Delta x_1\Delta x_2\Delta x_3)^{1/3}$ is the geometrical mean local grid resolution. Various derivations which result in different values for the constant C_S are possible (p.587 in [106]). In the numerical experiments presented in section 5.1, simulations with the SM model are done for λ^2=0.01 and λ^2=0.02. Taking the constant $C_S = 0.1$, this may be interpreted as varying the numerical accuracy from $\Delta/h = 1$ to $\Delta/h = \sqrt{2}$. This is the usual range for physical LES using dissipative numerical schemes (question 7 in [107]).

3.2.1.2 THE YOSHIZAWA MODEL

The isotropic part

$$A_{1ij}^{I} = \frac{1}{3}A_{1kk}\delta_{ij} = -\frac{2}{3}\overline{\rho}k_{sgs}\delta_{ij} \tag{3.61}$$

can be represented by the Yoshizawa model [129] as

$$\overline{\rho}k_{sgs} = \overline{\rho}C_I\Delta^2|\widetilde{S^*}|^2 \tag{3.62}$$

However, it may be neglected if the sub-grid Mach number $\mathrm{M}_{sgs}^2 = \overline{\rho}k_{sgs}/\gamma\overline{p}$ is small [86, 34]. The sub-grid Mach number will be verified *a priori* later in section 5.1.5.

3.2.1.3 THE SELECTIVE STRUCTURE FUNCTION MODEL

The SSF model is based on the standard structure function (SF) model [85] for μ_{sgs}^t in A_{1ij}^D. In the SF model, the second order velocity structure function $F_2(\overrightarrow{x}, \Delta)$ is used

$$F_2(\vec{x}, \Delta x) = \left\langle \left\| \vec{\tilde{u}}(\vec{x}, t) - \vec{\tilde{u}}(\vec{x} + \vec{r}, t) \right\|^2 \right\rangle_{\|\vec{r}\| = \Delta x} \tag{3.63}$$

In practice, the velocity structure function is computed over differences in the resolved velocity field at adjacent grid points. The SF on uniform grid Δx_i =Const. in direction x_i with unit vector $\overrightarrow{e_i}$ is

$$\begin{aligned} F_2^{(i)} &= \|\overrightarrow{\tilde{u}}(\overrightarrow{x}) - \overrightarrow{\tilde{u}}(\overrightarrow{x} + \Delta x_i \overrightarrow{e_i})\|^2 \\ &+ \|\overrightarrow{\tilde{u}}(\overrightarrow{x}) - \overrightarrow{\tilde{u}}(\overrightarrow{x} - \Delta x_i \overrightarrow{e_i})\|^2 \end{aligned} \tag{3.64}$$

The model may be modified for non-uniform rectilinear grid [86]

$$F_2(\overrightarrow{x}, \Delta) = \frac{1}{6} \sum_{i=1}^{3} F_2^{(i)} \left(\frac{\Delta c}{\Delta x_i} \right)^{2/3} \tag{3.65}$$

The SF model gives good results for flows in which turbulence in small scales is close to isotropy, but it is too dissipative for shear layers. The SSF model is an improved version of SF model[21]. It allows to switch-off the model in regions where sharp gradients are present but where the flow is not three-dimensional enough. This is typically the case in the core region of high-speed jets, where transition to turbulence has not yet occurred. The measure of three dimensionality is chosen as the angle θ between the local vorticity and the space averaged value of the vorticity over the six closest neighboring points. The SSF model reads

$$\mu_{sgs}^t = f_{\theta_0}(\theta) C_{SF} \Delta \overline{\rho} \left[F_2(\overrightarrow{x}, \Delta) \right]^{1/2} \tag{3.66}$$

where

$$f_{\theta_0}(\theta) = \begin{cases} 1 & \text{if } \theta \geq \theta_0 = 20^\circ \\ 0 & \text{else} \end{cases} \tag{3.67}$$

The model constant is taken as

$$C_{SF} = 0.105 C_K^{-3/2} = 0.0634 \tag{3.68}$$

where $C_K = 1.4$ is the Kolmogorov constant. The choice of the C_{SF} value is discussed in [21, 30, 31, 85].

3.2.2 CLOSING THE FILTERED ENERGY EQUATION

In the filtered energy equation, the sum of the major sub-grid terms $B_{1j} + B_{2j}$ is modeled as whole with a gradient assumption, using a constant $\mathrm{Pr}_{sgs} = \mu^t_{sgs} Cp/\lambda^t_{sgs}$ number.

$$B_{1j} + B_{2j} = -\frac{\mu^t_{sgs} Cp}{\mathrm{Pr}_{sgs}} \hat{T}_{,j} = -\lambda^t_{sgs} \hat{T}_{,j} \tag{3.69}$$

in which the thermal conductivity for energy is connected to the eddy viscosity through unity Pr_{sgs}.

3.2.3 CLOSING THE FILTERED SPECIES EQUATION

The same is done for the $C_{1\alpha j}$ term of the species equations, equation (3.14), using a constant sub-grid Schmidt number

$$C_{1\alpha j} = -\frac{\mu^t_{sgs}}{\mathrm{Sc}_{sgs}} \widetilde{Y_{\alpha,j}} = -\overline{\rho} D^t_{sgs} \widetilde{Y_{\alpha,j}} \tag{3.70}$$

This is quite a crude -although commonly used- modeling compared, for example, to the dynamic methodology proposed in [56] which closes the major part (3.50) of (3.43) leading to $\hat{T} \approx \widetilde{T}$. However, it is sufficient to assess the aim of this study, which is to compare LES and MILES for high speed shear flows. In this state of mind, it will simply taken that $Pr_{sgs} = Sc_{sgs} = 1$.

Modeling the sub-grid chemical source term $C_{3\alpha}$ is the cornerstone of LES of reacting flows. Most of the models for non-premixed combustion rely on a conserved scalar like the mixture fraction, for which a filtered (joint)probability density function (FPDF) has to be prescribed (usually a β-function). Examples are flamelet models [20], progress-variable models [101]) and conditional moment closure (CMC) models [75]. These models also require the variance of the mixture fraction and/or its dissipation rate at the smallest turbulent scales, which is difficult to achieve in implicit LES [103]. Hence, in the framework of the present study, the $C_{3\alpha}$ reaction term is left to the numerical diffusion.

3.3 Implicit LES

In the simulations, a set of non-linear PDEs is being solved. In order to satisfy stability and monotonicity of solutions including discontinuities, specially designed schemes are applied.

These schemes, by their nature, cause the waves speed and amplitude of the solution to deviate from theoretical exact solution. In "numerical LES" approach, the deformation due to the numerical scheme, linked to the resolving efficiency of the derivation scheme, contributes as SGS motions. This argument is equivalent to what is indicated by Boris: *"monotone CFD algorithms readily have built-in filter, and corresponding built-in SGS model"* [12]. The numerical deformation of wave speeds and amplitudes due to the numerical schemes are dispersive and dissipative errors respectively. The dissipative and dispersive errors may be separated analytically, applying the modified wave number (MWN) spectral analysis. This analysis may be done analytically for linear numerical schemes.

3.3.1 MWN ANALYSIS

Consider the one-dimensional scalar function $F_k(x)$, $x \in [0, 2\pi]$ for simplicity, containing a single Fourier mode k. On a regular grid $x_i = i\Delta x$, $\Delta x = 2\pi/N$, $i = 0, \ldots, N$, k must stay within the numerical cutoff $|k| \leq N/2$, $|k\Delta x| \leq \pi$ to avoid aliasing errors. The discrete projection of $F_k(x)$ is

$$F_k(x_i) = \widehat{F_k} e^{jkx_i} \equiv F_{k,i} \tag{3.71}$$

Linear MWN analysis

A linear scheme produces a numerical derivative at the single mode k

$$\left.\frac{\delta F_k}{\delta x}\right|_i^L = \widehat{\frac{\delta F_k}{\delta x}}(k) e^{jkx_i} = jk'(k)\widehat{F_k} e^{jkx_i} \tag{3.72}$$

where $k'(k\Delta x)$ is the MWN of the scheme, whose real and imaginary parts are associated respectively with dispersive and dissipative errors. The analysis of response produced by some linear schemes on mode k may be demonstrated as follows.

- Second order centered scheme

$$\left.\frac{\partial F_k}{\partial x}\right|_i = \frac{F_{k,i+1} - F_{k,i-1}}{2\ \Delta x} = \sum_{k=-N/2}^{N/2} \widehat{F_k} \left(\frac{e^{jk\Delta x} - e^{-jk\Delta x}}{2\Delta x} \right) e^{jkx_i}$$

$$k'(k\Delta x) = \frac{\sin(k\Delta x)}{\Delta x} \tag{3.73}$$

- First order upwind scheme

$$\left.\frac{\partial F_k}{\partial x}\right|_i = \frac{F_{k,i} - F_{k,i-1}}{\Delta x} = \sum_{k=-N/2}^{N/2} \widehat{F_k}\left(\frac{1 - e^{-jk\Delta x}}{\Delta x}\right) e^{-jkx_i}$$

$$k'(k\Delta x) = \frac{\sin(k\Delta x)}{\Delta x} - j\left(\frac{1 - \cos(k\Delta x)}{\Delta x}\right) \tag{3.74}$$

- Second order upwind scheme

$$\left.\frac{\partial F_k}{\partial x}\right|_i = \frac{3F_{k,i} - 4F_{k,i-1} + F_{k,i-2}}{2\Delta x} = \sum_{k=-N/2}^{N/2} \widehat{F_k}\left(\frac{3 - 4e^{-jk\Delta x} + e^{-jk2\Delta x}}{2\Delta x}\right) e^{jkx_i}$$

$$k'(k\Delta x) = \frac{1}{2\Delta x}\left[4\sin(k\Delta x) - \sin(2k\Delta x)\right] - \frac{j}{2\Delta x}\left[3 - 4\cos(k\Delta x) + \cos(2k\Delta x)\right] \tag{3.75}$$

Non-linear MWN analysis

In this study, the non-linear WENO procedure, which will be detailed in the next chapter, is applied to compute reconstructed vectors $\hat{\vec{F}}_{i+1/2}$. Separation of dissipative and dispersive errors of non-linear schemes is not possible analytically. However, the numerical error analysis which will be presented in this section, may be done for any scheme.

In the present case of WENO, at a point $\{x_i = i\Delta x\}$ of a structured cartesian grid, the conservative approximation to the first derivative at fifth-order

$$\left.\frac{\partial \vec{F}}{\partial x}\right|_i = \frac{\hat{\vec{F}}_{i+1/2} - \hat{\vec{F}}_{i-1/2}}{\Delta x} + O(\Delta x^5) \tag{3.76}$$

applies in smooth regions of the flow. The following spectral analysis of the non-linear WENO scheme (4.14) was introduced by N. Lardjane [80] and further developed by S. Pirozzoli [102]. A non-linear scheme will produce a response at other frequencies which may be separated applying the modified wave number (MWN) analysis numerically.

$$\left.\frac{\delta F_k}{\delta x}\right|_i^{NL} = \sum_{n=-N/2}^{N/2} \widehat{\frac{\delta F_k}{\delta x}}(n) e^{jnx_i} \tag{3.77}$$

The MWN k'_k of the non-linear scheme is introduced, such that

$$\left.\frac{\delta F_k}{\delta x}\right|_i^{NL} = jk'_k \widehat{F_k} e^{jkx_i} \tag{3.78}$$

in which one can separate the contribution to mode k from the contribution to other modes

$$jk'_k \widehat{F_k} e^{jkx_i} = \widehat{\frac{\delta F_k}{\delta x}}(k) e^{jkx_i} + \sum_{\substack{n=-N/2 \\ n\neq k}}^{N/2} \widehat{\frac{\delta F_k}{\delta x}}(n) e^{jnx_i} \tag{3.79}$$

By analogy with (3.72), $k'_k = k'_L(k) + k'_{NL}(k)$ is written with

$$k'_L(k) = \frac{-j}{\widehat{F_k}} \widehat{\frac{\delta F_k}{\delta x}}(k) \tag{3.80}$$

and

$$k'_{NL}(k) = -\frac{-j}{\widehat{F_k}} \sum_{\substack{n=-N/2 \\ n \neq k}}^{N/2} \widehat{\frac{\delta F_k}{\delta x}}(n) e^{j(n-k)x_i} \tag{3.81}$$

The linear MWN (3.80) has been computed on a grid of size $N = 1024$, without (smooth function) and with the non-linear WENO weights. In the former case, the WENO scheme simply becomes linear. Figure 3.1 displays the real and imaginary parts of the scaled linear MWN, $\omega'(\omega) = \Delta x k'_L(k\Delta x)$, for each case. The effective spectral properties of the WENO scheme are very different from the theoretical ones, and the peaks intentionally kept on the curves show that the stiffness sensors may be put in default for some specific frequencies on a given grid. An analysis of the non-linear MWN (3.81) can be found in [80].

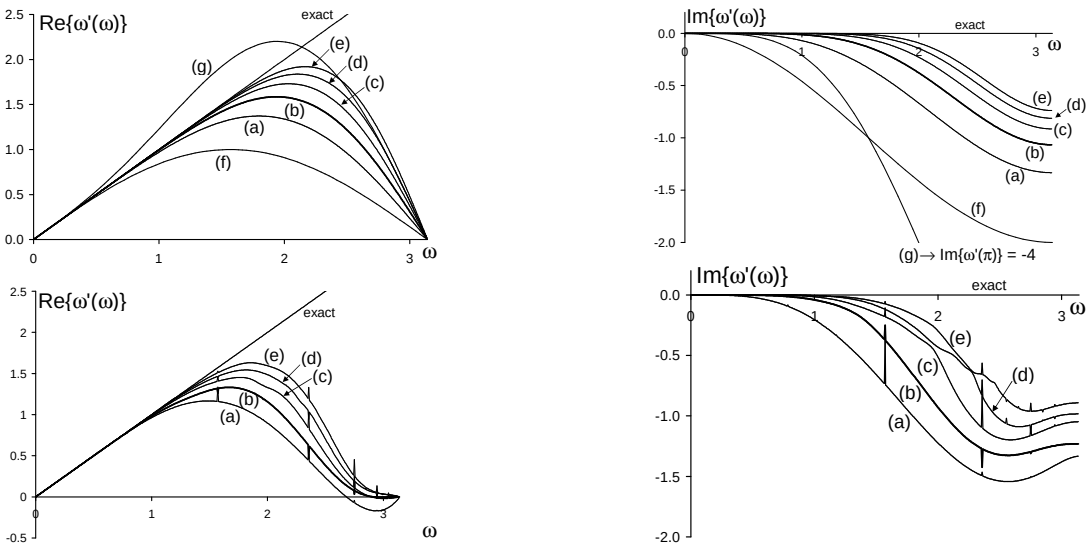

Figure 3.1: Linear Modified Wave Number without (top) and with (bottom) non-linear WENO weight. Left : real part, right : imaginary part. (a) 3^{rd} order WENO, (b) 5^{th} order WENO, (c) 7^{th} order WENO, (d) 9^{th} order WENO, (e) 11^{th} order WENO, (f) 1^{st} order upwind FD, (g) 2^{nd} order upwind FD

3.3.2 THE INTERACTION BETWEEN NUMERICAL ERRORS AND EXPLICIT SUB-GRID MODELING

The following 1D Fourier analysis simply demonstrates the interaction of SGS model with numerical errors. As the MWN analysis, this analysis may be conducted for any numerical scheme. Consider the viscous linear wave equation

$$\frac{\partial u}{\partial t} + c\frac{\partial u}{\partial x} = \nu\frac{\partial^2 u}{\partial x^2} \tag{3.82}$$

whose dispersion relation is $\Omega(k) = kc - j\nu k^2$ for a single Fourier mode $u(x,t) = \hat{u}(k,t)e^{jkx}$. A "physical LES" for equation (3.82) may be considered, in which the advection term is computed with a WENO scheme, and the diffusion term with a central FD scheme for first order derivative, applied twice. Introducing the scaled MWN of both schemes, the numerical LES dispersion relation can be written

$$\Omega_{num}^{LES}(k) = kc\left(\frac{\omega'_L}{\omega}\right) - j\nu_{sgs}^t k^2\left(\frac{\omega'_{FD}}{\omega}\right)^2 \tag{3.83}$$

where $\omega'_{FD}(\omega) = \frac{1}{6}(8\sin(\omega) - \sin(2\omega))$ for the 4th order central FD scheme.

In 1D, the Smagorinsky model reads

$$\nu_{sgs}^{t,\,SM} = \sqrt{2}\,C_S^2\,\Delta^2\left|\frac{\partial u}{\partial x}\right| \approx \sqrt{2}\,C_S^2\,\Delta x\,\omega'_{FD}|\hat{u}| \tag{3.84}$$

The second order structure function in the SSF model is

$$F_2(x,t) = <\|u(x,t) - u(x+r,t)\|^2>_{|r|=\Delta x} \approx \Delta x^2\left.\frac{\partial u}{\partial x}\right|_{FD}^2 \tag{3.85}$$

hence

$$\nu_{sgs}^{t,\,SSF} \approx C_{SF}\,\Delta x\,\omega'_{FD}|\hat{u}| \tag{3.86}$$

Setting $C = C_{SGS}|\hat{u}|/c$ with $C_{SGS} = \sqrt{2}C_S^2$ (SM model) or $C_{SGS} = C_{SF}$ (SSF model) yields

$$\frac{1}{kc}\,\Omega_{num}^{LES}(\omega) = \frac{\omega'_L}{\omega} - j\frac{\omega'^3_{FD}}{\omega}\,C \tag{3.87}$$

to be compared with

$$\frac{1}{kc}\,\Omega_{exact}^{LES}(\omega) = 1 - j\omega^2 C \tag{3.88}$$

for exact derivatives. The departure from 1 (resp. 0) of the real (resp. imaginary) part of the ratio

$$\eta = \Omega_{num}^{LES}/\Omega_{exact}^{LES} \tag{3.89}$$

indicates the frequency range, depending on the value of C, for which numerical errors begin to interact with the sub-grid model. For a given frequency $\omega \neq 0$, when $C = 0$, $\eta = \omega'_L/\omega$, and when $C \to \infty$, $\eta \to \left(\omega'_{FD}/\omega\right)^3$. Figure 3.2 shows the real and imaginary parts of (3.89) for the 5th order WENO scheme, associated with the 4th order central FD scheme. About 20% of the frequencies that the grid can capture are not affected by numerics.

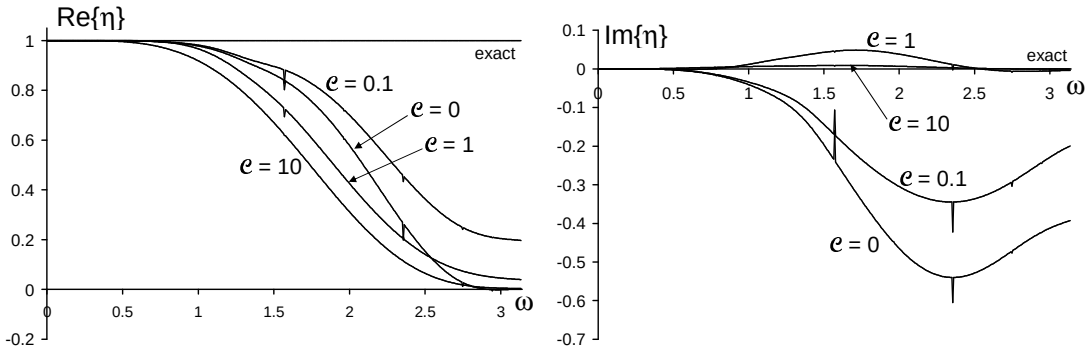

Figure 3.2: Interaction indicator eq. (3.89) for $C = 0$, 0.1, 1 and 10. Left: real part, right: imaginary part.

CHAPTER 4

THE WENO SOLVER

The vector representation of the Navier-Stokes equations for multi-species flows (2.53) is given by

$$\frac{\partial \vec{\tilde{U}}}{\partial t} + \frac{\partial \vec{\tilde{F}}}{\partial x} + \frac{\partial \vec{\tilde{G}}}{\partial y} + \frac{\partial \vec{\tilde{H}}}{\partial z} = \vec{V} + \vec{S} \tag{4.1}$$

In this chapter,˜ indicates the conservative variables, and not Favre variables.

$$\vec{\tilde{U}} = {}^{T}\left[\rho, \rho u, \rho v, \rho w, \rho e_t, \rho Y_1, ..., \rho Y_{N_{sp}-1}\right] \tag{4.2}$$

The Euler equations ($\vec{V} = \vec{0}, \vec{S} = \vec{0}$) are a set of hyperbolic PDEs in each plane (x, t), (y, t) and (z, t)

$$\frac{\partial \vec{\tilde{U}}}{\partial t} + \frac{\partial \vec{\tilde{F}}}{\partial x} + \frac{\partial \vec{\tilde{G}}}{\partial y} + \frac{\partial \vec{\tilde{H}}}{\partial z} = \vec{0} \tag{4.3}$$

In order to illustrate the WENO method, consider a 1D hyperbolic problem

$$\frac{\partial \vec{\tilde{U}}}{\partial t} + \frac{\partial \vec{\tilde{F}}}{\partial x} = \vec{0} \tag{4.4}$$

The finite difference spatial derivative of the conservative flux ($\vec{\tilde{F}}$) is computed to advance the solution in time. Use of the conservative form guarantees discontinuities to move at the correct speed satisfying Rankine-Hugoniot conditions. WENO method with Lax Friedrichs flux splitting is applied for ensuring stability of the scheme. The 1D system (4.4) is diagonalized then flux splitting and WENO reconstruction are applied on characteristic fields. Derivatives at grid points are computed using reconstructed fluxes at cell interfaces for each direction, separately.

In this chapter, firstly transformations between conservative $\vec{\tilde{U}}$, primitive $\vec{U}$ and characteristic $\vec{W}$ variables are explained. Then, the conservative finite difference scheme is defined. In

the third part, the WENO reconstruction with Lax-Friedrischs flux splitting algorithm is explained. The time integration and boundary conditions are presented in sections 4.4 and 4.5. Finally, some specificities of the numerical tool are listed.

4.1 TRANSFORMATION BETWEEN CONSERVATIVE, PRIMITIVE AND CHARACTERISTIC FORMS

The notations for transformations between conservative, primitive and characteristic forms of the EULER system, in x direction is presented in this section. The system in conservative form is written as

$$\frac{\partial \vec{\vec{U}}}{\partial t} + \left[\widetilde{A}\right] \frac{\partial \vec{\vec{U}}}{\partial x} = \vec{0} \quad ; \quad \left[\widetilde{A}\right]_{ij} = \frac{\partial \vec{\vec{F}}_i}{\partial \vec{\vec{U}}_j} \tag{4.5}$$

Conservative variables are transformed into primitive form using matrix $[P] = \partial \vec{\vec{U}} / \partial \vec{U}$

$$\frac{\partial \vec{U}}{\partial t} + [A] \frac{\partial \vec{U}}{\partial x} = \vec{0} \quad \text{where} \quad [A] = [P^{-1}][\widetilde{A}][P] \tag{4.6}$$

The vector of primitive variables is

$$\vec{U} = {}^{T}\left[\rho, u, v, w, T, Y_1, ..., Y_{N_{sp}-1}\right] \tag{4.7}$$

Matrix $[A]$ is diagonalized with left and right eigenmatrices, $[L]$ and $[R]$ respectively.

$$[\Lambda] = [L][A][R] \tag{4.8}$$

Explicitly, the terms of the system with size $(N_{sp} + 4)$ with the eigenvalues ordered $\vec{\lambda} = {}^{T}[u - c, u, u, u, u + c, ..., u]$ are as follows

$$[L] = {}^{T}\left[\vec{l}^{(1)}, \vec{l}^{(2)}, ..., \vec{l}^{(N_{sp}+4)}\right] \tag{4.9}$$

where $\vec{l}^{(i)}$ are the left eigenvectors of primitive jacobian matrix $[A]$ (Figure 4.1) related to the eigenvalue $\lambda^{(i)}$

$$\vec{l}^{(i)}[A] = \lambda^{(i)} \vec{l}^{(i)} \quad \text{for} \quad i = 1, ..., N_{sp} + 4 \tag{4.10}$$

Diagonalization is done on primitive form since it is difficult to obtain $[\widetilde{L}]$ and $[\widetilde{R}]$ which are left and right eigenmatrices of the conservative jacobian matrices $[\widetilde{A}]$.

$$\frac{\partial \vec{W}}{\partial t} + [\Lambda] \frac{\partial \vec{W}}{\partial x} = \vec{0} \quad \text{where} \quad \vec{W} = [L]\vec{U} \tag{4.11}$$

The definitions and notations are summarized in Figure 4.1 The transformation matrices

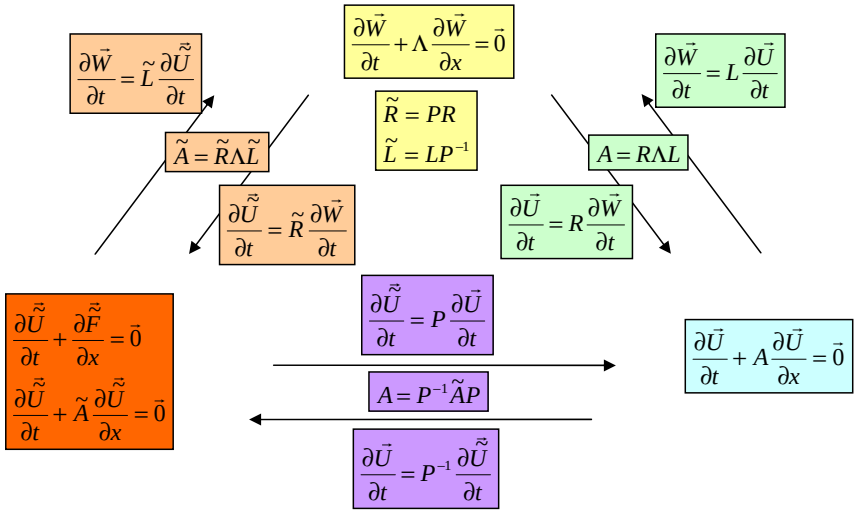

Figure 4.1: Transformations between different forms for the Euler system of equations.

$[\widetilde{R}]$ and $[\widetilde{L}]$ are given in appendix D. Although the derived transformation matrices are of size $N_{sp} + 5$, the mass fraction of the last species $Y_{N_{sp}}$ is computed out of the others. The same derivation for the characteristic boundary conditions is conducted for $N_{sp} + 4$ system of equations, presented in appendix E.

4.2 CONSERVATIVE FORM FOR DIFFERENTIAL OPERATOR

The objective of the finite difference spatial discretization scheme is to compute the spatial derivative of any function. f is the flux function of a non-linear PDE

$$\begin{aligned} \frac{\partial u}{\partial t} + \frac{\partial f}{\partial x} &= 0 \\ u(x,0) &= u_0(x) \end{aligned} \tag{4.12}$$

Then the solution may be advanced in time with an integration scheme like a TVD Runge Kutta method. Consider pointwise function $f \equiv f(x_i)$ defined on a grid $(x_0, ..., x_i, ..., x_N)$. A conservative approximation for equation (4.12) is of the form

$$\left.\frac{df}{dx}\right|_i = \frac{1}{\Delta x}\left(\hat{f}_{i+1/2} - \hat{f}_{i-1/2}\right)$$

where,

$$\hat{f}_{i+1/2} = \hat{f}_{i+1/2}\left(f_{i-r}, ..., f_{i+s}\right) \quad i = 0, ..., N \tag{4.13}$$

r and s are positive integers. Conservative approximation for derivative of flux function yields discontinuities in the solution to move at physically correct speed [126]. However, stability is not ensured by conservative schemes.

4.3 WENO SCHEME

The importance of the numerical solutions to the Navier-Stokes equations increases due to improvements enabling solutions for real problems of concern. One side of this improvement is in computational capacity. The growth in understanding of PDE theory and development of new numerical techniques, is the other side. Godunov's "order barrier theorem" is one of the milestones for numerical solution of flow problems including discontinuities [57], in 1959. After this early work, in the 80's Lax, Van Leer, Harten and many others published on approximate solution methods for the Riemann problem [108, 120]. Harten presented his work on total variation diminishing (TVD) schemes. This work opens the door for higher order "monotonicity preserving" schemes that do not contravene Godunov's theorem [61]. Later, Harten introduced the "essentially non-oscillatory" (ENO) scheme with his colleagues [62]. ENO scheme is based on the choice of the smoothest shifted stencil for flux reconstruction near discontinuities. ENO schemes are successful for shock capturing. Shu and Osher suggested TVD Runge-Kuta time discretization and application of ENO procedure directly on flux values rather than on the variables [113]. These modifications enhance the accuracy of ENO schemes for lower cost. Later, in a second paper they introduced ENO-Roe, ENO-LLF (local Lax-Friedrichs flux splitting) methods for improvement [113]. Weighted essentially non oscillatory scheme (WENO) which is applied in the numerical method of this thesis is developed by Liu, Osher and Chan [88]. Recently, modifications to improve the accuracy of WENO method, in the literature. Mapped WENO schemes achieving $(2r-1)^{\text{th}}$ order accuracy near discontinuities [64], more accurate band-width optimized WENO scheme [93, 118] and low cost WENO-Z schemes [10] are some examples. These improvements are not considered, since the scope is not related to achieve higher accuracy.

The key idea in WENO is constructing flux values using the weighted average of approximate flux values at cell interfaces. Normalized weights are determined depending on the smoothness of the ENO approximations at shifted sub-stencils shown in Figure 4.2.

In the WENO procedure, $\hat{f}_{i+1/2}$ in equation (4.13) is reconstructed using ENO approximations

on different sub-stencils ($S_i^{(r)}$in Figure 4.2) including $x_{i+1/2}$. The overall stencil (S_i) size for k^{th} order reconstruction of $\hat{f}_{i+1/2}$ by WENO scheme is $2k-1$. Weighted average of k number of approximations $\hat{f}_{i+1/2}^{(r)}$ for $r = 0, ..., k-1$ gives reconstructed flux

$$\hat{f}_{i+1/2} = \sum_{r=0}^{k-1} w_r \hat{f}_{i+1/2}^{(r)} \tag{4.14}$$

As an example for the fifth order WENO reconstruction Figure 4.2 the approximations $\hat{f}_{i+1/2}^{(0-2)}$ are computed on sub-stencils $S^{(0-2)}$ of size k (Figure 4.2).

$$\hat{f}_{i+1/2} = \hat{f}_{i+1/2}^{(0)} w_0 + \hat{f}_{i+1/2}^{(1)} w_1 + \hat{f}_{i+1/2}^{(2)} w_2 \tag{4.15}$$

and $\hat{f}_{i+1/2}^{(r)}$ is obtained from k^{th} order ENO approximation.

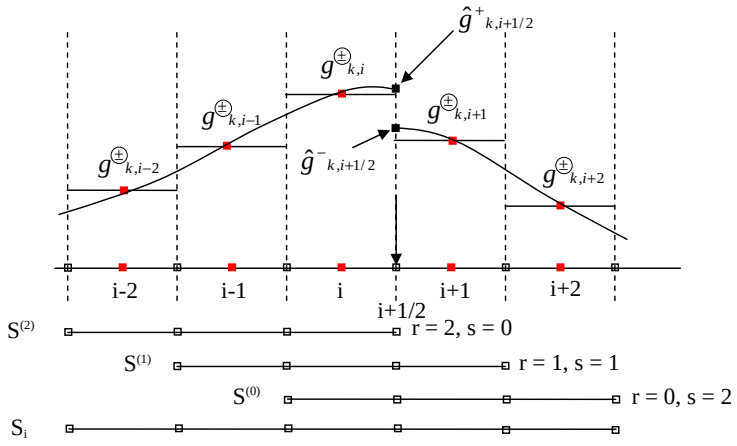

Figure 4.2: 5^{th} order WENO stencil demonstration.

4.3.1 ENO APPROXIMATION

$\hat{f}_{i+1/2}^{(r)}$ are values of the interpolating polynomials, the coefficients of which are derived on following grid, cells and grid points

$$a = x_{1/2} < x_{3/2} < .... < x_{N-1/2} < x_{N+1/2} = b \tag{4.16}$$

$$I_i = [x_{i-1/2}, x_{i+1/2}]; \quad x_i = \frac{1}{2}(x_{i-1/2} + x_{i+1/2})$$

At the cell I_i, $\hat{f}_{i+1/2}^{(r)}$ which is k^{th} order accurate approximation is based on stencil $S_i^{(r)}$ of length k cells, r cells to the right, and s cells to the left, with $r + s + 1 = k$

$$S_i^{(r)} \equiv \{I_{i-r}, ..., I_{i+s}\} \tag{4.17}$$

The approximations are constrained by the integral equality for conservative schemes

$$\overline{f_j} \equiv \frac{1}{\Delta x_j}\int_{x_{j-1/2}}^{x_{j+1/2}} f(\xi)d\xi \equiv \frac{1}{\Delta x_j}\int_{x_{j-1/2}}^{x_{j+1/2}} \hat{f}^{(r)}(\xi)d\xi \quad j = i-r,...,i+s \tag{4.18}$$

There exists a unique polynomial approximation of degree $k-1$, on nodes of stencil $S_i^{(r)}$ matching f_j values in the sub-stencil. So, there exists linear set of coefficients c_{rj} depending on left shift for $\hat{f}_{i+1/2}^{(r)}$.

$$\hat{f}_{i+1/2}^{(r)} = \sum_{j=0}^{k-1} c_{rj} f_{i-r+j} \tag{4.19}$$

The linear coefficients which are derived starting from the Lagrange form of approximate polynomials by Shu are

$$c_{rj} = \left(\sum_{m=j+1}^{k} \frac{\sum_{l=0_{l\neq m}}^{k} \prod_{q=0_{q\neq m,l}}^{k} (x_{i+\frac{1}{2}} - x_{i-r+q-\frac{1}{2}})}{\prod_{l=0_{l\neq m}}^{k} (x_{i-r+m-\frac{1}{2}} - x_{i-r+l-\frac{1}{2}})} \right) \Delta x_{i-r+j} \tag{4.20}$$

If the grid is uniform, the coefficients do not depend on i ($\Delta x_i = \Delta x$)

$$c_{rj} = \sum_{m=j+1}^{k} \frac{\sum_{l=0_{l\neq m}}^{k} \prod_{q=0_{q\neq m,l}}^{k} (r-q+1)}{\prod_{l=0_{l\neq m}}^{k} (m-l)} \tag{4.21}$$

The constants c_{rj} are listed in Table at appendix G for k = 1,...,6.

4.3.2 1D WENO RECONSTRUCTION PROCEDURE

The reconstruction procedure to compute $\hat{f}_{i+1/2}$ using f_i is as follows.

- At $x_{i+1/2}$, k approximate values $\hat{f}_{i+1/2}^{(r)}$ of k^{th} order accuracy are computed over sub-stencil $S_i^{(r)}$.

$$\hat{f}_{i+1/2}^{(r)} = \sum_{j=0}^{k-1} c_{rj} f_{i-r+j} \quad ; \quad S_i^{(r)} = \{x_{i-r}, .., x_{i-r+k-1}\} \tag{4.22}$$

- The reconstruction is done by weighted averaging of $\hat{f}_{i+1/2}^{(r)}$ as seen in equation (4.14).

- The normalized weights w_r are related to smoothness. w_r are used to increase the contribution of the approximation at the sub-stencil $S_i^{(r)}$ where interpolated polynomial is smoother.

$$w_r = \frac{\alpha_r}{\sum_{s=0}^{k-1} \alpha_s} \quad r = 0,..,k-1 \quad \alpha_r = \frac{d_r}{(\epsilon + \beta_r)^2} \tag{4.23}$$

β_r is called the smoothness indicator which is a measure of discontinuity (stiffness) of the solution. ϵ is a positive small coefficient to avoid division by zero. The ideal weights d_r which generate $(2k-1)^{th}$ order upwind scheme are tabulated in appendix G for $k = 1, ..., 6$. If the function is smooth in the stencil $S_i^{(r)}$ the value of the smoothness indicator $\beta_r = O(\Delta x^2)$ so that $w_r = O(1)$. When there exists a discontinuity in the stencil $\beta_r = O(1)$ so that $w_r = O(\Delta x^4)$. The numerical formulation suggested by Shu is presented in appendix G for $k = 1, ..., 6$.

4.3.3 FLUX SPLITTING

Application of Lax-Friedrichs flux splitting is suggested by Shu to enhance the stability characteristics of ENO [114]. The same enhancement is extended to WENO schemes. In ICASE report, Shu states that the flux splitting algorithm is cost effective and improves stability characteristics [112]

$$f(u) = f^+(u) + f^-(u) \tag{4.24}$$

where for Lax-Friedrichs flux splitting,

$$f^{\pm}(u) = \frac{1}{2}(f(u) \pm \alpha u) \quad \alpha = max_u \left| f'(u) \right| \tag{4.25}$$

The range of relevant u for taking maximum may be chosen at the overall domain or locally as the stencil S_i. Depending on the choice, the method is named “local LF” or “global LF”. In application, WENO procedure is applied on split fluxes $f^+_{i+1/2}$ and $f^-_{i+1/2}$. Note that, in the c_{rj} Table which is presented in appendix G, r takes the value -1. The transformation of coefficients $\tilde{c}_{rj} = c_{r-1,j}$ is for $\hat{f}^+_{i-1/2}$ as, c_{rj} is for $\hat{f}^-_{i+1/2}$. After WENO procedure, fluxes are reconstructed

$$\hat{f}_{i+1/2} = \hat{f}^+_{i+1/2} + \hat{f}^-_{i+1/2} \tag{4.26}$$

Lax-Friedrichs flux splitting is the less expensive but one of the most dissipative flux splitting algorithms. However, as the order of the scheme increases, this dissipation effect decreases [2].

4.3.4 SOLUTION FOR SYSTEM OF EQUATIONS

It is explained in the introduction of this chapter, that the 1D flux derivative is computed in x direction and this formulation is used for y and z directions. Application of WENO scheme directly to the coupled system of equations is possible. However, this is reported to cause spurious oscillations for higher order approximations [112]. 1D characteristic system of variable is

$$\frac{\partial \vec{W}}{\partial t} + \left[\widetilde{L}\right] \frac{\partial \vec{\vec{F}}}{\partial x} = \vec{0} \quad ; \quad \left[\widetilde{L}\right] \frac{\partial \vec{\vec{F}}}{\partial x} = \frac{\partial \vec{g}}{\partial x} \tag{4.27}$$

which may be written in component form as

$$\frac{\partial W_k}{\partial t} + \frac{\partial g_k}{\partial x} = 0 \quad ; \quad k = 1, ..., N_{sp} + 5 \tag{4.28}$$

where $\vec{g}$ is the flux for the characteristic system. The overall procedure of WENO scheme for flux derivative computation having the conservative variables $\vec{\vec{U}}_i$ and the flux values $\vec{\vec{F}}_i$ at grid points, is as follows.

- Transformation matrices from conservative to characteristic variables $[\widetilde{R}]$, $[\widetilde{L}]$ and $[\Lambda]$, are constructed at $x_{i+1/2}$. Matrices are given analytically in appendix D.

$$[\widetilde{R}] = [\widetilde{R}]\left(\vec{U}_{i+1/2}\right) \quad [\widetilde{L}] = [\widetilde{L}]\left(\vec{U}_{i+1/2}\right) \quad [\Lambda] = [\Lambda]\left(\vec{U}_{i+1/2}\right) \tag{4.29}$$

- These matrices are assumed to be constant in the stencil of concern S_i. The cell interface values of the primitive variables $\vec{U}_{i+1/2}$ in equations (4.29) are deduced from conservative variables $\vec{\vec{U}}_{i+1/2}$ which are computed by simple averaging.

$$\vec{\vec{U}}_{i+1/2} = \frac{1}{2}\left(\vec{\vec{U}}_i + \vec{\vec{U}}_{i+1}\right) \tag{4.30}$$

- Having obtained the left eigenvectors $\vec{\vec{l}}$ (lines of left eigenmatrice $[\widetilde{L}]$) the characteristic system flux values are computed.

$$g_k = \sum_{p=1}^{5+N_{sp}} \widetilde{l}_p^{(k)} \widetilde{F}_p = \lambda^{(k)} W_k$$

$$k = 1, ..., N_{sp} + 5 \tag{4.31}$$

- Lax-Friedrichs flux splitting is applied on g_k as

$$g_k = g_k^+ + g_k^- \tag{4.32}$$

$$g_k^{\pm} = \frac{1}{2}\left[g_k(\vec{W}) \pm \alpha_k W_k\right]$$
$$\alpha_k = \max\left|\frac{\partial g_k}{\partial W_k}\right| = \max\left|\lambda^{(k)}\right| \tag{4.33}$$

- WENO procedure is applied to obtain reconstructed fluxes at cell interfaces $\hat{g}^{\pm}_{k,i+1/2}$

$$\hat{g}^{\pm(r)}_{k,i+1/2} = \sum_{j=0}^{k-1} c_{rj} g^{\pm}_{k,i-r+j}$$
$$\hat{g}^{\pm}_{k,i+1/2} = \sum_{r=0}^{k-1} \omega_r \hat{g}^{\pm(r)}_{k,i+1/2} \tag{4.34}$$

- Back transformation is applied from characteristic to conservative flux.

$$\hat{\vec{\tilde{F}}}^{\pm}_{i+1/2} = \left[\widetilde{R}\right]_{i+1/2} \vec{\hat{g}}^{\pm}_{i+1/2} \tag{4.35}$$

- Finally, the overall reconstructed numerical fluxes are evaluated as

$$\vec{\tilde{F}}_{i+1/2} = \vec{\tilde{F}}^{+}_{i+1/2} + \vec{\tilde{F}}^{-}_{i+1/2} \tag{4.36}$$

4.4 TIME DISCRETIZATION

Having computed the flux derivative in space, the solution is advanced using explicit Runge-Kutta time discretization.

4.4.1 RK$_P$ TVD TIME STEPPING

General form of Runge-Kutta methods to solve initial value problem of ODE: $u_t = L(u)$, which is obtained from spatial discretization of PDE: $u_t = f(u)_x$, is

$$\begin{aligned} u^{(p)} &= \sum_{k=0}^{p-1}(\alpha_{pk} u^{(k)} + \Delta t \beta_{pk} L(u^{(k)})), \quad p = 1, ..., m \\ u^{(0)} &= u^n, \quad u^{(m)} = u^{n+1} \end{aligned} \tag{4.37}$$

Considering an ODE (in time), the total variation $TV(u) = \sum_j |u_{j+1} - u_j|$ for first order in time Euler forward stepping, does not increase under the restriction

$$\Delta t \leq \Delta t_{FE} \tag{4.38}$$

Time integration is stable provided that $\Delta t \leq c\ \Delta t_{FE}$ where c is the CFL coefficient. It is proved, higher order explicit Runge-Kutta time discretization (eq. 4.37) is TVD under the CFL-like condition [113]

$$c = \min_{i,k} \frac{\alpha_{ik}}{\beta_{ik}} \quad \alpha_{ik} > 0, \beta_{ik} > 0 \tag{4.39}$$

The third order TVD Runge Kutta method with c= 1 is

$$\begin{aligned} u^{(1)} &= u^n + \Delta t L(u^n) \\ u^{(2)} &= \frac{3}{4}u^n + \frac{1}{4}u^{(1)} + \frac{1}{4}\Delta t L(u^{(1)}) \\ u^{n+1} &= \frac{1}{3}u^n + \frac{2}{3}u^{(2)} + \frac{2}{3}\Delta t L(u^{(2)}) \end{aligned} \tag{4.40}$$

4.4.2 CALCULATING THE TIME STEP

A non dimensional CFL condition is used to calculate the time step for time integration. CFL value less than unity guaranties the stability of the time integration.

$$\Delta t_{max} = \frac{C\ \Delta x_{min}}{|\lambda_x|_{max}} \tag{4.41}$$

where λ_x is the set of eigenvalues of the system ($\lambda_x = \{u + c, u, u - c\}$) that correspond to the wave speed. In application, three time steps considering stability of hydrodynamics, viscous terms and chemical reaction mechanism are determined. The minimum time step for stability of time integration is chosen.

$$\Delta t = \min\left(\Delta t_{hydro}, \Delta t_{visc}, \Delta t_{chem}\right) \tag{4.42}$$

The hydrodynamic time step is computed applying CFL condition [70] as

$$\Delta t_{hydro} = \frac{C}{\left|\frac{\lambda_x}{\Delta_x}\right|_{\max} + \left|\frac{\lambda_y}{\Delta_y}\right|_{\max} + \left|\frac{\lambda_z}{\Delta_z}\right|_{\max}} \tag{4.43}$$

The CFL number is chosen to be 0.7 for the computations. The time step determined for viscous stability criteria is computed (for Navier-Stokes solutions) as

$$\Delta t_{visc} = \frac{1}{2\mu\left(\frac{1}{\Delta_x^2} + \frac{1}{\Delta_y^2} + \frac{1}{\Delta_z^2}\right)} \tag{4.44}$$

Δ_x, Δ_y and Δ_z are the grid spacing in directions x, y and z.

The chemical source terms are highly non-linear. Maximum time step for the reacting cases (Δt_{chem}) to prevent instability due to mechanism is determined conducting 0D, constant volume H_2/air mixture ignition tests. These tests are presented with the results since they are specific to the reaction mechanism and the conditions.

4.5 BOUNDARY CONDITIONS

Boundary conditions (BC) are of critical importance in numerical simulations. Indeed they are necessary to implement the physical requirements of the problem and to prevent unphysical wave reflections at the boundaries of the domain. BCs must assure the system to be "well-posed". The system constrained by the BCs must reveal a unique outcome. The first way of constraining boundaries is direct implementation of physical values at the boundaries of the domain. This forcing is applied repeatedly at every time step. Secondly, "ghost cells" which are virtual cells prolongated outside at the domain boundaries may be utilized like boundary nodes. The presence of ghost cells is unavoidable for the spatial discretization stencils of nodes at the boundaries. However, forcing all conditions will generate unphysical waves to reflect at the boundaries. As a result, a method based on 1D characteristic analysis along the direction perpendicular to the boundary is applied. The first systematic work on non-reflecting inlet, outlet, slip and no-slip wall boundary conditions implemented on subsonic and supersonic inviscid flow problems is published by Kevin Thompson [79], to the author's knowledge. The system for derivation of BC's is called "local one-dimensional inviscid" (LODI) system of equations. Thompson refers to Heldstrom, who developed characteristic boundary conditions for one-dimensional, nonlinear and hyperbolic PDE solutions, on rectangular domain [63]. Thompson states his work is application of Hedstrom's method on multidimensional Euler equations on non-rectangular domains with transformed coordinates. Later, Poinsot and Lele presented LODI system BC's modified for Navier-Stokes equations [105]. Baum, Poinsot and Thévenin expanded the BC's to multispecies reacting cases for gases with realistic thermodynamic properties [5]. Explanation of applied BCs and details of application are expressed in two classifications. The physical BCs are the ones implementing known physical properties at the boundaries. When the physically definite conditions are not enough to constrain the equations at the boundaries, numerical BCs are applied. The LODI system for application of BCs on characteristic basis is as follows.

4.5.1 LODI SYSTEM

When the number of definite physical BCs are not enough for well posedness of the solution, BCs may be applied on wave amplitude variations $\vec{\mathcal{L}}$ in characteristic form. *The idea is based on the fact the solution is not only governed by the state of the problem but the waves entering*

to the domain also [79].

One-dimensional (normal direction to the boundary), inviscid, characteristic form is used for $\vec{\mathcal{L}}$ formulation. The effect of waves in tangential directions and viscous terms on the boundaries are neglected for the test cases studied. This type of BCs are called Euler Characteristic Boundary Conditions (ECBC).

$$\frac{\partial \vec{W}}{\partial t} + \vec{\mathcal{L}} = \vec{0} \quad ; \quad \vec{\mathcal{L}} = [\Lambda]\frac{\partial \vec{W}}{\partial x} = [\Lambda][L]\frac{\partial \vec{U}}{\partial x} \tag{4.45}$$

$\vec{\mathcal{L}}$ vector is written explicitly as

$$\begin{aligned} \mathcal{L}_i &= \lambda^{(i)} \sum_{j=1}^{N_{sp}+4} l_j^{(i)} \frac{\partial U_j}{\partial x} \\ i &= 1, ..., N_{sp}+4 \end{aligned} \tag{4.46}$$

The components of $\mathcal{L}$ in x, y and z are presented in appendix F. Once all components of wave amplitude variations are computed, time derivatives of conservative variables to advance in time, may be obtained applying transformation. Firstly, it is necessary to determine the direction of the waves related to $\mathcal{L}_i$'s, as explained in Figure 4.5 depending on

- nature of the flow, supersonic or subsonic
- direction of the flow, $u < 0$ or $u > 0$

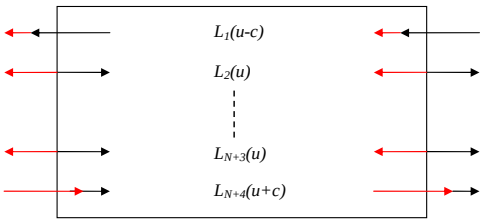

Figure 4.3: ECBC subsonic flux directions

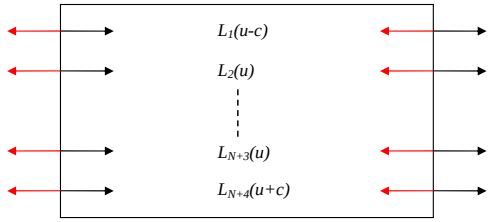

Figure 4.4: ECBC supersonic flux directions

Figure 4.5: Direction of the waves for subsonic and supersonic conditions for both $u > 0$ (black arrows) and $u < 0$ (red arrows) cases.

Amplitude variations $\mathcal{L}_i$ of the waves which leave the domain are computed applying equation (4.46), using one-sided derivatives based on interior data. $\mathcal{L}_i$'s of waves which enter the

domain can not be computed this way. Depending of the type of boundary, these amplitude variations are

- either set to *zero* : numerical BC.
- or related to outgoing waves by physical restrictions applied on time derivatives of primitive variables : physical BC.

$$\begin{aligned} [R]\frac{\partial \vec{W}}{\partial t} + [R]\vec{\mathcal{L}} &= \vec{0} \\ \frac{\partial \vec{U}}{\partial t} + \vec{d} &= \vec{0} \quad ; \quad \vec{d} = [R]\vec{\mathcal{L}} \end{aligned} \tag{4.47}$$

This system which relates wave amplitude variations to time derivatives of primitive variables is called local one-dimensional inviscid (LODI) system. Detailed formulations of $\vec{\mathcal{L}}$ and $\vec{d}$ for each direction x, y and z are presented in appendix F. Having explained the basis and definitions for ECBC, specific implementations depending on the type of BC will be presented.

4.5.2 FREE NON-REFLECTING BCS

At free boundaries none of the primitive variables may be implemented explicitly. $\mathcal{L}_i$'s for incoming waves are equated to *zero*.

4.5.3 PHYSICAL NON-REFLECTING INLET BOUNDARY CONDITIONS

Physical non-reflecting boundary conditions are applied at $x = 0$ inlet only. The incoming wave amplitude variations for subsonic and supersonic case are computed as follows.

4.5.3.1 SUBSONIC FORCED NON-REFLECTING INLET

All characteristic waves, except $\mathcal{L}_1$ related to eigenvalue $(u - c)$, enter the domain. $\mathcal{L}_1$ is computed from interior points. Other wave amplitude variations are expressed in terms of $\mathcal{L}_1$ solving the LODI system (4.47). The physical BC for a subsonic inlet at $x = 0$ are constant velocity components $(u = u_{inlet}, v = 0, w = 0)$, temperature $(T = T_{inlet})$ and mass fractions

($\left\{Y_1, Y_2, ..., Y_{N_{sp}}\right\}$ = Const). The wave amplitude variations $\mathcal{L}_i$ are deduced equating time derivatives of these primitive variables which are presented in appendix F.2 to *zero*.

$$\begin{aligned}
\mathcal{L}_2 &= 0 \\
\mathcal{L}_3 &= 0 \\
\mathcal{L}_4 &= -2\mathcal{L}_1 \\
\mathcal{L}_{\alpha+3} &= 0 \quad \alpha = (2, ..., N_{sp} - 1) \\
\mathcal{L}_{N_{sp}+3} &= -\frac{\rho}{T}\mathcal{L}_4 \\
\mathcal{L}_{N_{sp}+4} &= \mathcal{L}_1
\end{aligned} \tag{4.48}$$

4.5.3.2 SUPERSONIC FORCED NON-REFLECTING INLET

In supersonic flow case, all the waves enter into the domain. All time derivatives of primitive variables are equated to *zero*.

4.6 SOME SPECIFICITIES

4.6.1 THE LARROUTUROU METHOD

As mentioned early in section 2.1, numerical simulation of multi-species flows with the conservative form of equations poses difficulty to keep species mass fractions positive. This problem is especially encountered for reacting flows involving large numbers of species. The positivity problem which has been the subject of many works [4, 82] are related to the resolution of Navier-Stokes equations in conservation form. Larrouturou method is applied for preserving positivity of the species mass fractions

4.6.1.1 IDEA OF LARROUTUROU

The mass fraction of species α is computed as the ratio of two conservative variables

$$Y_{\alpha,i} = \frac{(\rho Y_\alpha)_i}{\rho_i} \quad \alpha = 1, ..., N_{sp} - 1 \tag{4.49}$$

Due to the numerical scheme employed, the mass fractions obtained do not respect the discrete maximum principle ($0 \leq Y_\alpha \leq 1$). Larrouturou proposed to use the same discrete mass flux

for continuity ($f^{\rho}_{i+1/2}$) and species mass fraction ($f^{\alpha}_{i+1/2}$) fluxes

$$f^{\alpha}_{i+1/2} = f^{\rho}_{i+1/2} \begin{cases} Y_{\alpha,i} & \text{if} \quad u_{i+1/2} > 0 \\ Y_{\alpha,i+1} & \text{if} \quad u_{i+1/2} < 0 \end{cases} \tag{4.50}$$

This modification guaranties maximum principle with suitable CFL condition [82].

4.6.1.2 APPLICATION TO WENO SOLVER

Larrouturou suggests to advance the numerical solution for whole system as coupled flow and species equations, then apply the method for species mass fluxes $\hat{f}^{\alpha^{\pm}}_{i+1/2}$. It is intended to keep the accuracy of approximation at the same order for both flow and species variables. The method is applied as follows

$$\hat{f}^{\alpha}_{i+1/2} = \hat{f}^{\rho}_{i+1/2} \begin{cases} \widehat{Y}^{-}_{\alpha,i+1/2} & \text{if} \quad \hat{f}^{\rho}_{i+1/2} > 0 \\ \widehat{Y}^{+}_{\alpha,i+1/2} & \text{if} \quad \hat{f}^{\rho}_{i+1/2} < 0 \end{cases} \tag{4.51}$$

The conservation of mass as sum of species mass fractions ($\sum_{\alpha=1}^{N_{sp}} \hat{Y}_{\alpha,i+1/2} = 1$) is satisfied applying the same weights for all species. It corresponds to the maximum of all the weights of WENO reconstruction for the species.

4.6.2 STRUCTURE OF THE CODE

The structure for single processor case is presented in Figure (4.6). In parallel case each processor follows this task and communicates at each time step for ghost cells on interior faces.

4.6.3 THE QUESTION OF $\mathbf{D}_{H0}$

The energy is expressed in terms of the total energy which is computed with a reference to temperature T_0 that is chosen as $T_0 = 298.15K$. This the energy variable which is zero at this reference temperature $T = T_0$, is called sensible energy. The conservative variable for energy equation is given in (2.48)

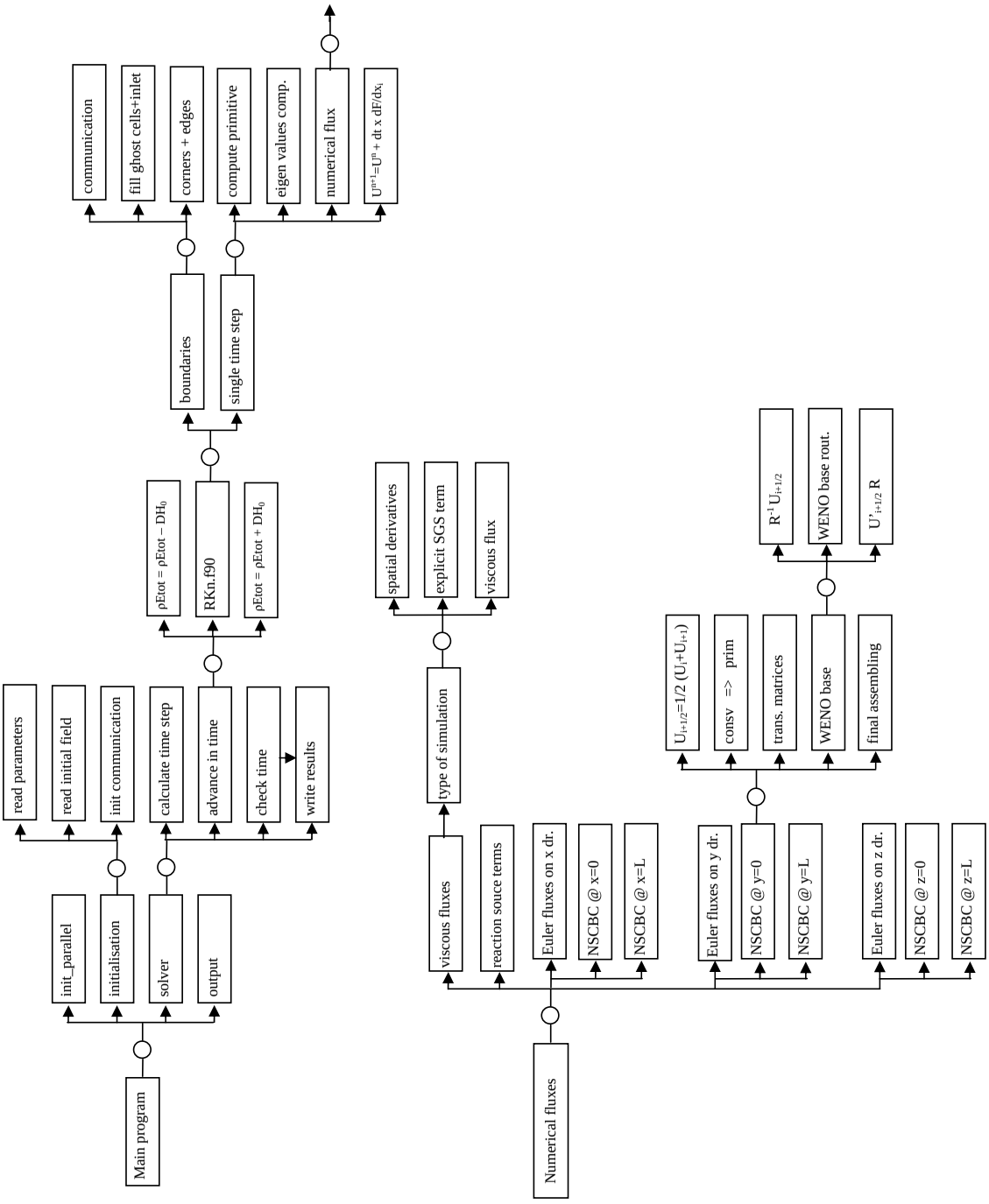

Figure 4.6: Schematic diagram of structure of the code.

$$\rho e_t = \rho \sum_{\alpha=1}^{N_{sp}} \left(\int_0^T C p_\alpha(\theta) d\theta \right) Y_\alpha - p + \frac{1}{2} \rho u_i u_i + \rho D_{H0} \tag{4.52}$$

with

$$\rho D_{H0} = \rho \sum_{\alpha=1}^{N_{sp}} \left(\Delta h_{f,\alpha}^0 - \int_0^{T_0} C p_\alpha(\theta) d\theta \right) Y_\alpha$$

Since solution is concerned with variation in total energy, it is suitable to carry on calculations for sensible energy, adding and subtracting ρD_{H_0} to ρe_t every time step.

4.6.4 THE METRICS

At some regions of the domain where the flow is turbulent and mixing and reactions take place, high resolution is necessary. However there are regions where the solution is smooth, so there is no need for high resolution. The grid is clustered introducing geometric transformation in each direction in order to reduce the computational cost

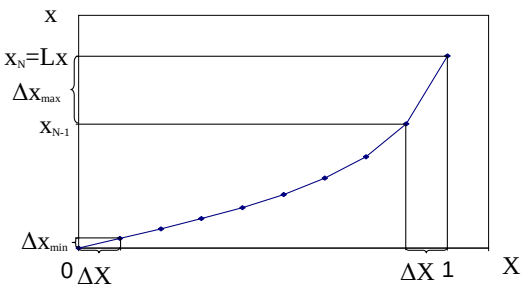

Figure 4.7: Coordinate transformation for clustering the grid

$$x = L \frac{X}{\sqrt{1 - X^2}}, \quad \frac{dX}{dx} = \frac{L^2}{(X^2 + L^2)^{3/2}} \tag{4.53}$$

The capital X stands for numerical coordinates, x is for physical coordinates and L is a constant for the ratio of minimum physical to numerical grid spacing. Spatial derivatives are transformed by chain rule.

$$\frac{\partial}{\partial x} = \frac{\partial}{\partial X} \frac{dX}{dx} \tag{4.54}$$

The filtering operation explained in chapter 3 does not commute with differential operator. It is shown that the commutation error is significant when the truncation error is higher than second order [53]. In this work the commutation errors are assumed to be negligible, since

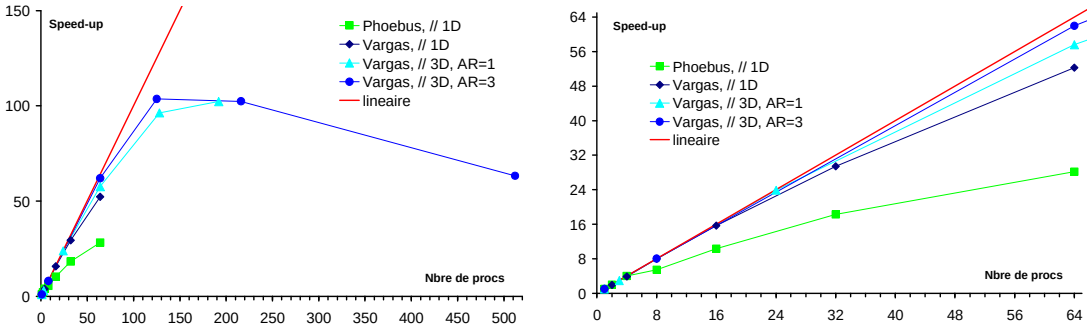

Figure 4.8: A. Speedup curves for WENO code on clusters VARGAS and Phoebus, B. 2D MPI cartesian topology.

the clustering is mostly effective at the region of smooth solution [92]. It is also applied by Lardjane [80] and Gougeon [59].

4.6.5 PARALLEL IMPLEMENTATION

Parallelization of the code is achieved by domain decomposition in all directions. Standard MPI routines for cartesian topology are used for parallelization.

The parallel efficiency may be represented in terms of scalability curves in Figure 4.8.A. Speed-up is calculated dividing wall time for a task for sequential processing by wall time for the same task processed with N processors.

$$S_N = \frac{T_{\text{1 proc}}}{T_{\text{N procs}}} \tag{4.55}$$

The speed-up curves presented are for clusters VARGAS/IDRIS and Phoebus/CCRC (Centre de Calcul en région Centre).

- Phoebus : 42 nodes of 4 Intel XEON E5450 3.00 Ghz cores with 25Gb for each node.
- Vargas :
  - 112 nodes of 32 core Power 6 4.7 Ghz core with 128 Gb memory
  - 84 nodes and 256 Gb memory 28 nodes.

AR: the ratio of long edge to short edge for the square prism sub-domain blocks. AR is an indicator of ratio of communication (at surfaces) to computation (within volume) of each node.

4.6.6 LES STRATEGIES

The set of governing LES equations (3.8)(3.27)(3.32)(3.14) can be written in the following form, including the contribution of the sub-grid scales

$$\frac{\partial \vec{\vec{U}}}{\partial t} + \frac{\partial \vec{\vec{F}}}{\partial x} + \frac{\partial \vec{\vec{G}}}{\partial y} + \frac{\partial \vec{\vec{H}}}{\partial z} = \vec{V} + \vec{\tau} + \vec{S} \tag{4.56}$$

where $\vec{\vec{F}}$, $\vec{\vec{G}}$ and $\vec{\vec{H}}$ are the inviscid fluxes in the x, y and z direction, respectively, $\vec{V}$ is the vector of viscous fluxes, $\vec{S}$ is the vector of chemical source terms, and $\vec{\tau}$ represents the vector of explicit sub-grid terms. The different approaches are characterized by:

$$\begin{aligned}
\text{LES_SM} &: \vec{V} \neq \vec{0} \;\; ; \;\; \vec{\tau} : \text{SM model} \\
\text{LES_SSF} &: \vec{V} \neq \vec{0} \;\; ; \;\; \vec{\tau} : \text{SSF model} \\
\text{MILES_NS} &: \vec{V} \neq \vec{0} \;\; ; \;\; \vec{\tau} = \vec{0} \\
\text{MILES_EULER} &: \vec{V} = \vec{0} \;\; ; \;\; \vec{\tau} = \vec{0}
\end{aligned}$$

In the non-reacting cases, $\vec{S} \neq \vec{0}$, and in the reacting ones,

$$\vec{S} = {}^{T}\{0, 0, 0, 0, 0, \; \hat{\omega}_\alpha \; ; \; \alpha = 1, \ldots, N_{sp}\}$$

CHAPTER 5

NUMERICAL EXPERIMENTS

In this thesis, experiments are presented focused on the following questions by S.B. Pope [107]; –*"Is LES a physical model, a numerical procedure or a combination of both?"* and –*"How are different LES models to be appraised?"*. Different LES strategies are evaluated and compared for the numerical simulation of high-speed non-reacting and reacting air/H_2 jets. Widely studied simple turbulent jet case is chosen as the flow prototype. The complexities like multi-injection or chamber geometry are excluded. The focus is shifted to the behavior of the numerical approaches on the main problems of mixing, transition and interaction of turbulence with chemistry [28].

The simple turbulent jet is a good flow prototype for the evaluation of MILES and LES, indeed;

- High-speed compressible flows do usually involve shocks. Consequently, it is mandatory to apply dissipative numerical methods for the simulation of these flows.
- The time scales are at the order less than one millisecond. Considering that the turbulent mixing and chemical reaction are included in the problem, the parameters questioned in the simulation (potential core length, ignition length ...) are sensitive to the molecular transport.

The conditions for the test cases are based on the experimental data published in the literature. The non-reacting case is taken from the experiments of J.M. Eggers [32], and the reacting one is from the experiments conducted at LAERTE supersonic combustion chamber of ONERA [19, 90]. These free shear flows are selected at first because Kelvin-Helmholtz instabilities, primarily responsible for large scale turbulent mixing, are not much influenced by diffusion,

and because large scale turbulent mixing is determinant for non-premixed combustion which occurs at the molecular level due to micro-mixing or diffusion of reactants. The non-reacting test case isolates the first aspect and the reacting one includes both aspects.

In both cases, complete inlet profiles, necessary for constructing a simulation, are not available. Also, in the available data significant inconsistencies are reported. Therefore, approximate profiles that include assumptions are applied for the inlet conditions. It is pragmatically assumed that LES method (of dissipative schemes) is not sensitive to the accuracy of the inlet conditions as much as RANS approach does [22].

Numerical simulations are performed using a 5^{th} order WENO scheme[1], with resolutions ranging from $32 \times 32 \times 128$ to $256 \times 256 \times 1024$, with (LES) and without (MILES) explicit sub-grid model. MILES simulations are carried out for the Navier-Stokes equations and for the Euler equations, i.e. without any molecular transport terms. LES simulations include molecular transport terms.

The sensitivities of different numerical approaches to initial and boundary conditions are also assessed. It is intended to obtain experience in solving high speed reacting flows like those existing in scramjet engines, beyond the purpose of qualitative comparison.

In this chapter, LES solutions of non-reacting and reacting compressible H_2/air jets for different approaches are presented. In each case, first the flow problem is explained in detail including available experimental data and parameters for numerical simulations. Later, results showing interpretation of flow structure for straightforward visualization and statistical results for more thorough analysis are presented. The simulation results are also compared with the published experimental data.

5.1 NON-REACTING CASE

5.1.1 TEST CASE DESCRIPTION

The first simulated test case is a non-reacting transonic round H_2 jet which is in a co-flowing supersonic round air jet. This coaxial mixing experiment was conducted in 1971 by Eggers [32]. The simple schematic diagram of the experiment is shown in Figure 5.1. The internal

[1] Although WENO schemes are not monotone, MILES will be used to designate numerical LES in this thesis.

and external diameters of hydrogen injector are 11.6 mm and 12.7 mm, respectively. The diameter of the co-flowing air nozzle is 152 mm. Mixing occurs in unconfined region, so the flow static pressure is close to atmospheric pressure. The dimensions of the flow domain to be simulated are $Ly \times Lz \times Lx = 70 \times 70 \times 700$ mm^3, x being the axial direction of the jet starting from the injector exit. The inner shear layer is assumed not to be affected by the outer shear layer for the region of interest.

Primary variables which have been measured by Eggers are pitot pressure, total temperature

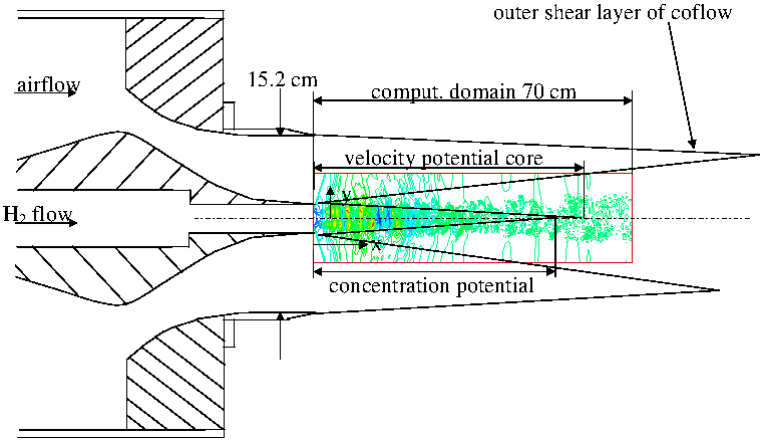

Figure 5.1: Schematic diagram of Eggers jet.

and the volume concentration of hydrogen (H_2) at different locations. Radial measurements were taken at x =0, x =6.39 cm, x =11.11 cm, x =17.91 cm, x =29.23 cm and x =49.65 cm axial locations of the domain. A measurement rake containing static and pitot pressure probe was used. Static pressure measurements were discarded by Eggers, since they were found to be biased because of the presence of shock waves. H_2 concentrations were measured over collected samples with a gas chromatograph. The Mach number was computed from the Rayleigh pitot formula for supersonic flow

$$\frac{P_{tot}}{P} = \left[\frac{(\gamma+1)}{2}M^2\right]^{\frac{\gamma}{\gamma-1}}\left[\frac{\gamma+1}{2\gamma M^2-(\gamma-1)}\right]^{\frac{1}{\gamma-1}} \tag{5.1}$$

and from the basic isentropic relations for a subsonic flow. The local values of the total temperature are computed knowing the total temperatures in the pure H_2 and in the pure air streams, using an energy balance as

$$T_{tot} = \frac{Cp_{H_2}Y_{H_2}T_{tot,H_2} + Cp_{air}(1-Y_{H_2})T_{tot,air}}{Cp_{H_2}Y_{H_2} + Cp_{air}(1-Y_{H_2})} \tag{5.2}$$

The static temperature was then deduced from the total temperature and the Mach number. Finally, the velocity was obtained from the local Mach number and the speed of sound. Eggers indicated a [-16%, +4%] uncertainty in the integrated H_2 mass flow rate over transverse planes. The reliability of the velocity data is also affected by experimental uncertainity. The results of this experiment are frequently used in the literature for the validation of compressible RANS solvers [22, 28, 33].

5.1.2 PHYSICAL AND NUMERICAL PARAMETERS

Physical parameters of the flow are gathered in Table 5.1. The subscript $_{jet}$ stands for H_2 jet conditions. Re_u in the Table is the Reynolds number per meter. Data taken from report of Eggers are written in bold. The other parameters of the initial field are computed assuming a constant static pressure of 100 kPa and using the thermodynamic properties explained in chapter 2. A guess-and-try technique is used to find the static temperature that gives the experimental total temperature, knowing the Mach number in both streams. The characteristics of the flow may be estimated depending on parameters as density ($\rho_{jet}/\rho_{co-flow}$) and velocity ($U_{jet}/U_{co-flow}$) ratios. The convective Mach number M_c is suggested by Bogdanoff [8] for parametrization of compressibility. It is the Mach number of the free streams adjacent to the shear layer, relative to the coherent structures velocity U_c (Figure 5.2). The convection velocity U_c is given as

Table 5.1: Physical parameters for the non-reacting air/H_2 jet. In bold, data from Eggers [32], other values are computed.

	H_2 jet	air co-flow
U (m/s)	**1074**	**394**
T_{stat}/T_{tot} (K)	$260/\mathbf{300}^{+6}_{-12}$	$222/\mathbf{300}^{+3}_{-2}$
P_{stat}/P_{tot} (kPa)	100/167	100/285
Mach	**0.886**	**1.32**
μ (kg.m^{-1}.s^{-1})	0.878 10^{-5}	1.687 10^{-5}
ρ(kg.m^{-3})	0.093	1.563
Re_u (1/m)	11.6 10^6	36.6 10^6
Re_{jet}	1.34 10^5	
M_c	0.44	

$$U_c = \frac{c_2\ U_1 + c_1\ U_2}{c_1 + c_2} \tag{5.3}$$

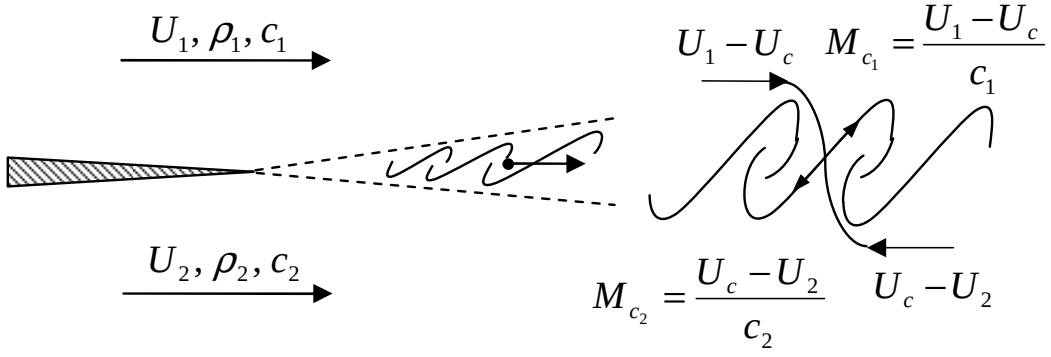

Figure 5.2: Shear layer convective velocity and Mach numbers[8].

The shear layer convective Mach number is calculated by equating the convective Mach numbers of adjacent flows assuming constant specific heat ratio ($\gamma_1 = \gamma_2$)

$$\frac{U_1 - U_c}{c_1} = \frac{U_c - U_2}{c_2} \quad \Rightarrow \quad M_c = \frac{U_1 - U_2}{c_1 + c_2} \tag{5.4}$$

As in the current case of low convective Mach numbers, the assumption for the equality of M_{c_1} and M_{c_2} is relatively accurate [100]. It is important to note that convective Mach number is one of the parameters for characterization of jet but not the only one. It is shown by Fedioun and Lardjane that temperature and density ratio differentiate the characteristics of binary temporal shear layer even if the convective Mach number is constant [41].

It is interesting to have an estimate, or at least an order of magnitude of the range of turbulent scales to be resolved. Large scales of the flow are produced by initial Kelvin-Helmholtz inflexional instability at the jet/co-flow interface, as illustrated in Figure 5.3. From experimental

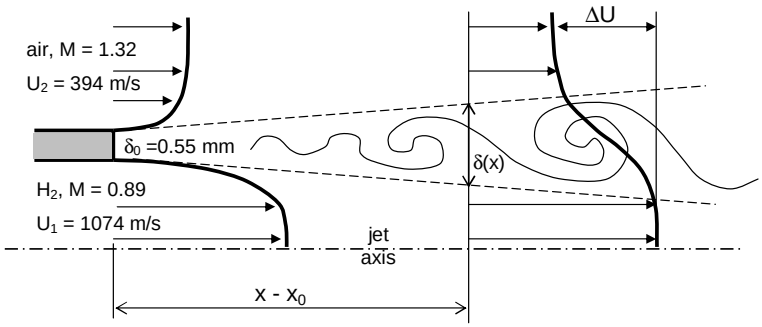

Figure 5.3: Inlet velocity profile for the non-reacting air/H_2 Eggers jet.

velocity profiles, the end of the potential core is at about 5.5 jet diameters, i.e. $x - x_0 \approx 64$ mm. At this location, the estimated shear layer width $\delta(x) = \delta_0 + \delta'(x - x_0)$ is about 8mm

(Figure 11 (a) of [32]), giving the scale of the largest eddies. This value corresponds to a growth rate $\delta' \approx 0.12$, coherent with the literature [26] for compressible, high density ratio shear layers. The velocity scale of the largest eddies is typically half the velocity difference, $\Delta U/2 = 170$ m/s. Taking an average viscosity and an average density for the values listed in Table 5.1, one finds the large-scale Reynolds number as

$$Re_{(\Delta U/2,\,\delta)} = \frac{\overline{\rho}\Delta U/2\;\delta}{\overline{\mu}} \approx 88000 \tag{5.5}$$

Hence, the Kolmogorov scale is about $\eta \approx \delta \times Re^{-3/4}_{(\Delta U/2,\,\delta)} \approx 0.0015$ mm and the Taylor micro-scale is about $\lambda \approx \delta \times Re^{-1/2}_{(\Delta U/2,\,\delta)} \approx 0.027$ mm.

The grid resolution is indicated as $Ny \times Nz \times Nx$. Simulations are performed for 4 different grids namely 32×32×128, 64×64×256, 128×128×512 and 256×256×512. In the latter case, the computational domain is shorten to half length, i.e. $Lx = 350$ mm. The grid is refined in the transverse direction toward the jet centerline, using analytical metrics explained previously in section 4.6.4 with $z \in [-Lz/2, +Lz/2]$ for $Z \in]-1, +1[$. The size parameter L is chosen such that the ratio of the longest to the shortest cell is 5. The grid is also refined in the axial direction toward the inlet, with a ratio of 6. The 2D views of 32×32×128 resolution grid are shown in Figure 5.4. For the fine grid, the shortest grid cell is $\Delta x_{min} = 0.323$ mm and

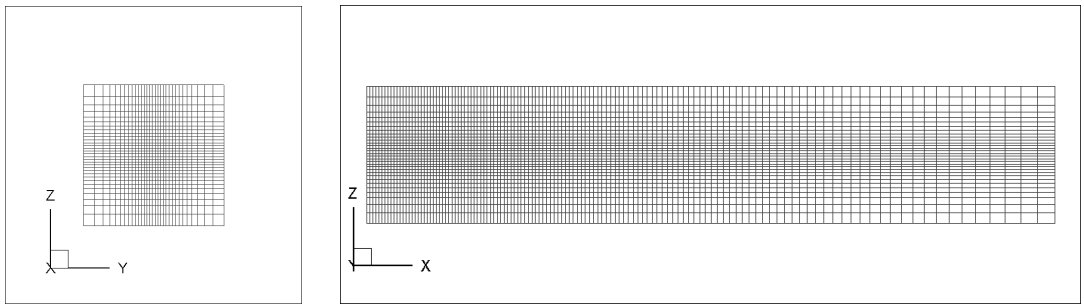

Figure 5.4: Grid for the Eggers jet of resolution 32×32×128

$\Delta y_{min} = \Delta z_{min} = 0.160$ mm. Assuming $\Delta \approx \Delta y_{min}$, gives $\Delta/\eta \approx 100$ and $\Delta/\lambda \approx 6$. Hence, even on the fine grid, the simulation is far from a DNS. The numerical cut-off is probably in the inertial range. The approximations of the scales for all grid resolutions are listed in Table 5.1.2.

The inlet velocity profiles for all grids are shown in Figure 5.5. The profiles are fitted to the

Table 5.2: Ratios of approximate Kolmogorov scale and Taylor microscale to the minimum grid spacing.

Grid	Δ x$_{min}$	Δ y$_{min}$	Δ/η	Δ/λ
32×32×128	0.303×10^{-2}	0.132×10^{-2}	880	49
64×64×256	0.151×10^{-2}	0.612×10^{-3}	408	23
128×128×512	0.754×10^{-3}	0.322×10^{-3}	215	12
256×256×512	0.323×10^{-3}	0.161×10^{-3}	107	6

Eggers experimental results using hyperbolic tangent equation 5.6

$$\begin{aligned} f &= \frac{f_{\max}}{2}\left\{1+\tanh\left[A\left(\left(\frac{B}{rC}\right)^{E}+\frac{1}{rC-D}\right)\right]\right\} \\ r &= \left(y^2+z^2\right)^{1/2} \end{aligned} \tag{5.6}$$

The coefficients for the velocity profiles (co-flow/jet) and for the air mass fraction profile are listed in Table 5.3. Air is assumed to be composed of N_2 and O_2 in the atmospheric concentration ratio. Hydrogen mass fraction is computed full-filing the sum of all species mass fractions to unity. While adopting the hyperbolic tangent profiles the following issues

Table 5.3: Coefficients which are used for the inlet velocity profile.

var:	U_{jet}	$U_{co-flow}$	Y$_{air}$
$f_{\max}$	1074	394	1
A	10	4	12
B	0.2	1.428	1
C	0.2	-0.525	-0.9
D	1	-1	0
E	1	1	-1

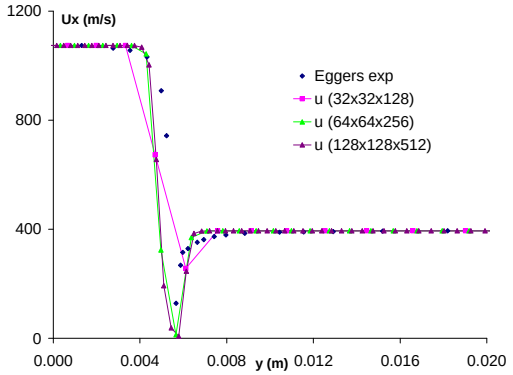

Figure 5.5: Inlet velocity profile for the non-reacting air/H_2 Eggers jet.

are considered:

- The H_2 jet and air jet profile must be distinct at pitot region of nozzle. As there exists high density and velocity ratio. Otherwise, air at the speed of hydrogen jet may cause significant momentum injection at shear layer.
- At the pitot region, as the gradients of inlet profiles are high, the number of nodes

must be more then the WENO sub-stencil size. Otherwise the scheme will smooth the profiles and even out the effect of pitot at inlet.

This slight modification of the initial field causes some error in the volumetric flow rate which is 6×10^{-2} (m^3/s) (computed by trapezoidal rule) for the experimental profiles. The error is at most 10% for the 64×64×256 grid and around 5% for the other resolutions. This is within the uncertainity limits of Eggers data.

In order to trigger the transition to turbulence, a random noise is applied for the *y* and *z* velocity components. First, for each line 20 random values are generated using the portable random number generator presented in the literature [68, 89]. By applying back Fourier transform a function is obtained using these random numbers. The noise which is confined by Gaussian distribution in the H_2 central jet, vanishes in the air co-flow (Figure 5.6) The normalized weight of the Gaussian distribution Conf is computed as

$$\text{Conf} = a\, e^{-\frac{r^2}{2(bL)^2}} \tag{5.7}$$

The amplitude *a* and parameter *b* controlling the Gaussian shape are respectively taken to be 10 m/s and 0.04. *L* is the size of the window for Gaussian shape (diagonal length of the YZ surface where the bruit is applied.). No other tunable parameter is introduced in the initial

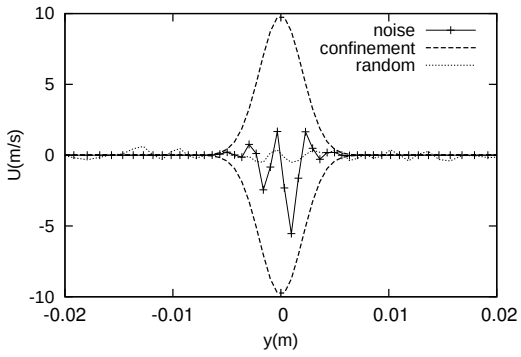

Figure 5.6: Radial distribution of confinement function, samples of generated 'random' field and the noise applied on transverse velocity components.

field. Non-reflecting boundary conditions are applied for open boundaries.

At the co-flow velocity, one crossing of the full computational domain takes 1.8 ms. At the three lowest resolutions, time averaging of the flow variables are computed for 0.7 ms after the simulation is allowed to progress for 2 ms from the initial field. Simulation with the finer

grid (half domain) is progressed for 0.82 ms before averaging for 0.15 ms only, due to the high computational cost (see appendix I).

5.1.3 FLOW STRUCTURE

In Figures 5.7 - 5.11, results of LES_SM, LES_SSF, MILES_NS and MILES_EULER simulations are shown from top to bottom. Vertical and horizontal contour maps are the projections of the instantaneous pressure fields and the instantaneous H_2 mass fraction fields in the corresponding symmetry planes, respectively. For a better visualization, *y* and *z* scales are magnified by a factor of two. These figures allow a straightforward comparison of the behavior of LES and MILES at different grid resolutions. Mixing and pressure fluctuations may be observed from the hydrogen mass fraction and the pressure contours, respectively.

The structure of the flow is displayed at all resolutions as the Q-criterion [29, 67] iso-surface which is commonly used for coherent structure identification. Q-criterion is the measure of domination of the strain S^*_{ij} by the rotation Ω_{ij} which are the symmetric and the antisymmetric parts of the velocity gradient tensor, respectively.

$$Q = \frac{1}{2}\left(\Omega_{ij}\Omega_{ij} - S^*_{ij}S^*_{ij}\right) \tag{5.8}$$

where

$$\Omega_{ij} = \frac{1}{2}\left(u_{i,j} - u_{j,i}\right) \tag{5.9}$$

Q-criterion is also related to the Lagrangian of pressure for incompressible formulation, by the well known Poisson equation.

$$Q = -\frac{1}{\rho}\Delta p \tag{5.10}$$

Results for 32×32×128 grid resolution (Figure 5.7) :

The SM model introduces excessive (more than physical) amount of sub-grid viscosity. This results in the damping of flow shear and also delays transition to downstream locations where the stretching of the grid may even out the linear instabilities. These solutions are not considered to be physical since the flow field is not resolved.

Results for 64×64×256 grid resolution (Figure 5.8) :

Although the spatial resolution is still not adequate at this grid level, the obtained results are more amended for physical interpretation. The difference of the LES_SM result compared to

the other solutions is apparent. Coherent structures for LES_SSF solution are of larger intensity since the explicit sub-grid model damps the small perturbations. For the LES_SSF solution, the large scale structures disappear approximately at the end of concentration potential core. MILES_EULER and MILES_NS simulations generate similar results. In the MILES_NS solution the light turbulent structures are further damped out. Disturbances which are present in the pressure field are associated with the flow instabilities can be called as Mach waves [94]. Hydrogen mixing starts to be observed at this resolution. The concentration potential core lengths for MILES_EULER, MILES_NS and LES_SSF are close.

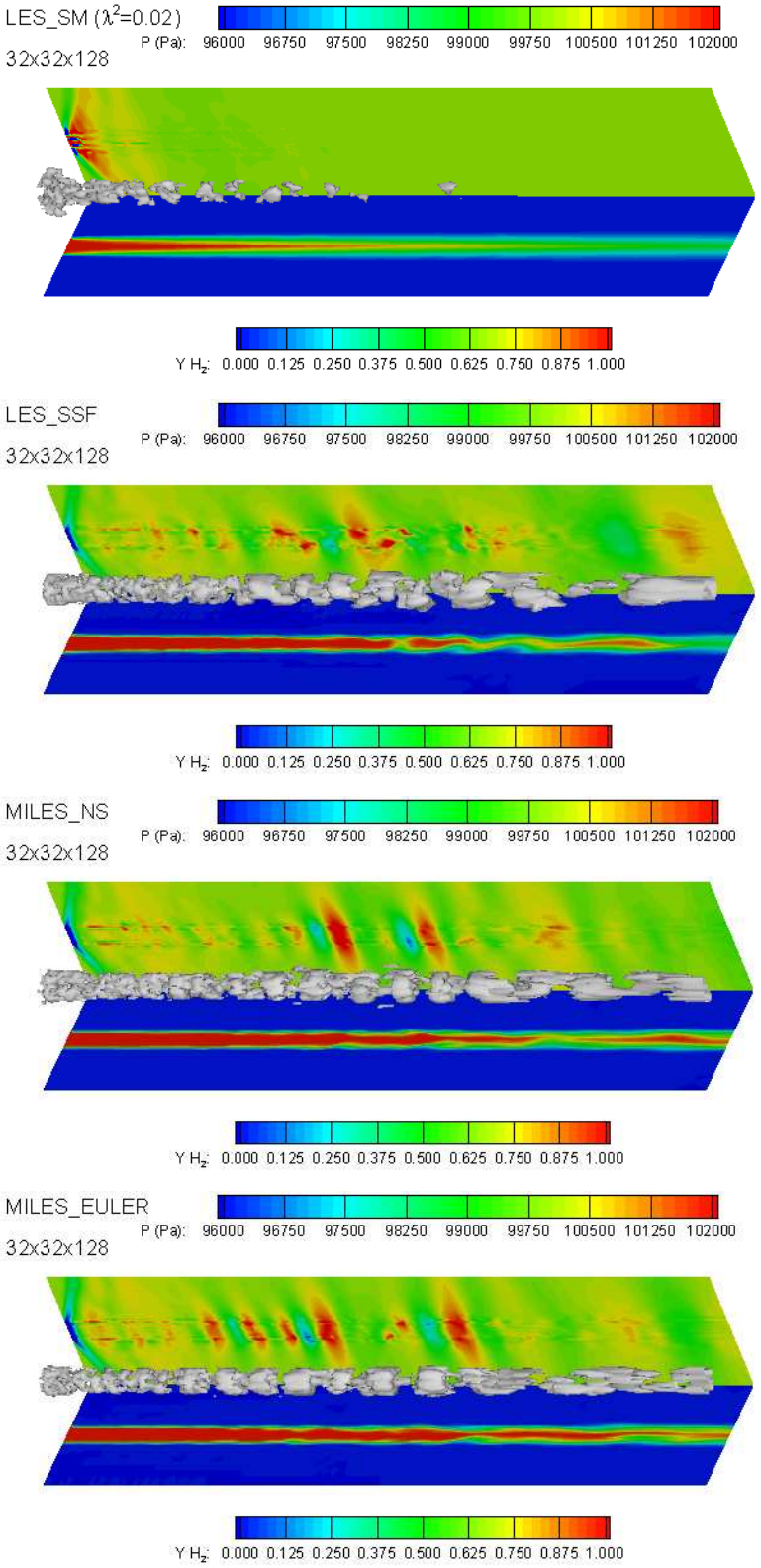

Figure 5.7: Eggers jet results on 32×32×128 grid. Instantaneous structure of the flow visualized using iso-Q. Pressure and Hydrogen mass fraction in the symmetry planes for different approaches.

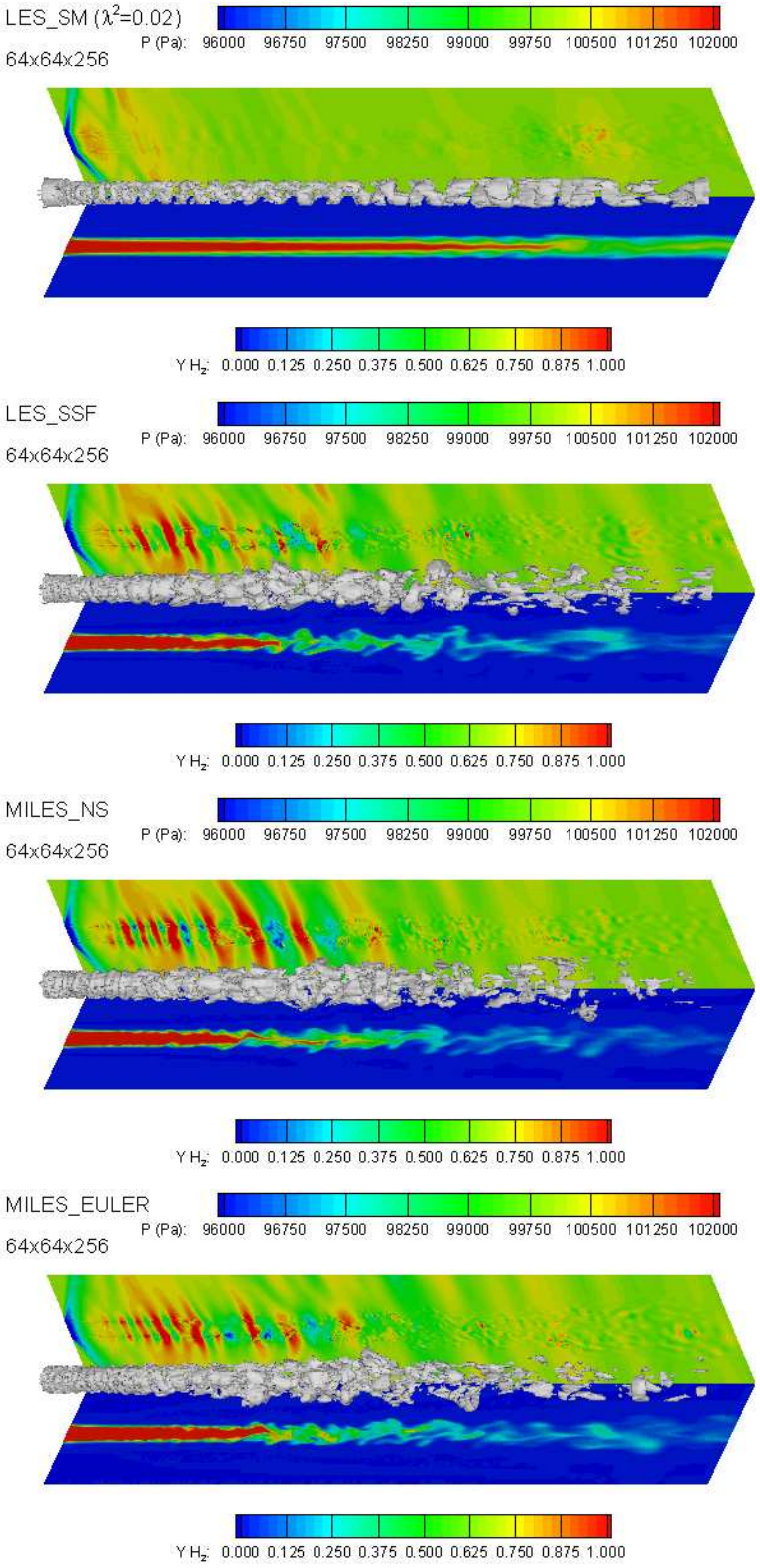

Figure 5.8: Eggers jet results on 64×64×256 grid. Instantaneous structure of the flow visualized using iso-Q. Pressure and Hydrogen mass fraction in the symmetry planes for different approaches.

Results for 128×128×512 grid resolution (Figure 5.10) : The solutions at the initial core of the jet for MILES_EULER, MILES_NS and LES_SSF are identical at 128×128×512 resolution. After the transition, the structures displayed as Q-criterion iso-surfaces are damped along the axial direction earlier in the LES_SSF solution. The sensor (3.67) initially switch off the SSF model in the initial core of the jet where the gradients are naturally high and later, when the flow is 3D enough, model is switched on to diffuse turbulence effectively. Concentration potential core lengths of all numerical approaches are identical and shorter than the ones for 64×64×256 grid solution. LES_SM solution is observed to be more dissipative at this resolution. This solution is more comparable with lower resolution of 64×64×256 grid MILES_EULER, MILES_NS solutions in Figure 5.8. Simulation for lower Smagorinsky constant (half) is conducted for understanding the effect of the SM model (Figure 5.9). The solution at the initial core region became identical to the solutions for other numerical approaches and coherent structures propagate downstream for the LES_SM solution which is sensitive to the Smagorinsky constant.

Results for 256×256×512 grid resolution (Figure 5.11) :

Figures at fine grid resolution are almost identical to the solutions for 128×128×512. The LES_SM solution is closer to the solutions of the other approaches however the flow field at the beginning of the shear layer is still very much affected by the model. The pressure waves are more clustered compared to the results obtained with lower grid resolutions.

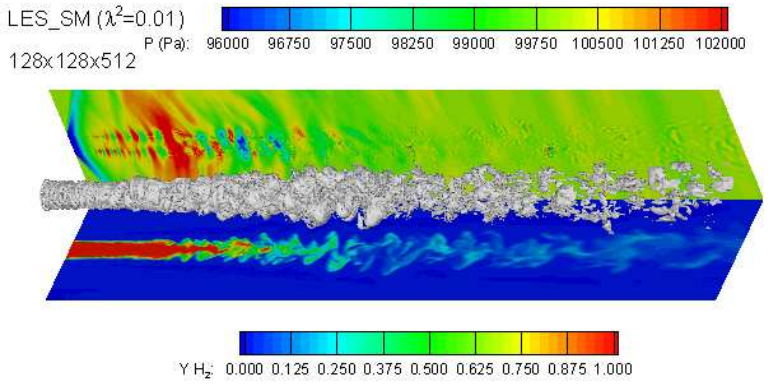

Figure 5.9: Eggers jet result on 128×128×512 grid with reduced Smagorinsky constant. Instantaneous structure of the flow visualized using iso-Q. Pressure and Hydrogen mass fraction in the symmetry planes for different approaches.

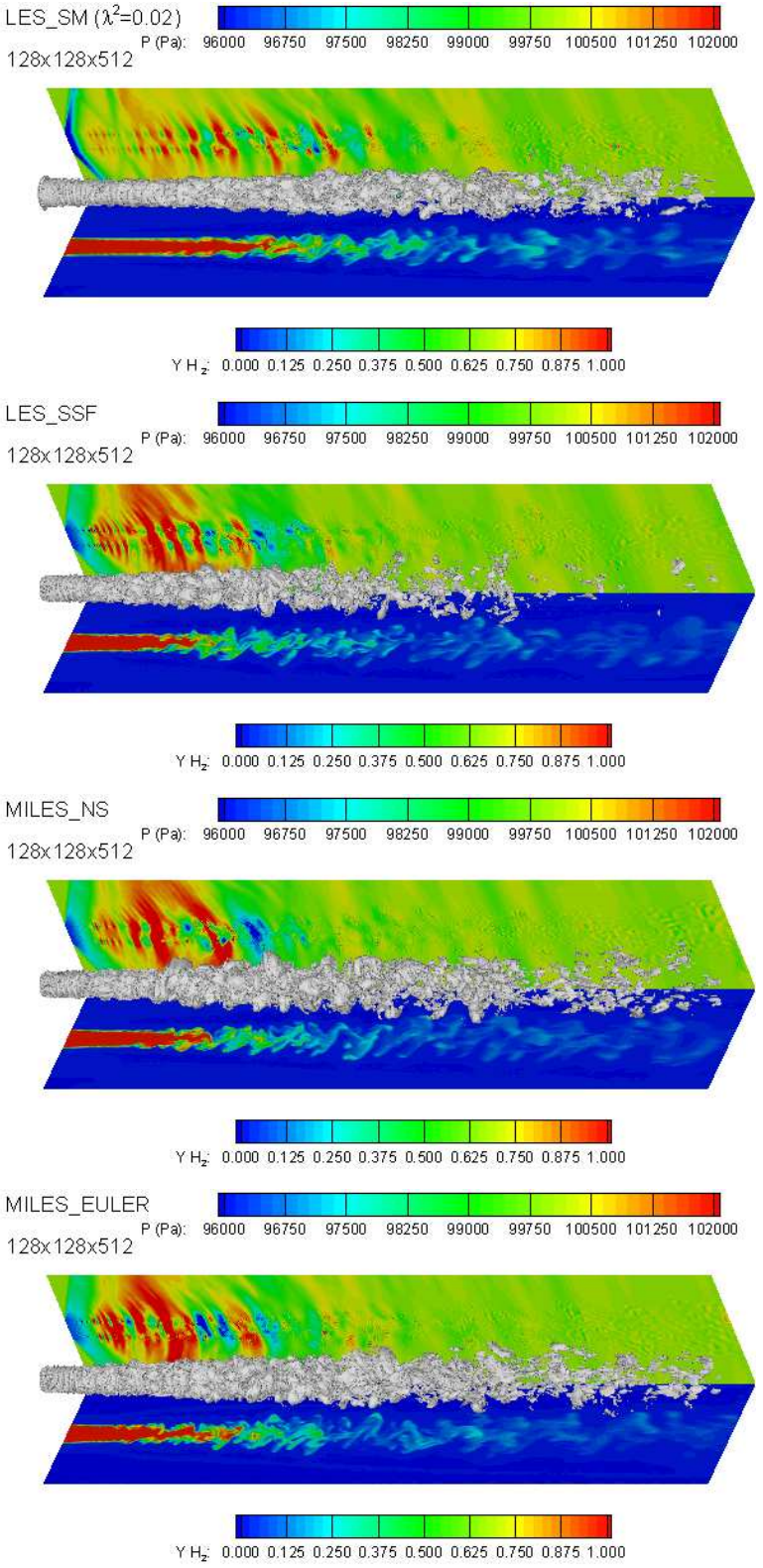

Figure 5.10: Eggers jet results on 128×128×512 grid. Instantaneous structure of the flow visualized using iso-Q. Pressure and Hydrogen mass fraction in the symmetry planes for different approaches.

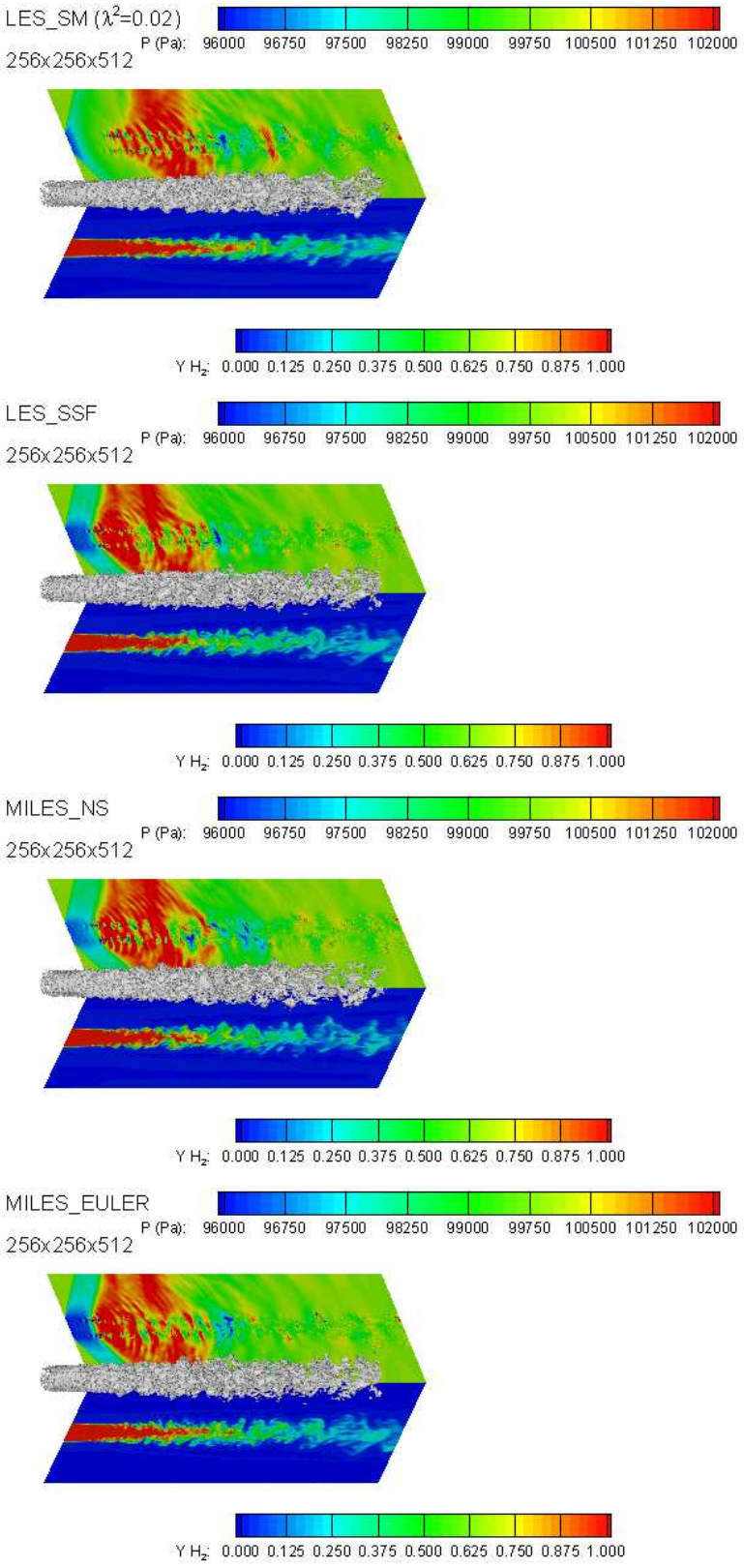

Figure 5.11: Eggers jet results on 256×256×512 grid. Instantaneous structure of the flow visualized using iso-Q. Pressure and Hydrogen mass fraction in the symmetry planes for different approaches.

5.1.4 STATISTICAL RESULTS

The center-line, time-averaged, *x*-velocity distribution (axial decay) is shown in Figure 5.12, for the different simulations. Clockwise from top-left, sub-figures display LES_SM, LES_SSF, MILES_NS and MILES_EULER results for different resolutions. The lowest resolution

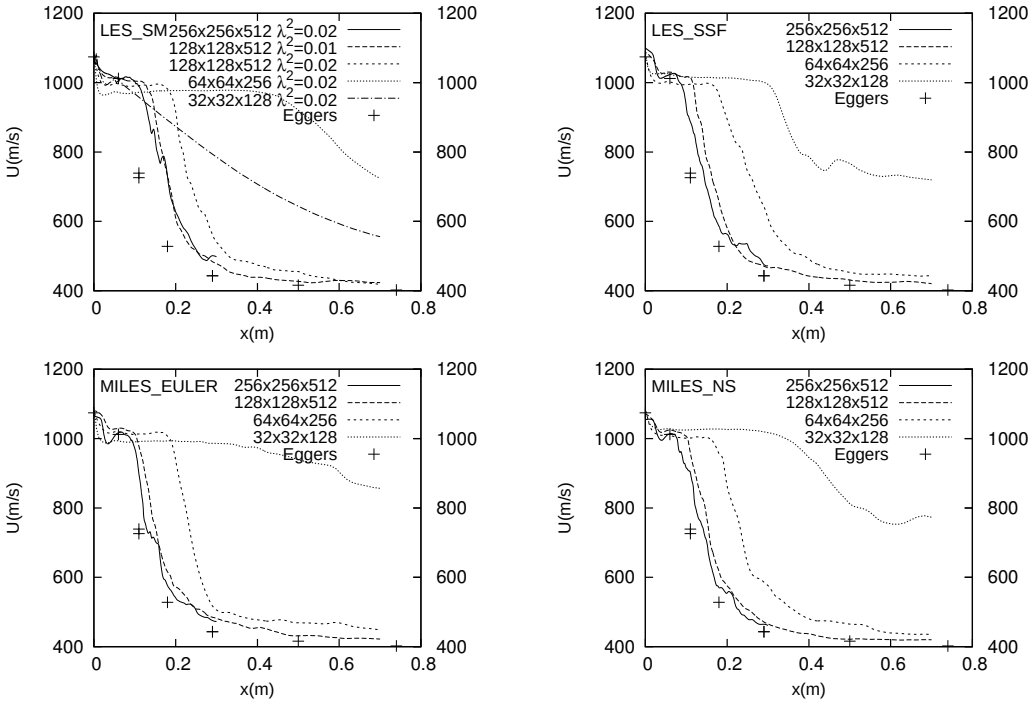

Figure 5.12: Eggers jet : axial velocity decay. Clockwise from top-left : LES_SM, LES_SSF, MILES_NS and MILES_EULER

32×32×128 is physically inadequate for all numerical approaches. Increasing the resolution to 64×64×256 improves slightly the results, but the grid is still too coarse to capture the initial development of shear instabilities. They are damped by the numerical dissipation, and the transition is delayed far downstream. The worst case is observed for LES_SM (top-left) because the Smagorinsky model, can not distinguish the mean flow gradients from turbulent structures. Hence, the model is active and introduces additional dissipation in the laminar, high-shear, jet entrance region. Increasing again the grid resolution up to 128×128×512 improves dramatically the results. Except for LES_SM with $\lambda^2 = 0.02$ which is still too dissipative, all the simulations show convergence toward the experimental results. MILES_EULER (bottom-left) and MILES_NS (bottom-right) are very close to each other, but MILES_NS is a little closer to the experiment at the end of the computational domain. The LES with explicit

SSF sub-grid model does not show any improvement compared to the MILES. At the highest resolution 256×256×512, results are further closer to the experimental data and grid convergence is almost achieved, even with MILES_EULER although there is no physical cutoff in this calculation. As mentioned above, the curves are a little wavy because time statistics are not perfectly converged. Transverse velocity profiles at four specific downstream locations investigated by Eggers are shown on the 128×128×512 and 256×256×512 grids in Figures 5.13 and 5.14 respectively. With the exception of LES_SM with $\lambda^2 = 0.02$, all numerical approaches under-predicts qualitatively, the spreading of the jet. On the finer grid 256×256×512 (Figure 5.14), results are further closer to the experimental data.

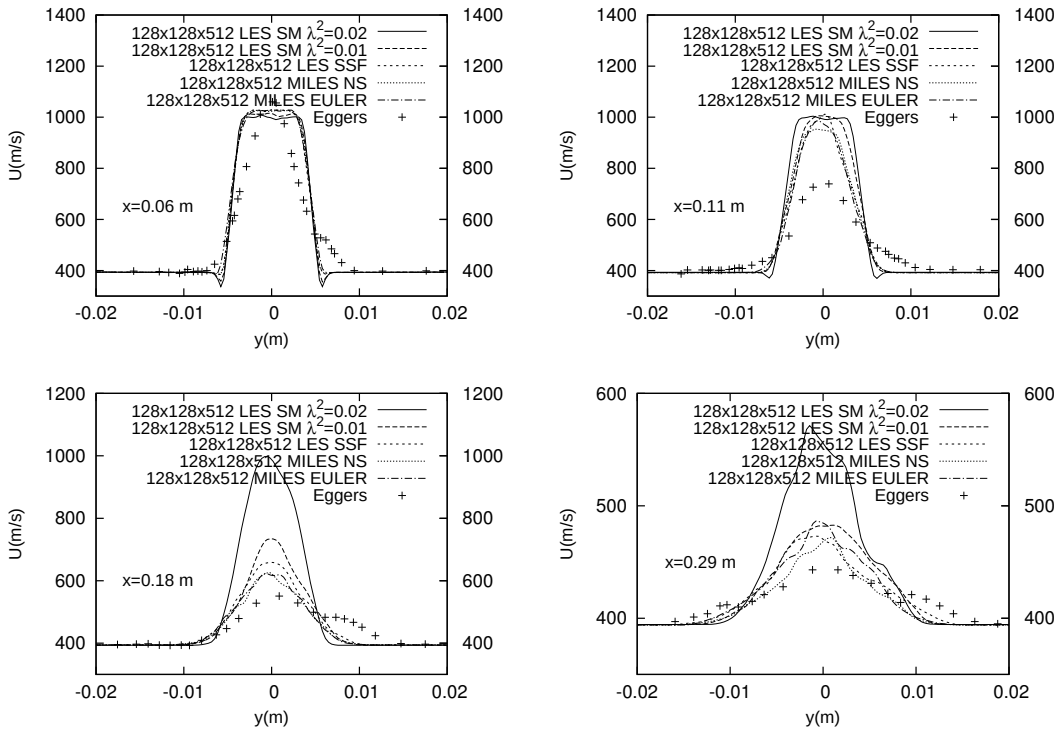

Figure 5.13: Eggers jet : transverse velocity profiles at x =0.06, 0.11, 0.18 and 0.29 m from the exit. Resolution 128×128×512

Figure 5.15 shows the hydrogen mass fraction along the centerline. Although the agreement is not so good as for the dynamic field, most of the previous conclusions can still be observed again, here. One may have to keep in mind the uncertainty in the experimental data as well.

In order to evaluate the axial variation of a quantity $Q(x, y, z, t)$, it is appropriate to look at the variation of time averaged variable ($\bar{Q}(x, y, z)$) at the centerline ($Q_0(x)$) (Figure 5.17). The subscripts $_0$ and $_\infty$ are respectively the centerline and far-field average values of the quantity

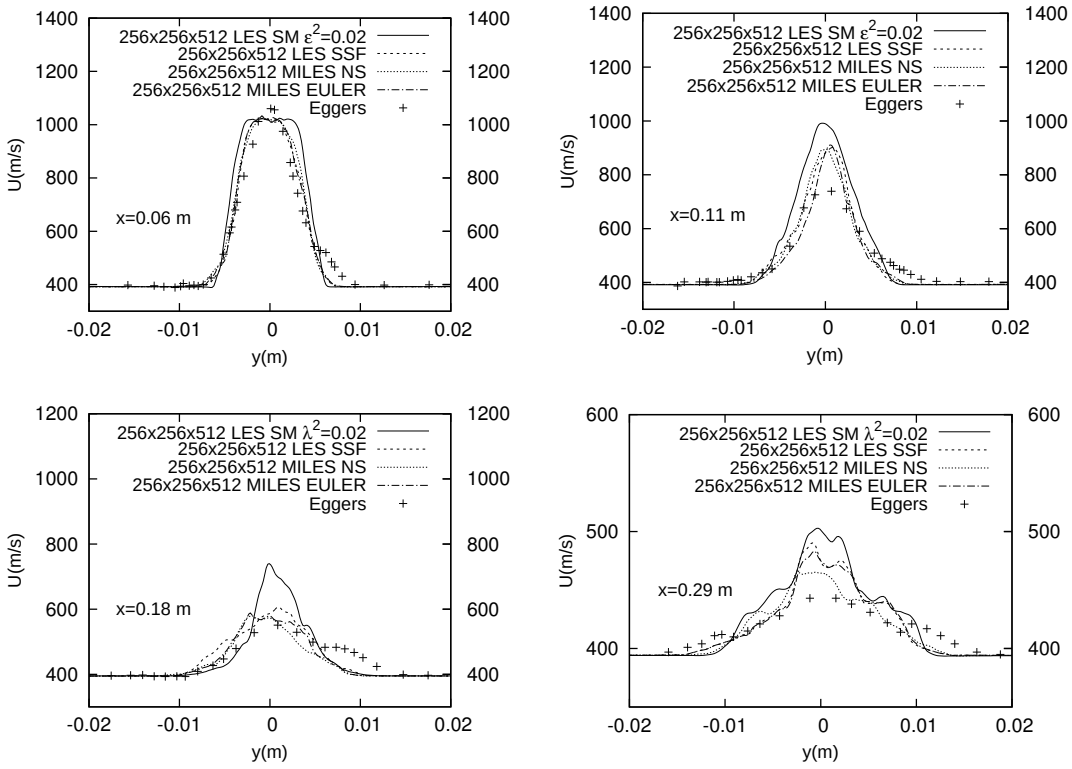

Figure 5.14: Eggers jet : transverse velocity profiles at x =0.06, 0.11, 0.18 and 0.29 m from the exit. Resolution 256×256×512

(Figure 5.16). x_0 is the fictitious center of the jet. Considering the above definitions the definition for an inverse normalized time averaged quantity [106] at the centerline is

$$Q_* = \frac{Q_{jet} - Q_\infty}{Q_0(x) - Q_\infty} \approx \frac{x - x_0}{B_Q\, d} \tag{5.11}$$

B_Q is the spreading rate of quantity after the initial region of the jet. The variations of the inverse of quantities eventually appear to show a linear trend as shown in Figure 5.18. The axial normalized inverse of velocity and hydrogen mass fraction profiles are shown in Figure 5.19 for all grids except 32×32×128 grid. The B and x_0 values for the axial velocity and for the hydrogen mass fraction are listed respectively in Tables 5.4 and 5.5. These results show that at low resolution of 64×64×256, the potential core estimated far downstream and the spreading rate are larger. At low resolution the gradients of the inlet profile are smoother since there are few points at the pitot region of the inlet. High numerical diffusion, because of the very low resolution, enlarges the spreading angle. It is observed in the profiles shown on Figure 5.19 that the Smagorinsky model is not able to resolve most physical properties related to the problem. The velocity decay for MILES_EULER is one of the fastest which has an

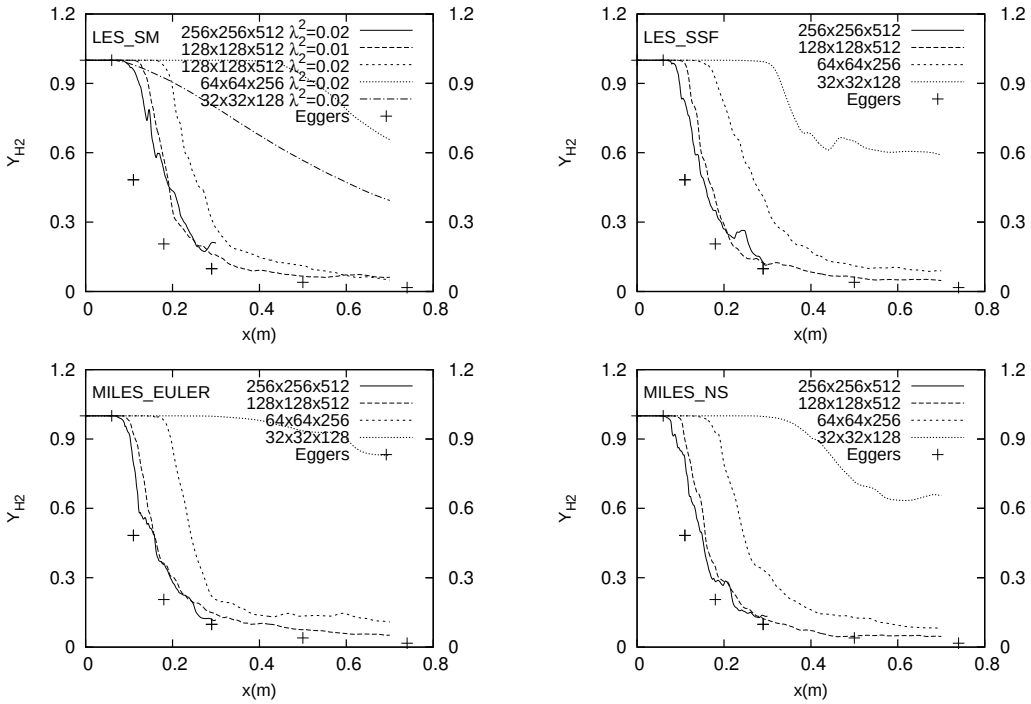

Figure 5.15: Eggers jet : H_2 mass fraction axial decay. Clockwise from top-left : LES_SM, LES_SSF, MILES_NS and MILES_EULER

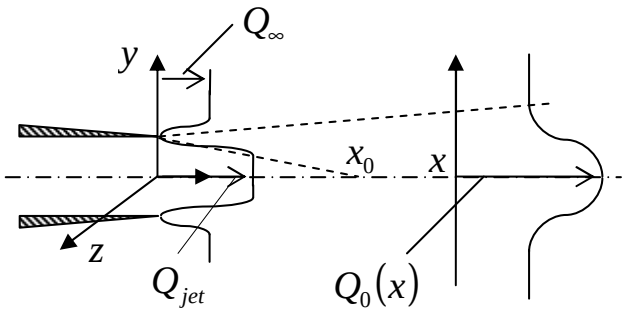

Figure 5.16: Definitions for inverse normalized time averaged quantity.

early plateau around x=0.5 m. The hydrogen concentration shows similar behavior. At higher resolutions of 128×128×512 and 256×256×1024 the simulations give similar results except for the Smagorinsky model. The Smagorinsky model causes transition delay by smoothing the gradients which are present in the initial region. However the velocity decay slopes of the solutions of Smagorinsky model are close to the MILES_NS and LES_SSF results. At 64×64×256 Smagorinsky gives unrealistic results as stated earlier in section 5.1.3. At high

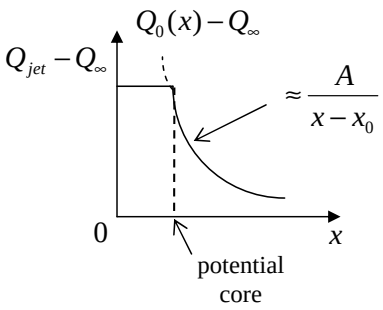

Figure 5.17: Variables for inverse normalized average quantity.

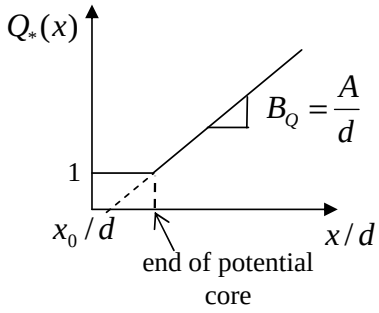

Figure 5.18: Variation of the inverse normalized quantities Q^* on the axis of turbulent jet.

resolution all cases give similar behavior as shown in Figure 5.19 and tabulated data (Table 5.4).

The H_2mass fraction potential core values for all cases are smaller than the velocity potential core values, by a factor of %4 ± 2. The diffusion of momentum is more than the diffusion of species so that the overal Schmidt Sc number is less than unity.

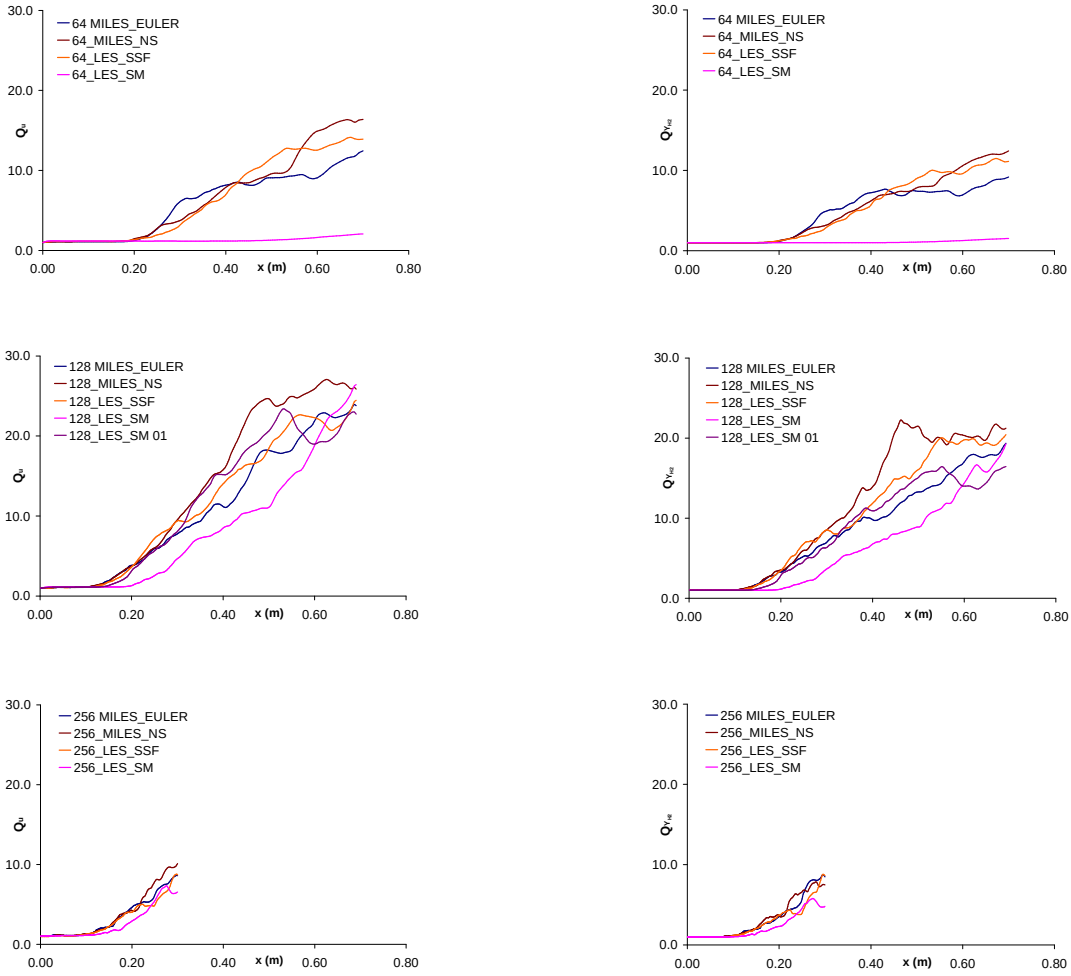

Figure 5.19: The inverse normalized velocity $Q_{*\,U}$(left) and the inverse normalized H_2 mass fraction $Q_{*Y_{H_2}}$(right) for 64×64×256, 128×128×512 and 256×256×512 resolutions (from upper to lower).

Table 5.4: The slope and fictitious center of inverse normalized time averaged velocity.

	64×64×256		128×128×512		256×256×512	
	$B_U d$	x_{0_u}	$B_U d$	x_{0_u}	$B_U d$	x_{0_u}
MILES_EULER	6.12	0.215	4.45	0.129	3.97	0.105
MILES_NS	3.72	0.206	6.08	0.136	4.12	0.109
LES_SSF	3.49	0.219	5.43	0.138	4.15	0.113
LES_SM 01	-	-	5.29	0.153	-	-
LES_SM	0.38	0.298	4.30	0.203	2.80	0.128

Table 5.5: The slope and fictitious center of inverse normalized time averaged hydrogen mass fraction.

	64×64×256		128×128×512		256×256×512	
	$B_{Y_{H_2}} d$	$x_{0_{Y_{H_2}}}$	$B_{Y_{H_2}} d$	$x_{0_{Y_{H_2}}}$	$B_{Y_{H_2}} d$	x_{0_u}
MILES_EULER	5.53	0.222	3.98	0.133	3.10	0.109
MILES_NS	2.74	0.214	5.32	0.144	4.22	0.118
LES_SSF	2.88	0.220	4.60	0.132	3.37	0.114
LES_SM 01	-	-	4.71	0.162	-	-
LES_SM	2.46	0.472	3.34	0.211	2.45	0.134

5.1.5 VARIATION OF VELOCITY, SPECIES MASS FRACTION AND PRESSURE

The variation of velocity, hydrogen mass fraction and pressure are computed and stored once these flow statistics have reached steady state, for different axial locations of the jet flow field.

The numerical probe locations are indicated over the instantaneous velocity contours on the symmetry axis (figures 5.25 and 5.26), the time variation of velocity at these locations and spectra of velocity data are also given on the same figures.

In the coarser grid, core flow tends to persist for a longer time downstream the computational domain. In figure 5.25, the coherent structures in the flow are more pronounced in MILES_NS and LES_SSF. Amplitude variation of oscillations for MILES EULER is large especially in the jet core region. This leads to an earlier end up of the velocity potential core before reaching two third of the computational domain. The end of velocity potential core for MILES_NS solution is in the second half of the domain. LES_SSF results are similar to MILES_NS results. The velocity spectra of LES_SSF and MILES NS also carry the same slope characteristics. This is also true for the solution on high resolution grid given in figure 5.26. The velocity data of MILES_EULER shows high amplitude fluctuations which is also

reflected in the corresponding velocity spectra. In LES_SM solution (figure 5.25) higher rate of dissipation is observed and oscillations are damped. Whenever the resolution increases, this effect disappears.

The passage frequency of linear instability waves are recognized in time variation figures. The size of the coherent structures is approximately 8 mm based on the observation of instantaneous velocity histogram along the shear region (figure 5.20). The convective velocity of these structures U_c is calculated to be approximately ~518.2 m/s (equation 5.3). So the passage frequency of the linear instabilities is roughly ~70 kHz in accordance with the peak frequencies of the velocity spectra displayed in figures 5.26.

Next two figures 5.27 and 5.28 relate to the hydrogen mass fraction time variations for two

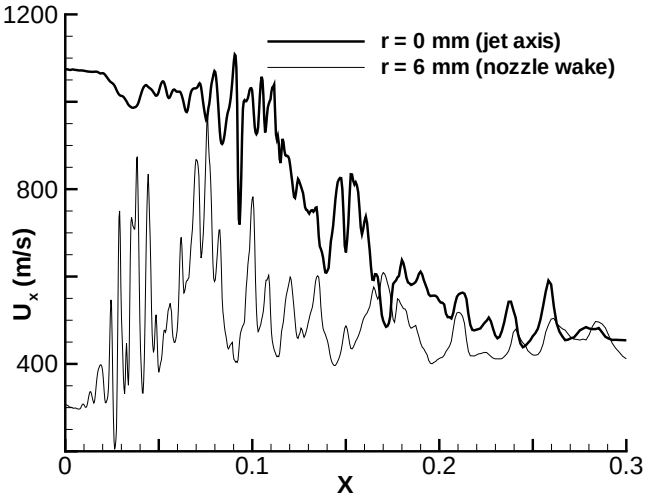

Figure 5.20: Instantaneous axial velocity component on the jet axis at 256×256×512.

highest resolutions of 128×128×512 and 256×256×512. The concentration related results which are obtained by MILES_NS and LES_SSF are similar for both resolutions. Whereas the concentration potential core for MILE_EULER is shorter. It persists longer in LES_SM results at 128×128×512 grid resolution. Higher resolution results also show that the jet core persists for larger distance in LES_SSF and MILES_NS. Larger structures are present for LES_SM and MILES_EULER results.

Low resolution LES_SM does not capture the pressure wave fluctuations which do appear for higher resolution shown in figure 5.30. The LES SSF, MILES EULER and MILES NS show

a higher much resolved Mach wave clustering near the jet inlet. As a result, relatively smaller eddies and smaller fluctuations are present in the flow domain. The velocity spectra for all high resolution solutions look alike.

In figures for pressure (figure 5.29 and 5.30) there exists two peaks in time variation spectra. The frequency of the first peak is at the order of the linear instability passage frequency. This is related to the Mach waves radiated by the growth and decay of linear instability waves [94]. The frequency of these waves is the same for all numerical approaches.

The time series taken are used to compute second order moments for the resolved velocity field $\widetilde{u_i}$ and the Nitrogen mass fraction $\widetilde{Y}_{N_2}$, at the probe locations. The resolved kinetic energy $\hat{k}(\vec{x},t)$ in (3.48) written using the Reynolds decomposition, e.g. $\widetilde{u_i} = <\widetilde{u_i}> + \widetilde{u_i}'$ is

$$\hat{k}(\vec{x},t) = \frac{1}{2} <\widetilde{u_i}><\widetilde{u_i}> + \widetilde{u_i}' <\widetilde{u_i}> + \frac{1}{2}\widetilde{u_i}'\widetilde{u_i}' \tag{5.12}$$

where $<\tilde{\cdot}>$ represents time average. The values of numerically resolved turbulent kinetic energy $\hat{k}' = \frac{1}{2} <\widetilde{u_i}'\widetilde{u_i}'>$ and the Nitrogen mass fraction variance $<\hat{Y}'_{N_2}>$ are plot in Figures 5.21-5.22 and Figures 5.23-5.24, respectively for 128×128×512 and 256×256×512 grid solutions. Decay of turbulent kinetic energy observed in Figure 5.21. As the resolution increase the results make more sense. MILES produces higher second order statistics than LES in the early development of turbulent processes (probe at x =0.11 m, Figures 5.23 and 5.24). Mixing in LES_SM, associated with the peak in $<\hat{Y}'_{N_2}>$, is delayed downstream compared to other simulations. Since small-scales are dissipated by the SM model, large energy-containing eddies dominate in LES_SM. Hence, both $\hat{k}'$ and $<\hat{Y}'_{N_2}>$ overtake the values of other solutions in the downstream region of the jet. The peak turbulent Mach number $M_{RANS} = (\overline{\rho}\hat{k}'/\gamma\overline{p})^{1/2}$ is about 0.1 in the H_2 jet. This result justifies the assumption that the isotropic part (3.61) of the SGS term (3.28) is negligible since the isotropic term can be written as $A^I_{1ij} = \gamma M^2_{sgs}\overline{p}$ [34].

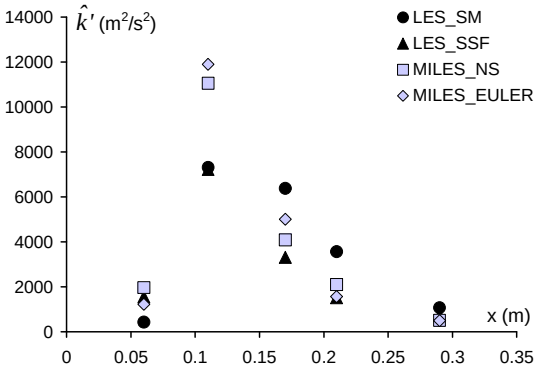

Figure 5.21: Eggers jet: Resolved turbulent kinetic energy, resolution 128×128×512.

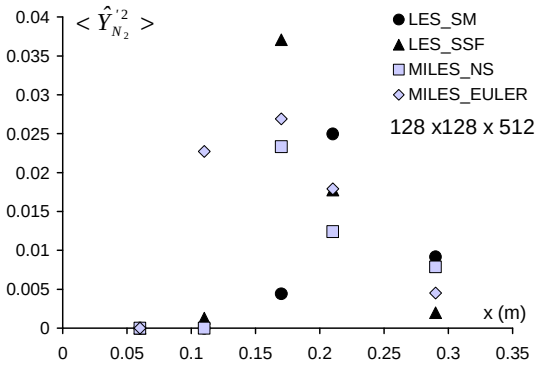

Figure 5.22: Eggers jet: Nitrogen mass fraction variance, resolution 128×128×512.

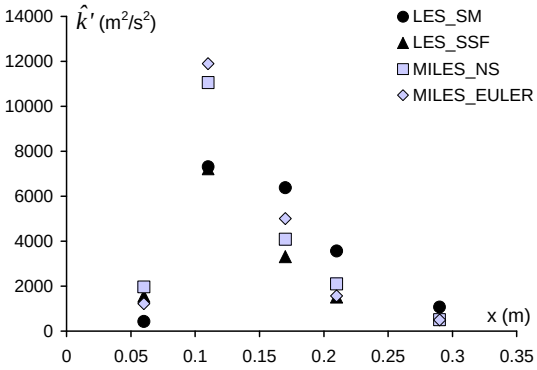

Figure 5.23: Eggers jet: Resolved turbulent kinetic energy, resolution 256×256×512.

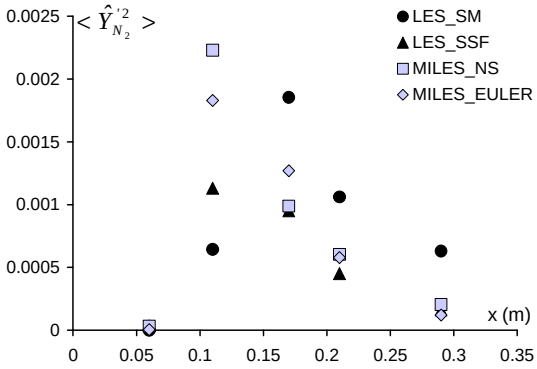

Figure 5.24: Eggers jet: Nitrogen mass fraction variance, resolution 256×256×512.

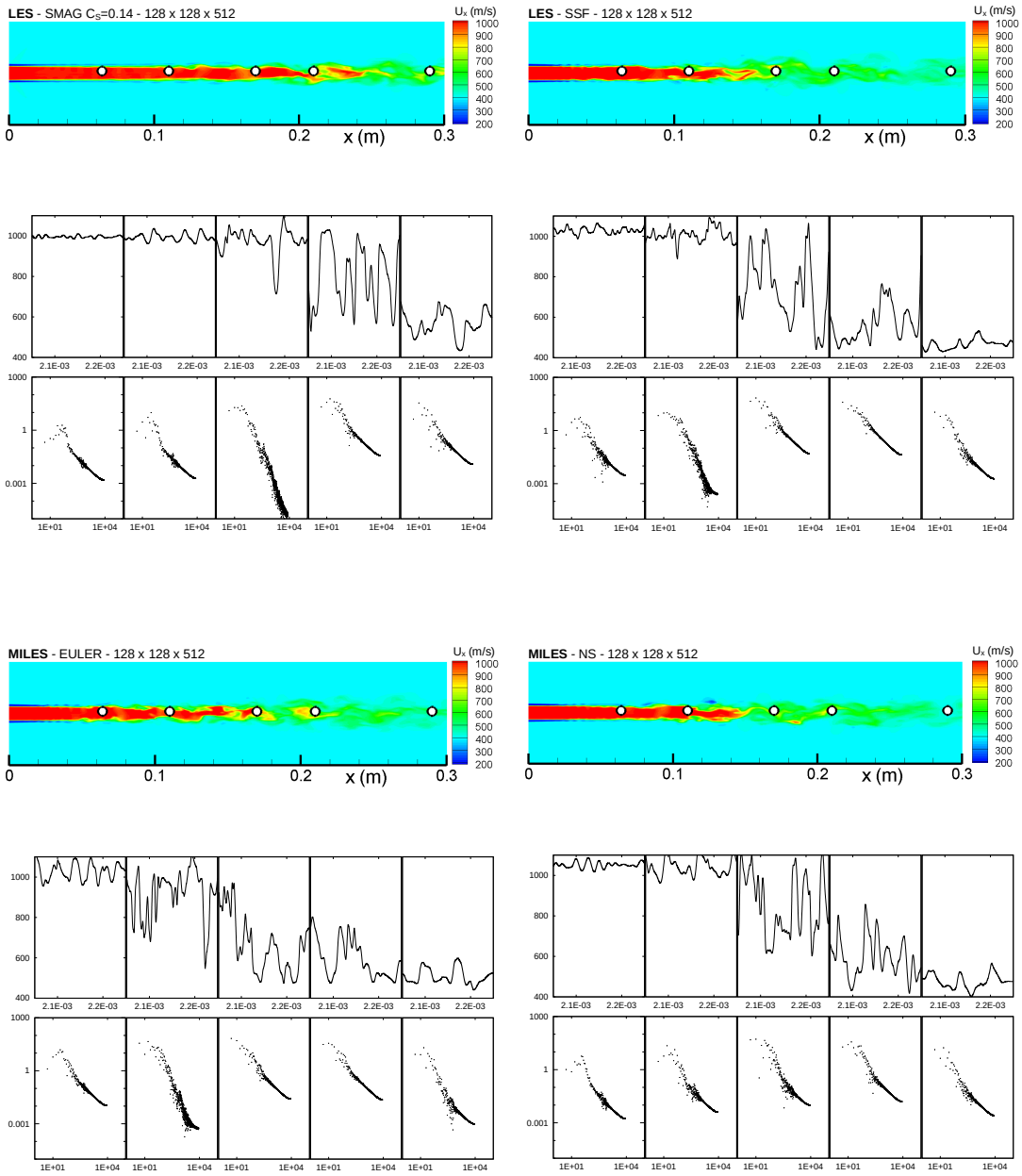

Figure 5.25: Sub-figures demonstrating from top : instantaneous velocity over symmetry axis, sampled time variation and spectra of sampled data of 128×128×512 grid solutions (velocity in m/s and frequency in kHz).

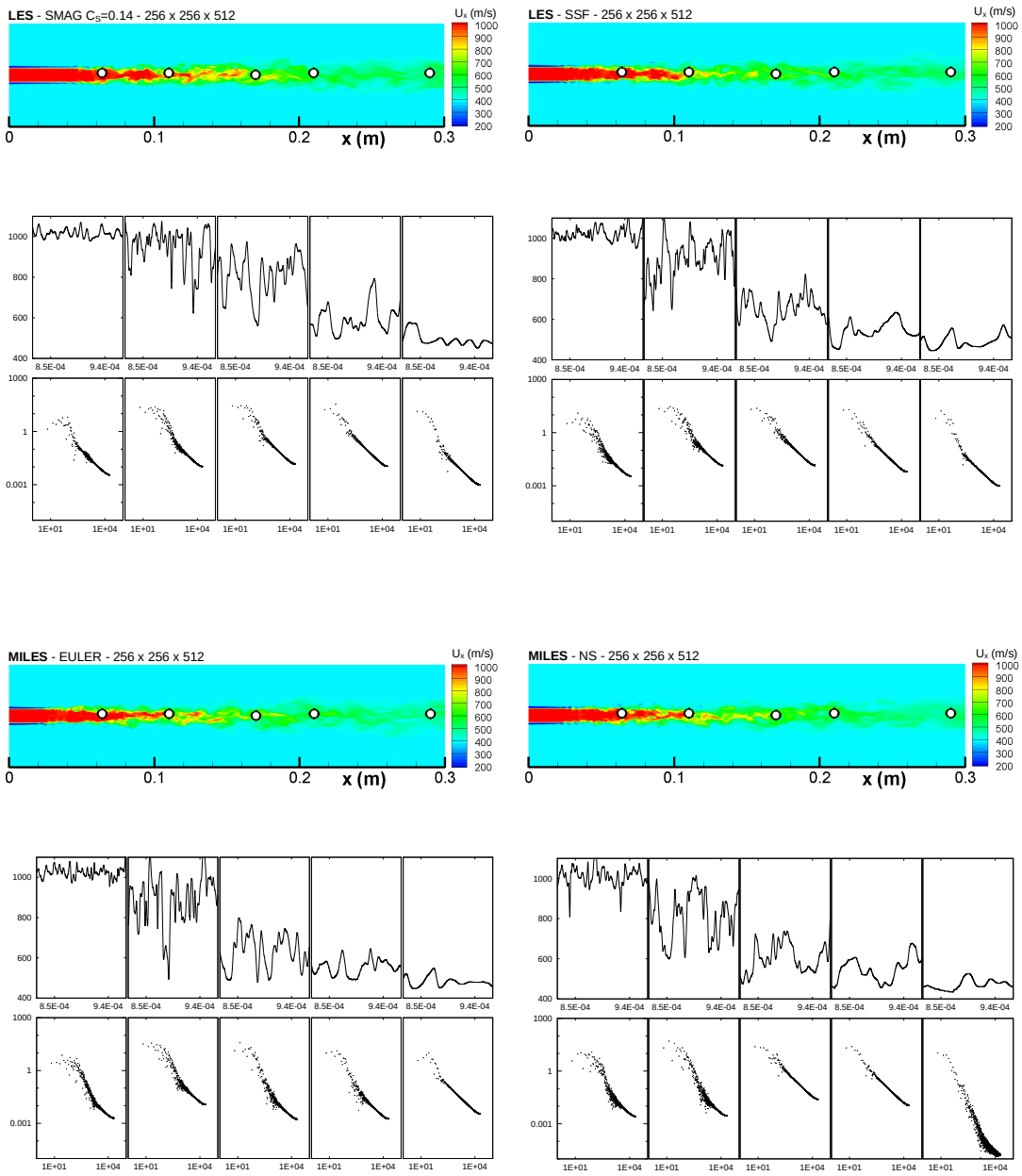

Figure 5.26: Sub-figures demonstrating from top : instantaneous velocity over symmetry axis, sampled time variation and spectra of sampled data of 256×256×512 grid solutions (velocity in m/s and frequency in kHz).

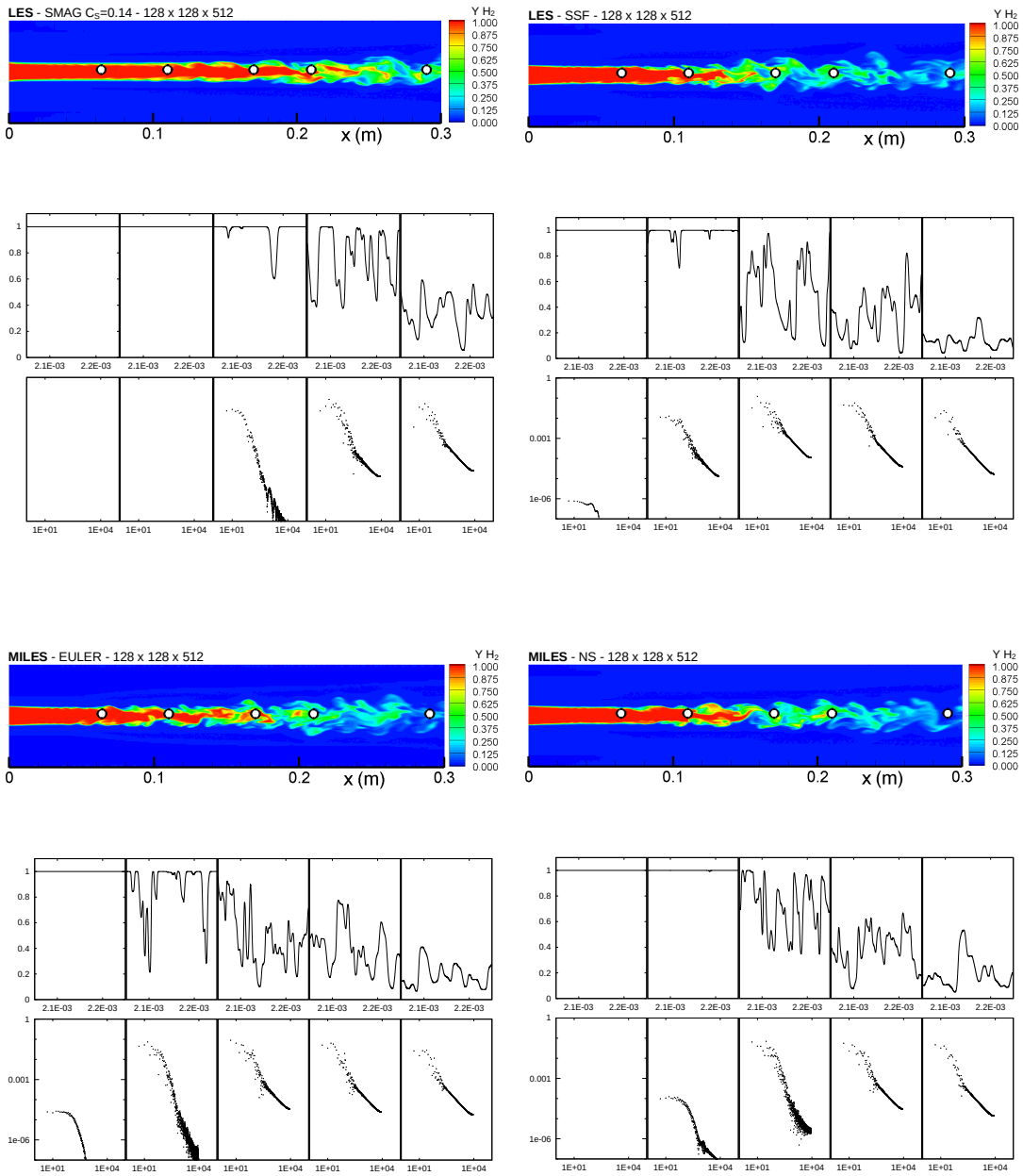

Figure 5.27: Sub-figures demonstrating from top : instantaneous hydrogen mass fraction over symmetry axis, sampled time variation and spectra of sampled data of 128×128×512 grid solutions (frequency in kHz).

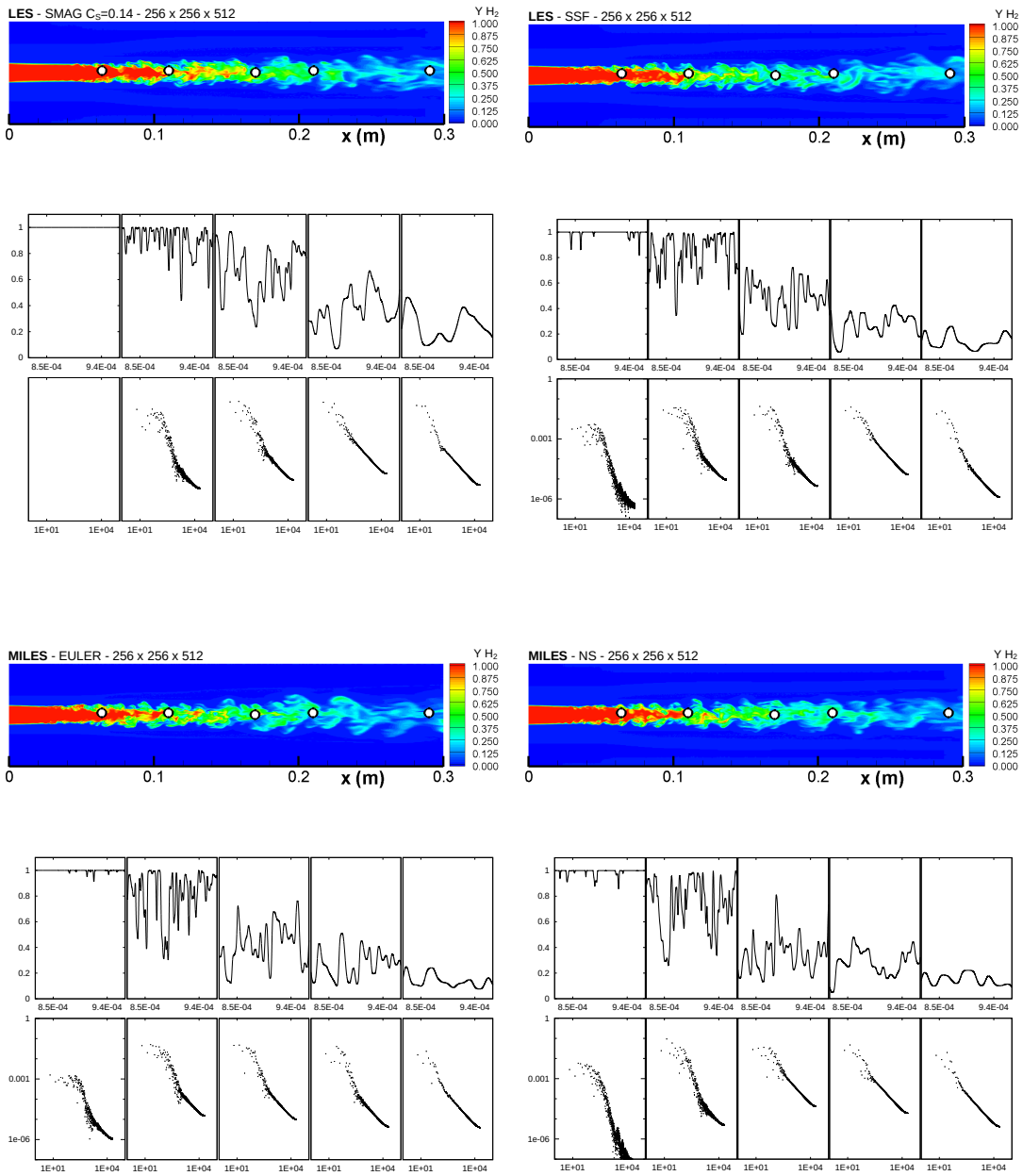

Figure 5.28: Sub-figures demonstrating from top : instantaneous hydrogen mass fraction over symmetry axis, sampled time variation and spectra of sampled data of 256×256×512 grid solutions (frequency in kHz).

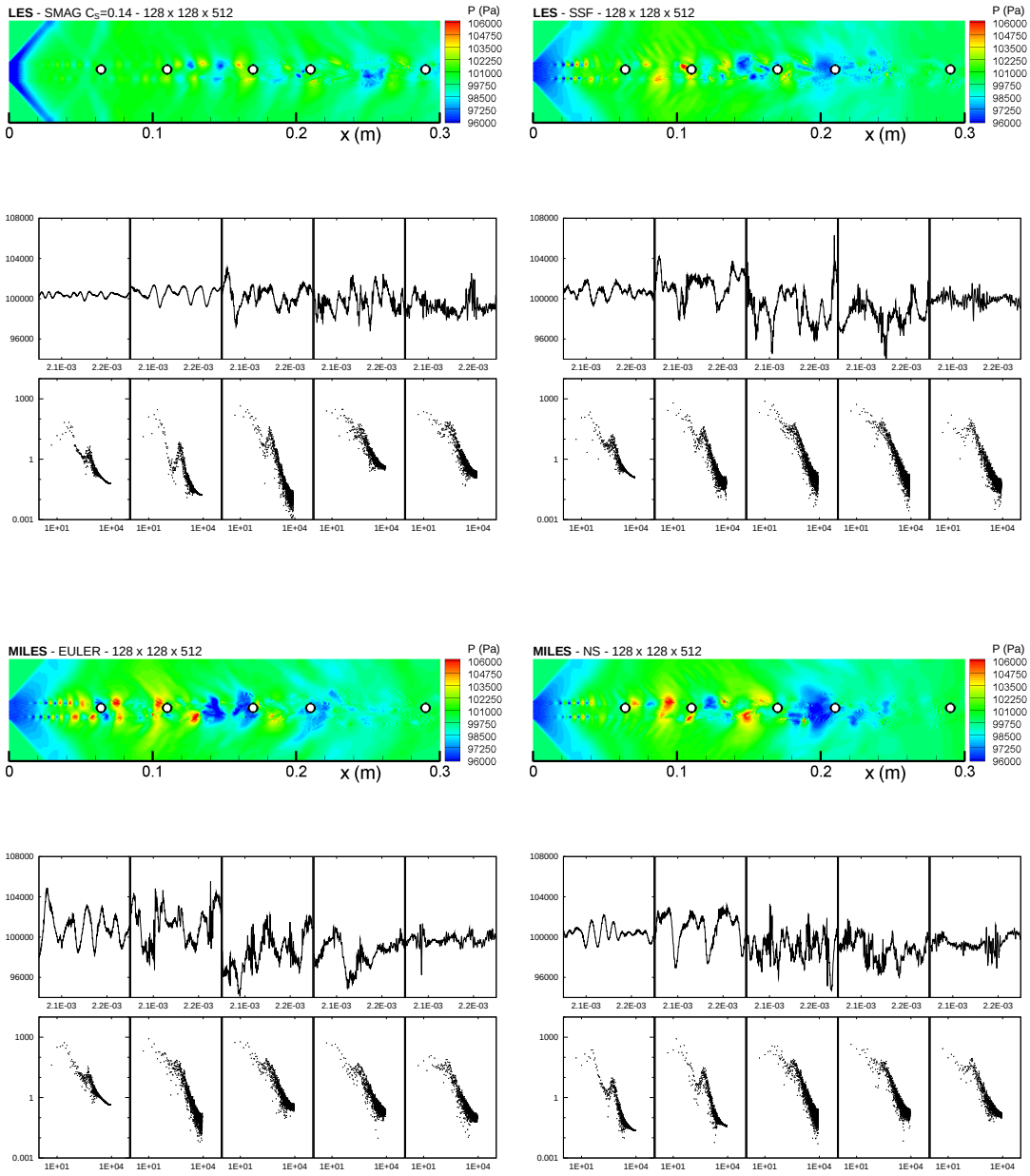

Figure 5.29: Sub-figures demonstrating from top : instantaneous pressure over symmetry axis, sampled time variation and spectra of sampled data of 128×128×512 grid solutions (pressure in Pa and frequency in kHz).

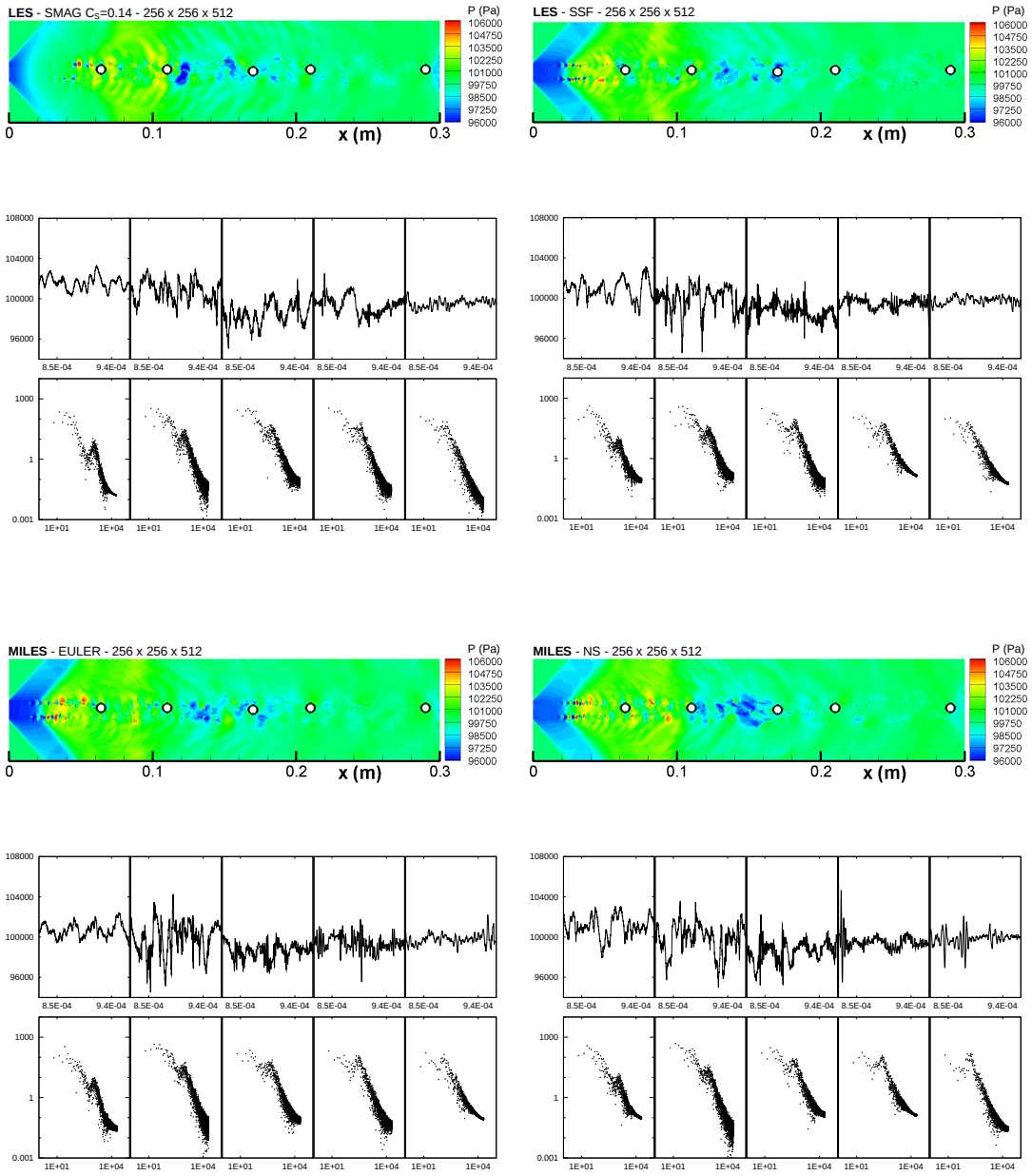

Figure 5.30: Sub-figures demonstrating from top : instantaneous pressure over symmetry axis, sampled time variation and spectra of sampled data of 256×256×512 grid solutions (pressure in Pa and frequency in kHz).

5.1.6 IS THE DNS LEVEL REACHED ?

The question that naturally arises is to know if the explicit sub-grid model is still active at the finest grid resolution. An appropriate numerical indicator is the eddy-viscosity ratio μ^t_{sgs}/μ. In a free shear flow, one can consider that for $\mu^t_{sgs}/\mu \lesssim 1$, the model is no more active. This would not be the case in the boundary layer for a wall-bounded flow where the flow exhibits large gradients. Figures 5.31 and 5.32 show respectively the instantaneous distribution of μ^t_{sgs}/μ for LES_SM and LES_SSF. At resolutions 64×64×256 and 128×128×512,

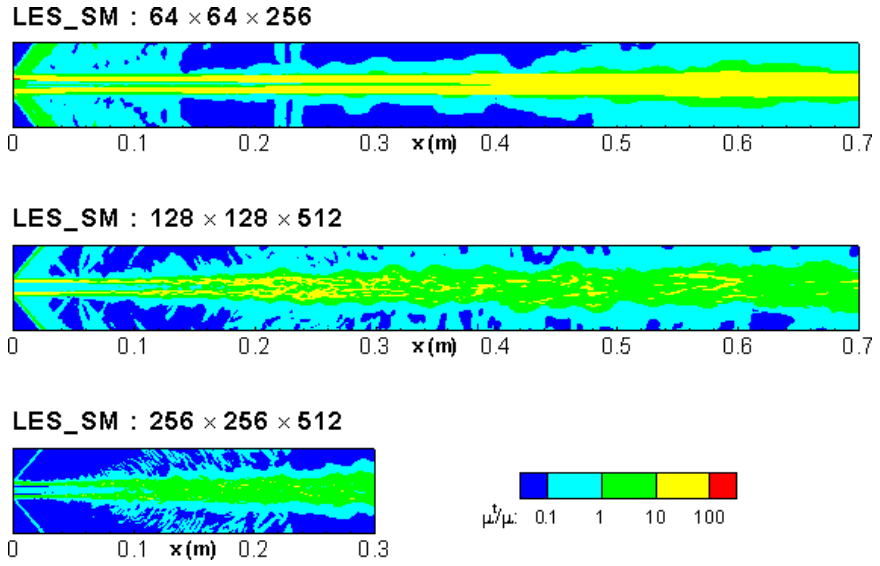

Figure 5.31: Eddy-viscosity ratio, LES_SM.

the models are very pronounced in both LES_SM and LES_SSF. The effect of the laminarity sensor (3.67) in the SSF model is apparent, and the model is globally less dissipative than the Smagorinsky model, although instantaneous and local peak values may be higher. At the highest resolution 256×256×512, the SM model is still active whereas the SSF model is almost vanished. Although the DNS limit is far from being reached as the ratio of minimum grid spacing to Taylor microscale is 6 (Table 5.1.2). This means that the numerical dissipation of the WENO scheme is responsible for most of the sub-grid modeling on the finer grid.

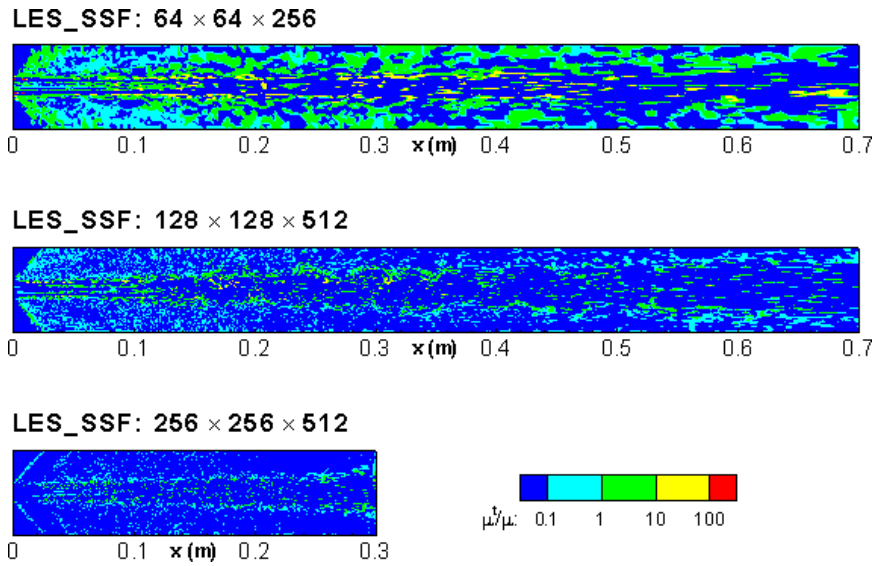

Figure 5.32: Eddy-viscosity ratio, LES_SSF.

5.1.7 CONCLUSIONS

The main conclusion for this non-reacting test-case is that conventional LES does not show any superiority compared to MILES. The Smagorinsky model deteriorates the results due to its over-dissipative behavior. The SSF model is less dissipative, but does not improve the results, whatever the grid resolution is. MILES_EULER and MILES_NS give almost similar results, the molecular dissipation being far below the numerical one. This means that the computational effort involved in highly accurate transport models is simply wasted, when shock capturing schemes are used to solve the compressible Navier-Stokes equations. The results of MILES_EULER surprisingly seem to show grid convergence toward the experimental data although no physical cutoff is present in the simulation. This is an open question for further research.

5.2 REACTING CASE

5.2.1 TEST CASE DESCRIPTION

Having investigated the mixing problem of a compressible H_2/air jet, the experimental results from LAERTE combustion chamber of ONERA [50, 86] are chosen as the reacting flow test case. This test facility is designed for the fundamental study of supersonic combustion and is intended to develop background data material on hypersonic air-breathing propulsion.

The experimental setup consists of;

- an initial section of the air pre-heater and the supersonic air nozzle for co-flow,
- the supersonic injector for nitrogen or fuel (H_2),
- the combustion chamber.

A sketch demonstrating the setup is given in Figure 5.33.

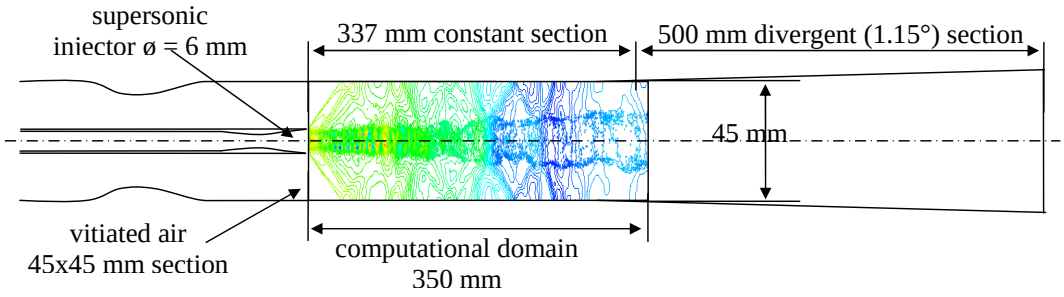

Figure 5.33: Schema of the LAERTE experiment.

Co-flowing air is first heated by a primary heater up to 850 K then a secondary hydrogen flame heater is used to elevate the temperature up to 1850 K. Before entering into the chamber, the co-flow is enriched with oxygen to the atmospheric concentration (%21). The supersonic air nozzle accelerates the flow to Mach 2. The vitiation of the co-flow with water, by the flame heater, is around %16 (molar fraction). Total flow rate of vitiated air is 0.65 kg/s and the static pressure is around 80 kPa. Hydrogen is injected through a round supersonic injector of inner and outer diameters of 6 mm and 10 mm, respectively. The fuel flow rate is 6.2 g/s at Mach 2 and the static pressure is also around 80 kP. The combustion chamber starts with a 45x45 mm

constant section part of 370 mm then the section diverges at an angle of 1.15° equal at upper and lower surfaces for 500 mm along the axis. Optical access is provided on the sides of the chamber using silica windows for measurements.

Since the injector and the air nozzle are subject to elevated temperatures, they are cooled with water. The experiment can be conducted for short durations at the order of seconds (15 s for H_2 combustion [22]).

Available experimental results which are obtained within the combustion chamber are listed below [19]:

- pressure measurements are taken at different axial locations on both upper and lower wall surfaces.
- radial temperature profiles are measured at at x = 10mm, x = 72mm, x = 210mm and x = 288mm.
- radial OH concentration distribution is measured by planar laser induced florescence (PLIF) technique at x = 210mm.
- velocity measurements are taken applying LDA or PIV methods at x = 10mm, x = 210mm and x = 288mm.
- the ignition position is reported to be roughly at x = 17cm

The data available are shown in Figure 5.34. In the present study, only the first constant

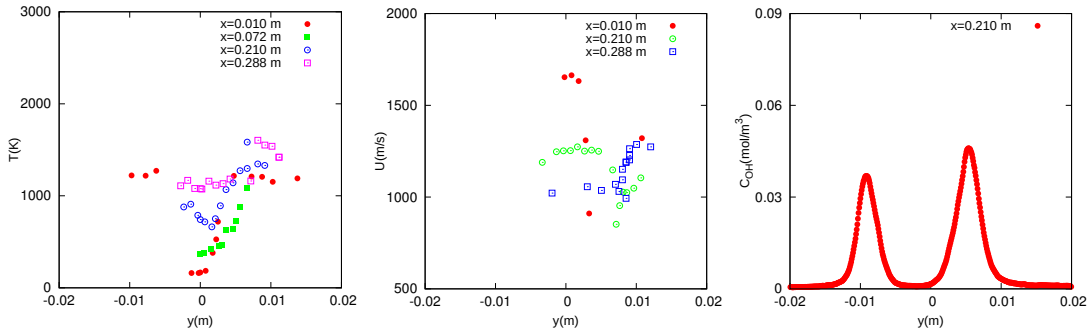

Figure 5.34: Experimental data available. From left to right: temperature, velocity and OH molar concentration.

section part is simulated.

Computations are performed over a domain with the dimensions 45×45×350 mm^3. The domain is the section of the combustion chamber located after the end of hydrogen injector. The following assumptions are applied on the computational domain for the sake of simplicity.

- Slip wall (symmetric) boundary conditions are applied on the sides of the domain, to avoid the necessity of resolving wall boundary layers.
- Divergent section at the last 13 mm of the computational domain is not considered.

The purpose is not to reproduce strictly the experimental data numerically, so simplifications are applied despite their significant effect.

5.2.2 INLET FIELD

There exists no detailed quantitative experimental flow field measurement at the inlet. It is reasonable to fit a hyperbolic tangent profile for the velocity of the pure hydrogen injection that satisfies the mass flow rate measurement. However, the initial field of variables for the co-flow, especially the species mass fractions are not easy to predict. Davidenko simulated the hydrogen heater and the co-flow nozzle in his work in order to generate inlet BCs for the combustion chamber problem [22]. 1D profiles (Figure 5.35) for the radial distribution of the primitive variables, at the inlet of the combustion chamber are taken from these solutions.

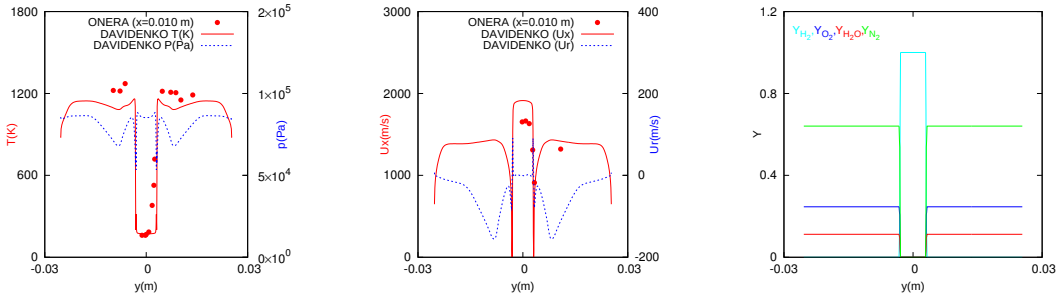

Figure 5.35: Initial field data taken from RANS solutions Davidenko [22]; from left to right radial profiles for temperature, velocity and species concentrations.

This RANS simulation was conducted with the initial flow composition of 0.542 kg/s air, 0.1 kg/s O_2 and 8 g/s H_2 at total temperature of 850 K at the inlet of the hydrogen heater. Calculated profiles by Davidenko for the inlet field are in good agreement with the total temperature

data measured very near the inlet, located at x=10 mm (shown in Figure 5.35). Also, the estimated co-flow inlet oxygen concentration is at atmospheric level (%21), showing agreement with reported experimental data [24]. Therefore, it is assumed that the inlet conditions applied in this secttion are adequate.

Two set of initial fields are deduced from the results of Davidenko. The simulations with first simple profile intended to the comparison of numerical approaches. The second inlet profile is more complex, including the radial velocity and pressure profiles. These complexities induce strong shocks within the flow which are reflected at the walls and affect the flowfield. Sensitivity of the solution to the inlet field conditions is investigated with this improved inlet.

5.2.2.1 SIMPLE PROFILE

Using a simplified initial field is generated fitting hyperbolic tangent profiles over the given initial conditions, (equation 5.6) similar to the Eggers jet. The walls are subject to sudden

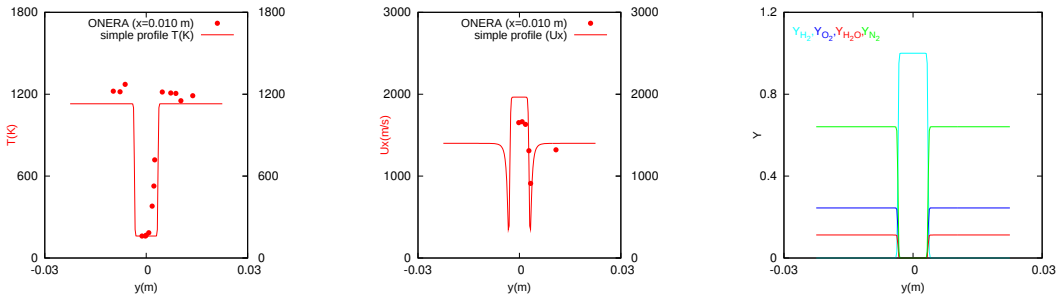

Figure 5.36: Simplified initial field data deduced from RANS solutions by Davidenko [22]; from left to right radial profiles for temperature, velocity and species concentrations.

temperature change and also the wall boundary layer can have significant effect on the flow inside. Therefore, Davidenko applied various conditions for the walls. The profiles considered in this study are corresponding to adiabatic wall boundary conditions for the cooled nozzle and hydrogen injector. However, to be able to include wall effects a high resolution is necessary around such flow domain. As an alternative, symmetric boundary conditions are applied on wall at low resolution and the velocity gradients at the wall boundaries are removed. As such, the profiles are modified to be normal at the wall boundaries. Also, the radial component of the velocity and the pressure profiles which lead to strong shock patterns are neglected. This also allows to single out the analysis of turbulent flame without occurrence of shock

turbulence interaction effects.

The simple profiles of temperature, velocity and species concentrations (except radicals) are shown in Figure 5.36. The chemical composition of the vitiated air co-flow also includes radicals (not shown in Figure 5.36) : Y_{OH}=2.285×10^{-4}, Y_O=1.8×10^{-4} which have an important effect on ignition.

The coefficients for hyperbolic tangent profiles used in equation 5.6 for the jet and the co-flow are given in Table 5.6. In the Figure 5.37, the jet core region inlet velocity profiles are shown with different resolutions. The shear layer is shown to be highly resolved especially with the fine grid.

Table 5.6: LAERTE inlet hyperbolic tangent profile coefficients for equation 5.6.

var:	U_{jet}	$U_{co-flow}$	Y_{air}
$f_{\max}$	1970	1400	1
A	9	0.8	12
B	10	0.75	1
C	10	-1.33	-1.11
D	1	-1	0
E	1	-1	-1

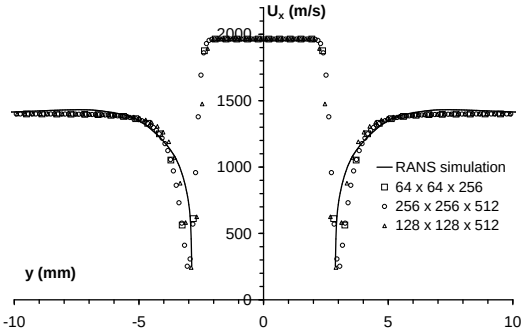

Figure 5.37: Inlet velocity profile for the reacting air/H_2 LAERTE jet.

5.2.2.2 IMPROVED PROFILE

The simulations are conducted with more realistic conditions that also include radial velocity and pressure profiles at the inlet. These additional profiles generate strong shocks through the flow. The resolution of the wall shear layer is not tractable even with the fine grid spacing so the velocity decay on the walls is not included in these simulations. The additional radial flow field and pressure profiles computed by Davidenko normal to the axis of the jet is shown on the set of Figures 5.38. The concentrations of the radicals (not shown in the Figure) in the co-flow are taken to be: Y_{OH}=2.285×10^{-4}, Y_O=1.8×10^{-5} and Y_H = 8.2 ×10^{-7}.

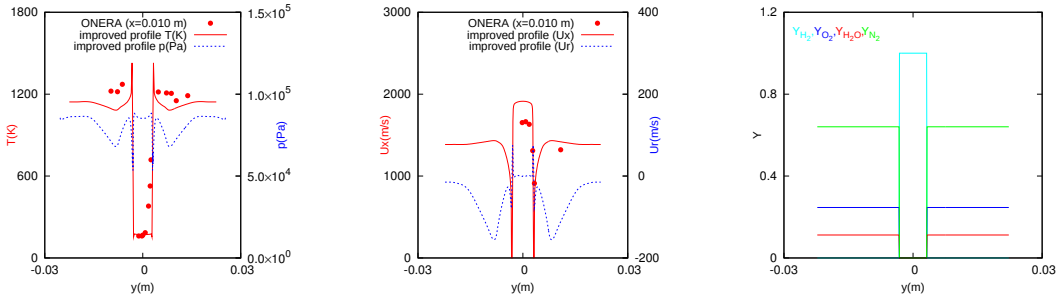

Figure 5.38: Initial field data deduced from Davidenko RANS solutions [22] including shock patterns at inlet; from left to right radial profiles for temperature, velocity and species concentrations

5.2.3 NUMERICAL PARAMETERS

5.2.3.1 FLOW PARAMETERS

The flow conditions at the inlet of the chamber are summarized in Table 5.7.

Table 5.7: LAERTE experimental conditions.

	H_2 jet	air co-flow
U (m/s)	**1970**	**1336**
T_{stat}/T_{tot} (K)	**160/300**	**1200/1850**
P_{stat}/P_{tot} (kPa)	**80/680**	**80/720**
Mach	**2**	**2**
$\dot{q}$ (g/s)	**6.2**	**650**
μ (kg.m^{-1}.s^{-1})	0.729 10^{-5}	0.729 10^{-5}
ρ(kg.m^{-3}	0.104	0.283
Re_{jet}	2.05 10^5	
M_c	0.39	

The variables that are written in bold are taken from experiments while the remaining ones are calculated.

5.2.3.2 SPATIAL PARAMETERS

Grid resolutions are 64×64×256, 128×128×512 and 256×256×1024 with the same clustering characteristics of grid nodes as for the Eggers jet (equation (4.53)). The size of the smallest cell for the fine grid is $\Delta x_{min} = 0.216$ mm and $\Delta y_{min} = \Delta z_{min} = 0.110$ mm. Assuming the size of the large scales to be approximately 5 mm in the mixing region, a calculation similar to equation (5.5) gives $Re_{(\Delta U/2,\, \delta)} \approx 1300$, a Kolmogorov scale $\eta \approx 0.023$ mm and a Taylor micro-scale $\lambda \approx 0.14$ mm. The resolution characteristics for all grids are listed in Table 5.8. Comparing non-reacting Eggers and reacting LAERTE test cases, it is seen that the flow field is more resolved for reacting test case on the fine grids.

Table 5.8: Ratios of approximate Taylor micro-scale and Kolmogorov scale to the minimum grid spacing.

Grid	Δx_{min}	Δy_{min}	Δ/η	Δ/λ
64×64×256	0.865×10^{-2}	0.450×10^{-3}	20	3.2
128×128×512	0.430×10^{-3}	0.223×10^{-3}	10	1.6
256×256×512	0.226×10^{-3}	0.110×10^{-3}	5	0.8

5.2.3.3 TIME PARAMETERS

The chemical source terms are non-linear, so that it is not possible to deduce analytical restriction for time step. The maximum time step constraint Δt_{chem} is validated by numerical 0D tests. Since the current problem is in more or less atmospheric conditions, it is proper to conduct the tests for constant pressure ($dp/dt = 0$). Time derivative of pressure is related to the enthalpy

$$\rho \frac{dh}{dt} = \frac{dp}{dt} \tag{5.13}$$

When the enthalpy is written explicitly, it yields

$$\rho C_p \frac{\partial T}{\partial t} = -\sum_{\alpha=1}^{N_{sp}} \left(\Delta h_\alpha^0 + \int_{T_0}^{T} C p_\alpha(\theta) d\theta \right) \dot{\omega}_\alpha \tag{5.14}$$

0D tests are conducted by iterating the time step for pure stoichiometric and vitiated stoichiometric (Y_{H_2O}=0.1124) mixtures. Initial pressure and temperature values are taken to be

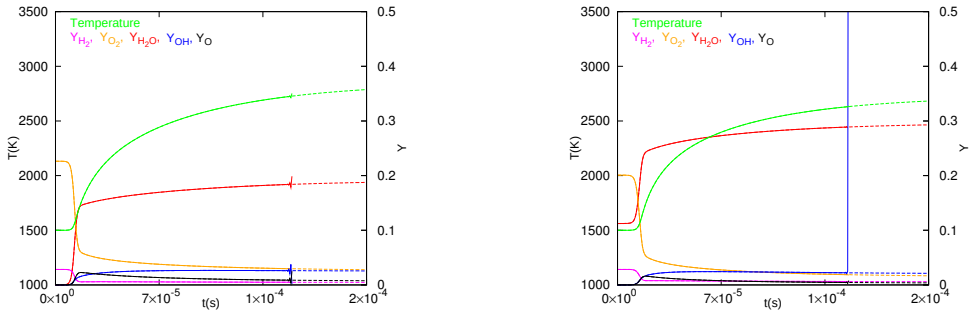

Figure 5.39: 0D constant pressure tests for stoichiometric H_2/air (left) and stoichiometric vitiated H_2/air (right) mixtures. The dashed lines refer to the stable solutions and the solid lines to the unstable ones.

respectively 80 kPa and 1500 K. Third order Runge-Kutta method is applied for time integration. The variation of temperature and species mass fractions are shown in Figure 5.39 s.

The dashed lines refer to stable solutions. The solid lines refer to the unstable solutions. The maximum time step for both pure and vitiated H_2-air mixtures is Δt_{chem} =1.3×10^{-7}.

However, the 0D calculations with constant volume conditions are more severe than constant pressure. Also, it is more representative of the flow enclosed with walls including pressure jumps due to shocks. 0D constant volume ($dv/dt = 0$) conditions refer to constant energy condition

$$\frac{dv}{dt} = 0 \quad \Rightarrow \quad \frac{de}{dt} = 0 \tag{5.15}$$

When the enthalpy is written explicitly, it yields

$$\rho C v \frac{dT}{dt} = -\sum_{\alpha=1}^{N_{sp}} \left(\Delta h_\alpha^0 + \int_{T_0}^{T} C p_\alpha(\theta) d\theta - \frac{RT}{M_\alpha} \right) \dot{\omega}_\alpha \tag{5.16}$$

0D constant volume tests (Figure 5.40) are conducted with the same conditions of constant pressure tests. Both constant volume computations for stoichiometric H_2/air (left) and stoichiometric vitiated H_2/air (right) mixtures are stable with the maximum time step constraint of Δt_{chem} =0.6×10^{-7} s. Considering that Δt_{chem} reduces by increasing initial pressure and

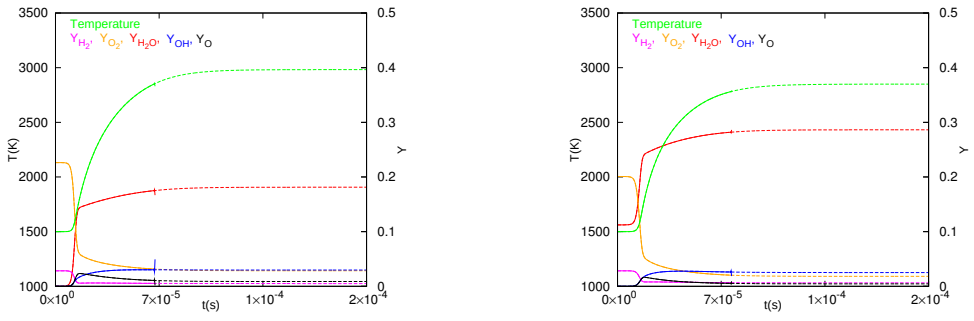

Figure 5.40: 0D constant volume tests for stoichiometric H_2/air (left) and stoichiometric vitiated H_2/air (right) mixtures. The dashed lines refer to the stable solutions and the solid lines to the unstable one.

temperature, the chemical constraint for time step is chosen to be Δt_{chem} =0.2×10^{-7} s [58]. In application, at high resolution of 256×256×1024, Δt_{hydro} which is computed out of CFL condition, is less than the chemical time step limit.

5.2.4 RESULTS

5.2.4.1 RESULTS FOR SIMPLE INLET PROFILE

The LAERTE chamber simulation results, with the simple inlet field (section 5.2.2.1), are presented in this section. In summary, the inlet radial velocity and the inlet pressure profiles, estimated numerically by Davidenko for the experiment, are not applied for the simulations that are presented here. All the inlet profiles are smoothed and mass fraction of the radical O is taken to be more than the numerical estimations by one order. Because of poor performance of Smagorinsky model in non-reacting case, only LES_SSF, MILES_NS and MILES_EULER are considered.

5.2.4.1.1 FLAME STRUCTURE

The flame structure is analyzed from the fuel/oxidizer mixture fraction

$$z = \frac{Z - Z^{\text{co-flow}}}{Z^{\text{jet}} - Z^{\text{co-flow}}} \tag{5.17}$$

$$Z = sY_{H_2} - Y_{O_2} \tag{5.18}$$

Z is the first of the three Schwab-Zeldovitch variables for a single-step reaction (e.g. [104] p.84), and $s = Y_{O_2}/Y_{H_2}|_{st} = 8$ is the mass stoichiometric ratio for the H_2/O_2 chemistry. Hence, in the pure H_2 central jet

$$Y_{H_2}^{\text{jet}} = 1 \quad ; \quad Y_{O_2}^{\text{jet}} = 0 \quad ; \quad Z^{\text{jet}} = s = 8 \quad ; \quad z = 1 \tag{5.19}$$

and in the vitiated air co-flow

$$Y_{H_2}^{\text{co-flow}} = 0 \quad ; \quad Y_{O_2}^{\text{co-flow}} = 0.2447 \quad ; \quad Z^{\text{co-flow}} = -Y_{O_2}^{\text{co-flow}} \quad ; \quad z = 0 \tag{5.20}$$

Introducing boundary conditions (5.19)(5.20) for Z in equation 5.17, and making use of the flame equivalence ratio ϕ_0 yields

$$\phi_0 = s\frac{Y_{H_2}^{\text{jet}}}{Y_{O_2}^{\text{co-flow}}} = 32.69 \tag{5.21}$$

z obtained by mixing the same amount mass of fluid taken in the fuel stream and in the oxidizer stream with incorporated equation 5.17 becomes

$$z = \frac{s\left(Y_{H_2}/Y_{O_2}^{\text{co-flow}}\right) - \left(Y_{O_2}/Y_{O_2}^{\text{co-flow}}\right) + 1}{1 + \phi_0} \tag{5.22}$$

The flame front is supposed to be where $Y_{H_2} = Y_{O_2} = 0$, i.e. at stoichiometric locations where

$$z_{st} = \frac{1}{1 + \phi_0} = 0.0297 \tag{5.23}$$

This value follows from the assumption of a unitary Lewis number in both fuel and oxidizer streams.

The distribution of fuel/oxidizer mixture fraction is showing over 128×128×512 resolution MILES_NS solution data to have an idea of the distribution, in Figure 5.41. In Figures 5.42-

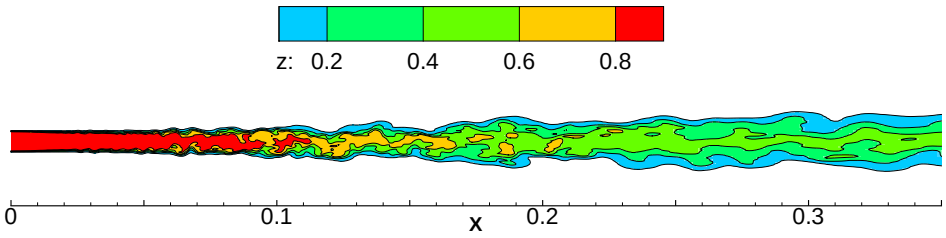

Figure 5.41: Fuel/oxidizer mixture fraction distribution.

5.44, 3D instantaneous iso-surface of the mixture fraction (z_{st}) at the stoichiometric value are plotted for LES_SSF, MILES_NS and MILES_EULER on different grid resolutions. The mixture fraction definition given in equation 5.22 is derived for one-step infinitely fast chemistry. When finite rate chemistry is considered, other passive scalar derivations may be constructed using

- the atomic mass fractions [6, 7]

$$z = \frac{0.5(\mathrm{Z}_H - \mathrm{Z}_{H,O_x})/W_H - (\mathrm{Z}_O - \mathrm{Z}_{O,O_x})}{0.5(\mathrm{Z}_{H,f} - \mathrm{Z}_{H,O_x})/W_H - (\mathrm{Z}_{O,f} - \mathrm{Z}_{O,O_x})/WO} \tag{5.24}$$

  where Z is the elemental mass fraction

- the mass fraction of an inert species, if there exists any. In current study, N_2 is the inert species.

$$z = \frac{Y_{\mathrm{N}_2} - Y_{\mathrm{N}_2}\big|_{jet}}{Y_{\mathrm{N}_2}\big|_{co-flow} - Y_{\mathrm{N}_2}\big|_{jet}} \tag{5.25}$$

A lifted diffusion flame can then be traced using passive scalar definition based on atomic mass fractions (equation 5.24). However, since the co-flow includes combustion products,

equations 5.24, 5.25 and 5.41 are giving similar stoichiometric iso-surfaces at the shear layer. The first definition is (equation 5.22) kept for mixture fraction definition for visualization.

Vertical and horizontal contour maps are the projections of the instantaneous temperature field and water mass fractions in the corresponding symmetry planes, respectively.

Increasing the grid resolution produces a more wrinkled flame. But for a given resolution, there are apparently no major differences between LES and MILES. Some subtle differences are present however. The solution at coarse grid of 64×64×256 (Figure 5.42) is reasonable, even though the gradients at shear region of inlet profiles are poorly resolved. Although there is no molecular transport except for the numerical diffusion the MILES_EULER solution gives qualitatively similar results when compared to MILES_NS and LES_SSF. The flame region is designated as the warm color areas in the temperature and water mass fraction contour plots. It consists of a diffusion layer surrounding the reactive layer, embedded in the stoichiometric surface. The reactive layer at the jet/co-flow interface is wrinkled by large-scale turbulent eddies, which bring in contact reactants and mix them at the turbulent level. During that time, the finite-rate chemistry proceeds.

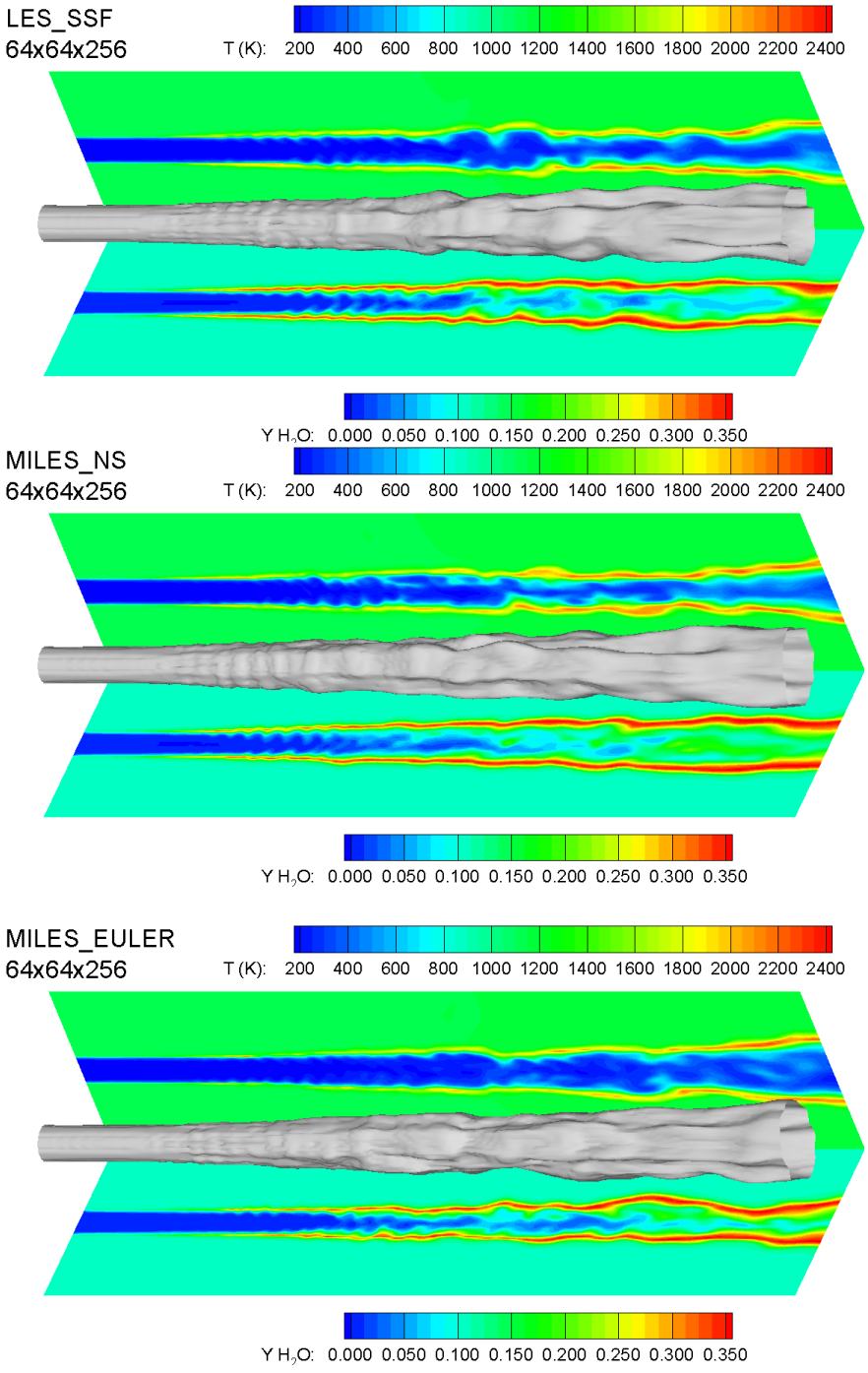

Figure 5.42: Instantaneous iso-surfaces of the stoichiometric mixture fraction, temperature contours and water mass fraction contours on the symmetry planes for 64×64×256 grid. From top to bottom : LES_SSF, MILES_NS, MILES_EULER.

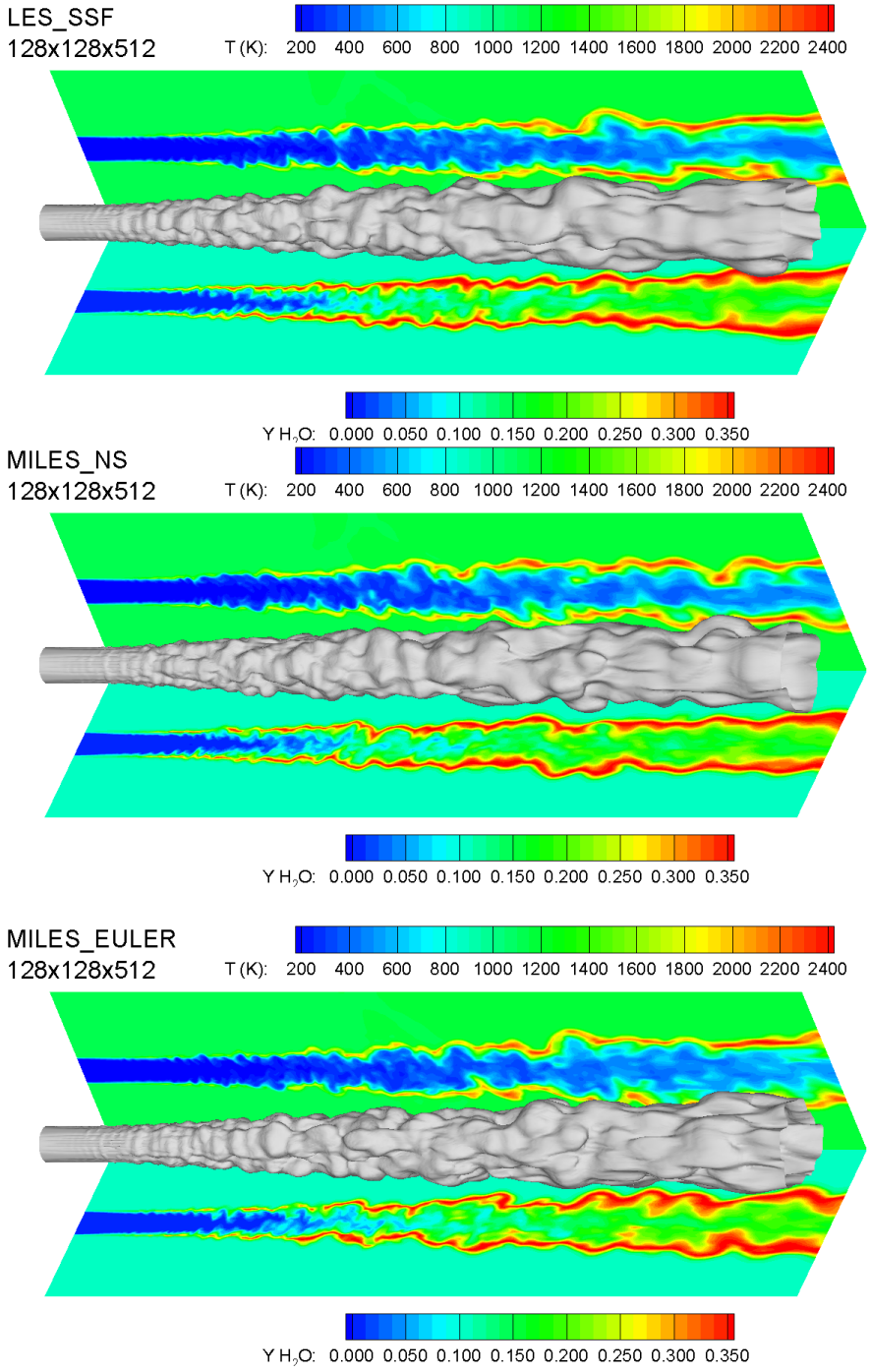

Figure 5.43: Instantaneous iso-surfaces of the stoichiometric mixture fraction, temperature contours and water mass fraction contours in the symmetry planes for 128×128×512 grid. From top to bottom : LES_SSF, MILES_NS, MILES_EULER.

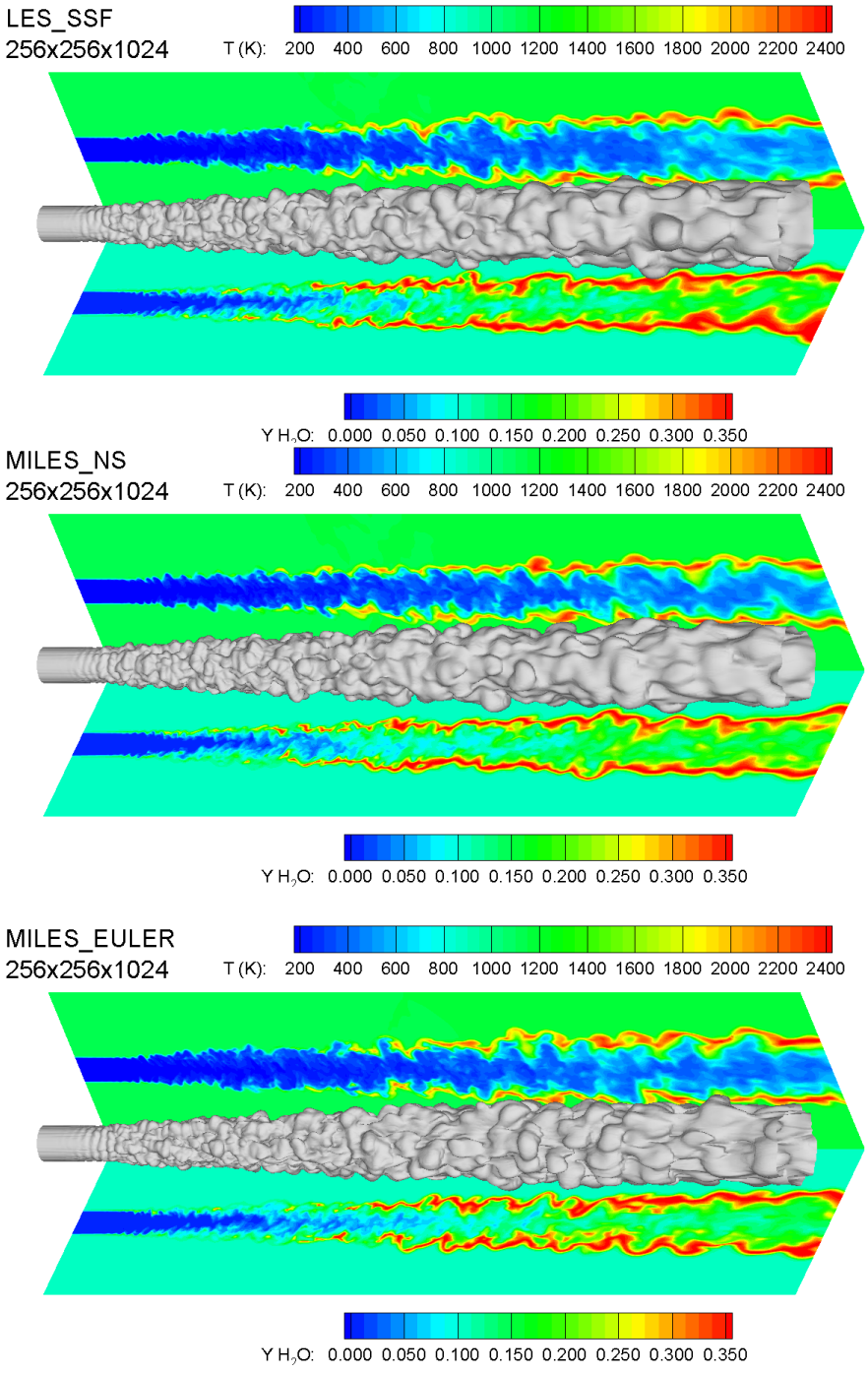

Figure 5.44: Instantaneous iso-surfaces of the stoichiometric mixture fraction, temperature contours and water mass fraction contours in the symmetry planes for 256×256×1024 grid. From top to bottom : LES_SSF, MILES_NS, MILES_EULER.

5.2.4.1.2 STATISTICAL RESULTS

In the MILES_NS 256×256×1024 simulation, the turbulent time scale can be estimated from Figure 5.45. The Figure shows the instantaneous distribution of U_x along two longitudinal lines one located on the jet axis (r=0 mm) and the other in the shear region (r=3.2 mm, wake of jet nozzle). At the end of the potential core, the turbulent length scale deduced from the mean distance between major peaks is about 1 cm or less. Applying the so-called Taylor hypothesis with a mean velocity of about 1500 m/s gives a turbulent time scale $\tau_t \approx 5.10^{-6}$ s. Figures 5.39 and 5.40 show the time evolution of the species mass fractions and the temperature in a premixed stoichiometric 0D air/H_2 flame at constant volume and at constant pressure conditions, respectively. In both cases the ignition delay is around 3.10^{-5}s, and the time for the reaction to complete is $\tau_c \approx 5.10^{-5}$s. Hence, there is a strong interaction between chemistry and turbulence in a thick flame region since the estimated the Damköhler number is around

$$\mathrm{Da} = \frac{\tau_t}{\tau_c} \approx 0.1 \tag{5.26}$$

As in the non-reacting case, the grid spacing is mostly influencing the amount of turbulent

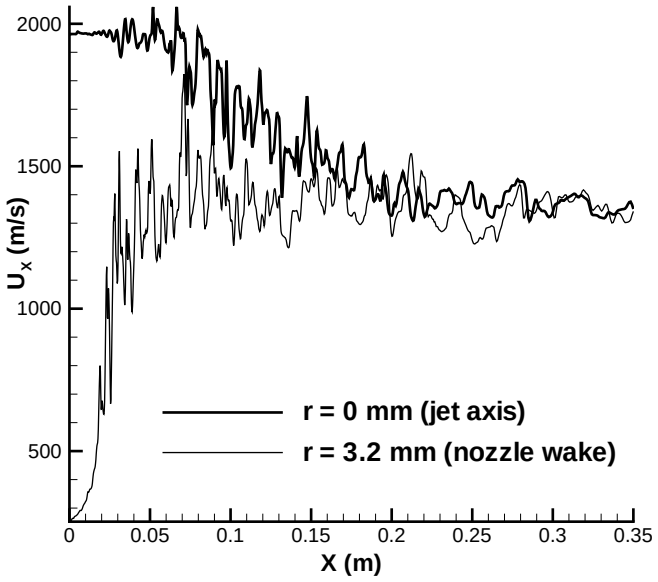

Figure 5.45: Instantaneous axial velocity component on the jet axis and in the main shear region. MILES_NS, 256×256×1024.

mixing. The finer is the grid spacing, the lower is the sub-grid scale dissipation. This is either present as numerical dissipation in MILES or numerical and explicit dissipation in LES.

Increased grid resolution also leads to more finer turbulent structures in the flow field. The residual numerical diffusion combines with molecular transport -except in MILES_EULER- to finally shape the mixture fraction across the diffusion layer and control the reaction rate.

Further insight can be gained from the scatter-plots of Figures 5.46 and 5.47. The most dissipative simulation is the top-left sub-figure and the less dissipative one is the bottom-right sub-figure. In the scatter plots the mixture fraction definition is chosen as the normalized nitrogen mass fraction (equation 5.25). In order to indicate the position of points on scatter plots relative to the flame front, color that represent an index related to the water concentration is used

$$c_{H_2O} = \left| \left(\frac{Y_{H_2O} - Y_{H_2O}\big|_{jet}}{Y_{H_2O}\big|_{\max} - Y_{H_2O}\big|_{jet}} \right) \left(\frac{Y_{H_2O} - Y_{H_2O}\big|_{co-flow}}{Y_{H_2O}\big|_{\max} - Y_{H_2O}\big|_{co-flow}} \right) \right| \tag{5.27}$$

c_{H_2O} is an index indicating the relative mass fraction of water which is the main product of chemical reactions. By definition c_{H_2O} takes the value 1 in the flame and 0 elsewhere. The points colored in green correspond to flow regions close to the flame front. Finite-rate, reversible full chemistry is clearly felt since the flame structure departs strongly from infinitely fast, irreversible one-step chemistry (straight lines). The temperature mixing line is curved and is below the theoretical linear mixing line (Figure 5.46). This is due to the cold hydrogen stream at 160K (see Table 5.7) which has a very high heat capacity (13200 J/kg.K at 160K) when compared to that of air (1170 J/kg.K at 1200K). The dark blue color points are at high mixture fraction region, indicate the initial core, far from the flame front. When hydrogen mixes with surrounding air, it takes heat from the oxidizer stream and lowers the mixture temperature below the self-ignition limit ($\approx$ 1000K at stoichiometry).

On the coarse grid (left columns of Figures 5.46 and 5.47), the flame structure is almost the same for all simulations. The points are clustered close to the equilibrium states, indicating a relatively fast chemistry compared to large-eddies turbulent time scale (higher Damköhler number). Few points are close to the mixing line at $z \approx z_{st}$ indicating "mixed is burned" behavior : the high level of numerical diffusion artificially brings reactants together at the molecular level and reactions are completed.

On the intermediate grid 128×128×512 (central columns), a stronger departure from irreversible infinitely fast chemistry is observed. Diagrams are more "filled" because turbulent mixing is more intense and the reactive mixture can be found in various intermediate states combining reactants and products, especially in LES_SSF due to the explicit sub-grid turbu-

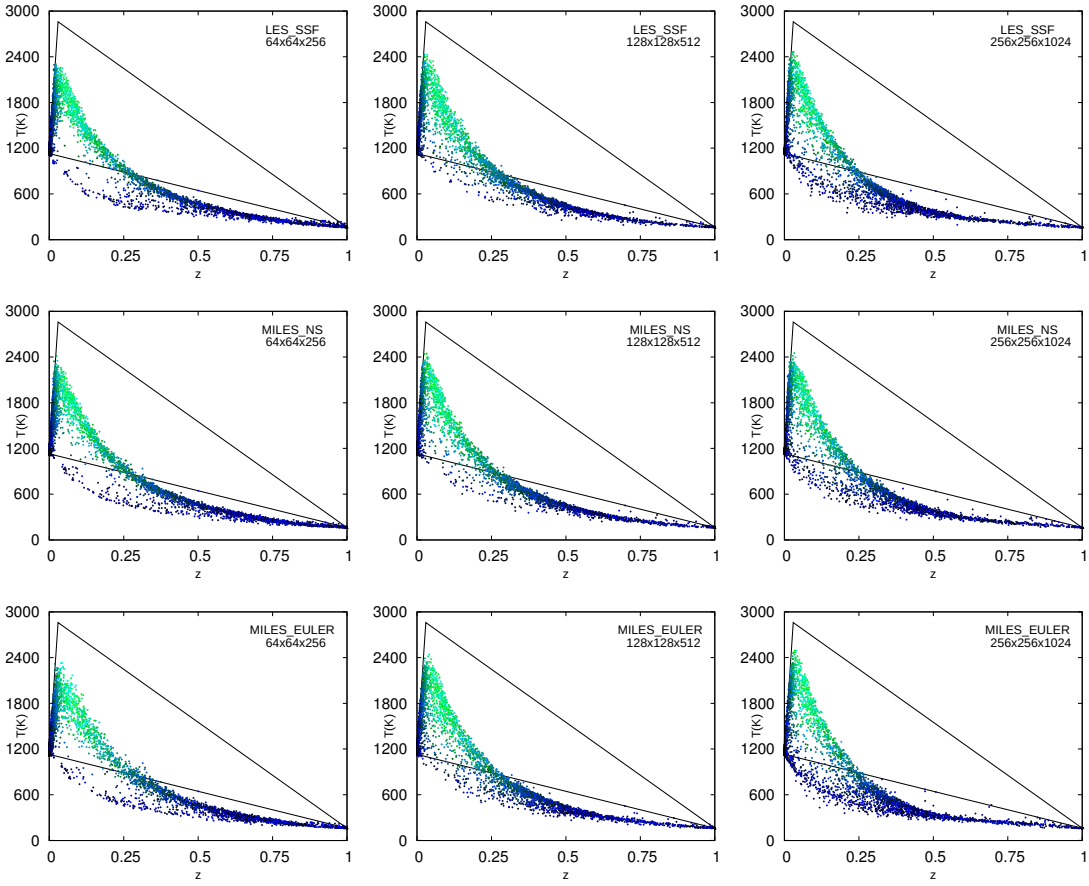

Figure 5.46: Scatter plots of temperature. Top to bottom : LES_SSF, MILES_NS, MILES_EULER. Left to right : 64×64×256, 128×128×512, 256×256×1024.

lent diffusion. More points can also be found near stoichiometry where reaction does not occur (high Y_{O_2}, low T) due to a "lack of time". Physical LES and MILES are close to each other indicating that the contributions of the explicit sub-grid model and the numerical diffusion in MILES are at the same level.

On the fine grid, the scatter plots for the flame are slightly different. More points can be found close the mixing lines, mainly in the H_2 stream ($z \rightarrow 1$) where O_2 is present without reaction, because of the low temperature. This is due to fast and efficient turbulent mixing relative to the chemistry. This is mainly true for the MILES_EULER simulation (bottom-right sub-figure in Figure 5.47) which differs clearly from LES_SSF and MILES_NS : the low level of numerical diffusion and the absence of viscous model restrict the small scale molecular mixing, hence the reaction rates are reduced.

The velocity, temperature and H_2 mass fractions of the average fields at the center line and

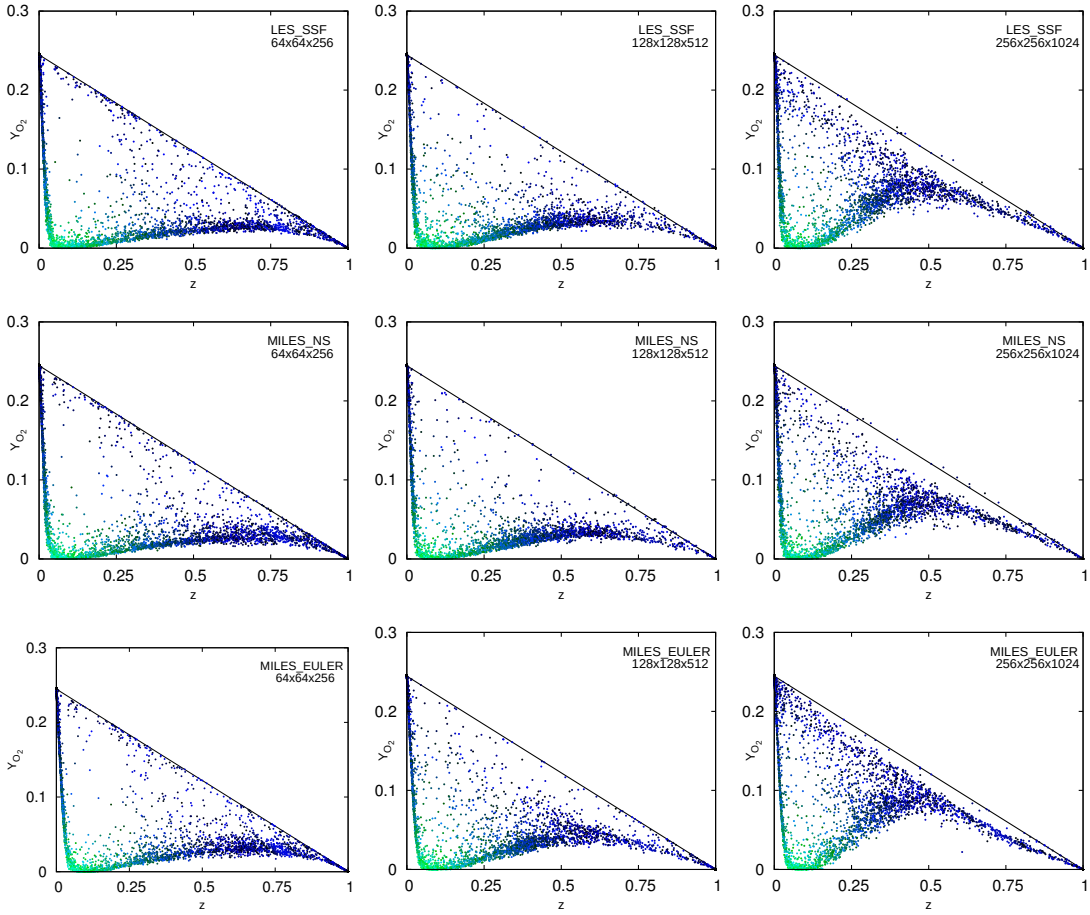

Figure 5.47: Scatter plots of O_2 mass fraction. Top to bottom : LES_SSF, MILES_NS, MILES_EULER. Left to right : 64×64×256, 128×128×512, 256×256×1024.

the maximum temperature value on transverse planes along *x* axis are plotted for different resolutions in Figure 5.48. The average profiles are approaching each other for high grid resolutions. Both velocity potential core and concentration potential core lengths are longer for low resolution of 64×64×512, regardless of numerical approach. At this initial region of the flow shear layer instabilities are mostly responsible of mixing and transition to turbulence. At low resolution since the sharp gradients are smoothed due to large amount of dissipation, transition and mixing are delayed. At low resolutions high level oscillations are noticed at the location where jet is entering the computational domain. This may be attributed to the sharpness of the oblique shock forming immediately around the inlet region. At the two higher resolutions potential core lengths for the solutions are the same (four sub-figures top right). The dynamics of the flow is resolved for 128×128×512 and higher resolution. Although the resolution is increased, the potential core length remains the same.

The maximum temperature distribution along the jet axis on the normal planes are plotted to denote the ignition location along the axis as the temperature jump (bottom sub-figures in 5.48). As the resolution is increased, the jump in the maximum temperature for MILES_EULER slightly deviates to an upstream axial position (bottom right sub-figure in 5.48). As diffusion is enhanced with molecular transport and physical LES, this jump can

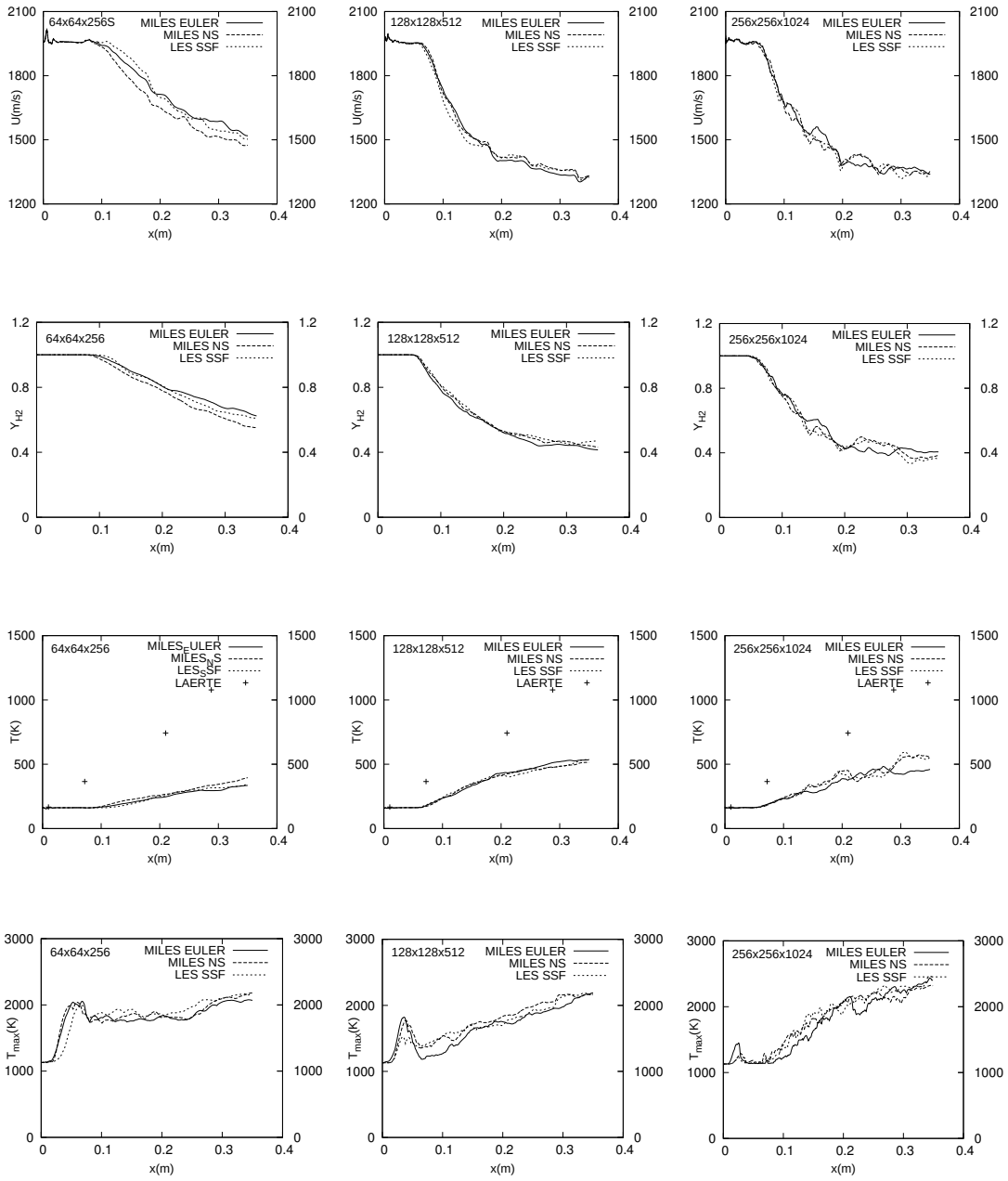

Figure 5.48: Average profiles of velocity, H_2 mass fraction and temperature at the center line of the jet and maximum temperature at the transverse sections along x axis. Left to right : 64×64×256, 128×128×512, 256×256×1024.

be expected to be earlier for MILES_NS and LES_SSF. However, further analysis shows that after the occurrence of ignition, the penetration of the high temperature zones associated with transverse diffusion is prevented by the cold hydrogen flow close to the inlet. Taking into account the fact that the molecular transport enhances cooling, the temperature jump rise along the axis is delayed. Temperature jumps for MILES_NS and LES_SSF are exactly at the same axial positions for all resolutions.

Radial profiles of axial velocity and temperature at $x = 210$ mm are shown in Figure 5.49, with experimental measurements of ONERA. For these measurements, temperature is obtained with CARS (Coherent Anti-Stokes Raman Scattering) and velocity with the LDA technique. The computed velocity that is overestimated compared to experiments, is probably because particles cannot follow perfectly the fast and low-density flow. Computations underestimate the mean experimental temperature in the center because the jet is flapping and the points of measurement are alternatively in the central jet or in the surrounding reaction zone. Also, the high temperature wall boundary layer which is not considered may lead temperature to increase in the actual flow.

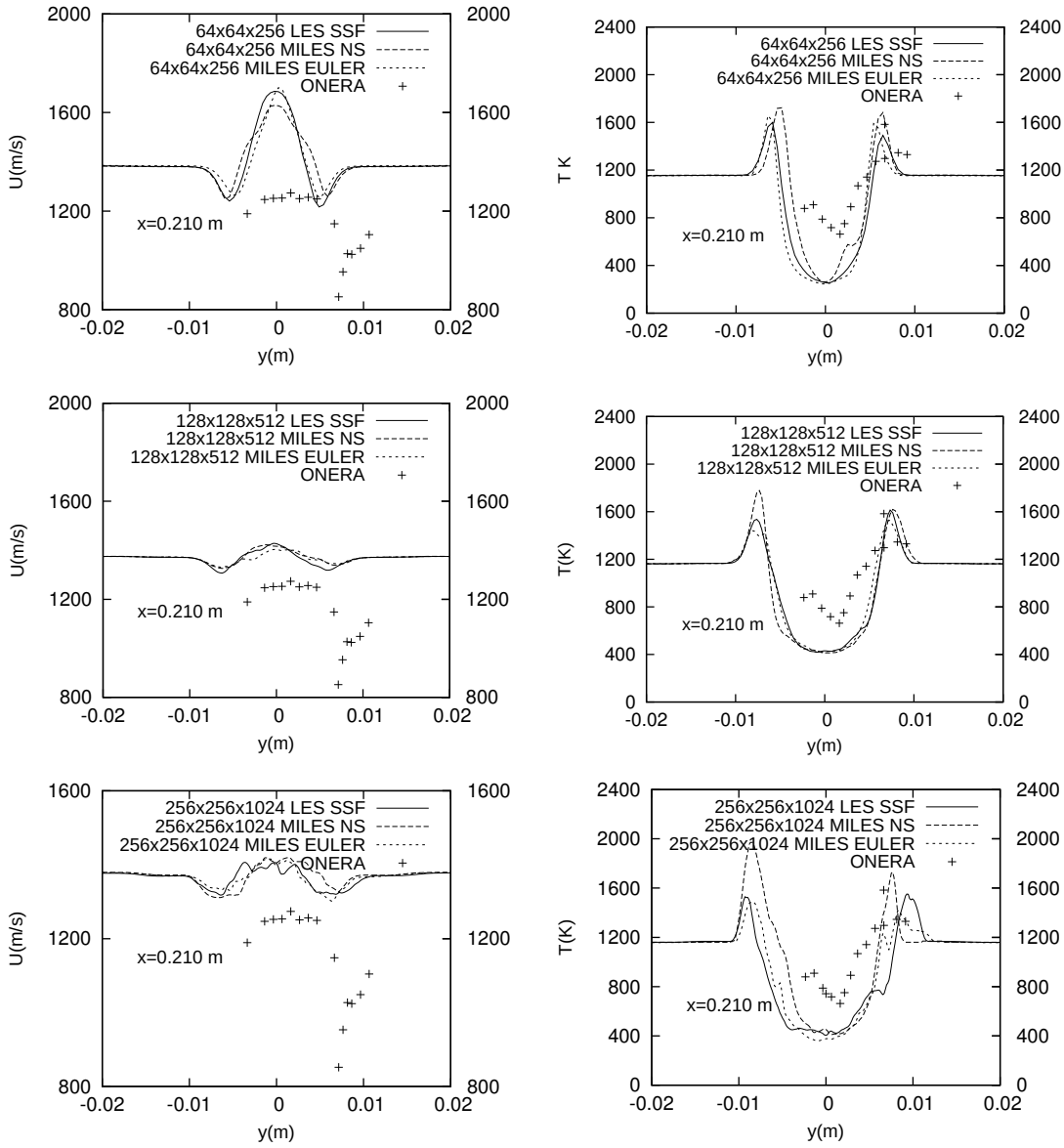

Figure 5.49: Tranverse profiles of axial velocity (left) and temperature (right) at $x = 210$ mm. Top to bottom : 64×64×256, 128×128×512, 256×256×1024.

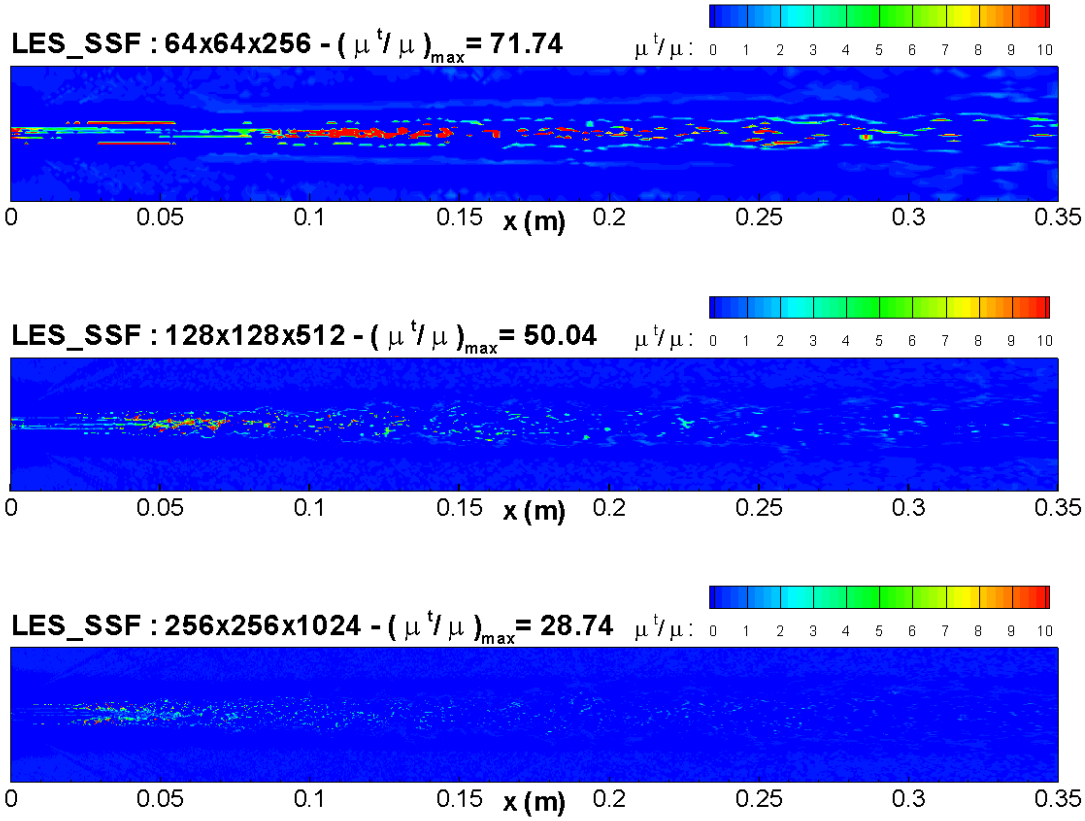

Figure 5.50: Eddy-viscosity, LES_SSF

Figure 5.50 displays the instantaneous distribution of sub-grid eddy-viscosity ratio μ_t/μ in the vertical symmetry plane, for the different resolutions. On the 256×256×1024 grid, the SSF model is barely active within the flame. The turbulent oscillations which emanate from the inlet noise clustered at the jet center are laminarized while passing through the flame surface. The SSF model is not active outside the flame.

5.2.4.2 RESULTS FOR IMPROVED INLET PROFILE

In the previous part the behavior of numerical approaches MILES and LES are investigated using a simplified initial field with weak shocks which is deduced from simulation results of Davidenko for the LAERTE chamber [22]. In this section, the improved inlet conditions explained in section 5.2.2.2 are applied. The inlet field is improved adding the pressure and radial velocity profiles calculated in the work by Davidenko. So that strong shock patterns which do emanate from the inlet are included in the solution. Also, the concentration of rad-

ical O is reduced to the level of numerical estimations by Davidenko whereas in previous section 5.2.4.1 O mass fraction were calculated as $(1 - \sum Y_{\alpha \neq \mathrm{O}})$. The effect of radical O mass fraction is showing itself as a late ignition. MILES_EULER and MILES_NS simulations are conducted at 128×128×512 and 256×256×1024 resolutions. LES_SSF simulation is not performed since it is shown that it converges to the same statistics with MILES_NS for reacting and non-reacting flows.

5.2.4.2.1 FLAME STRUCTURE

Flame structure for the LAERTE solution is shown as the mixture fraction stoichiometric value iso-surfaces together with temperature and water concentration contours on the corresponding symmetry axis, in Figure 5.51. When compared with the previous simulations of simple BCs (presented in section 5.2.4.1), MILES_EULER has larger structures especially in the second half of the computational domain. The MILES_ EULER solution is more wrinkled compared to the MILES_NS solution. Considering both temperature and water mass fraction contours, it is observed that ignition occurs at a later axial location as the radical O concentration in the co-flow is less than the value in previous simulations with a simplified initial field. Instantaneous pressure contours on the axis of the jet are shown on Figure 5.52. The resolved shock patterns are almost the same for both MILES_NS and MILES_EULER solutions. As the stoichiometric iso-surfaces are passing across the shock, the corresponding surface is contracted. Thin layers of quenching can be observed on temperature and water mass fraction contours which occur at these contraction regions.

When comparing medium and high resolution solutions, it is seen that ignition occurs at the same axial location. Higher temperatures occur after ignition. More pronounced quenching effect is also seen. This may be due to the increase in the sharpness of the shocks on the high resolution grid. The shock patterns for the medium and high resolution solutions look alike. Even though, in the solution on high resolution grid, much sharper shocks are resolved. As a result, the radial extent of higher pressure zones along the oblique shocks is increased. The turbulent structures in the first diamond shape shock structure near the inlet are also more pronounced and sharper.

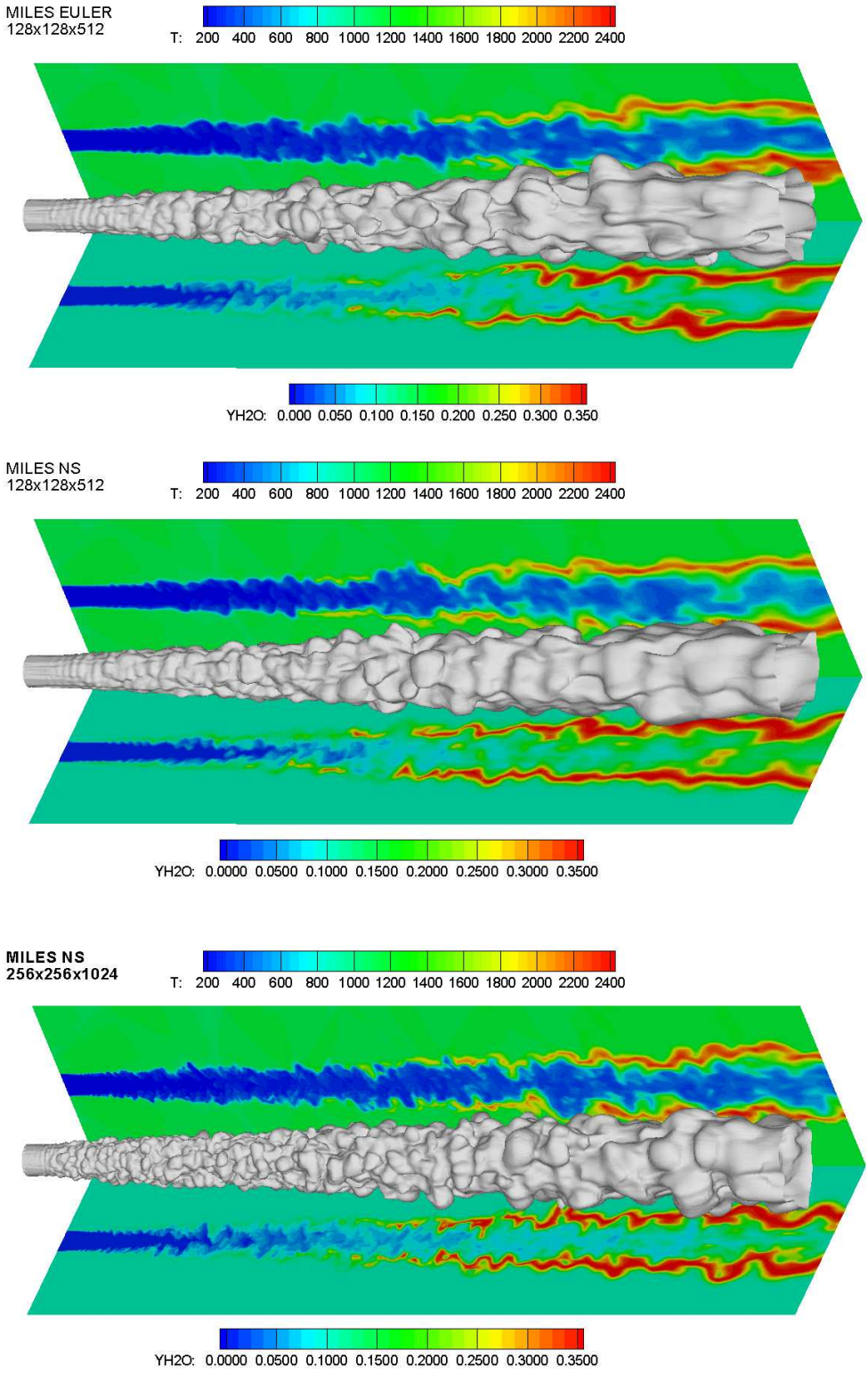

Figure 5.51: Flame structure of LAERTE chamber with precise initial field, including strong shock patterns.

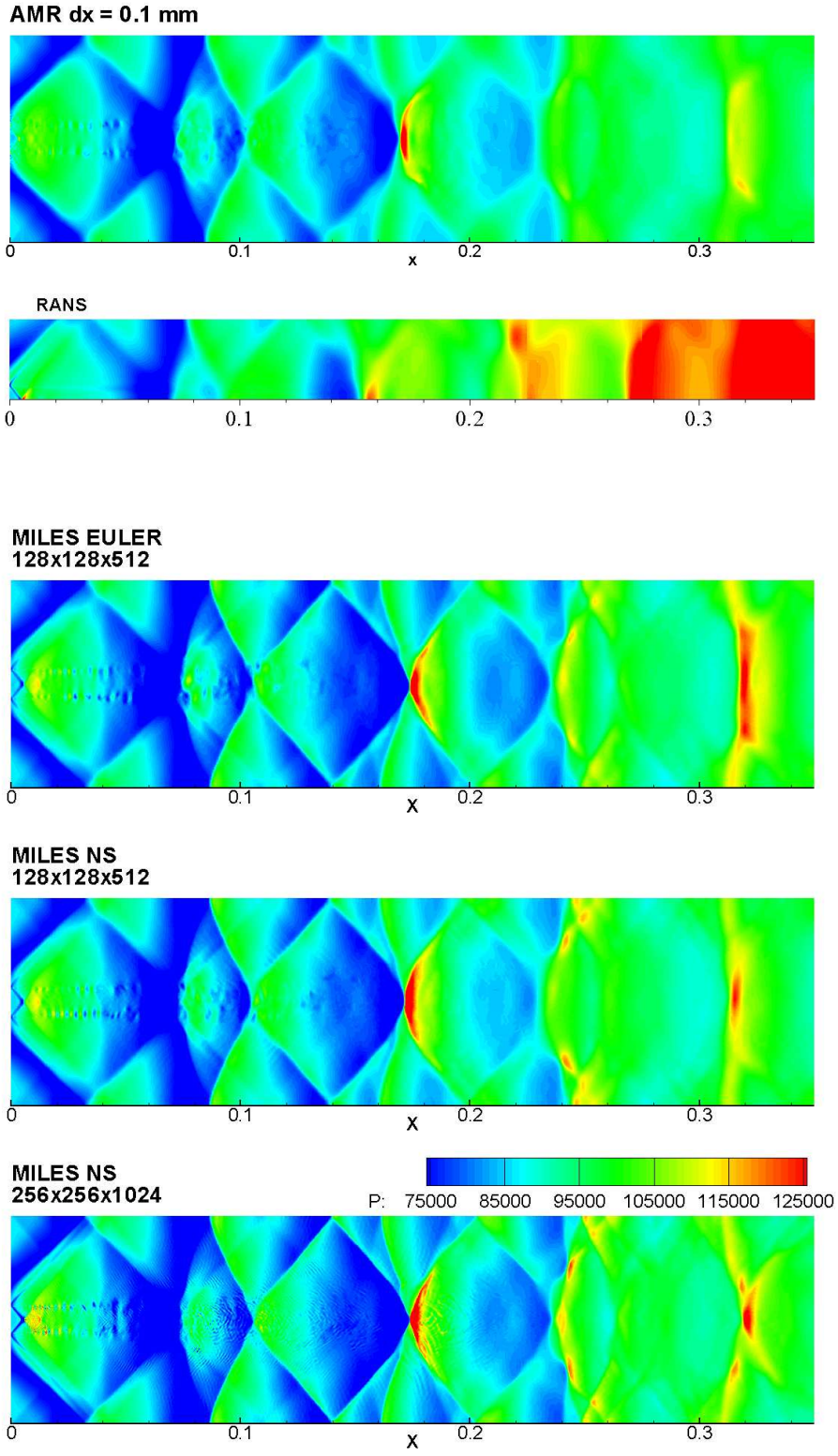

Figure 5.52: Pressure contours on the symmetry axis, of LAERTE chamber with precise initial field.

5.2.4.2.2 STATISTICAL RESULTS

The experimental pressure measurements over the chamber wall are compared with time averaged numerical results on Figure 5.53. The statistical results of these simulations are also compared to the numerical results obtained by RANS and adaptive mesh refinement (AMR) methods. The AMR simulation results are taken from Eude. Since wall boundaries are not considered in the MILES_NS and MILES_EULER computations, the experimental pressure growth is larger than that computed. As in RANS calculations these wall boundary conditions are considered, agreement with the experimental data is apparent. The experimental pressure growth is reasonably higher due to velocity decay on the boundaries. There exists quite good agreement in shock reflection positions despite the stretched grid at the boundaries.

In the Figure 5.54, maximum temperature distribution over YZ planes along the *x* axis is

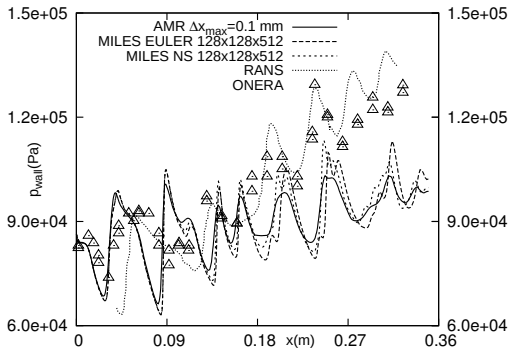

Figure 5.53: Wall pressure axial distribution numerical results and experimental data.

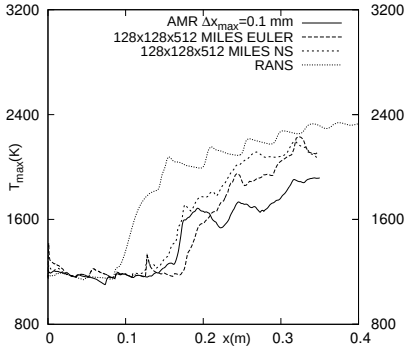

Figure 5.54: Maximum temperature distribution along the jet axis computed over normal planes.

shown. Although results of MILES_NS MILES_EULER and AMR are similar for pressure (Figure 5.53), they differ with each other for maximum temperature. The ignition location which is denoted as the temperature jump in this Figure 5.54, occurs earlier in MILES_NS solution. This delay is also observed in flame structure Figures. In the LAERTE experiment the ignition point is given roughly at 10 diameters along the axis form the jet entrance. This location is in good agreement with the axial temperature profile jump location computed by MILES_EULER MILES_NS and AMR methods.

The radial distribution of OH molar concentration measurements are compared with the numerical results in Figure 5.55. Both AMR and MILES solutions give quantitatively good agreement with the experimental results. On the other hand RANS simulation results overestimate OH concentrations.

Both transverse velocity and temperature distributions at different axial locations on the sym-

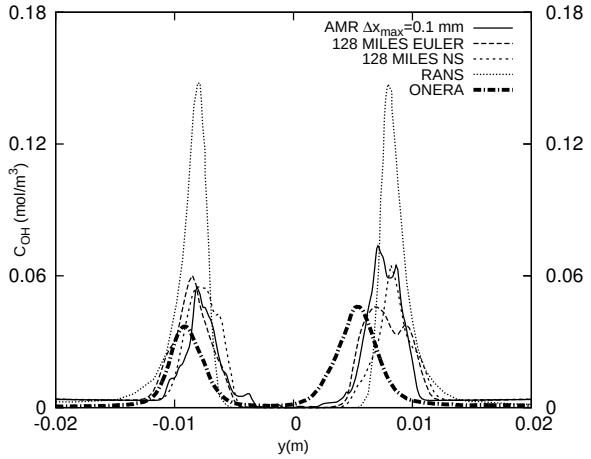

Figure 5.55: Transverse OH concentration profiles at x=0.21 m along the axis.

metry axis of the domain are shown on Figure 5.56. At the far-field (x = 288 mm) both set of results deviate from the experimental measurements. This may be attributed at the neglect of the temperature and the velocity gradients near the wall. Furthermore, there may exist some errors in the measurements due to flame flapping and insufficient transport of PIV particles in low density flows. When comparing Figure 5.49 (simplified inlet field) and Figure 5.56 it is seen that transverse profiles of average temperature and velocity are not much affected at the far-field by the change of inlet field conditions. Despite the reduced scalar concentration (Y_O) and radial inlet pressure and velocity profiles which generate strong shocks, the transverse profiles are identical to the results of the previous section.

5.2.5 CONCLUSIONS

In this section, reacting tests conducted for the LAERTE chamber, are simulated. At first, a simplified initial field is used for the comparative evaluation of the numerical approaches. Later, a more precise initial condition is applied in order to enhance flow physics. In conclu-

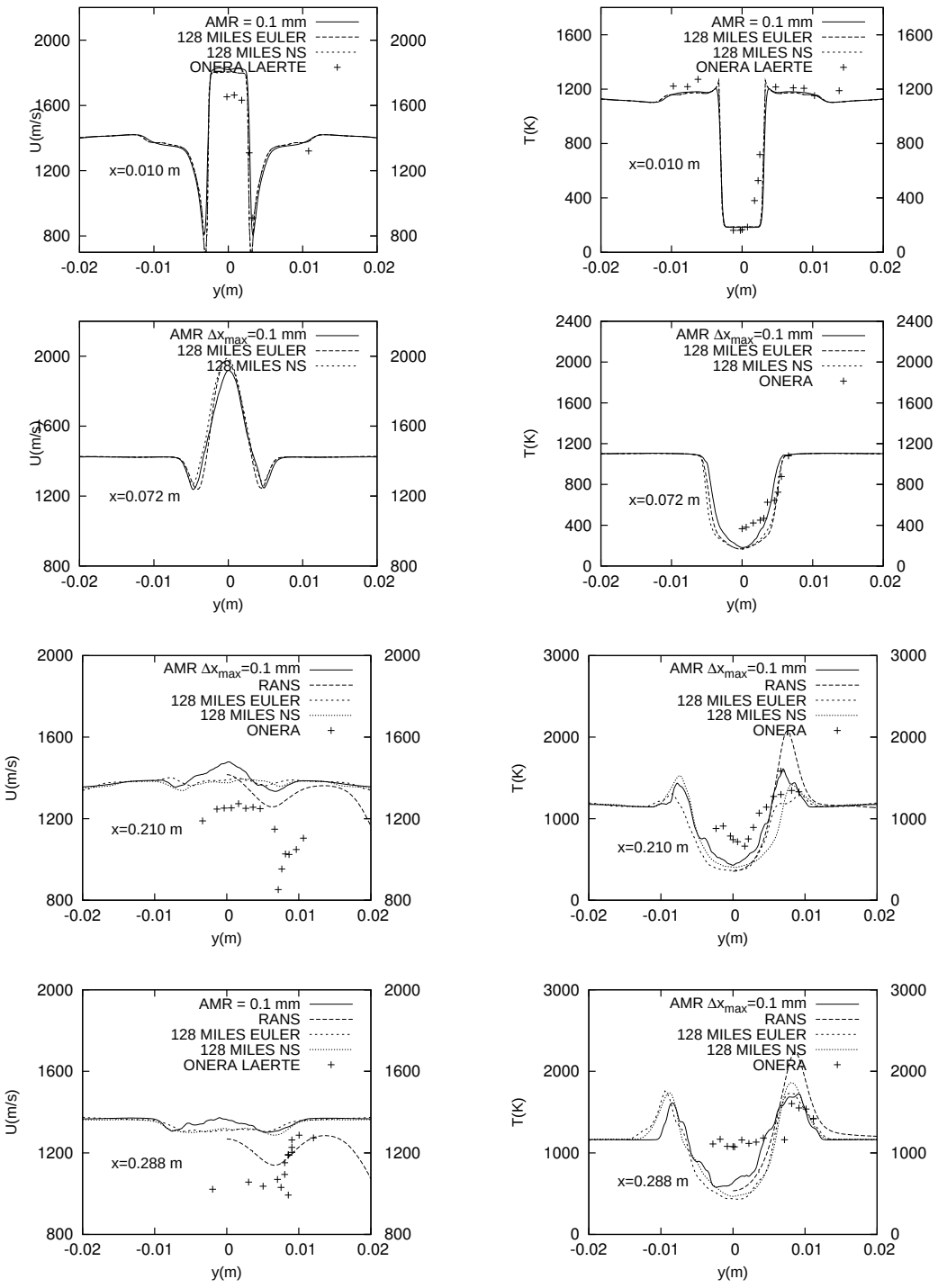

Figure 5.56: Experimental transverse profiles of axial velocity (left) and temperature (right) at x=10 mm, x=72 mm, x=210 mm and x=288 mm.

sion for the first case, flow statistics converge to physical results as the resolution is increased for both MILES_NS and LES_SSF computations. However at high resolution MILES_EULER

results differ from those of MILES_NS and LES_SSF. The achieved LES asymptotes for the statistics also explained in the paper by Pope are similar to these two approaches. The more precise inlet conditions are applied in the second case. Both MILES_NS and MILES_EULER simulation results are in good agreement. Even if the inlet profiles are improved, the average field results are similar to the solutions for simplified inlet profiles. Present results are also compared with the AMR results with precise initial conditions and they are in good agreement.

CHAPTER 6

CONCLUSIONS

In this study three dimensional computations are performed for reacting and non-reacting compressible H2/air jets. In the computations, fifth order WENO scheme is used. The main objective is to investigate the respective performance of LES and MILES numerical approaches in the context of high speed reacting flows. It was also the intention of this work to determine the sensitivities of a high speed reacting jet flow simulations to various physical models. In the non-reacting case, the time step is limited by the CFL condition. In the reacting case the time step is limited to 2×10^{-8} s as dictated by the chemistry. The relative cost of the different simulations is presented at Table I.1 in appendix I.

The following conclusions are derived from the simulation of non-reacting Eggers jet [71]:

- The Smagorinsky model is found to be over-dissipative, hence inhibiting the initial development of instabilities. The three-dimensionality sensor in the Selective Structure Function model fixes the problem.

- In particular, LES solutions do not show superiority compared to MILES, Navier-Stokes or Euler, considering the statistics related to the mixing and the dynamics of the flow.

- In the non-reacting case, calculation of the molecular transport model in MILES_NS represents an extra cost around 18%. The cost of introducing the Smagorinsky model in LES_SM is hardly felt because the velocity derivatives required in the model are already computed in viscous terms. The SSF model is a little more expensive due to the calculation of velocity differences and of the three-dimensionality sensor, (equation 3.67), but is also negligible.

- MILES_EULER simulations are showing grid convergence although there exists no physical cutoff in the simulation. This is an open question for further research.

In the reacting LAERTE chamber case, the main conclusions are [72]:

- The trend is the same as in the Eggers jet, but depending on the grid resolution, chemistry can be faster or slower relatively to the flow dynamics.
- One of the most sensitive parameter to the molecular transport is the ignition point. When comparing the maximum temperature change on the normal planes along the axis, a slight shift of temperature jump is observed at the order of jet diameter between EULER and NS solutions.
- When comparing MILES_NS and LES_SSF average field results, no significant differences are found. This similarity is valid even in the scatter plots of temperature (Figure 5.46) and O_2 mass fraction (Figure 5.47) which are representing the interactions at the molecular level.
- The high sensitivity to the inlet profiles of RANS method is not found in LES.
- The 7 species, 14 reactions chemistry in the reacting MILES_ EULER represent 85% of the WENO effort, although the routines for source terms are thoroughly optimized.

In conclusion, the non-linear WENO scheme is self-adapting to the flow gradients, and a balance is achieved between the explicit sub-grid scale hyperviscosity in physical LES and the numerical dissipation of the scheme. In a physical LES on a coarse grid, the proper modeling of the sub-grid chemical source term is important, but the molecular transport is not. In a numerical LES however, a molecular viscous cut-off in the simulation is mandatory. The choice of whether to introduce or not an explicit sub-grid model in the simulation is not a matter of computational cost. MILES-Navier-Stokes performed with "clever" dissipative numerics provides almost the same grid-independent flow statistics as physical LES. Quoting S.B. Pope's conclusion [107] *"The most that an LES calculation can hope to achieve, is to obtain an accurate estimate of the intermediate asymptote [...]"*. This is achieved for the two finest grids used in this study, with and without explicit sub-grid model.

REFERENCES

[1] *Theory of Propagation of Flames. Part 1: General Equations*, 1948.

[2] A. Akturk. *Two Dimensional Finite Volume Weighted Essentially Non-Oscillatory Euler Schemes with Different Flux Algorithms*. PhD thesis, Middle East Technical University, 2005.

[3] D. Andreadis. Scramjet engines enabling the seamless integration of air & space operations. *The Industrial Physicist*, Aug/Sept 2004.

[4] D. S. Balsara and C. W. Shu. Monotonicity preserving weighted essentially non-oscillatory schemes with increasingly high order of accuracy. *Journal of Computational Physics*, 160, 2000.

[5] M. Baum, T. Poinsot, and D. Thevenin. Accurate boundary conditions for multicomponent reactive flows. *Journal of Computational Physics*, 116, 1994.

[6] R.W. Bilger. Reaction rates in diffusion flames. *Combustion and Flames*, 30:277–284, 1977.

[7] R.W. Bilger. On reduced mechanisms for methane-air combustion in nonpremixed flames. *Combustion and Flames*, 80:135–149, 1990.

[8] D.W. Bogdanoff. Compressibility effects in turbulent shear layers. *AIAA Journal*, 21(6):926–927, 1983.

[9] M. Boileau, B. Staffelbach, B. Cuenot, T. Poinsot, and C. Bérat. LES of an ignition sequence in a gas turbine engine. *Combustion and Flames*, 154(1-2):2–22, 2008.

[10] R. Borges, M. Carmona, B. Costa, and W.S. Don. An improved weighted essentially non-oscillatory scheme for hyperbolic conservation laws. *Journal of Computational Physics*, 227:3191–3211, 2008.

[11] Jay Boris. On large eddy simulation using subgrid turbulence models comment 1. In *Whither Turbulence? Turbulence at the Crossroads*, volume 357 of *Lecture Notes in Physics*, pages 344–353. Springer Berlin / Heidelberg, 1990.

[12] J.P. Boris. *More for LES: A Brief Perspective History of MILES*. 2007.

[13] G. Boudier, N. Lamarque, G. Staffelbach, L.Y.M. Gicquel, and T. Poinsot. Thermoacoustic stability of a helicopter gas turbine combustor using large eddy simulation. *Aeroacoustics*, 8(1):69–94, 2009.

[14] A. Burcat and B. Ruscic. Ideal gas thermodynamic data in polynomial form for combustion and air pollution use, December 2006. Third Millennium Ideal Gas and Condensed Phase Thermochemical Database for Combustion [on line database].

[15] D. Chakraborty, H.V. Nagaraj Upadhyaya, P.J. Paul, and Mukunda H.S. A thermochemical exploration of a two-dimensional reacting supersonic mixing layer. *Physics of Fluids*, 9(11):3513–3522, November 1997.

[16] S. Chapman and T.G. Cowling. *The mathematical theory of non-uniform gases*. Cambridge Mathematical Library, 1953.

[17] J.P. Chollet and M. Lesieur. Parametrization of small scales of three-dimensional isotropic turbulence using spectral closures. *Journal of the Atmospheric Sciences*, 38:2747–2757, December 1981.

[18] T.P. Coffee and J.M. Heimerl. Transport algorithms for premixed, laminar steady-state flames. *Combustion and Flame*, 43:273 – 289, 1981.

[19] C. Collin, O. Dessornes, and P. Magre. Installations d'essais pour les recherches fondamentales en propulsion = test facilities for fundamental research in propulsione. In *Communication to : PEP/FDP AGARD on aerospace technology in the service of the alliance*, Paleisau, France, 15 - 16 April, 1997.

[20] A.W. Cook and J. Riley. Subgrid-scale modeling for turbulent reacting flows. *Combustion and Flame*, 112:593–606, 1998.

[21] E. David. *Modélisation des écoulements compressibles et hypersoniques: une approche instationnaire*. PhD thesis, Institut National Polytechnique de Grenoble, France, 1993.

[22] D. Davidenko. *Contribution au développement des outils de simulation numérique de la combustion supersonique*. PhD thesis, Université d'Orléans, France, 2005.

[23] D. Davidenko, I. Gökalp, E. Dufour, and Ph. Magre. Numerical modeling of inert and reacting compressible turbulent jets. In *AIAA paper 2005-3237*, 13^{th} *AIAA/CIRA International Space Planes and Hypersonic Systems and Technologies Conference*, Capua, Italy, 16 - 20 May, 2005.

[24] D. Davidenko, I. Gökalp, E. Dufour, and Ph. Magre. Systematic numerical study of the supersonic combustion in an experimental combustion chamber. In *AIAA paper 2006-7913*, 14^{th} *AIAA/AHI International Space Planes and Hypersonic Systems and Technologies Conference*, Canberra, Australia, 6 - 9 November, 2006.

[25] J. de Charentenay and A. Ern. Multicomponent transport impact on turbulent premixed H_2/O_2 flames. *Combustion Theory and Modelling*, 6(3):439–462, 2002.

[26] P.E. Dimotakis. Turbulent free shear layer mixing and combustion. In S.N.B. Murthy and E.T. Curran, editors, *High-speed flight propulsion systems*, volume 137 of *Progress in Astronautics and Aeronautics*, pages 265–340. AIAA, 1991.

[27] G. Dixon-Lewis. Flame structure and flame reaction kinetics. i. solution of conservation equations and application to rich hydrogen-oxygen flames. *Proceedings of the Royal Society of London. Series A. Mathematical and Physical Sciences*, 298(1455):495–513, 1967.

[28] J. P. Drummond, Diskin G. S., and A. D. Cutler. Fuel air mixing and combustion in scramjets. In *AIAA paper 2002-3878*, 38^{nd} *AIAA/ASME/SAE/ASEE Joint Propulsion Conference & Exhibit*, 7-10 July 2002 Indianapolis, IN, 2002.

[29] Y. Dubief and F. Delcayre. On coherent-vortex identification in turbulence. *Journal of Turbulence*, 1(011):1–22, 2000.

[30] F. Ducros. *Simulations numériques directes et des grandes échelles de couches limites compressibles*. PhD thesis, Institut National Polytechnique de Grenoble, France, 1995.

[31] F. Ducros, V. Ferrand, F. Nicoud, C. Weber, D. Darracq, C. Gacherieu, and T. Poinsot. Large-eddy simulation of the shock/turbulence interaction. *Journal of Computational Physics*, 152:517–549, 1999.

[32] J.M. Eggers. Turbulent mixing of coaxial compressible hydrogen-air jets. Technical Report NASA-TN-D-6487, NASA, 1971.

[33] D. R. Eklund, J. P. Drummond, and H. A. Hassan. Calculation of supersonic reacting coaxial jets. *AIAA Journal*, 28(9), 1990.

[34] G. Erlebacher, M.Y. Hussaini, C.G. Speziale, and T.A. Zang. Toward the large eddy simulation of compressible turbulent flows. *Journal of Fluid Mechanics*, 238:155–185, 1992.

[35] A. Ern and V. Giovangigli. Fast and accurate multicomponent transport property evaluation. *Journal of Computational Physics*, 120(1):105 – 116, 1995.

[36] A. Ern and V. Giovangigli. *Multicomponent Transport Algorithms*. Lecture Notes in Physics, New Series Monographs. 1994, Springer-Verlag.

[37] F. Falempin, M. Bouchez, L. Serre, C. Bruno, and P. Hendrick. Air-breathing propulsion for future space launchers proposal for a minimum r & t program on for europe. Dayton, Ohio, 2005.

[38] F. Falempin and L. Serre. French flight test program lea status. In *High Speed Propulsion: Engine Design - Integration and Thermal Management, RTO-EN-AVT-185*, Bruxelles, Belgium, September, 2010.

[39] A. Favre. Equations des gaz turbulents compressibles. *Journal de Mécanique*, 4:391–421, 1965.

[40] A. Favre. Turbulence: space-time properties and behavior in supersonic flows. *Physics of Fluids*, 26:2851–2863, 1983.

[41] I. Fedioun and N. Lardjane. Temporal linear stability analysis of three-dimensional compressible binary shear layers. *AIAA Journal*, 43(1):111–123, 2005.

[42] I. Fedioun and N. Lardjane. Turbulent multicomponent turbulent flows : how DNS is useful for LES and RANS modeling. Private communication, METU, Ankara, May 2009.

[43] I. Fedioun, N. Lardjane, and I. Gökalp. Revisiting numerical errors in direct and large-eddy simulations of turbulence: Physical and spectral spaces analysis. *Journal of Computational Physics*, 174:816–851, 2001.

[44] J.H. Ferziger and Kaper H.G. *Mathematical theory of transport process in gases*. North-Holland Publishing Company, 1972.

[45] R.S. Frey. A century of ramjet propulsion. *Journal of Propulsion and Power*, 20(1), 2004.

[46] E. Garnier. *Simulation des grandes échelles en régime transsonique*. PhD thesis, Université Paris XI, Orsay, France, 2000.

[47] E. Garnier, M. Mossi, P. Sagaut, P. Comte, and M. Deville. On the use of shock-capturing schemes for large-eddy simulation. *Journal of Computational Physics*, 153:273–311, 1999.

[48] E. Garnier, P. Sagaut, and N. Adams. *Large Eddy Simulation for Compressible Flows*. Springer, 2009.

[49] E. Garnier, P. Sagaut, and M. Deville. Large-eddy simulation of shock/turbulence interaction. *Computers and Fluids*, 31:245–268, 2002.

[50] E. George, Ph. Magre, and V. Sabel'nikov. Numerical simulations of self-ignition of hydrogen-hydrocarbons mixtures in a hot supersonic air flow. In *AIAA paper 2006-4611, 42nd AIAA/ASME/SAE/ASEE Joint Propulsion Conference & Exhibit*, Sacramento, California, 9-12 July, 2006.

[51] M. Germano. Turbulence: the filtering approach. *Journal of Fluid Mechanics*, 238:325–336, 1992.

[52] S. Ghosal. An analysis of numerical errors in large-eddy simulations of turbulence. *Journal of Computational Physics*, 125:187–206, 1996.

[53] S. Ghosal and P. Moin. The basic equations for the large eddy simulations of turbulent flows in complex geometry. *Journal of Computational Physics*, 118:24–37, 1995.

[54] V. Giovangigli. Convergent iterative methods for multicomponent diffusion. *Impact of Computing in Science and Engineering*, 2:73–97, 1990.

[55] V. Giovangigli. Mass conservation and singular multicomponent diffusion algorithms. *Impact of Computing in Science and Engineering*, 2:73–97, 1990.

[56] F. Génin and S. Menon. Studies of shock/turbulent shear layer interaction using large-eddy simulation. *Computers and Fluids*, 39:800–819, 2010.

[57] S.K. Godunov. A difference scheme for numerical solution of discontinuos solution of hydrodynamic equations. *Mathe Sborni*, 30:61–117, 1959.

[58] L. Gougeon. Simulation numérique de flammes laminaires prémélangées. Rapport de stage dea/ingénieur, ICARE/CNRS, 2003.

[59] L. Gougeon. *Comparaision de schémas numériques pour la similation d'ecoulements turbulent réactifs*. PhD thesis, Université de d'Orléans, France, 2007.

[60] F.F. Grinstein, L.G. Margolin, and W.J. Rider. *Implicit Large Eddy Simulation : computing turbulent fluid dynamics*. Cambridge University Press, 2007.

[61] A. Harten. High resolution schemes for hyperbolic conservation laws. *Journal of Computational Physics*, 49:357–393, 1983.

[62] A. Harten, B.V. Leer, and P.D. Lax. On upstream differencing and godunov-type schemes for hyperbolic conservation laws. *SIAM Rev.*, 25:35–61, 1983.

[63] G.W. Hedstrom. Nonreflecting boundary conditions for nonlinear hyperbolic systems. *Journal of Computational Physics*, 30:222–237, 1979.

[64] A.K. Henrick, T.D. Aslam, and M. Powers. Mapped weighted essentially non-oscillatory schemes: Achieving optimal order near critical points. *Journal of Computational Physics*, 207:542–567, 2005.

[65] R. Hilbert, F. Tap, H. El-Rabii, and D. Thévenin. Impact of detailed chemistry and transport models on turbulent combustion simulations. *Progress in Energy and Combustion Science*, 30:61–117, 2004.

[66] J.O. Hirschfelder, C.F. Curtiss, and R.B. Bird. *Molecular Theory of Gases and Liquids*. JJohn Wiley, New York, 1954.

[67] J. C. R. Hunt, A. A. Wray, and P. Moin. Eddies, streams, and convergence zones in turbulent flows. pages 193–208, 1988.

[68] F. James. A review of pseudorandom number generators. *Computer Physics Communications*, 60:329–344, 1990.

[69] G.S. Jiang and C.W. Shu. Efficient implementation of weighted ENO schemes. *Journal of Computational Physics*, 126:202–228, 1996.

[70] J.R. Julien. *Accélération de la Convergence vers une Solution Stationnaire des Calculs en Aérothermique = Convergence Acceleration of Navier-Stokes Computations*. PhD thesis, Université de Clermont-Ferrand 2, Clermont-Ferrand, FRANCE, 1997.

[71] M. Karaca, I. Fedioun, and N. Lardjane. LES/MILES of non-reacting and reacting high speed jets. In 8^{th} *Euromech Fluid Mechanics Conference, EFMC-8*, Bad Reichenhall, Germany, 13 - 16 September, 2010.

[72] M. Karaca, I. Fedioun, and N. Lardjane. High-speed turbulent mixing and combustion : MILES vs physical LES. In *accepted for oral presentation at the* 7^{th} *International Symposium on Turbulence and Shear Flow Phenomena-7, TSFP7*, Ottawa, Canada, 28 - 31 July, 2011.

[73] R.J. Kee, F.M. Rupley, J.A. Miller, M.E. Coltrin, J.F. Grcar, E. Meeks, H.K. Moffat, A.E. Lutz, G. Dixon-Lewis, M.D. Smooke, J. Warnatz, G.H. Evans, R.S. Larson, R.E. Mitchell, L.R. Petzold, W.C. Reynolds, M. Caracotsios, W.E. Stewart, and P. Glarborg. *CHEMKIN collection*. release 3.5. Reaction Design, Inc., San Diego, CA, 1999.

[74] J-H. Kim, Y. Yoon, I-S. Jeung, H. Huh, and J-Y. Choi. Numerical study of mixing enhancement by shock waves in model scramjet engine. *AIAA Journal*, 41(6):1074–1080, 2003.

[75] S.H. Kim and H. Pitsch. Conditional filtering method for large-eddy simulation of turbulent nonpremixed combustion. *Physics of Fluids*, 17:105103, 2005.

[76] A.G. Kravchenko and P. Moin. On the effect of numerical errors in large-eddy simulations of turbulent flows. *Journal of Computational Physics*, 131:310–322, 1997.

[77] P. Kuentzmann and F. Falempin. Ramjet, scramjet and pde. In *Encyclopedia of Physical Science and Technology*. Elsevier Science Ltd., 2002.

[78] K.K. Kuo. *Principles of Combustion*. John Wiley Sons, Inc., 2005.

[79] Thompson K.W. Time dependent boundary conditions for hypersonic systems. *Journal of Computational Physics*, 68, 1987.

[80] N. Lardjane. *Etude théorique et numérique des écoulements cisaillés libres à masse volumique fortement variable*. PhD thesis, Université de d'Orléans, France, 2002.

[81] N. Lardjane, I. Fedioun, and I. Gökalp. Direct numerical simulation of binary mixing layers. In *Proceedings of the* 2^{nd} *International Symposium on Turbulence and Shear Flow Phenomena, TSFP-2, vol. I*, pages 317–322, Stockholm, Sweeden, June, 2001.

[82] B. Larrouturou. How to preserve the mass fractions positivity when computing compressible multi-component flows. *Journal of Computational Physics*, 95, 1991.

[83] S.K. Lele. Compact finite difference schemes with spectral-like resolution. *Journal of Computational Physics*, 103:16–42, 1992.

[84] E. Lenormand, P. Sagaut, and L. Ta Phuoc. Large eddy simulation of subsonic and supersonic channel flow at moderate Reynolds number. *International Journal for Numerical Methods in Fluids*, 32:369–406, 2000.

[85] M. Lesieur. *Turbulence in Fluids, Fourth edition*. Fluid mechanics and its applications, Vol. 84. Springer, 2008.

[86] M. Lesieur and P. Compte. Large-eddy simulation of compressible turbulent flows. Technical Report 4, 1997.

[87] M. Lesieur and O. Métais. New trends in large-eddy simulations of turbulence. *Annual Review of Fluid Mechanics*, 28:45–82, 1996.

[88] X.D. Liu, S. Osher, and T. Chan. Weighted essentially non-oscillatory schemes. *Journal of Computational Physics*, 115:200–212, 1994.

[89] M. Luscher. A portable high-quality random number generator for lattice field theory simulations. *Computer Physics Communications*, 79:100–110, 1994.

[90] Ph. Magre and V. Sabel'nikov. Self-ignition of hydrogen-ethylene mixtures in a hot supersonic air flow. In *AIAA paper 2002-5205*, 11^{th} *AIAA/AAAF International Space Planes and Hypersonic Systems and Technologies Conference*, Orléans, France, 29 September - 4 October, 2002.

[91] L.G. Margolin, W.J. Rider, and F.F. Grinstein. Modeling turbulent flows with implicit LES. *Journal of Turbulence*, 7(15):1–27, 2006.

[92] A. L. Marsden, O. V. Vasilyev, and P. Moin. Construction of commutative filters for les on unstructured meshes. *Journal of Computational Physics*, 175, 2002.

[93] M.P. Martin, E.M. Taylor, M. Wu, and V.G. Weirs. A bandwidth-optimized weno scheme for the effective direct numerical simulation of compressible turbulence. *Journal of Computational Pysics*, 220:270–289, 2006.

[94] B. E. Mitchell, S. K. Lele, and P. Moin. Direct computation of mach wave radiation in an axisymmetric supersonic jet. *AIAA Journal*, 35:1574–1580, 1997.

[95] L. Monchick, R.J. Munn, and E.A. Mason. Thermal diffusion in polyatomic gases: A generalized stefan maxwell diffusion equation. *The Journal of Chemical Physics*, 45(10):3051–3058, 1966.

[96] O. Métais and M. Lesieur. Spectral large-eddy simulation of isotropic and stably-stratified turbulence. *Journal of Fluid Mechanics*, 239:157–194, 1992.

[97] E.S. Oran and Boris J.P. Detailed modeling of combustion systems. *Progress in Energy and Combustion Science*, 7(1):1–71, 1981.

[98] E.S. Oran and Boris J.P. *Numerical Simulation of Reactive Flow*. Elsevier, 1987.

[99] E. Orlic. *Etude du champ aérodynamique et de la transition laminaire-turbulent sur l'avantcorps d'un véhicule hypersonique*. PhD thesis, Université de d'Orléans, France, 2009.

[100] D. Papamoschou. Structure of the compressible turbulent shear layer. *AIAA Journal*, 29(5):680–681, 1991.

[101] C.D. Pierce and P. Moin. Progress-variable approach for large-eddy simulation of non-premixed turbulent combustion. *Journal of Fluid Mechanics*, 504:73–97, 2004.

[102] S. Pirozzoli. On the spectral properties of shock-capturing schemes. *Journal of Computational Physics*, 219:489–497, 2006.

[103] H. Pitsch. Large-eddy simulation of turbulent combustion. *Annual Review of Fluid Mechanics*, 38:453–482, 2006.

[104] T. Poinsot and D. Veynante. *Theoretical and Numerical Combustion*. 2^{nd} edition. Edwards, 2005.

[105] T.J. Poinsot and S.K. Lele. Boundary conditions for direct simulations of compressible viscous flows. *Journal of Computational Physics*, 101, 1992.

[106] S. B. Pope. *Turbulent Flows*. Cambridge University Press, 2000.

[107] S.B. Pope. Ten questions concerning the large-eddy simulation of turbulent flows. *New Journal of Physics*, 6(35):1–24, 2004.

[108] P.L. Roe. Approximate riemann solvers, parameter vectors and difference schemes. *Journal of Computational Physics*, (43), 1981.

[109] R. S. Rogalo and P. Moin. Numerical simulation of turbulent flows. *Annual Review of Fluid Mechanics*, 16:99–137, 1984.

[110] P. Sagaut. *Large-Eddy Simulation for Incompressible Flows*. 3^{rd} edition. Springer, Berlin, 2006.

[111] P. Sagaut, S. Deck, and M. Terracol. *Multiscale and multiresolution approaches in turbulence*. Imperial College Press, 2006.

[112] C.W. Shu. Essentially non-oscillatory and weighted essentially non-oscillatory schemes for hyperbolic conservation laws. Technical Report CR-97-206253, ICASE report No.97-65, NASA, November 1997.

[113] J.W. Shu and Osher S. Efficient implementation of essentially non-oscillatory shock-capturing schemes. *Journal of Computational Physics*, 77:37–78, 1988.

[114] J.W. Shu and Osher S. Efficient implementation of essentially non-oscillatory shock-capturing schemes, ii. *Journal of Computational Physics*, 83:439–471, 1989.

[115] J. Smagorinsky. General circulation experiments with the primitive equations i. the basic experiment. *Monthly Weather Review*, 91(3):99–164, 1963.

[116] C.G. Speziale, G. Erlebacher, T.A. Zang, and M.Y. Hussaini. The subgrid-scale modeling of compressible turbulence. *Physics of Fluids*, 31(4):940–942, 1988.

[117] A. Stoukov. *Etude numérique de la couche de mélange réactive supersonique*. PhD thesis, Université de Rouen, France, 1996.

[118] E.M. Taylor, M. Wu, and M.P. Martin. Optimization of nonlinear error for weighted essentially non-oscillatory methods in direct numerical simulations of compressible turbulence. *Journal of Computational Physics*, 223:384–397, 2007.

[119] B. Thornber, D. Drikakis, and D. Youngs. Large-eddy simulation of multi-component compressible turbulent flows using high resolution methods. *Computers and Fluids*, 37:867–876, 2008.

[120] B. Van Leer. Towards the ultimate conservative difference scheme. ii. monotonicity and conservation combined in a second-order scheme. *Journal of Computational Physics*, 14:361–370, 1974.

[121] D. Veynante. Large eddy simulations of turbulent combustion. In M. Deville, T.H. Lê, and P. Sagaut, editors, *Turbulence and interactions*, volume 105/2009 of *Notes on Numerical Fluid Mechanics and Multidisciplinary Design*, pages 113–138. Springer, 2009.

[122] A.W. Vreman. *Direct and Large-Eddy Simulation of the Compressible Turbulent Mixing Layer*. PhD thesis, University of Twente, The Netherlands, 1995.

[123] B. Vreman, B. Geurts, and Kuerten H. A priori tests of large eddy simulation of the compressible plane mixing layer. *Journal of Engineering Mathematics*, 29:299–327, 1995.

[124] P.J. Waltrup, White M.E., Zarlingo F., and Gravlin E.S. History of us navy ramjet, scramjet and mixed-cycle development. *Journal of propulsion and power.*, 18(1), 2002.

[125] J. Warnatz, U. Maas, and R.W. Dibble. *Combustion*. Springer, 2001.

[126] P. Wesseling. *Principles of Computational Fluid Dynamics*. Springer, 2001.

[127] C.R. Wilke. A viscosity equation for gas mixture. *Chemical Physics*, 18:517–19, 1950.

[128] F.A. Williams. *Combustion Theory*. The Benjamin/Cummins Publishing Comp., 1985.

[129] A. Yoshizawa. Statistical theory for compressible turbulent shear flows, with the application to subgrid modeling. *Physics of Fluids*, 29(7):2152–2164, 1986.

APPENDIX A

TRANSPORT COEFFICIENTS

In this appendix the constants for the curve fits of viscosity, thermal conductivity versus temperature and binary diffusion coefficients versus temperature and pressure are tabulated.

Table A.1: Thermal conductivity coefficients for second order polynomial fit (i.e. equation 2.50).

α	$\lambda_{\alpha 0}$	$\lambda_{\alpha 1}$	$\lambda_{\alpha 2}$
H_2	8.252657E−02	3.571108E−04	-1.065945E−08
O_2	7.823695E−03	6.765939E−05	-4.206463E−09
H	1.324366E−01	6.079185E−04	-5.378665E−08
O	2.463573E−02	8.861247E−05	-7.426621E−09
OH	2.303120E−02	1.220661E−04	-5.555844E−09
H_2O	-2.298272E−02	1.501943E−04	-2.770068E−09
N_2	8.124867E−03	6.467204E−05	-4.751436E−09

Table A.2: Coefficients of viscosity for second order polynomial fit (i.e. equation 2.37).

α	$\mu_{\alpha 0}$	$\mu_{\alpha 1}$	$\mu_{\alpha 2}$
H_2	4.817404E−06	1.558606E−08	-1.263024E−12
O_2	1.005179E−05	3.965070E−08	-3.402360E−12
H	4.281418E−06	1.965283E−08	-1.738818E−12
O	1.264157E−05	4.547059E−08	-3.810896E−12
OH	1.303709E−05	4.687465E−08	-3.927133E−12
H_2O	-1.447952E−06	4.034792E−08	-2.764521E−12
N_2	8.959686E−06	3.408293E−08	-2.898343E−12

Table A.3: Power law fitted diffusion coefficients for P_0(=1bar), T (i.e. equation 2.21).

α	β	$a_{\alpha\beta 0}$	$b_{\alpha\beta}$
H_2	H_2	1.169336E−08	1.655943
O_2	H_2	6.491853E−09	1.660466
O_2	O_2	1.567353E−09	1.672389
H	H_2	1.700467E−08	1.662801
H	O_2	9.259134E−09	1.683814
H	H	2.165726E−08	1.685359
O	H_2	8.765136E−09	1.657728
O	O_2	2.533007E−09	1.668124
O	H	1.338447E−08	1.675000
O	O	3.908707E−09	1.664289
OH	H_2	8.738485E−09	1.657728
OH	O_2	2.481736E−09	1.668088
OH	H	1.336130E−08	1.675031
OH	O	3.850414E−09	1.664290
OH	OH	3.791110E−09	1.664289
H_2O	H_2	5.802656E−09	1.697037
H_2O	O_2	1.267896E−09	1.737231
H_2O	H	6.695257E−09	1.750332
H_2O	O	2.362321E−09	1.711888
H_2O	OH	2.325140E−09	1.711866
H_2O	H_2O	3.499347E−10	1.926722
N_2	H_2	6.277844E−09	1.659863
N_2	O_2	1.579563E−09	1.670803
N_2	H	8.972560E−09	1.681871
N_2	O	2.502788E−09	1.666851
N_2	OH	2.454388E−09	1.666818
N_2	H_2O	1.294409E−09	1.731984
N_2	N_2	1.591546E−09	1.669076

APPENDIX B

THERMODYNAMIC DATA

The thermodynamic data used in the calculation are presented in Table B.2, following the format given in Table B.1. It is assumed that the pressure is not elevated so thermodynamic properties are function of temperature only. The data are the coefficients of fitted polynomials on the temperature functions of heat capacities Cp_α and Cv_α of species α.

$$\frac{Cp_\alpha}{R} = Cp_{0\alpha} + TCp_{1\alpha} + Cp_{2\alpha}T^2 + Cp_{3\alpha}T^3 + Cp_{4\alpha}T^4 \tag{B.1}$$

Enthalpy H°/RT and entropy S°/RT of species are computed using this data. There exists two sets of coefficients referring to two different polynomials for low temperature $[T_{min} - 1000K]$ and high temperature $[1000K - T_{max}]$ intervals. The coefficients Cp_5 and Cp_6 are used to compute the enthalpy ΔH^0 and the entropy ΔS^0 of system.

Table B.1: Thermodynamic property data format.

species		T_{min} (K)	T_{max} (K)	M (g.mol^{-1})
$Cp_{0,H}$	$Cp_{1,H}$	$Cp_{2,H}$	$Cp_{3,H}$	$Cp_{4,H}$
$Cp_{5,H}$	$Cp_{6,H}$	$Cp_{0,L}$	$Cp_{1,L}$	$Cp_{2,L}$
$Cp_{3,L}$	$Cp_{4,L}$	$Cp_{5,L}$	$Cp_{6,L}$	

Table B.2: Thermodynamic properties. (Burcat [14]).

H		300	5000	1,00794
0.02500000E+02	0.00000000E+00	0.00000000E+00	0.00000000E+00	0.00000000E+00
0.02547163E+06	-0.04601176E+01	0.02500000E+02	0.00000000E+00	0.00000000E+00
0.00000000E+00	0.00000000E+00	0.02547163E+06	-0.04601176E+01	
H_2		300	5000	2.01588
0.02991423E+02	0.07000644E−02	-0.05633829E−06	-0.09231578E−10	0.01582752E−13
-0.08350340E+04	-0.01355110E+02	0.03298124E+02	0.08249442E−02	-0.08143015E−05
-0.09475434E−09	0.04134872E−11	-0.01012521E+05	-0.03294094E+02	
O		300	5000	15.99940
0.02542060E+02	-0.02755062E−03	-0.03102803E−07	0.04551067E−10	-0.04368052E−14
0.02923080E+06	0.04920308E+02	0.02946429E+02	-0.01638166E−01	0.02421032E−04
-0.01602843E−07	0.03890696E−11	0.02914764E+06	0.02963995E+02	
O_2		300	5000	31.99880
0.03697578E+02	0.06135197E−02	-0.01258842E−05	0.01775281E−09	-0.01136435E−13
-0.01233930E+05	0.03189166E+02	0.03212936E+02	0.01127486E−01	-0.05756150E−05
0.01313877E−07	-0.08768554E−11	-0.01005249E+05	0.06034738E+02	
OH		300	5000	17.00734
0.02882730E+02	0.01013974E−01	-0.02276877E−05	0.02174684E−09	-0.05126305E−14
0.03886888E+05	0.05595712E+02	0.03637266E+02	0.01850910E−02	-0.01676165E−04
0.02387203E−07	-0.08431442E−11	0.03606782E+05	0.01358860E+02	
H_2O		300	5000	18.01528
0.02672146E+02	0.03056293E−01	-0.08730260E−05	0.01200996E−08	-0.06391618E−13
-0.02989921E+06	0.06862817E+02	0.03386842E+02	0.03474982E−01	-0.06354696E−04
0.06968581E−07	-0.02506588E−10	-0.03020811E+06	0.02590233E+02	
N2		300	5000	28.01348
0.02926640E+02	0.01487977E−01	-0.05684761E−05	0.01009704E−08	-0.06753351E−13
-0.09227977E+04	0.05980528E+02	0.03298677E+02	0.01408240E−01	-0.03963222E−04
0.05641515E−07	-0.02444855E−10	-0.01020900E+05	0.03950372E+02	

APPENDIX C

CHEMICAL KINETICS

The chemical kinetics data used for source term calculation are presented in Table C.2. The rate constant K_r is computed applying Arrhenius law :

$$K_r = A_r T^{b_r} \exp\left(-\frac{E_r}{\mathcal{R}T}\right)$$

where for the r^{th} reaction:

- A_r is the pre-exponential factor.
- E_r is the activation energy.
- b_r constant for pre-exponential factor T^{b_r}.

The efficiencies of the species included in the H_2/Air chemical kinetics mechanism is :

Table C.1: Efficiency of the species for the ONERA scheme.

	H	H_2	H_2O	O	OH	O_2	N_2	Ar
ONERA	1,0	2,5	12	1,0	1,0	1,00		1,0

Table C.2: H_2/air Chemical reaction mechanism by ONERA.

r	Reaction	A_r (cm.mol.s)	b_r	E_r (kJ.mol^{-1})
1	$H_2 + O_2 \longrightarrow OH + OH$	1.70E+13	0.0	199.9122
2	$OH + OH \longrightarrow H_2 + O_2$	4.03E+10	0.3168	121.0074
3	$H + O_2 \longrightarrow OH + O$	1.99E+14	0.0	70.3043
4	$O + OH \longrightarrow H + O_2$	8.93E+11	0.3383	-0.9778
5	$H_2 + OH \longrightarrow H_2O + H$	1.02E+08	1.6	13.8008
6	$H + H_2O \longrightarrow H_2 + OH$	7.96E+08	1.528	77.3248
7	$H_2 + O \longrightarrow OH + H$	5.12E+04	2.67	26.3016
8	$OH + H \longrightarrow H_2 + O$	2.70E+04	2.649	18.6212
9	$OH + OH \longrightarrow H_2O + O$	1.51E+09	1.14	0.4142
10	$H_2O + O \longrightarrow OH + OH$	2.22E+10	1.089	71.6144
11	$H + OH + M \longrightarrow H_2O + M$	2.21E+22	-2.0	0.0
12	$H_2O + M \longrightarrow H + OH + M$	8.94E+22	-1.835	496.7304
13	$H + H + M \longrightarrow H_2 + M$	9.79E+16	-0.6	0.0
14	$H_2 + M \longrightarrow H + H + M$	5.09E+16	-0.3624	433.2265

APPENDIX D

TRANSFORMATION MATRICES FOR SYSTEM OF N_{SP}+5 EQUATIONS

The following matrices are used for finite difference characteristic discretization. The vector of conservative variables is :

$$\vec{\vec{U}} = \left[\rho,\, \rho u,\, \rho v,\, \rho w,\, \rho e_t,\, \rho Y_1,\, \ldots,\, \rho Y_{N_{sp}}\right]^T$$

and the vector of primitive variables is considered as :

$$\vec{U} = \left[\rho,\, u,\, v,\, w,\, T,\, Y_1,\, \ldots,\, Y_{N_{sp}}\right]^T$$

Here the matrices for transformation between conservative variables to characteristic variables are presented, for the spatial discretization $\tilde{R}$ et $\tilde{L}$. These can be directly obtained diagonalizing the conservative jacobian matrices $\widetilde{A}$ but the easier way is using the relations $\widetilde{R} = PR$ and $\tilde{L} = LP^{-1}$.

with

1. $K = \frac{1}{2} u_i u_i$
2. $\epsilon_\alpha = h_\alpha - r_\alpha T$
3. $\epsilon = \sum_{\alpha=1}^{N_{sp}} h_\alpha Y_\alpha - rT$

$$\widetilde{R} = \begin{pmatrix} \rho & \rho & 0 & 0 & \rho & \rho\frac{r-r_1}{r} & \dots & \dots & \dots & \rho\frac{r-r_{N_{sp}}}{r} \\ \rho(u-c) & \rho u & 0 & 0 & \rho(u+c) & \rho u\frac{r-r_1}{r} & \dots & \dots & \dots & \rho u\frac{r-r_{N_{sp}}}{r} \\ \rho v & \rho v & \rho & 0 & \rho v & \rho v\frac{r-r_1}{r} & \dots & \dots & \dots & \rho v\frac{r-r_{N_{sp}}}{r} \\ \rho w & \rho w & 0 & \rho & \rho w & \rho w\frac{r-r_1}{r} & \dots & \dots & \dots & \rho w\frac{r-r_{N_{sp}}}{r} \\ \rho e_t + P - \rho uc & \rho e_t - \frac{P}{\gamma-1} & \rho v & \rho w & \rho e_t + P + \rho uc & \rho e_t\frac{r-r_1}{r} + \rho(\epsilon_1 - \epsilon) & \dots & \dots & \dots & \rho e_t\frac{r-r_{N_{sp}}}{r} + \rho(\epsilon_{N_{sp}} - \epsilon) \\ \rho Y_1 & \rho Y_1 & 0 & 0 & \rho Y_1 & \rho Y_1\frac{r-r_1}{r} + \rho & \rho Y_1\frac{r-r_2}{r} & \dots & \dots & \rho Y_1\frac{r-r_{N_{sp}}}{r} \\ \rho Y_2 & \rho Y_2 & 0 & 0 & \rho Y_2 & \rho Y_2\frac{r-r_1}{r} & \ddots & \ddots & & \vdots \\ \vdots & \vdots & \vdots & \vdots & \vdots & \vdots & \ddots & \ddots & \ddots & \vdots \\ \vdots & \vdots & \vdots & \vdots & \vdots & \vdots & & \ddots & \ddots & \vdots \\ \rho Y_{N_{sp}} & \rho Y_{N_{sp}} & 0 & 0 & \rho Y_{N_{sp}} & \rho Y_{N_{sp}}\frac{r-r_1}{r} & \dots & \dots & \rho Y_{N_{sp}}\frac{r-r_{N_{sp}-1}}{r} & \rho Y_{N_{sp}}\frac{r-r_{N_{sp}}}{r} + \rho \end{pmatrix} \tag{D.1}$$

and

$$\widetilde{L} = \begin{pmatrix} \frac{c^2+\gamma uc+\gamma(\gamma-1)(K-\epsilon)}{2\gamma\rho c^2} & -\frac{(\gamma-1)u-c}{2\rho c^2} & -\frac{(\gamma-1)v}{2\rho c^2} & -\frac{(\gamma-1)w}{2\rho c^2} & \frac{\gamma-1}{2\rho c^2} & \frac{(\gamma-1)(\epsilon-\epsilon_1)+(r_1-r)T}{2\rho c^2} & \dots & \dots & \frac{(\gamma-1)(\epsilon-\epsilon_{N_{sp}})+(r_{N_{sp}}-r)T}{2\rho c^2} \\ \frac{\gamma-1}{\gamma\rho c^2}(c^2-\gamma(K-\epsilon)) & \frac{(\gamma-1)u}{\rho c^2} & \frac{(\gamma-1)v}{\rho c^2} & \frac{(\gamma-1)w}{\rho c^2} & -\frac{\gamma-1}{\rho c^2} & (\gamma-1)\frac{(r_1-r)T-(\epsilon-\epsilon_1)}{\rho c^2} & \dots & \dots & (\gamma-1)\frac{(r_{N_{sp}}-r)T-(\epsilon-\epsilon_{N_{sp}})}{\rho c^2} \\ -\frac{v}{\rho} & 0 & \frac{1}{\rho} & 0 & 0 & 0 & \dots & \dots & 0 \\ -\frac{w}{\rho} & 0 & 0 & \frac{1}{\rho} & 0 & 0 & \dots & \dots & 0 \\ \frac{c^2-\gamma uc+\gamma(\gamma-1)(K-\epsilon)}{2\gamma\rho c^2} & -\frac{(\gamma-1)u+c}{2\rho c^2} & -\frac{(\gamma-1)v}{2\rho c^2} & -\frac{(\gamma-1)w}{2\rho c^2} & \frac{\gamma-1}{2\rho c^2} & \frac{(\gamma-1)(\epsilon-\epsilon_1)+(r_1-r)T}{2\rho c^2} & \dots & \dots & \frac{(\gamma-1)(\epsilon-\epsilon_{N_{sp}})+(r_{N_{sp}}-r)T}{2\rho c^2} \\ -\frac{Y_1}{\rho} & 0 & 0 & 0 & 0 & \frac{1}{\rho} & 0 & \dots & 0 \\ -\frac{Y_2}{\rho} & 0 & 0 & 0 & 0 & 0 & \frac{1}{\rho} & \dots & 0 \\ \vdots & \dots & \dots & \dots & \dots & \ddots & \ddots & \ddots & \vdots \\ \vdots & \dots & \dots & \dots & \dots & \dots & \ddots & \ddots & 0 \\ -\frac{Y_{N_{sp}}}{\rho} & 0 & \dots & \dots & \dots & \dots & \dots & 0 & \frac{1}{\rho} \end{pmatrix} \tag{D.2}$$

APPENDIX E

TRANSFORMATION MATRICES FOR SYSTEM OF N_{SP}+4 EQUATIONS

Matrices for the transformation between conservative, primitive and characteristic forms of governing equations are presented in this appendix. The derivations for these matrices were held over equations for N_{sp}-1 species.

E.1 TRANSFORMATION MATRICES BETWEEN THE PRIMITIVE VARIABLES AND THE CONSERVATIVE VARIABLES

The vector of conservative variable is :

$$\vec{\vec{U}} = {}^{T}\left[\rho,\, \rho u,\, \rho v,\, \rho w,\, \rho e_t,\, \rho Y_1,\, \ldots,\, \rho Y_{N_{sp}-1}\right]$$

and primitive variable vector is considered as :

$$\vec{U} = {}^{T}\left[\rho,\, u,\, v,\, w,\, T,\, Y_1,\, \ldots,\, Y_{N_{sp}-1}\right]$$

The transformation matrices of the conservative variables to primitive variables and vice versa are given below respectively P and P^{-1}.

$$P = \begin{pmatrix} 1 & 0 & 0 & 0 & 0 & 0 & 0 & \cdots & \cdots & 0 \\ u & \rho & 0 & 0 & 0 & 0 & 0 & \cdots & \cdots & 0 \\ v & 0 & \rho & 0 & 0 & 0 & 0 & \cdots & \cdots & 0 \\ w & 0 & 0 & \rho & 0 & 0 & 0 & \cdots & \cdots & 0 \\ P_{5,1} & \rho u & \rho v & \rho w & \rho Cv & P_{5,6} & P_{5,7} & \cdots & \cdots & P_{5,N_{sp}+4} \\ Y_1 & 0 & 0 & 0 & 0 & \rho & 0 & \cdots & \cdots & 0 \\ Y_2 & 0 & 0 & 0 & 0 & 0 & \rho & 0 & \cdots & 0 \\ \vdots & \vdots & \vdots & \vdots & \vdots & \vdots & 0 & \ddots & & \vdots \\ \vdots & \vdots & \vdots & \vdots & \vdots & \vdots & \vdots & & \ddots & 0 \\ Y_{N_{sp}-1} & 0 & 0 & 0 & 0 & 0 & 0 & \cdots & 0 & \rho \end{pmatrix}$$

with

- $P_{5,1} = h - rT + 1/2 u_i u_i$
- $P_{5,5+\alpha} = \rho[h_\alpha - h_{N_{sp}} - (r_\alpha - r_{N_{sp}})T]$ avec α=1,...,N_{sp}-1

$$P^{-1} = \begin{pmatrix} 1 & 0 & 0 & 0 & 0 & 0 & 0 & \cdots & \cdots & 0 \\ -u/\rho & 1/\rho & 0 & 0 & 0 & 0 & 0 & \cdots & \cdots & 0 \\ -v/\rho & 0 & 1/\rho & 0 & 0 & 0 & 0 & \cdots & \cdots & 0 \\ -w/\rho & 0 & 0 & 1/\rho & 0 & 0 & 0 & \cdots & \cdots & 0 \\ P^{-1}_{5,1} & \frac{-u}{\rho Cv} & \frac{-v}{\rho Cv} & \frac{-w}{\rho Cv} & \frac{1}{\rho Cv} & P^{-1}_{5,6} & P^{-1}_{5,7} & \cdots & \cdots & P^{-1}_{5,N_{sp}+4} \\ -Y_1/\rho & 0 & 0 & 0 & 0 & 1/\rho & 0 & \cdots & \cdots & 0 \\ -Y_2/\rho & 0 & 0 & 0 & 0 & 0 & 1/\rho & 0 & \cdots & 0 \\ \vdots & \vdots & \vdots & \vdots & \vdots & \vdots & 0 & \ddots & & \vdots \\ \vdots & \vdots & \vdots & \vdots & \vdots & \vdots & \vdots & & \ddots & 0 \\ -Y_{N_{sp}-1}/\rho & 0 & 0 & 0 & 0 & 0 & 0 & \cdots & 0 & 1/\rho \end{pmatrix}$$

avec

- $P^{-1}_{5,1} = \frac{1}{\rho Cv}[r_{N_{sp}} T - h_{N_{sp}} + 1/2 u_i u_i]$
- $P^{-1}_{5,5+\alpha} = \frac{1}{\rho Cv}[(r_\alpha - r_{N_{sp}})T - (h_\alpha - h_{N_{sp}} -)]$ avec α=1,...,N_{sp}-1

E.2 TRANSFORMATION MATRICES BETWEEN THE PRIMITIVE VARIABLES AND THE CHARACTERISTIC VARIABLES

The system for multispecies compressible flow equations may be identified with the matrices *A*. Considering the x direction, the matix *A* associated with the primitive variables defined in the previous section is

$$A = \begin{pmatrix} u & \rho & 0 & 0 & \cdots & \cdots & \cdots & \cdots & 0 \\ \frac{RT}{\rho M} & u & 0 & 0 & \frac{R}{M} & A_{2,6} & A_{2,7} & \cdots & A_{2,N_{sp}+4} \\ 0 & 0 & u & 0 & \cdots & \cdots & \cdots & & 0 \\ 0 & 0 & 0 & u & 0 & \cdots & \cdots & & \vdots \\ 0 & \frac{RT}{C_v M} & 0 & 0 & u & 0 & \cdots & & \vdots \\ 0 & 0 & 0 & \ddots & \ddots & \ddots & \ddots & & \vdots \\ \vdots & & & \ddots & \ddots & 0 & u & 0 & \vdots \\ \vdots & & & & \ddots & \ddots & 0 & u & 0 \\ 0 & \cdots & \cdots & \cdots & \cdots & 0 & 0 & 0 & u \end{pmatrix}$$

with $A_{2,5+i} = R(1/M_\alpha - 1/M)$ i=1,...,$N_{sp} - 1$.

The jacobian for primitive variables A is diagonalized using the derivation of left and right eigenvector matrices R and L (this definition is implemented for the derivation of characteristic boundary conditions § 4.5.1) as $A = R\Lambda L$. Diagonal matrice of eigenvalues Λ is as follows :

$$\begin{pmatrix} u-c & 0 & 0 & \cdots & \cdots & \cdots & \cdots & 0 \\ 0 & u & 0 & & & & & \vdots \\ \vdots & 0 & u & 0 & & & & \vdots \\ \vdots & & 0 & \ddots & \ddots & & & \vdots \\ \vdots & & & \ddots & \ddots & \ddots & & \vdots \\ \vdots & & & & 0 & u & 0 & \vdots \\ \vdots & & & & & 0 & u & 0 \\ 0 & \cdots & \cdots & \cdots & \cdots & \cdots & 0 & u+c \end{pmatrix}$$

Matricies for right and left eigenvectors are given below

$$L = \begin{pmatrix} \frac{\rho Cp}{c^2} & 0 & 0 & 0 & 0 & \cdots & \cdots & 0 & 1 & \frac{\rho Cp}{c^2} \\ -\frac{Cp}{c} & 0 & 0 & 0 & 0 & \cdots & \cdots & 0 & 0 & \frac{Cp}{c} \\ 0 & 1 & 0 & 0 & 0 & \cdots & \cdots & 0 & 0 & 0 \\ 0 & 0 & 1 & 0 & 0 & \cdots & \cdots & 0 & 0 & 0 \\ 1 & 0 & 0 & 1 & 1 & \cdots & \cdots & 1 & 0 & 1 \\ 0 & 0 & 0 & \frac{-r}{(r_1-r_{Nsp})T} & 0 & \cdots & \cdots & 0 & \frac{-r}{(r_1-r_{sp})\rho} & 0 \\ 0 & 0 & 0 & 0 & \frac{-r}{(r_2-r_{Nsp})T} & 0 & \cdots & 0 & 0 & 0 \\ \vdots & \vdots & \vdots & \vdots & 0 & \ddots & & \vdots & \vdots & \vdots \\ \vdots & \vdots & \vdots & \vdots & \vdots & & \ddots & \vdots & \vdots & \vdots \\ 0 & 0 & 0 & 0 & \cdots & \cdots & 0 & \frac{-r}{(r_{Nsp-1}-r_{Nsp})T} & 0 & 0 \end{pmatrix}$$

$$R = \begin{pmatrix} \left(\frac{\gamma-1}{2\gamma}\right)\frac{T}{\rho} & -\frac{c}{2Cp} & 0 & 0 & \left(\frac{\gamma-1}{2\gamma}\right) & \left(\frac{\gamma-1}{2\gamma}\right)\frac{r_1-r_{Nsp}}{\overline{r}}T & \left(\frac{\gamma-1}{2\gamma}\right)\frac{r_2-r_{Nsp}}{\overline{r}}T & \cdots & \cdots & \left(\frac{\gamma-1}{2\gamma}\right)\frac{r_{Nsp-1}-r_{Nsp}}{\overline{r}}T \\ 0 & 0 & 1 & 0 & 0 & 0 & 0 & \cdots & \cdots & 0 \\ 0 & 0 & 0 & 1 & 0 & 0 & 0 & \cdots & \cdots & 0 \\ -\left(\frac{\gamma-1}{\gamma}\right)\frac{T}{\rho} & 0 & 0 & 0 & \frac{1}{\gamma} & -\left(\frac{\gamma-1}{\gamma}\right)\frac{r_1-r_{Nsp}}{\overline{r}}T & \frac{r_2-r_{Nsp}}{\gamma\overline{r}}T & \cdots & \cdots & \frac{r_{Nsp-1}-r_{Nsp}}{\gamma\overline{r}}T \\ 0 & 0 & 0 & 0 & 0 & 0 & -\frac{r_2-r_{Nsp}}{\overline{r}}T & 0 & \cdots & 0 \\ \vdots & \vdots & \vdots & \vdots & \vdots & \vdots & 0 & \ddots & 0 & \vdots \\ \vdots & \vdots & \vdots & \vdots & \vdots & \vdots & \vdots & 0 & \ddots & 0 \\ 0 & 0 & 0 & 0 & 0 & 0 & 0 & \cdots & 0 & \frac{r_{Nsp-1}-r_{Nsp}}{\overline{r}}T \\ \frac{\gamma-1}{\gamma} & 0 & 0 & 0 & -\frac{\rho}{\gamma T} & -\frac{\rho}{\gamma}\frac{r_1-r_{Nsp}}{\overline{r}} & -\frac{\rho}{\gamma}\frac{r_2-r_{Nsp}}{\overline{r}} & \cdots & \cdots & -\frac{\rho}{\gamma}\frac{r_{Nsp-1}-r_{Nsp}}{\overline{r}} \\ \left(\frac{\gamma-1}{2\gamma}\right)\frac{T}{\rho} & \frac{c}{2Cp} & 0 & 0 & \left(\frac{\gamma-1}{2\gamma}\right) & \left(\frac{\gamma-1}{2\gamma}\right)\frac{r_1-r_{Nsp}}{\overline{r}}T & \left(\frac{\gamma-1}{2\gamma}\right)\frac{r_2-r_{Nsp}}{\overline{r}}T & \cdots & \cdots & \left(\frac{\gamma-1}{2\gamma}\right)\frac{r_{Nsp-1}-r_{Nsp}}{\overline{r}}T \end{pmatrix}$$

E.3 TRANSFORMATION MATRICES BETWEEN THE CONSERVATIVE VARIABLES AND THE CHARACTERISTIC VARIABLES

Here the matrices for transformation between conservative variables and characteristic variables are presented, for the spatial discretization $\tilde{R}$ et $\tilde{L}$. These can be directly obtained diagonalizing the conservative jacobian matrices $\widetilde{A}$ but the easier way is using the relations $R = PR$ and $\tilde{L} = LP^{-1}$.

$$\tilde{R} = \begin{pmatrix} \frac{\rho C_p}{c^2} & 0 & 0 & 0 & 0 & \dots & \dots & 0 & 1 & \frac{\rho C_p}{c^2} \\ \frac{\rho C_p}{c^2}(u-c) & 0 & 0 & 0 & 0 & \dots & \dots & 0 & u & \frac{\rho C_p}{c^2}(u+c) \\ \frac{\rho C_p}{c^2}v & \rho & 0 & 0 & 0 & \dots & \dots & 0 & v & \frac{\rho C_p}{c^2}v \\ \frac{\rho C_p}{c^2}w & 0 & \rho & 0 & 0 & \dots & \dots & 0 & w & \frac{\rho C_p}{c^2}w \\ \frac{\rho C_p}{c^2}(h+K-uc) & \rho v & \rho w & R_{5,4} & R_{5,5} & \dots & \dots & R_{5,N_{sp}+3} & h - r\frac{h_1 - h_{N_{sp}}}{r_1 - r_{N_{sp}}} + K & \frac{\rho C_p}{c^2}(h+K+uc) \\ \frac{\rho C_p}{c^2}Y_1 & 0 & 0 & -\frac{\rho r}{(r_1 - r_{N_{sp}})T} & 0 & \dots & \dots & 0 & Y_1 - \frac{r}{r_1 - r_{N_{sp}}} & \frac{\rho C_p}{c^2}Y_1 \\ \frac{\rho C_p}{c^2}Y_2 & 0 & 0 & 0 & -\frac{\rho r}{(r_2 - r_{N_{sp}})T} & \dots & \dots & 0 & Y_2 & \frac{\rho C_p}{c^2}Y_2 \\ \vdots & \vdots & \vdots & \vdots & 0 & \ddots & \ddots & \vdots & \vdots & \vdots \\ \vdots & \vdots & \vdots & \vdots & \vdots & 0 & \ddots & 0 & \vdots & \vdots \\ \frac{\rho C_p}{c^2}Y_{N_{sp}-1} & 0 & 0 & 0 & \dots & \dots & 0 & -\frac{\rho r}{(r_{N_{sp}-1} - r_{N_{sp}})T} & Y_{N_{sp}-1} & \frac{\rho C_p}{c^2}Y_{N_{sp}-1} \end{pmatrix}$$

and

$$\tilde{L} = \begin{pmatrix}
R^{-1}_{1,1} & -\frac{c+(\gamma-1)u}{2\rho C_p} & -\frac{v(\gamma-1)}{2\rho C_p} & -\frac{w(\gamma-1)}{2\rho C_p} & \frac{\gamma-1}{2\rho C_p} & R^{-1}_{1,6} & R^{-1}_{1,7} & \dots & \dots & R^{-1}_{1,N_{sp}+4} \\
-\frac{v}{\rho} & 0 & \frac{1}{\rho} & 0 & 0 & 0 & 0 & \dots & \dots & 0 \\
-\frac{w}{\rho} & 0 & 0 & \frac{1}{\rho} & 0 & 0 & 0 & \dots & \dots & 0 \\
R^{-1}_{4,1} & -\frac{u}{\rho C_p} & -\frac{v}{\rho C_p} & -\frac{w}{\rho C_p} & \frac{1}{\rho C_p} & -\frac{h_1-h_{N_{sp}}}{\rho C_p} & \frac{(r_2-r_{N_{sp}})T}{\rho r} - \frac{h_2-h_{N_{sp}}}{\rho C_p} & \dots & \dots & \frac{(r_{N_{sp}-1}-r_{N_{sp}})T}{\rho r} - \frac{h_{N_{sp}-1}-h_{N_{sp}}}{\rho C_p} \\
\frac{(r_2-r_{N_{sp}})T}{\rho r}Y_2 & 0 & 0 & 0 & 0 & 0 & -\frac{r_2-r_{N_{sp}}}{\rho r}T & 0 & \dots & 0 \\
\vdots & \vdots & \vdots & \vdots & \vdots & \vdots & 0 & \ddots & & \vdots \\
\vdots & \vdots & \vdots & \vdots & \vdots & \vdots & \vdots & & \ddots & 0 \\
\frac{(r_{N_{sp}-1}-r_{N_{sp}})T}{\rho r}Y_{N_{sp}-1} & 0 & 0 & 0 & 0 & 0 & 0 & \dots & 0 & -\frac{(r_{N_{sp}-1}-r_{N_{sp}})T}{\rho r} \\
\frac{r-r_{N_{sp}}}{r} - \frac{-h_{N_{sp}}+K}{C_pT} & \frac{u}{C_pT} & \frac{v}{C_pT} & \frac{w}{C_pT} & -\frac{1}{C_pT} & -\frac{r_1-r_{N_{sp}}}{r} + \frac{h_1-h_{N_{sp}}}{C_pT} & \dots & \dots & \dots & -\frac{r_{N_{sp}-1}-r_{N_{sp}}}{r} + \frac{h_{N_{sp}-1}-h_{N_{sp}}}{C_pT} \\
R^{-1}_{N_{sp}+4,1} & \frac{c-(\gamma-1)u}{2\rho C_p} & -\frac{v(\gamma-1)}{2\rho C_p} & -\frac{w(\gamma-1)}{2\rho C_p} & \frac{\gamma-1}{2\rho C_p} & R^{-1}_{N_{sp}+4,6} & R^{-1}_{N_{sp}+4,7} & \dots & \dots & R^{-1}_{N_{sp}+4,N_{sp}+4}
\end{pmatrix}$$

with

- $K = 1/2 u_i u_i$
- $R_{5,\alpha+3} = \rho C_p - \frac{\rho r (h_\alpha - h_{N_{sp}})}{T(r_\alpha - r_{N_{sp}})}$
- $R^{-1}_{1,1} = \frac{\gamma r_{N_{sp}} T + (\gamma - 1)(-h_{N_{sp}} + K) + uc}{2\rho C_p}$
- $R^{-1}_{4,1} = \frac{1}{\rho C_p}\left[\frac{T\gamma}{\gamma - 1}\sum_{\alpha=2}^{N_{sp}}(r_{N_{sp}} - r_\alpha)Y_\alpha - h_{N_{sp}} + K\right]$
- $R^{-1}_{1,\alpha+5} = \frac{\gamma T(r_\alpha - r_{N_{sp}}) - (\gamma - 1)(h_\alpha - h_{N_{sp}})}{2\rho C_p}$ with $\alpha = 1, \ldots, N_{sp} - 1$
- $R^{-1}_{N_{sp}+4,1} = \frac{\gamma r_{N_{sp}} T + (\gamma - 1)(-h_{N_{sp}} + K) - uc}{2\rho C_p}$
- $R^{-1}_{N_{sp}+4,\alpha+5} = R^{-1}_{1,\alpha+5}$ with $\alpha = 1, \ldots, N_{sp} - 1$

APPENDIX F

WAVE AMPLITUDES AND LODI SYSTEM IN TERMS OF PRIMITIVE VARIABLES

LODI system wave amplitudes in x direction :

$$
\begin{aligned}
\mathcal{L}_1 &= \frac{u-c}{2\,\rho C p}\left(\frac{\partial P}{\partial x}-\rho c\frac{\partial u}{\partial x}\right)\\
\mathcal{L}_2 &= u\frac{\partial v}{\partial x}\\
\mathcal{L}_3 &= u\frac{\partial w}{\partial x}\\
\mathcal{L}_4 &= u\;T\left[\frac{1}{\rho}\left(\frac{1}{c^2}\frac{\partial P}{\partial x}-\frac{\partial \rho}{\partial x}\right)-\left(\frac{r_1-r_{N_{sp}}}{r}\right)\frac{\partial Y_1}{\partial x}\right]\\
\mathcal{L}_{\alpha+3} &= -u\;T\left(\frac{r_\alpha-r_{N_{sp}}}{r}\right)\frac{\partial Y_\alpha}{\partial x}\quad;\quad \alpha=(2,...,N_{sp}-1)\\
\mathcal{L}_{N_{sp}+3} &= u\left(\frac{\partial \rho}{\partial x}-\frac{\partial P}{\partial x}\frac{1}{c^2}\right)\\
\mathcal{L}_{N_{sp}+4} &= \frac{u+c}{2\,\rho C p}\left(\frac{\partial P}{\partial x}+\rho\;c\;\frac{\partial u}{\partial x}\right)
\end{aligned}
\tag{F.1}
$$

LODI system primitive derivatives in x direction :

$$
\begin{aligned}
d_1 &= \frac{\partial \rho}{\partial t} = \frac{\rho C_p}{c^2}(\mathcal{L}_1+\mathcal{L}_{N_{sp}+4})+\mathcal{L}_{N_{sp}+3}\\
d_2 &= \frac{\partial u}{\partial t} = \frac{C_p}{c}(\mathcal{L}_{N_{sp}+4}-\mathcal{L}_1)\\
d_3 &= \frac{\partial v}{\partial t} = \mathcal{L}_2\\
d_4 &= \frac{\partial w}{\partial t} = \mathcal{L}_3\\
d_5 &= \frac{\partial T}{\partial t} = \mathcal{L}_1+\mathcal{L}_4+\sum_{\alpha=2}^{N_{sp}-1}\mathcal{L}_{\alpha+3}+\mathcal{L}_{N_{sp}+4}\\
d_6 &= \frac{\partial Y_1}{\partial t} = -\left(\frac{r}{r_1-r_{N_{sp}}}\right)\left(\frac{\mathcal{L}_{N_{sp}+3}}{\rho}+\frac{\mathcal{L}_4}{T}\right)\\
d_{5+\alpha} &= \frac{\partial Y_\alpha}{\partial t} = -\left(\frac{r}{r_\alpha-r_{N_{sp}}}\right)\frac{\mathcal{L}_{\alpha+3}}{T}\quad \alpha=(2,...,N_{sp}-1)
\end{aligned}
\tag{F.2}
$$

LODI system wave amplitudes in y direction :

$$
\begin{aligned}
\mathcal{L}_1 &= \frac{v-c}{2\,\rho C p}\left(\frac{\partial P}{\partial y}-\rho c\frac{\partial v}{\partial y}\right)\\
\mathcal{L}_2 &= v\frac{\partial u}{\partial y}\\
\mathcal{L}_3 &= v\,T\left[\frac{1}{\rho}\left(\frac{1}{c^2}\frac{\partial P}{\partial y}-\frac{\partial \rho}{\partial y}\right)-\left(\frac{r_1-r_{N_{sp}}}{r}\right)\frac{\partial Y_1}{\partial y}\right]\\
\mathcal{L}_4 &= v\frac{\partial w}{\partial y}\\
\mathcal{L}_{\alpha+3} &= -v\,T\left(\frac{r_\alpha-r_{N_{sp}}}{r}\right)\frac{\partial Y_\alpha}{\partial y} \quad ; \quad \alpha=(2,\ldots,N_{sp}-1)\\
\mathcal{L}_{N_{sp}+3} &= v\left(\frac{\partial \rho}{\partial y}-\frac{\partial P}{\partial y}\frac{1}{c^2}\right)\\
\mathcal{L}_{N_{sp}+4} &= \frac{v+c}{2\,\rho C p}\left(\frac{\partial P}{\partial y}+\rho\,c\,\frac{\partial v}{\partial y}\right)
\end{aligned}
\tag{F.3}
$$

LODI system primitive derivatives in y direction :

$$
\begin{aligned}
d_1 &= \frac{\partial \rho}{\partial t} = \frac{\rho C_p}{c^2}(\mathcal{L}_1+\mathcal{L}_{N_{sp}+4})+\mathcal{L}_{N_{sp}+3}\\
d_2 &= \frac{\partial u}{\partial t} = \mathcal{L}_2\\
d_3 &= \frac{\partial v}{\partial t} = \frac{C_p}{c}(\mathcal{L}_{N_{sp}+4}-\mathcal{L}_1)\\
d_4 &= \frac{\partial w}{\partial t} = \mathcal{L}_4\\
d_5 &= \frac{\partial T}{\partial t} = \mathcal{L}_1+\mathcal{L}_3+\sum_{\alpha=2}^{N_{sp}-1}\mathcal{L}_{\alpha+3}+\mathcal{L}_{N_{sp}+4}\\
d_6 &= \frac{\partial Y_1}{\partial t} = -\left(\frac{r}{r_1-r_{N_{sp}}}\right)\left(\frac{\mathcal{L}_{N_{sp}+3}}{\rho}+\frac{\mathcal{L}_3}{T}\right)\\
d_{5+\alpha} &= \frac{\partial Y_\alpha}{\partial t} = -\left(\frac{r}{r_\alpha-r_{N_{sp}}}\right)\frac{\mathcal{L}_{\alpha+3}}{T} \quad \alpha=(2,\ldots,N_{sp}-1)
\end{aligned}
\tag{F.4}
$$

LODI system wave amplitudes in z direction :

$$
\begin{aligned}
\mathcal{L}_1 &= \frac{w-c}{2\,\rho C p}\left(\frac{\partial P}{\partial z} - \rho c \frac{\partial w}{\partial z}\right) \\
\mathcal{L}_2 &= w\,T\left[\frac{1}{\rho}\left(\frac{1}{c^2}\frac{\partial P}{\partial z} - \frac{\partial \rho}{\partial z}\right) - \left(\frac{r_1 - r_{N_{sp}}}{r}\right)\frac{\partial Y_1}{\partial z}\right] \\
\mathcal{L}_3 &= w\frac{\partial u}{\partial z} \\
\mathcal{L}_4 &= w\frac{\partial v}{\partial z} \\
\mathcal{L}_{\alpha+3} &= -w\,T\left(\frac{r_\alpha - r_{N_{sp}}}{r}\right)\frac{\partial Y_\alpha}{\partial z} \quad ; \quad \alpha = (2, ..., N_{sp}-1) \\
\mathcal{L}_{N_{sp}+3} &= w\left(\frac{\partial \rho}{\partial z} - \frac{\partial P}{\partial z}\frac{1}{c^2}\right) \\
\mathcal{L}_{N_{sp}+4} &= \frac{w+c}{2\,\rho C p}\left(\frac{\partial P}{\partial z} + \rho\, c\,\frac{\partial u}{\partial z}\right)
\end{aligned}
\tag{F.5}
$$

LODI system primitive derivatives in z direction :

$$
\begin{aligned}
d_1 &= \frac{\partial \rho}{\partial t} = \frac{\rho C_p}{c^2}(\mathcal{L}_1 + \mathcal{L}_{N_{sp}+4}) + \mathcal{L}_{N_{sp}+3} \\
d_2 &= \frac{\partial w}{\partial t} = \frac{C_p}{c}(\mathcal{L}_{N_{sp}+4} - \mathcal{L}_1) \\
d_3 &= \frac{\partial u}{\partial t} = \mathcal{L}_3 \\
d_4 &= \frac{\partial v}{\partial t} = \mathcal{L}_4 \\
d_5 &= \frac{\partial T}{\partial t} = \mathcal{L}_1 + \mathcal{L}_2 + \sum_{\alpha=2}^{N_{sp}-1}\mathcal{L}_{\alpha+3} + \mathcal{L}_{N_{sp}+4} \\
d_6 &= \frac{\partial Y_1}{\partial t} = -\left(\frac{r}{r_1 - r_{N_{sp}}}\right)\left(\frac{\mathcal{L}_{N_{sp}+3}}{\rho} + \frac{\mathcal{L}_2}{T}\right) \\
d_{5+\alpha} &= \frac{\partial Y_\alpha}{\partial t} = -\left(\frac{r}{r_\alpha - r_{N_{sp}}}\right)\frac{\mathcal{L}_{\alpha+3}}{T} \quad \alpha = (2, ..., N_{sp}-1)
\end{aligned}
\tag{F.6}
$$

APPENDIX G

WENO COEFFICIENTS

Table G.1: Coefficients c_{rj} for k=1 to 6.

k	r	$j=0$	$j=1$	$j=2$	$j=3$	$j=4$	$j=5$
1	0	1					
2	0	1/2	1/2				
	1	-1/2	3/2				
3	0	1/3	5/6	-1/6			
	1	-1/6	5/6	1/3			
	2	1/3	-7/6	11/6			
4	0	1/4	13/12	-5/12	1/12		
	1	-1/12	7/12	7/12	-1/12		
	2	1/12	-5/12	13/12	1/4		
	3	-1/4	13/12	-23/12	25/12		
5	0	1/5	77/60	-43/60	17/60	-1/20	
	1	-1/20	9/20	47/60	-13/60	1/30	
	2	1/30	-13/60	47/60	9/20	-1/20	
	3	-1/20	17/60	-43/60	77/60	1/5	
	4	1/5	-21/20	137/60	-163/60	137/60	
6	0	1/6	29/20	-21/20	37/60	-13/60	1/30
	1	-1/30	11/30	19/20	-23/60	7/60	-1/60
	2	1/60	-2/15	37/60	37/60	-2/15	1/60
	3	-1/60	7/60	-23/60	19/20	11/30	-1/30
	4	1/30	-13/60	37/60	-21/20	29/20	1/6
	5	-1/6	31/30	-163/60	79/20	-71/20	49/20

Table G.2: Coefficients d_r for k=1 to 6.

K	r=0	r=1	r=2	r=3	r=4	r=5
1	1					
2	2/3	1/3				
3	3/10	3/5	1/10			
4	4/35	18/35	12/35	1/35		
5	5/126	40/126	60/126	20/126	1/126	
6	1/77	25/154	100/231	25/77	5/77	1/462

The coefficients β necessary for computation of the smoothness indicators β_r, for different stencils presented for reconstruction for k = 1 to 6.

k=1

There exist single stencil for reconstruction : $S_0 = (i)$.

$$\beta_0 = f_i f_i$$

k=2

There exist two stencils for reconstruction : $S_0 = (i, i+1) \quad S_1 = (i-1, i)$.

$$\begin{aligned} \beta_0 &= (f_{i+1} - f_i)^2 \\ \beta_1 &= (f_i - f_{i-1})^2 \end{aligned}$$

k=3

There exist three stencils for reconstruction : $S_0 = (i, i+1, i+2) \quad S_1 = (i-1, i, i+1) \quad S_2 = (i-2, i-1, i)$.

$$\begin{aligned} \beta_0 &= \frac{13}{12}(f_i - 2f_{i+1} + f_{i+2})^2 + \frac{1}{4}(3f_i - 4f_{i+1} + f_{i+2})^2 \\ \beta_1 &= \frac{13}{12}(f_{i-1} - 2f_i + f_{i+1})^2 + \frac{1}{4}(f_{i-1} - f_{i+1})^2 \\ \beta_2 &= \frac{13}{12}(f_{i-2} - 2f_{i-1} + f_i)^2 + \frac{1}{4}(f_{i-2} - 4f_{i-1} + 3f_i)^2 \end{aligned}$$

K=4

There exist four stencils for reconstruction : $S_0 = (i, i+1, i+2, i+3) \quad S_1 = (i-1, i, i+1, i+$

2) $S_2 = (i-2, i-1, i, i+1)$ $S_3 = (i-3, i-2, i-1, i)$.

$$
\begin{aligned}
\beta_0 &= 2107 f_i^2 - 9402 f_{i+1} f_i + 7042 f_{i+2} f_i - 1854 f_{i+3} f_i + 11003 f_{i+1}^2 - 17246 f_{i+2} f_{i+1} \\
&+ 4642 f_{i+3} f_{i+1} + 7043 f_{i+2}^2 - 3882 f_{i+3} f_{i+2} + 547 f_{i+3}^2 \\
\beta_1 &= 547 f_{i-1}^2 - 2522 f_i f_{i-1} + 1922 f_{i+1} f_{i-1} - 494 f_{i+2} f_{i-1} + 3443 f_i^2 - 5966 f_{i+1} f_i \\
&+ 1602 f_{i+2} f_i + 2843 f_{i+1}^2 - 1642 f_{i+2} f_{i+1} + 267 f_{i+2}^2 \\
\beta_2 &= 267 f_{i-2}^2 - 1642 f_{i-1} f_{i-2} + 1602 f_i f_{i-2} - 494 f_{i+1} f_{i-2} + 2843 f_{i-1}^2 - 5966 f_i f_{i-1} \\
&+ 1922 f_{i+1} f_{i-1} + 3443 f_i^2 - 2522 f_{i+1} f_i + 547 f_{i+1}^2 \\
\beta_3 &= 547 f_{i-3}^2 - 3882 f_{i-2} f_{i-3} + 4642 f_{i-1} f_{i-3} - 1854 f_i f_{i-3} + 7043 f_{i-2}^2 - 17246 f_{i-1} f_{i-2} \\
&+ 7042 f_i f_{i-2} + 11003 f_{i-1}^2 - 9402 f_i f_{i-1} + 2107 f_i^2
\end{aligned}
$$

K=5

There exist five stencils for reconstruction : $S_0 = (i, i+1, i+2, i+3, i+4)$ $S_1 = (i-1, i, i+1, i+2, i+3)$ $S_2 = (i-2, i-1, i, i+1, i+2)$ $S_3 = (i-3, i-2, i-1, i, i+1)$ $S_4 = (i-4, i-3, i-2, i-1, i)$.

$$
\begin{aligned}
\beta_0 &= 107918 f_i^2 - 649501 f_{i+1} f_i + 758823 f_{i+2} f_i - 411487 f_{i+3} f_i + 86329 f_{i+4} f_i \\
&+ 1020563 f_{i+1}^2 - 2462076 f_{i+2} f_{i+1} + 1358458 f_{i+3} f_{i+1} - 288007 f_{i+4} f_{i+1} + 1521393 f_{i+2}^2 \\
&- 1704396 f_{i+3} f_{i+2} + 364863 f_{i+4} f_{i+2} + 482963 f_{i+3}^2 - 208501 f_{i+4} f_{i+3} + 22658 f_{i+4}^2 \\
\beta_1 &= 22658 f_{i-1}^2 - 140251 f_i f_{i-1} + 165153 f_{i+1} f_{i-1} - 88297 f_{i+2} f_{i-1} + 18079 f_{i+3} f_{i-1} \\
&+ 242723 f_i^2 - 611976 f_{i+1} f_i + 337018 f_{i+2} f_i - 70237 f_{i+3} f_i + 406293 f_{i+1}^2 \\
&- 464976 f_{i+2} f_{i+1} + 99213 f_{i+3} f_{i+1} + 138563 f_{i+2}^2 - 60871 f_{i+2} f_{i+3} + 6908 f_{i+3}^2 \\
\beta_2 &= 6908 f_{i-2}^2 - 51001 f_{i-1} f_{i-2} + 67923 f_i f_{i-2} - 38947 f_{i+1} f_{i-2} + 8209 f_{i+2} f_{i-2} \\
&+ 104963 f_{i-1}^2 - 299076 f_i f_{i-1} + 179098 f_{i+1} f_{i-1} - 38947 f_{i+2} f_{i-1} + 231153 f_i^2 \\
&- 299076 f_{i+1} f_i + 67923 f_{i+2} f_i + 104963 f_{i+1}^2 - 51001 f_{i+2} f_{i+1} + 6908 f_{i+2} \\
\beta_3 &= 6908 f_{i-3}^2 - 60871 f_{i-2} f_{i-3} + 99213 f_{i-1} f_{i-3} - 70237 f_i f_{i-3} + 18079 f_{i+1} f_{i-3} \\
&+ 138563 f_{i-2}^2 - 464976 f_{i-1} f_{i-2} + 337018 f_i f_{i-2} - 88297 f_{i+1} f_{i-2} + 406293 f_{i-1}^2 \\
&- 611976 f_i f_{i-1} + 165153 f_{i+1} f_{i-1} + 242723 f_i^2 - 140251 f_{i+1} f_i + 22658 f_{i+1}^2 \\
\beta_4 &= 22658 f_{i-4}^2 - 208501 f_{i-3} f_{i-4} + 364863 f_{i-2} f_{i-4} - 288007 f_{i-1} f_{i-4} + 86329 f_i f_{i-4} \\
&+ 482963 f_{i-3}^2 - 1704396 f_{i-2} f_{i-3} + 1358458 f_{i-1} f_{i-3} - 411487 f_i f_{i-3} + 1521393 f_{i-2}^2 \\
&- 2462076 f_{i-1} f_{i-2} + 758823 f_i f_{i-2} + 1020563 f_{i-1}^2 - 649501 f_{i-1} f_i + 107918 f_i^2
\end{aligned}
$$

K=6

There exist six stencils for reconstruction : $S_0 = (i, i+1, i+2, i+3, i+4, i+5)$ $S_1 = (i-1, i, i+1, i+2, i+3, i+4)$ $S_2 = (i-2, i-1, i, i+1, i+2, i+3)$ $S_3 = (i-3, i-2, i-1, i, i+1, i+2)$ $S_4 = (i-5, i-4, i-3, i-2, i-1, i)$ $S_5 = (i-4, i-3, i-2, i-1, i)$.

$$
\begin{aligned}
\beta_0 &= 6150211 f_i^2 - 47460464 f_{i+1} f_i + 76206736 f_{i+2} f_i - 63394124 f_{i+3} f_i + 27060170 f_{i+4} f_i \\
&- 4712740 f_{i+5} f_i + 94851237 f_{i+1}^2 - 311771244 f_{i+2} f_{i+1} + 262901672 f_{i+3} f_{i+1} - 113206788 f_{i+4} f_{i+1} \\
&+ 19834350 f_{i+5} f_{i+1} + 260445372 f_{i+2}^2 - 444003904 f_{i+3} f_{i+2} + 192596472 f_{i+4} f_{i+2} \\
&- 33918804 f_{i+5} f_{i+2} + 190757572 f_{i+3}^2 - 166461044 f_{i+4} f_{i+3} + 29442256 f_{i+5} f_{i+3} \\
&+ 36480687 f_{i+4}^2 - 12950184 f_{i+5} f_{i+4} + 1152561 f_{i+5}^2 \\
\beta_1 &= 1152561 f_{i-1}^2 - 9117992 f_i f_{i-1} + 14742480 f_{i+1} f_{i-1} - 12183636 f_{i+2} f_{i-1} + 5134574 f_{i+3} f_{i-1} \\
&- 880548 f_{i+4} f_{i-1} + 19365967 f_i^2 - 65224244 f_{i+1} f_i + 55053752 f_{i+2} f_i - 23510468 f_{i+3} f_i \\
&+ 4067018 f_{i+4} f_i + 56662212 f_{i+1}^2 - 97838784 f_{i+2} f_{i+1} + 42405032 f_{i+3} f_{i+1} - 7408908 f_{i+4} f_{i+1} \\
&+ 43093692 f_{i+2}^2 - 37913324 f_{i+3} f_{i+2} + 6694608 f_{i+4} f_{i+2} + 8449957 f_{i+3}^2 - 3015728 f_{i+4} f_{i+3} \\
&+ 271779 f_{i+4}^2 \\
\beta_2 &= 271779 f_{i-2}^2 - 2380800 f_{i-1} f_{i-2} + 4086352 f_i f_{i-2} - 3462252 f_{i+1} f_{i-2} + 1458762 f_{i+2} f_{i-2} \\
&- 245620 f_{i+3} f_{i-2} + 5653317 f_{i-1}^2 - 20427884 f_i f_{i-1} + 17905032 f_{i+1} f_{i-1} - 7727988 f_{i+2} f_{i-1} \\
&+ 1325006 f_{i+3} f_{i-1} + 19510972 f_i^2 - 35817664 f_{i+1} f_i + 15929912 f_{i+2} f_i - 2792660 f_{i+3} f_i \\
&+ 17195652 f_{i+1}^2 - 15880404 f_{i+2} f_{i+1} + 2863984 f_{i+3} f_{i+1} + 3824847 f_{i+2} - 1429976 f_{i+3} f_{i+2} \\
&+ 139633 f_{i+3}^2 \\
\beta_3 &= 139633 f_{i-3}^2 - 1429976 f_{i-2} f_{i-3} + 2863984 f_{i-1} f_{i-3} - 2792660 f_i f_{i-3} + 1325006 f_{i+1} f_{i-3} \\
&- 245620 f_{i+2} f_{i-3} + 3824847 f_{i-2}^2 - 15880404 f_{i-1} f_{i-2} + 15929912 f_i f_{i-2} - 7727988 f_{i+1} f_{i-2} \\
&+ 1458762 f_{i+2} f_{i-2} + 17195652 f_{i-1}^2 - 35817664 f_i f_{i-1} + 17905032 f_{i+1} f_{i-1} - 3462252 f_{i+2} f_{i-1} \\
&+ 19510972 f_i^2 - 20427884 f_{i+1} f_i + 4086352 f_{i+2} f_i + 5653317 f_{i+1}^2 - 2380800 f_{i+2} f_{i+1} \\
&+ 271779 f_{i+2}^2 \\
\beta_4 &= 271779 f_{i-4}^2 - 3015728 f_{i-3} f_{i-4} + 6694608 f_{i-2} f_{i-4} - 7408908 f_{i-1} f_{i-4} + 4067018 f_i f_{i-4} \\
&- 880548 f_{i+1} f_{i-4} + 8449957 f_{i-3}^2 - 37913324 f_{i-2} f_{i-3} + 42405032 f_{i-1} f_{i-3} - 23510468 f_i f_{i-3} \\
&+ 5134574 f_{i+1} f_{i-3} + 43093692 f_{i-2}^2 - 97838784 f_{i-1} f_{i-2} + 55053752 f_i f_{i-2} - 12183636 f_{i+1} f_{i-2} \\
&+ 56662212 f_{i-1}^2 - 65224244 f_i f_{i-1} + 14742480 f_{i+1} f_{i-1} + 19365967 f_i^2 - 9117992 f_{i+1} f_i \\
&+ 1152561 f_{i+1}^2
\end{aligned}
\tag{G.1}
$$

$$
\begin{aligned}
\beta_5 &= 1152561\, f_{i-5}^2 - 12950184\, f_{i-4} f_{i-4} + 29442256\, f_{i-3} f_{i-4} - 33918804\, f_{i-2} f_{i-4} \\
&+ 19834350\, f_{i-1} f_{i-4} - 4712740\, f_i f_{i-4} + 36480687\, f_{i-4}^2 - 166461044\, f_{i-3} f_{i-3} \\
&+ 192596472\, f_{i-2} f_{i-3} - 113206788\, f_{i-1} f_{i-3} + 27060170\, f_i f_{i-3} + 190757572\, f_{i-3}^2 \\
&- 444003904\, f_{i-2} f_{i-2} + 262901672\, f_{i-1} f_{i-2} - 63394124\, f_i f_{i-2} + 260445372\, f_{i-2}^2 \\
&- 311771244\, f_{i-1} f_{i-1} + 76206736\, f_i f_{i-1} + 94851237\, f_{i-1}^2 - 47460464\, f_i f_i + 6150211\, f_i^2
\end{aligned}
$$

APPENDIX H

COMPRESSIBLE TEMPORAL MIXING LAYER *A PRIORI* TESTS

The *a priori* tests which were conducted by Lardjane and Fedioun, for the sub-grid terms of NS equations in the framework of a temporal binary mixing layer are presented in this appendix.

The effect of physical parameters (density ratio, temperature, compressibility...) on the following sub-grid terms which were derived filtering the multicomponent compressible NS equations in convective form was investigated.

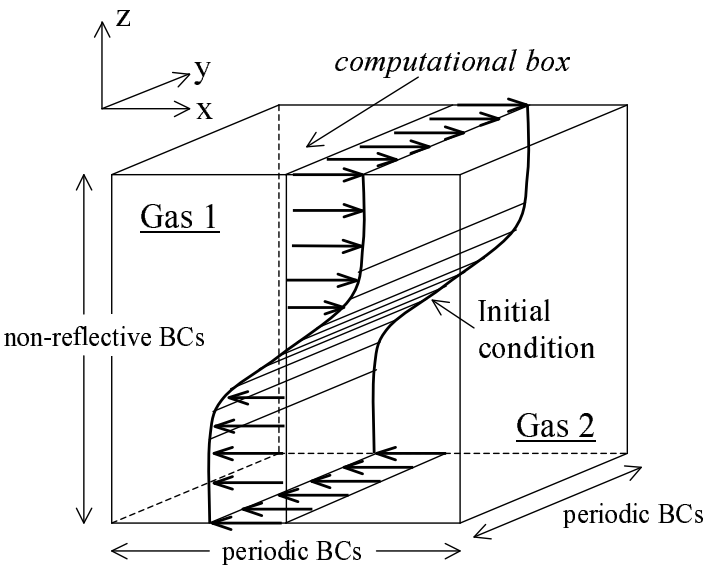

Figure H.1: Computational box for the temporal direct numerical simulation

- filtered equation of motion

$$\begin{aligned} A_{1i} &= -[\overline{\rho}(\widetilde{u_i u_j} - \widetilde{u_i}\widetilde{u_j})]_{,j} \\ A_{2i} &= (\overline{\mu S_{ij}} - \widetilde{\mu}\widetilde{S_{ij}})_{,j} \qquad \text{(H.1)} \\ A_{3i} &= -[\overline{\rho}\left(\widetilde{rT} - \widetilde{r}\widetilde{T}\right)]_{,i} \qquad \text{(H.2)} \end{aligned}$$

- filtered energy equation

$$\begin{aligned} B_1 &= \left(\overline{\lambda T_{,j}} - \widetilde{\lambda}\widetilde{T}_{,j}\right)_{,j} \\ B_2 &= -\left(\overline{pu_{j,j}} - \overline{p}\widetilde{u}_{j,j}\right) \qquad \text{(H.3)} \\ B_3 &= \overline{u_{i,j}\tau_{ij}} - \widetilde{u}_{i,j}\overline{\tau_{ij}} \end{aligned}$$

- filtered species equation

$$\begin{aligned} C_{\alpha 1} &= -[\overline{\rho}\left(\widetilde{Y_\alpha u_j} - \widetilde{Y}_\alpha \widetilde{u_j}\right)]_{,j} \qquad \text{(H.4)} \\ C_{\alpha 2} &= [\overline{\rho}\left(\widetilde{D_{\alpha m} Y_{\alpha,j}} - \widetilde{D}_{\alpha m}\widetilde{Y}_{\alpha,j}\right)]_{,j} \end{aligned}$$

The field of sub-grid terms was rebuilt out of D.N.S. flow variables by means of explicit S.O.C.F. box filtering of flow variables [53]. The DNS solutions were obtained applying 6^{th} order compact scheme for spatial discretization and 3^{rd} order time integration and accurate transport model. The physical and numerical parameters for several DNS computations are gathered in Tables H.1 and H.2. The sub-grid terms were quantified as r.m.s. of transverse

Table H.1: D.N.S. physical and numerical parameters for the O_2/N_2 pair.

O_2/N_2	#1	#2	#3	#4	#5
Re_{ref}	100	100	200	400	100
M_c	0.293	0.586	0.880	0.293	0.246
U (m/s)	±100	±200	±300	±100	±100
T_2/T_1 (K)	300/300	300/300	300/300	300/300	600/300
$Lx \times Ly \times Lz$	40×40×80	same as #1	40×40×40	28×28×40	same as #1
$Nx \times Ny \times Nz$	181×181×245	same as #1	255×255×257	same as #3	same as #1

profiles obtained averaging variables in homogeneous streamwise x and spanwise y directions. The relative magnitudes of sub-grid terms are presented in Figures H.2 - H.7. It is seen that, when the index i corresponds to the cross-flow direction, $A_{3,i}$ becomes non-negligible when the N_2 stream is heated relatively to the O_2 stream and may overcome $A_{1ij,j}$ in some cases.

Table H.2: D.N.S physical and numerical parameters for the O_2/H_2 pair.

O_2/H_2	#1	#2	#3	#4	#5
Re_{ref}	100	100	200	200	100
M_c	0.121	0.243	0.607	0.121	0.113
$U\ (m/s)$	±100	±200	±500	±100	±100
$T_2/T_1\ (K)$	300/300	300/300	300/300	300/300	600/300
$Lx \times Ly \times Lz$	33×33×60	20×20×60	same as #2	same as #1	same as #2
$Nx \times Ny \times Nz$	199×199×485	same as #1	same as #1	same as #1	same as #1

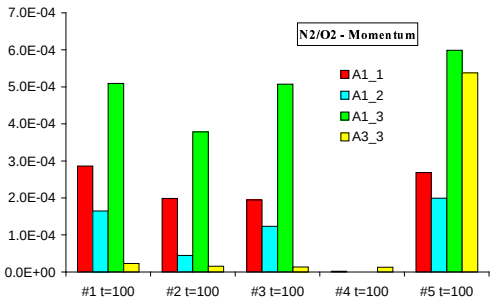

Figure H.2: Subrid terms (H.1). Relative magnitude: O_2/N_2

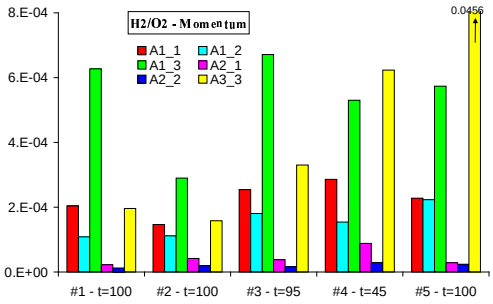

Figure H.3: same as Figure H.2: O_2/H_2

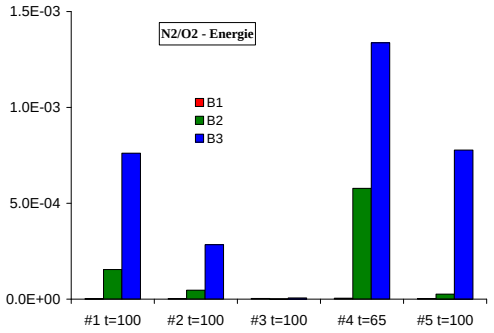

Figure H.4: Subrid terms (H.3). Relative magnitude: O_2/N_2

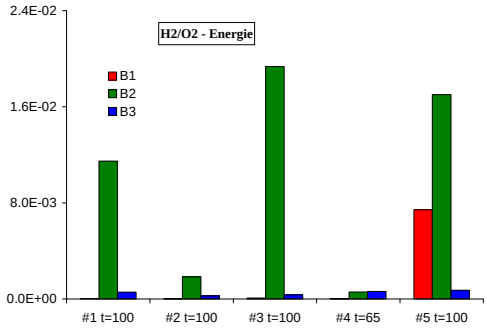

Figure H.5: same as Figure H.4: O_2/H_2

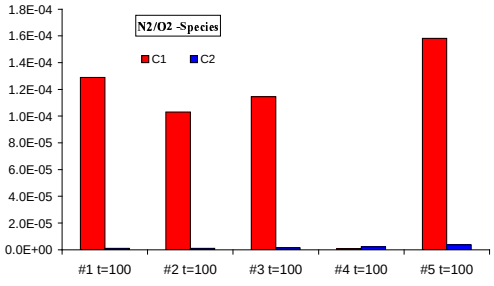

Figure H.6: Subrid terms (H.4). Relative magnitude: O_2/N_2

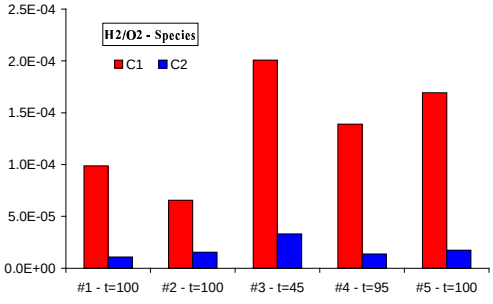

Figure H.7: same as Figure H.6: O_2/H_2

APPENDIX I

COMPUTATIONAL HOURS

	Non-Reacting			Reacting		
	wall time	CPU/step	cost	wall time	CPU/step	cost
MILES_EULER	14238 s	508.4 s	**1**	73314 s	938.0 s	**1.845**
MILES_NS	16581 s	599.2 s	**1.178**	88540 s	1132.9 s	**2.228**
LES_SSF	16482 s	625.1 s	**1.229**	90284 s	1155.2 s	**2.272**
LES_SM	15680 s	603.6 s	**1.187**	—	—	—

Table I.1: Relative cost of LES and MILES, non-reacting and reacting.